

---

FUNCTIONALIZATION OF TWO-DIMENSIONAL  
TRANSITION METAL OXIDES FOR THE SENSING  
APPLICATIONS

---

Thesis submitted for the degree of  
Doctor in Sciences: Physics

**ZIHAN WEI**

January 2021

Promoters: Prof. Dr. Serge Zhuiykov  
Prof. Dr. Stephen Depuydt

---

Functionalizeren van twee dimensionale transitie metaloxides  
voor sensor-toepassingen.

---

Thesis submitted for the degree of  
Doctor in Sciences: Physics

**ZIHAN WEI**

January 2021

Promotors: Prof. Dr. Serge Zhuiykov  
Prof. Dr. Stephen Depuydt

THE PAGE IS INHERENTLY BLANK

## ACADEMIC MEMBERS IN UNIVERSITEIT GENT

---

<b>Promoter:</b>	Prof. Dr. Ir. Serge Zhuiykov Faculty of Sciences Department of Solid State Sciences Universiteit Gent, Belgium Center for Environmental and Energy Ghent University Global Campus, Korea
<b>Co-promoter:</b>	Prof. Dr. Ir. Stephen Depuydt Faculty of Sciences Department of Plant Biotechnology and Bioinformatics Universiteit Gent, Belgium Ghent University Global Campus, Korea
<b>Dean of Faculty:</b>	Prof. Dr. Isabel Van Driessche Faculty of Sciences Universiteit Gent, Belgium
<b>Rector:</b>	Prof. Dr. ir. Rik Van de Walle Universiteit Gent, Belgium

## ACADEMIC MEMBERS IN DISSERTATION COMMITTEE

---

<b>Chairman</b>	<p><b>Prof. Dr. Christophe Detavernier</b>  Department of Solid State Sciences, Faculty of Science,  Universiteit Gent, Belgium</p>
<b>Promoter</b>	<p><b>Prof. Dr. Ir. Serge Zhuiykov</b>  Faculty of Sciences, Department of Solid State Sciences, Universiteit Gent  Belgium  Center for Environmental and Energy, Ghent University Global Campus,  Korea</p>
<b>Co-promoter</b>	<p><b>Prof. Dr. ir. Stephen Depuydt</b>  Department of Plant Biotechnology and Bioinformatics, Faculty of  Sciences, Universiteit Gent, Belgium  Ghent University Global Campus, Korea</p>
<b>Members of the Jury</b>	<p><b>Prof. Dr. Francis Verpoort</b>  Center for Chemical and Material Engineering, Wuhan University of  Technology, Wuhan, China  Faculty of Sciences, Department of Chemistry, Universiteit Gent,  Belgium</p> <p><b>Prof. Dr. Ir. Philippe M. Heynderickx</b>  Faculty of Bioscience Engineering, Universiteit Gent, Belgium  Center for Environmental and Energy research Ghent University Global  Campus, Korea</p> <p><b>Prof. Dr. Surender Kumar</b>  Department of Environmental Technology, Food Technology and  Molecular Biotechnology, Ghent University Global Campus, Korea</p> <p><b>Prof. Joondong Kim</b>  Photoelectric and Energy Device Application Lab (PEDAL),  Multidisciplinary Core Institute for Future Energies (MCIFE), Incheon  National University, Korea</p> <p><b>Prof. Malkeshkumar Patel</b>  Department of Electrical Engineering, Incheon National University,  Korea</p>

## PREFACE

---

The discovery of graphene in 2004 opened a door of a completely new playground of two-dimensional nanomaterials, which features atomic-level thickness, super high surface-to-volume ratio, and tunable electronic properties. Among them, single- and few-layer transition metal oxides have received relatively little attention compared to other families of atomically thin-layered transition metal dichalcogenides, even though they are more chemically stable and environmental friendly as well as easier to be prepared. 2D transition metal oxides can be fabricated by a variety of methods, including “top-down” and “bottom-up” approaches. In our work, 2D  $\alpha$ - $\text{MoO}_3$  and  $\text{WO}_3$  nanofilms with the controlled thickness were developed by an atomic layer deposition technique, due to the advantages of deposition of large-scale, conformal, dense nanofilms with precise thickness, and their applications in sensors were also investigated at the same time.

Since, in some cases, the properties of bare 2D transition metal oxides unable to meet most of the commercial requirements, 2D transition metal oxides-based heterostructures provide the strategies to improve their performances and broaden the scope of their applications. Based on the research survey about the methods of surface functionalization on 2D transition metal oxides and dichalcogenides, functionalization of 2D  $\text{WO}_3$  nanofilms with different kinds and amounts of noble metals was developed for the electrochemical sensing application. The functionalization of  $\text{Ga}_2\text{O}_3$  on the surface of 2D  $\text{WO}_3$  nanofilms to form p-n heterojunction for the improvement of gas sensing properties was also investigated.

## ACKNOWLEDGMENTS

---

My Ph.D. would not be possible without the help and support from the kind persons around me, my promotor, professors, colleagues, friends, and family. First of all, I would like to express my deep sense of gratitude to my promotor Professor Serge Zhuiykov for his continuous support, valuable advice, and especially his trust, which encourages me to explore the field I like. His guidance helped me in all the time of the research and writing this thesis. I also appreciate my copromoter, Professor Stephen Depuydt, for his patience, motivation, encouragement, and enthusiasm.

Besides, my special appreciation goes to Prof. Christophe Detavernier. Without the unlimited technical support and training opportunities of the ALD technique from him and his CoCooN group, my research work would not have been smooth, and I have learned a lot related to the ALD technique from him and his group.

Also, I would like to thank my colleagues and professors, Dr. Zhenyin Hai, Dr. Mohammad Karbalaee Akbari, Prof. Taejun Han, Prof. Francis Verpoort, Prof. Philippe M. Heynderickx, Prof. Jie Hu, Dr. Zhenting Zhao, and Dr. Yongjiao Sun for their scientific advice and also for their support and encouragement. In particular, I am grateful to Prof. Jie Hu for enlightening me when I have problems with my research and daily life.

Many thanks also go to my friends at Ghent University Global Campus, Lingdai Liu, Nathan Muyinda, Manuel Gasparyan, Christia Jabbor, Kashika Aroura, Noor Aljammal, Nikola Stevanovic, Krishna de Guzman and Amin Nikkhah Kolachahi, for their sincere friendship and all the fun we have had in the last four years.

My deepest gratitude goes to my family for their love, understanding, and support.

# TABLE OF CONTENTS

---

ACADEMIC MEMBERS IN UNIVERSITEIT GENT.....	iii
ACADEMIC MEMBERS IN DISSERTATION COMMITTEE.....	iv
PREFACE.....	v
ACKNOWLEDGMENTS.....	vi
TABLE OF CONTENTS.....	vii
LIST OF ABBREVIATIONS.....	x
LIST OF SYMBOLS.....	xii
LIST OF TABLES .....	xiii
LIST OF FIGURES.....	xiv
LIST OF PUBLICATIONS.....	xvii
AUTHOR'S CURRICULUM VITAE .....	xviii
Chapter 1 INTRODUCTION.....	1
1.1 Background .....	1
1.2 2D transition metal oxides and dichalcogenides (TMO&Ds).....	2
1.2.1 2D transition metal oxides (TMOs) .....	2
1.2.2 2D TMDs .....	3
1.3 Fabrication method .....	4
1.3.1 Mechanical cleavage.....	5
1.3.2 Liquid Exfoliation .....	6
1.3.3 Chemical vapor deposition (CVD) .....	6
1.3.4 Atomic layer deposition (ALD).....	8
1.3.5 Liquid phase techniques .....	10
1.4 Properties and Applications .....	10
1.4.1 Electrocatalysts .....	10
1.4.2 Photocatalysts .....	11
1.4.3 Photodetectors .....	12
1.4.4 Batteries .....	13
1.4.5 Supercapacitors.....	14
1.4.6 Sensors.....	16
1.5 Approaches to functionalization of 2D TMO&Ds .....	18
1.5.1 Noble metals.....	18
1.5.2 Metal oxides/chalcogenides .....	20
1.5.3 Carbonaceous nanomaterials .....	21

1.5.4 Metal-Organic Frameworks (MOFs) .....	24
1.5.5 Doping .....	25
1.5.6 Intercalation .....	27
1.5.7 In-plane alloy .....	28
1.6 Thesis outline .....	30
References.....	31
Chapter 2 ALD-DEVELOPED 2D $\alpha$ -MoO <sub>3</sub> WINDOWS SUPERIOR HYDROGEN PEROXIDE ELECTROCHEMICAL SENSING CAPABILITIES .....	45
2.1 Abstract.....	45
2.2 Introduction .....	45
2.3 Experimental .....	47
2.3.1 Chemicals .....	47
2.3.2 Sample fabrication.....	47
2.3.3 Characterization.....	51
2.3.4 Electrochemical testing .....	51
2.4 Results and discussion .....	52
2.4.1 Characterization of 2D $\alpha$ -MoO <sub>3</sub> nanofilms.....	52
2.4.2 Electrochemical performance of H <sub>2</sub> O <sub>2</sub> sensor based on 2D $\alpha$ -MoO <sub>3</sub> nanofilms .....	57
2.5 Conclusions .....	67
References.....	68
Chapter 3 ALD DEVELOPED 2D WO <sub>3</sub> NANOFILMS WITH DIFFERENT THICKNESS AND THEIR ELECTROCHEMICAL HYDRAZINE DETECTION .....	74
3.1 Abstract.....	74
3.2 Introduction .....	74
3.3 Experimental section.....	77
3.3.1 Materials .....	77
3.3.2 Sample Preparation.....	77
3.3.3 Characterization.....	78
3.3.4 Electrochemical Testing .....	79
3.4 Results and Discussion .....	79
3.5 Conclusions .....	91
References.....	92
Chapter 4 SURFACE FUNCTIONALIZATION OF WAFER-SCALE 2D WO <sub>3</sub> NANOFILMS BY NM ELECTRODEPOSITION (NM=AG, PT, PD) FOR ELECTROCHEMICAL H <sub>2</sub> O <sub>2</sub> REDUCTION IMPROVEMENT .....	97
4.1 Abstract.....	97

4.2 Introduction .....	97
4.3 Experimental section.....	99
4.3.1 Wafer-scale development of 2D WO <sub>3</sub> nanofilms.....	99
4.3.2 Fabrication of 2D NM-WO <sub>3</sub> nanofilms (NM=Ag, Pt and Pd) .....	100
4.4 Results and discussion.....	101
4.4.1. Characterization of 2D NM <sub>200</sub> -WO <sub>3</sub> nanofilms.....	101
4.4.2. Electrochemical characterization of 2D NM <sub>200</sub> -WO <sub>3</sub> nanofilms.....	104
4.4.3 Electrochemical performance of 2D NM <sub>200</sub> -WO <sub>3</sub> nanofilms towards H <sub>2</sub> O <sub>2</sub> .....	105
4.4.4. Effect of the amount of Ag nanoparticles on H <sub>2</sub> O <sub>2</sub> detection .....	109
4.4.5. Scan rate dependence investigation .....	111
4.4.6. The selectivity and long-time stability study.....	112
4.5 Conclusions .....	113
References.....	113
Chapter 5 SUB-10 NM Ga <sub>2</sub> O <sub>3</sub> -WO <sub>3</sub> HETEROSTRUCTURES DEVELOPED BY ALD FOR SENSITIVE AND SELECTIVE C <sub>2</sub> H <sub>5</sub> OH DETECTION ON PPM LEVEL .....	118
5.1 Abstract.....	118
5.2 Introduction .....	118
5.3 Experimental .....	121
5.3.1 Fabrication of Ga <sub>2</sub> O <sub>3</sub> -WO <sub>3</sub> heterostructures .....	121
5.3.2 Apparatus and Instruments.....	123
5.4 Results and discussion.....	124
5.4.1 Characterization of Ga <sub>2</sub> O <sub>3</sub> -WO <sub>3</sub> heterostructures .....	124
5.4.2 Gas sensing properties .....	128
5.4 Conclusions .....	134
References.....	134
Chapter 6 SUMMARY.....	140
<b>HOOFDSTUK 6 .....</b>	<b>142</b>

## LIST OF ABBREVIATIONS

---

1	2D	Two-dimensional
2	1D	One-dimensional
3	0D	Zero-dimensional
4	TMO&Ds	Transition metal oxides and dichalcogenides
5	TMDs	Transition metal dichalcogenides
6	TMOs	Transition metal oxides
7	FETs	Field-effect transistors
8	NMP	N-methyl pyrrolidone
9	DMF	Dimethylformamide
10	CB	Conduction band
11	VB	Valence band
12	CVD	Chemical vapor deposition
13	ALD	Atomic layer deposition
14	HERs	Hydrogen evolution reactions
15	LIBs	Lithium-ion batteries
16	EVs	Electric vehicles
17	HEVs	Hybrid electric vehicles
18	IEP	Isoelectric points
19	MOFs	Metal-organic frameworks
20	NPs	Nanoparticles
21	NC	Nanocrystal
22	GO	Graphene oxide
23	rGO	Reduced graphene oxide
24	FTIR	Fourier transform-Infrared spectroscopy
25	CV	Cyclic voltammetry
26	EIS	Electrochemical impedance spectroscopy
27	FE-SEM	Field Emission Scanning Electron Microscope

28	<b>AFM</b>	Atomic Force Microscopy
29	<b>XPS</b>	X-ray Photoelectron Spectroscopy
30	<b>RSD</b>	Relative standard deviation
31	<b>UV-vis</b>	Ultraviolet-visible
32	<b>LOD</b>	Limit of detection
34	<b>NM</b>	Noble metals
35	<b>EDLCs</b>	Electrochemical double-layer capacitors

## LIST OF SYMBOLS

---

	Symbols	Unit
1	$I_p$	A
2	A	cm <sup>2</sup>
3	C	mol/cm <sup>3</sup>
4	$\dot{v}$	V/s
5	$E_p$	V
6	R	JK <sup>-1</sup> mol <sup>-1</sup>
7	F	Cmol <sup>-1</sup>

## LIST OF TABLES

---

Table 2.1. The detailed ALD recipe for development of wafer-scaled MoO <sub>3</sub> ultra-thin nanofilms.....	50
Table 2.2. The EIS parameters (R <sub>s</sub> , R <sub>ct</sub> , and C <sub>dl</sub> ) comparison of 2D α-MoO <sub>3</sub> and blank substrate .....	57
Table 2.3. Performance comparison of the H <sub>2</sub> O <sub>2</sub> sensor based on ALD-developed 2D α-MoO <sub>3</sub> .....	58
Table 2.4. Determination of H <sub>2</sub> O <sub>2</sub> concentration in the milk sample (n=3). .....	66
Table 3.1. Characteristics of 2D WO <sub>3</sub> films with different thickness to hydrazine detection .....	88
Table 3.2. Comparison of characteristics of the present work to the typical characteristics .....	89
Table 4.1. Comparison of Ag <sub>200</sub> -WO <sub>3</sub> nanofilms with various Ag-based electrochemical H <sub>2</sub> O <sub>2</sub> . .....	109
Table 5.1. Comparison of gas sensing performances to ethanol based on different.....	132

## LIST OF FIGURES

---

Figure 1.1. Representative structures of some layered metal oxides .....	3
Figure 1.2. (a) Schematic structure of a typical $\text{TMX}_2$ structure, .....	4
Figure 1.3. Schematic diagram of the preparation process for the mechanical cleavage.....	5
Figure 1.4. A schematic diagram of the step-by-step synthesis process from bulk $\alpha\text{-MoO}_3$ .....	6
Figure 1.5. Schematic of TMDs in a CVD process .....	7
Figure 1.6. Schematic of one cycle of ALD-growth process.....	9
Figure 1.7. (a) Typical FESEM and (b) TEM images of 2D 1T/2H- $\text{MoS}_2$ nanosheets.....	11
Figure 1.8. (a) Schematic of back-gate 2D $\beta\text{-Ga}_2\text{O}_3$ solar blind photodetector, .....	13
Figure 1.9. (a) Typical FE-SEM and (b, c) TEM and (d) HRTEM images .....	14
Figure 1.10. (a, b) Charge/ discharge curves at a current density of $0.5 \text{ A g}^{-1}$ .....	16
Figure 1.11. (a) Representative TEM image of $\text{MoO}_3$ nanosheets. (.....	17
Figure 1.12. (a) TEM image of Pt NPs synthesized on a $\text{MoS}_2$ nanosheet.....	19
Figure 1.13. (a) TEM image of $\text{MoS}_2\text{@Cu}_2\text{O}$ composite. (b) Mechanism and. ....	21
Figure 1.14. SEM images of the devices after loading .....	23
Figure 1.15. (a) TEM of $\text{MoO}_3\text{@ZIF-8}$ core-shell nanorods.....	25
Figure 1.16. (a) SEM images of the Au-doped $\text{MoS}_2$ films. ....	27
Figure 1.17. (a) Diagram of space-confined growth of $\text{Ag}_3\text{PO}_4$ nanoparticles. ....	28
Figure 1.18. (a) HRTEM images of metallic ultrathin $\text{Mo}_{1-x}\text{W}_x\text{S}_2$ nanosheets .....	29
Figure 2.1. (a) The photo of the ALD instrument .....	48
Figure 2.2. Graphical scheme of the development of 2D $\alpha\text{-MoO}_3$ nanofilms.....	49
Figure 2.3. The map thickness (color bar in nm) vs. position extracted.....	49
Figure 2.4. Electrochemical properties testing system.....	52
Figure 2.5. (a) SEM, (b) AFM, and (c) 3D topographical AFM images of.....	52
Figure 2.6. (a) XPS spectrum of the 2D $\text{MoO}_3$ nanofilms and high-resolution.....	53
Figure 2.7. FTIR spectra of (a) commercial $\text{MoO}_3$ powder and (b) 2D $\alpha\text{-MoO}_3$ nanofilms.....	54
Figure 2.8. Raman spectra of commercial $\text{MoO}_3$ powder and 2D $\alpha\text{-MoO}_3$ nanofilms.....	55
Figure 2.9. (a) CV curves of the blank substrate and 2D $\alpha\text{-MoO}_3$ nanofilms .....	56
Figure 2.10. (a) CV curves of the blank substrate and ALD-developed 2D $\alpha\text{-MoO}_3$ nanofilms .....	57
Figure 2.11. CV curves of the ALD-developed 2D $\alpha\text{-MoO}_3$ nanofilms.....	59
Figure 2.12. (a) Chronoamperometric current response of 2D $\alpha\text{-MoO}_3$ nanofilms .....	60

Figure 2.13. (a) CV curves of 2D MoO <sub>3</sub> nanofilms in the presence of.....	61
Figure 2.14. CV curves of 2D MoO <sub>3</sub> nanofilms in the absence of 5 mM.....	62
Figure 2.15. (a) The dynamic current response of 2D $\alpha$ -MoO <sub>3</sub> films to H <sub>2</sub> O <sub>2</sub> under .....	63
Figure 2.16. (a) Response and recovery time of 2D $\alpha$ -MoO <sub>3</sub> films to 5 mM H <sub>2</sub> O <sub>2</sub> . ....	64
Figure 2.17. (a) Interference study for 2D $\alpha$ -MoO <sub>3</sub> nano-films in the presence of 10 $\mu$ M .....	65
Figure 2.18. Amperometric current response in the presence of 1 mM interfering substances .....	66
Figure 2.19. (a) The corresponding sensitivity obtained every six days. ....	67
Figure 3.1. Graphical scheme of the development of 2D WO <sub>3</sub> nanofilms.....	78
Figure 3.2. SEM images of (a) nanostructured Au films and.....	80
Figure 3.3. Ellipsometry measurement data for the monolayer WO <sub>3</sub> films.....	80
Figure 3.4. (a) XPS spectrum of the monolayer 2D WO <sub>3</sub> films and high-resolution XPS scan.....	81
Figure 3.5. (a) Nyquist plots of different thickness 2D WO <sub>3</sub> films with 1mM.....	82
Figure 3.6. (a, c, e, g) CVs of different thickness of WO <sub>3</sub> films with 1mM .....	83
Figure 3.7. CVs of Au electrodes and 2D WO <sub>3</sub> with different thicknesses . ....	84
Figure 3.8. CVs of 2D WO <sub>3</sub> with different thickness in the presence of different hydrazine .....	85
Figure 3.9. CVs of monolayer WO <sub>3</sub> in the presence of 500 $\mu$ M hydrazine.....	86
Figure 3.10. (a) Chronoamperometric current response of 2D WO <sub>3</sub> with different thickness .....	88
Figure 3.11. Long-term stability test of monolayer WO <sub>3</sub> .....	90
Figure 3.12. (a) Interference study for monolayer WO <sub>3</sub> in the presence of hydrazine .....	91
Figure 4.1. Ellipsometry measurement data for the developed 2D WO <sub>3</sub> nanofilms. ....	100
Figure 4.2. SEM images and EDS analysis of (a, c) 2D WO <sub>3</sub> , (b, d) Ag <sub>200</sub> -WO <sub>3</sub> , .....	101
Figure 4.3. XPS spectra of 2D WO <sub>3</sub> nanofilms (a, b) and the NM <sub>200</sub> -WO <sub>3</sub> nanofilms .....	103
Figure 4.4. (a) CV curves of 2D WO <sub>3</sub> and NM <sub>200</sub> -modified WO <sub>3</sub> nanofilms .....	104
Figure 4.5. CV curves of Au/Cr bare electrode, 2D WO <sub>3</sub> nanofilms, .....	106
Figure 4.6. (a) Chronoamperometric current response of 2D NM <sub>200</sub> -WO <sub>3</sub> nanofilms .....	107
Figure 4.7. Corresponding linear plot of the current versus H <sub>2</sub> O <sub>2</sub> concentration of .....	108
Figure 4.8. (a) CV curves of Ag <sub>t</sub> -WO <sub>3</sub> nanofilms (t = 0, 50, 100, 200, 300 and 400s) .....	110
Figure 4.9. SEM images of Ag <sub>t</sub> -WO <sub>3</sub> nanofilms at different electrodeposition time; .....	110
Figure 4.10. (a) CV curves of Ag <sub>200</sub> -WO <sub>3</sub> nanofilms at the presence of 5 mM H <sub>2</sub> O <sub>2</sub> .....	111
Figure 4.11. (a) Interference study for Ag <sub>200</sub> -WO <sub>3</sub> nanofilms at the presence of 100 $\mu$ M H <sub>2</sub> O <sub>2</sub> .....	112
Figure 5.1. (a) the graphical scheme of chemical formula of WN <sub>4</sub> C <sub>12</sub> H <sub>30</sub> precursor.....	121
<b>Figure 5.2. The intelligent gas sensing analysis system of gas sensor.....</b>	<b>123</b>
Figure 5.3. SEM images of the ALD-deposited (a) WO <sub>3</sub> and (b) .....	124

Figure 5.4. Raman spectra of Ga <sub>2</sub> O <sub>3</sub> -WO <sub>3</sub> heterostructures. ....	125
Figure 5.5. XPS spectra of Ga <sub>2</sub> O <sub>3</sub> -WO <sub>3</sub> heterostructures .....	126
Figure 5.6. The variation of average Hall coefficient vs applied current .....	128
Figure 5.7. Responses of WO <sub>3</sub> , Ga <sub>2</sub> O <sub>3</sub> , and Ga <sub>2</sub> O <sub>3</sub> -WO <sub>3</sub> heterostructures t.....	129
Figure 5.8. Response and recovery curves of (a) WO <sub>3</sub> , (b) Ga <sub>2</sub> O <sub>3</sub> , and (c) Ga <sub>2</sub> O <sub>3</sub> -WO <sub>3</sub> .....	130
Figure 5.9. (a) Dynamic responses of WO <sub>3</sub> , Ga <sub>2</sub> O <sub>3</sub> nanofilms,.....	130
Figure 5.10. Plots of (a) response and (b) recovery time versu.....	131
Figure 5.11. Responses of Ga <sub>2</sub> O <sub>3</sub> -WO <sub>3</sub> heterostructures to 100 ppm various gases at 275°C.....	132

## LIST OF PUBLICATIONS

---

- [1] Z. Wei, Z. Hai, M. Karbalaee Akbari, J. Hu, L. Hyde, S. Dpuydt, F. Verpoort, S. Zhuiykov, Ultrasensitive, Sustainable, and Selective Electrochemical Hydrazine Detection by ALD-Developed Two-Dimensional WO<sub>3</sub>, **ChemElectroChem**, 5 (2018) 266-272.
- [2] Z. Wei, Z. Hai, M. Karbalaee Akbari, D. Qi, K. Xing, Q. Zhao, F. Verpoort, J. Hu, L. Hyde, S. Zhuiykov, Atomic layer deposition-developed two-dimensional  $\alpha$ -MoO<sub>3</sub> windows excellent hydrogen peroxide electrochemical sensing capabilities, **Sensors and Actuators B: Chemical**, 262 (2018) 334-344.
- [3] Z. Wei, M. Karbalaee Akbari, Z. Hai, R. K. Ramachandran, C. Detavernier, F. Verpoort, E. Kats, H. Xu, J. Hu, S. Zhuiykov, Ultra-thin sub-10 nm Ga<sub>2</sub>O<sub>3</sub>-WO<sub>3</sub> heterostructures developed by atomic layer deposition for sensitive and selective C<sub>2</sub>H<sub>5</sub>OH detection on ppm level, **Sensors and Actuators B: Chemical**, 287 (2019) 147-156.
- [4] Z. Wei, Z. Hai, M. Karbalaee Akbari, Z. Zhao, Y. Sun, L. Hyde, F. Verpoort, J. Hu, S. Zhuiykov, Surface functionalization of wafer-scale two-dimensional WO<sub>3</sub> nanofilms by NM electrodeposition (NM= Ag, Pt, Pd) for electrochemical H<sub>2</sub>O<sub>2</sub> reduction improvement, **Electrochimica Acta**, 297 (2019) 417-426.
- [5] Z. Wei, S. Zhuiykov, Challenges and recent advancements of functionalization of two-dimensional nanostructured molybdenum trioxide and dichalcogenides, **Nanoscale**, 11 (2019) 15709-15738.
- [6] H. Xu, Z. Wei, F. Verpoort, J. Hu, S. Zhuiykov, Nanoscale Au-ZnO Heterostructure Developed by Atomic Layer Deposition Towards Amperometric H<sub>2</sub>O<sub>2</sub> Detection, **Nanoscale research letters**, 15 (2020) 1-14.

## AUTHOR'S CURRICULUM VITAE

---

Zihan Wei is a Ph.D. student at Gent University. At the same time, she is a teaching and research assistant at the Center for Environmental and Energy Research of Gent University Global Campus (GUGC). Her research interests focus on the development of 2D transition metal oxides and their hybrids using different techniques, such as atomic layer deposition, electrodeposition, and liquid exfoliation, and investigation of their applications in electrochemical and gas sensors.

# Chapter 1

## INTRODUCTION

---

### 1.1 Background

It is well-known that the development of material science is the driving force of technological progress, so advanced materials play essential roles in our daily lives. Since the 1980s, dimensionality has entered the horizons of material science and triggered rapid developments of low-dimensional materials. Low dimensional materials are the materials that have a nanoscale size at least in one dimension and can be divided into three categories: two-dimensional (2D), one-dimensional (1D), and zero-dimensional (0D) [1]. Low dimensional materials can exhibit unique properties from the quantum confinement effect of their nanoscale size. Among three types of low dimensional materials, 2D materials have been the most extensively studied materials [2]. First, the quantum confinement in the direction perpendicular to the 2D plane leads to novel electronic and optical properties, which make them appealing candidates for fundamental condensed matter study and electronic device applications [3]. Second, the atomic thickness offers them maximum mechanical flexibility and optical transparency, making them promising for the fabrication of highly flexible and transparent electronic/optoelectronic devices [3]. Third, the large lateral size and ultrathin thickness endow them with ultrahigh specific surface area, making them highly favourable for surface active applications, due to their unique large surface-to-volume ratio and confined thickness on the atomic scale [3].

As a representative 2D material, graphene, being one-atom-thick carbon nanosheets, features various unprecedented properties, such as large theoretical specific surface area (2630 m<sup>2</sup>/g), superior electrical conductivity (200 S/m), ultrahigh carrier mobility at room temperature ( $\sim 10000 \text{ cm}^2 \cdot \text{V}^{-1} \cdot \text{s}^{-1}$ ), remarkable mechanical strength with Young's modulus ( $\sim 1.0 \text{ TPa}$ ), outstanding optical transmittance ( $\sim 97.7\%$ ) and high thermal conductivity (3080-5150 W/mK) [3, 4]. However, graphene has its disadvantages, such as the lack of intrinsic band gap, its susceptibility to oxidative environments, which limit its applications, for example, field-

effect transistors (FETs) made from graphene cannot be effectively switched off and have low on/off switching ratios. Fortunately, graphene's invention has aroused enormous interest to explore other 2D materials, which possess similar layered structure features but possibly have more superior properties, such as hexagonal boron nitride (h-BN), transition metal dichalcogenides, graphitic carbon nitride (g-C<sub>3</sub>N<sub>4</sub>), layered metal oxides, and layered double hydroxides (LDHs). The common feature of these layered materials is that the bulk 3D crystals are stacked structures. They involve van der Waals interactions between adjacent sheets with strong covalent bonding within each sheet.

## 1.2 2D transition metal oxides and dichalcogenides (TMO&Ds)

### 1.2.1 2D transition metal oxides (TMOs)

Over the past few years, 2D TMO&Ds have attracted extensive attention in the research communities, as they showed some properties superior to those of graphene [5]. Compared with transition metal dichalcogenides (TMDs), TMOs are more chemically stable and environmental friendly as well as easier to be prepared. As functional materials, TMOs in the form of 0D (nanodots and fine nanoparticles), 1D (nanowires and nanotubes), and three dimensional (3D) mesoporous structures have been widely studied. In contrast, 2D structures, especially those with confined thickness, have remained conspicuously absent [6]. In nature, many-layered transition metal oxides are composed of negatively charged slabs with alkaline cations filling the interlayer spacing. These slabs are commonly made up of corner- or edge-shared octahedral units of MO<sub>6</sub> (M = Ti, Nb, Mn, W, Ta, Ru, Mo, etc.) [7-11], which can form ionic bonds with the surrounding alkaline cations, and the structures of some layered metal oxides were shown in Figure 1.1 (a-e) [12]. For this kind of material, the cation exchange-assisted liquid exfoliation can be applied to reduce these materials into 2D nanosheets, which will elaborate in the following part. In addition, some layered transition metal oxides are also found to be bonded by the weak Van der Waals force, such as  $\alpha$ -MoO<sub>3</sub> and V<sub>2</sub>O<sub>5</sub> [13, 14], and the structures can be seen in Figure 1.1 (e, f) [12]. For this kind of layered metal oxides, micromechanical cleavage or liquid exfoliation techniques have been developed to produce the 2D monolayers in these oxides. Transition metal oxides exhibit different polymorphs. For example, as one of the two main transition metal oxides were investigated in our work, MoO<sub>3</sub> has the  $\alpha$ -MoO<sub>3</sub> (orthorhombic phase) to  $\beta$ -MoO<sub>3</sub> (monoclinic phase) and h-MoO<sub>3</sub> (hexagonal

phase), depending on the arrangement of the building blocks of  $\text{MoO}_6$  octahedra. Of these,  $\alpha$ - $\text{MoO}_3$  is thermodynamically stable, while the other two phases are metastable. Generally, used 2D  $\text{MoO}_3$  has the thermodynamically stable orthorhombic phase ( $\alpha$  phase).  $\text{WO}_3$  crystals consist of  $\text{WO}_6$  octahedra linked by corner and edge sharing. The corner-sharing phases account for most of the tungsten trioxide phases, such as monoclinic II ( $\epsilon$ - $\text{WO}_3$ ), triclinic ( $\delta$ - $\text{WO}_3$ ), monoclinic I ( $\gamma$ - $\text{WO}_3$ ), orthorhombic ( $\beta$ - $\text{WO}_3$ ), tetragonal ( $\alpha$ - $\text{WO}_3$ ), and cubic  $\text{WO}_3$ . The different phases can be mutually transformed under different temperatures, while  $\gamma$ - $\text{WO}_3$  appears to be the most common and stable phase at room temperature.

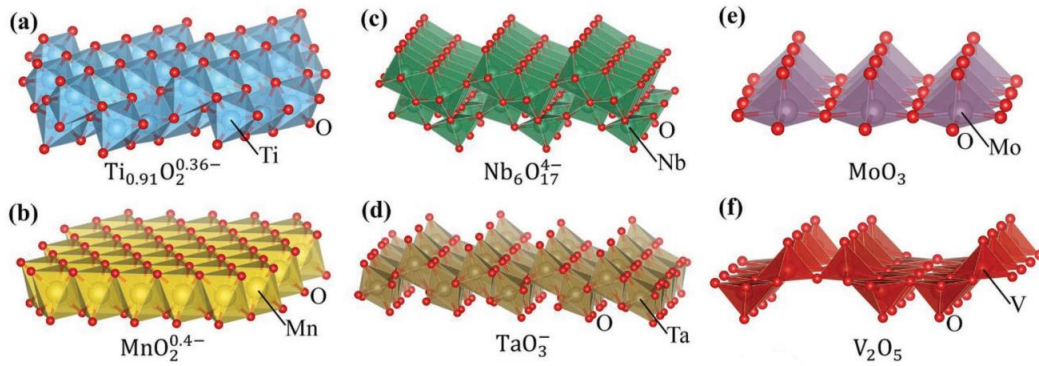


Figure 1.1. Representative structures of some layered metal oxides (a)  $\text{Ti}_{0.91}\text{O}_2^{0.36-}$ , (b)  $\text{MnO}_2^{0.4-}$ , (c)  $\text{Nb}_6\text{O}_{17}^{4-}$ , (d)  $\text{TaO}_3^-$ , (e)  $\text{MoO}_3$ , and (f)  $\text{V}_2\text{O}_5$  [12].

### 1.2.2 2D TMDs

TMDs are made of stacking of graphene-like layers of the general formula  $\text{TMX}_2$  in which M is the transition metal forming hexagonal layers sandwiched between two sheets of X, where X is a chalcogen ( $\text{X} = \text{S}, \text{Se}, \text{Te}$ ) [15], as shown in Figure 1.2 (a). Commonly studied polymorphs of  $\text{TMX}_2$  compounds are tetragonal 1T- $\text{TMX}_2$ , hexagonal 2H- $\text{TMX}_2$ , and rhombohedral 3R- $\text{TMX}_2$ , respectively, which are different in stacking sequence in their unit cell and metal atom coordination [16], as shown in Figure 1.2 (b). Phase transition is possible in some TMDs by intercalation with alkali metals [17-19]. For example, 2H- $\text{MoS}_2$  to 1T- $\text{MoS}_2$  transition by lithium intercalation [18] and reverse scenario of 1T- $\text{TaS}_2$  to 2H- $\text{TaS}_2$  change on lithium intercalation [19]. Moreover, as the 1T phase of some TMDs, such as 1T- $\text{MoS}_2$  and 1T- $\text{WS}_2$  exhibits metal character, partial phase transformation can be controlled, producing a 2H-1T structure to achieve a metal-semiconductor hybrid structure [20-22]. The layer-dependent properties of TMDs have recently been in the intensive investigation for their transition from an indirect

bandgap in bulk to a direct gap in the monolayer [23, 24]. This tunable bandgap in TMDs is accompanied by strong photoluminescence (PL) and large exciton energy, which make them highly attractive for optoelectronic devices [25]. Besides, the distinct features of weak Van der Waals force between each layer and the large specific surface area also make 2D TMDs become promising candidates for capacitive energy storage and sensing applications [26, 27].

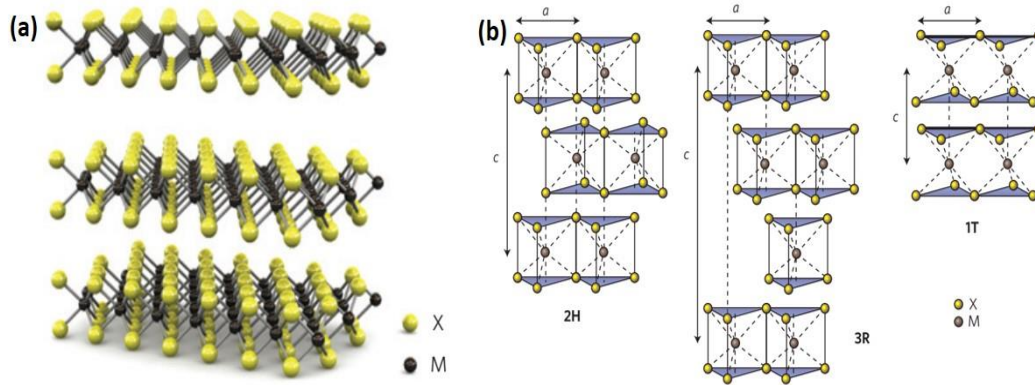


Figure 1.2. (a) Schematic structure of a typical  $\text{TMX}_2$  structure, with the chalcogen atoms (X) in yellow and the metal atoms (M) in grey [15]. (b) Schematics of the structural polytypes: 2H (hexagonal symmetry, two layers per repeat unit, trigonal prismatic coordination), 3R (rhombohedral symmetry, three layers per repeat unit, trigonal prismatic coordination) and 1T (tetragonal symmetry, one layer per repeat unit, octahedral coordination) [16].

### 1.3 Fabrication method

Following the success of graphene, many strategies have recently been developed for the fabrication of 2D TMO&Ds, which can broadly be classified into two major categories: top-down and bottom-up methods [5, 28]. The top-down approach relies on the processes to whittle down the size and dimension of layered bulk crystals or other forms to single- or few-layer nanosheets by mechanical cleavage or exfoliation. The bottom-up method is the opposite process, where 2D TMO&Ds are directly grown from different precursors via chemical reactions at certain experimental conditions by techniques of molecular self-assembly, layer-by-layer assembly, vapor deposition, and so on. Compared with top-down approach wafer-scale and high-quality 2D materials can be developed by bottom-up method, especially vapor-phase growth strategies, since scalable production of high-quality wafer-scale 2D materials has become significantly essential to bring us closer to practical industrial applications.

### 1.3.1 Mechanical cleavage

Mechanical cleavage, as a traditional and efficient method, also known as the Scotch-tape method, can yield pristine, clean, and high-quality single- and few-layer 2D nanosheets. In a typical process, the bulk crystal is first attached to a piece of Scotch tape, and the other piece of Scotch tape is adhered to the other crystal surface. After that, one of the Scotch tape pieces is detached from the crystal. This process can be repeated several times in order to obtain flakes that are thin enough and can be transferred onto a target substrate. Then, the Scotch tape with the thin flake is attached onto a target substrate under gentle pressure. Finally, the Scotch tape is peeled off from the substrate and single- or few-layer nanosheets can be easily found on the substrate using an optical microscope [2]. Since Novoselov, Geim, and co-workers successfully produce single-layer graphene from graphite by this method in 2004 [29], many 2D TMDs such as  $\text{MoS}_2$ ,  $\text{TiS}_2$ ,  $\text{TaS}_2$ ,  $\text{WS}_2$ ,  $\text{WSe}_2$ ,  $\text{TaSe}_2$  with single- or few-layer nanosheets have been prepared [30-32]. A typical mechanical cleavage process of few-layered  $\text{MoS}_2$  nanosheets is shown in Figure 1.3 [33]. However, the reports of the development of 2D transition metal oxides using this method are relatively less, as the problems of this method are the low yield, difficulties to control the thickness, scale-up and the size of the as-obtained nanosheets, and requirement of the huge amount of bulk materials [34].

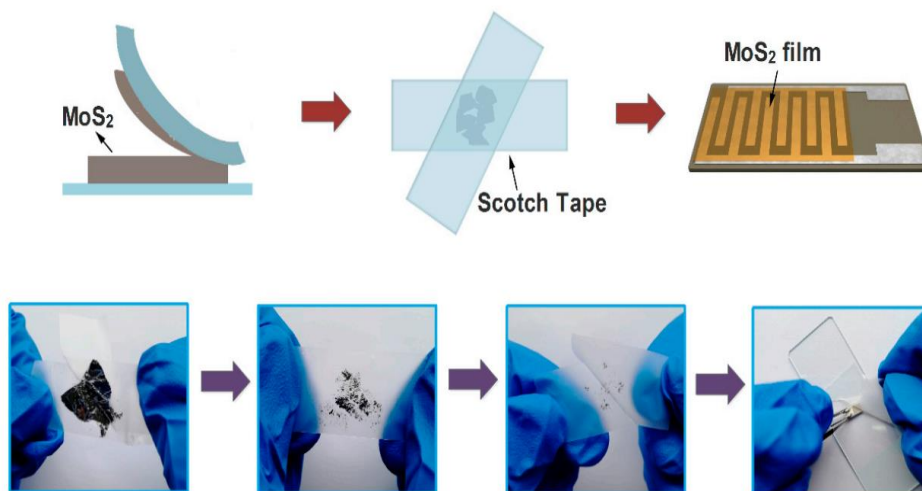


Figure 1.3. Schematic diagram of the preparation process for the mechanical cleavage  $\text{MoS}_2$  nanosheets [33].

### 1.3.2 Liquid Exfoliation

For TMO&Ds bonded by the weak Van der Waals force, liquid exfoliation technique has been widely used to produce large scale and few-layered nanosheets in the organic solvents, such as N-methyl pyrrolidone (NMP) and dimethylformamide (DMF) [35]. In this process, the sonication can break the weak Van der Waals interaction between layers, but cannot destroy the covalent bonding in each layer. It was found that proper matching of the surface tension between the layered crystal and the solvent is the critical factor in minimizing the energy and increasing the efficiency of exfoliation. Moreover, the solvent is also vital in stabilizing the exfoliated nanosheets and prohibiting their restacking and aggregating. Few layer TMDs,  $\text{MoO}_3$ , and  $\text{V}_2\text{O}_5$  nanosheets have been produced by this method [34, 36, 37, 13, 14], and as an example, the step-by-step synthesis process from bulk  $\alpha\text{-MoO}_3$  to nanosheets was illustrated in Figure 1.4 [13]. As mentioned above, for some layered TMOs composed of negatively charged slabs with alkaline cations, the cation exchange-assisted liquid exfoliation has been developed to reduce these materials into 2D nanosheets [1]. By treatment with an acid solution, the interlayer alkaline cations can be exchanged with  $\text{H}^+$  cations to form hydrated protonic compounds. In this reaction, a massive volume of water can be formed, which leads to a drastic decrease in the interlayer electrostatic interaction and the interlayer expansion. Subsequent mechanical shaking or sonication treatments can easily exfoliate the expanded materials into nanosheets.

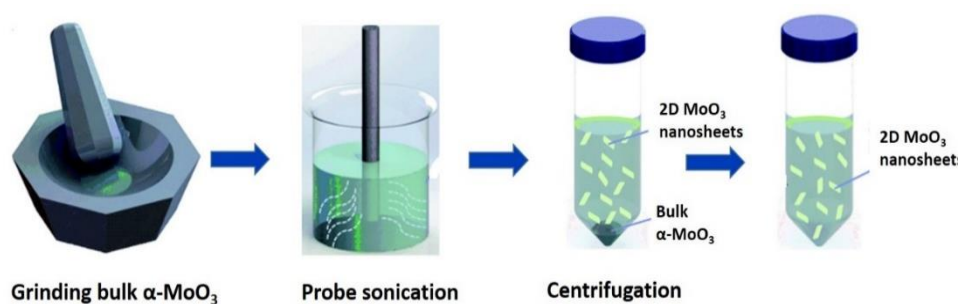


Figure 1.4. A schematic diagram of the step-by-step synthesis process from bulk  $\alpha\text{-MoO}_3$  to nanosheets [13].

### 1.3.3 Chemical vapor deposition (CVD)

The CVD method is one typical bottom-up process used to prepare ultrathin 2D nanomaterials on the substrate. In a typical procedure, the given substrate is exposed to reactive precursors at high temperature and high vacuum, in which the precursors react and/or decompose on the

surface of the substrate to form ultrathin 2D flakes or large-area ultrathin films. As is known, in the growth process, parameters including precursor, temperature, pressure, and type of substrate have effects on the size, morphology, and phase of 2D TMO&Ds [38], which are essential for the properties of 2D TMO&Ds.

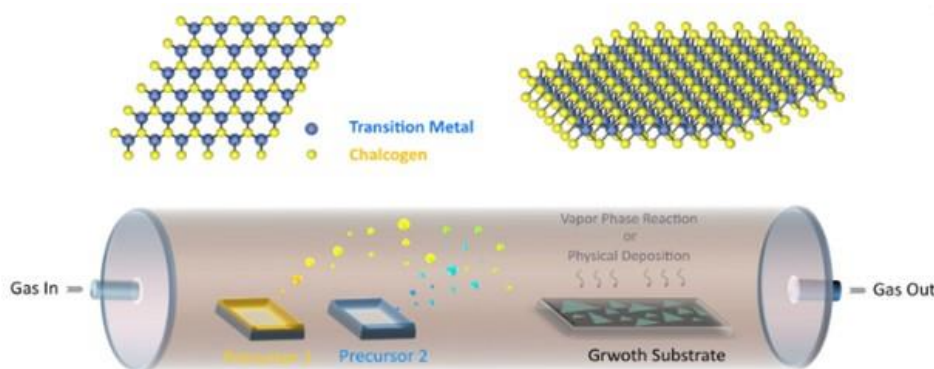


Figure 1.5. Schematic of TMDs in a CVD process [52].

Precursor, serving as the reactants in the CVD process, can be gaseous or solid, and compared to the solid precursor, gaseous precursor is more convenient for the CVD process due to the easy and accurate control of the gas flow rate over a wide range, allowing to precisely control the structure, morphology, and size of 2D materials [39, 40].

The temperature in a CVD system plays an even more critical role in the development of 2D materials because it can affect the flow of the carrier gas, chemical reactions of precursors in the gas phase, which suggests that temperature can determine the composition and uniformity of the products [1]. Generally, high-quality products can usually be obtained at relatively high temperatures.

Pressure, varying over a wide range from a few atmospheres to several millitorrs, has a tremendous effect on the gas flow behavior. Based on the ideal gas equation  $PV = nRT$ , for the same molar flow, at low pressure, the volume flow and the velocity of gas are much increased. In contrast, the precursor concentration decreases, which means the low concentration and high velocity of the mass feed of the precursor can make the reaction more controllable [1, 41, 42].

Substrate, used for the deposition of 2D materials in the CVD process, is important for morphology and crystal lattice control of 2D materials [43]. In addition, different substrates

were chosen for various applications of 2D materials, for example, because of the catalytic abilities, nickel and copper can be used as substrates for catalytic applications, and for electronic and optoelectronic applications, inert Si/SiO<sub>2</sub>, mica, and polyimide are commonly used [44-46].

So rational design and careful tuning of the CVD growth parameters are important for developing high-quality 2D materials. So far, this method has been successfully utilized to develop many 2D TMO&Ds, MoO<sub>3</sub>, WO<sub>3</sub>, TiO<sub>2</sub>, MoS<sub>2</sub>, WS<sub>2</sub>, and so on [47-51]. Figure 1.5 illustrated the schematic diagram of the development of 2D TMDs using the CVD method [52]. However, the growth of 2D TMO&Ds usually involves solid precursors, and their concentrations are not easy to control precisely. Defects are inevitable in current CVD-grown 2D TMO&Ds, which limited their applications in electronic and optoelectronic fields. The high temperature generally used in the CVD growth process limited their use in the flexible device. Great efforts have been paid to the low-temperature growth of 2D materials, but the temperature is still too high for most polymeric flexible substrates. In addition, wafer-scale and continuous 2D films are essential for practical uses, and new approaches in the CVD growth process has to be developed.

#### ***1.3.4 Atomic layer deposition (ALD)***

ALD technique is a special variant of CVD. However, in the CVD process, the precursors can react at the same time in the surface, and the precursors can decompose, while in the ALD process the precursors are not introduced into the reactor simultaneously, and are typically separated in time by inert gas purges without self-decomposition [53]. In addition, ALD is a surface controlled layer-by-layer process rather than process parameter controlled as in the case of CVD [26]. As depicted of a schematic illustration of the ALD process in Figure 1.6, each cycle of the ALD process consists of four essential steps [53, 54]:

- (1) Expose of the substrate surface to the pulse of the first gaseous precursor, typically of a metal reactant, and chemisorption of the first precursor happens onto the substrate.
- (2) Purge inert gas to remove the unreacted precursor and gaseous by-products from the chamber.
- (3) Expose of the second precursor, typically of non-metal reactant, and the surface reaction happens to produce the thin film.

(4) Again purge inert gas to remove the unreacted precursor and gaseous by-products from the chamber.

For the ALD process, the choice of the precursor is strict. Gaseous precursor or vaporizable processor at a temperature lower than ALD reaction temperature is required to enable transport in the gas phase, and the formed by-product should be inert and not interfere with the ALD growth. Moreover, the precursor should not decompose thermally during the storage at the vaporization temperature or the growth temperature [53]. Compared to the CVD method, there are some advantages of materials developed from the ALD method.

- (1) The deposition rate in ALD is rather low, one cycle requiring a few seconds typically, and the film of ALD is deposited in a full monolayer or a fraction of one monolayer, so the materials can be controlled down to a nanometer level and in the ideal case even to an atomic level.
- (2) The self-limiting growth mechanism makes each cycle deposit precisely the same amount of materials, and thus the film thickness may be accurately controlled by the number of deposition cycles.
- (3) Since in ALD, each layer reaction step is given enough time to reach completion while in other methods the new deposition materials may be covered by unreacted species because of the continuous growth process, the films from ALD often exhibit superior quality.
- (4) ALD processes are weak temperature dependency and can be performed at a relatively low temperature. CVD processes, in general, are strongly temperature-dependent. Therefore, a typical growth temperature can be found for different materials, which make it possible to deposit multilayer structures in a continuous process. In addition, 2D materials on the flexible polymer substrate can also be developed.

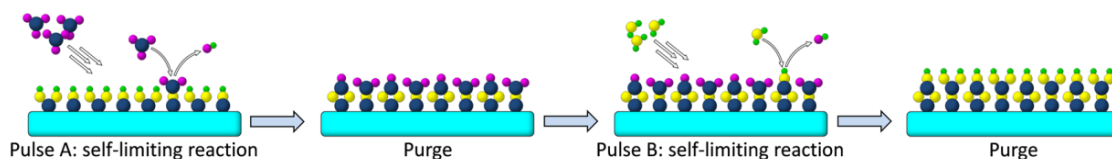


Figure 1.6. Schematic of one cycle of ALD-growth process [2].

### 1.3.5 Liquid phase techniques

Liquid phase techniques as different bottom-up approaches include many promising methods, for example, electrodeposition, solvothermal method and hydrothermal method [55-57]. It is used to synthesize target materials from specific precursors via chemical reactions in solution, in which surfactants are generally used to control the size, shape, and morphology as well as to stabilize the synthesized materials. Some widely used wet-chemical methods for nanomaterials include template synthesis, hydro/solvothermal synthesis, self-assembly of nanocrystals, and soft colloidal synthesis. Wet-chemical methods have been demonstrated to be effective for the synthesis of numerous ultrathin 2D nanomaterials. Importantly, the liquid phase techniques synthesis enables the realization of high-yield and massive production of ultrathin 2D nanomaterials in liquid at relatively low cost, which is potentially applicable for industrial production. However, it is hard to obtain single-layer nanosheets for most of the nanomaterials synthesized by wet-chemical methods, because the synthesis is easily affected by reaction parameters, including reaction temperature, reaction time, concentration of precursors, and solvents [2].

## 1.4 Properties and Applications

### 1.4.1 Electrocatalysts

Electrocatalysis is one of the most promising applications for 2D TMO&Ds, especially for the hydrogen evolution reactions (HERs), **due to the large surface area, active edge site effect and semiconducting to metallic phase transformation** [58]. Electrochemical HER is a highly efficient way for hydrogen generation under the presence of Pt, Pd, or Rh catalysts [59]. However, the scarcity and the cost of noble metals limit their commercialization and hence shift the research interests on looking for alternative cheaper HER catalysts. Specifically, 2D TMDs, as a member of the group of 2D nanomaterials, with their unique optical, mechanical, electronic and catalytic features have recently been explored as an alternative HER catalyst owing to its active edge site effects and the semiconducting (2H) to metallic (1T) phase transformation [17, 60]. It means the number of active sites can be increased, and the conductivity also can be improved in some 2D TMDs, which are the main parameters to improve the HER catalytic performance of 2D TMDs. As shown in Figure 1.7, the as-synthesized 2D 1T/2H-MoS<sub>2</sub> nanosheets through a facile hydrothermal method exhibit remarkable achievement for the HER with a small overpotential

of 220 mV at 10 mA/cm<sup>2</sup>, a low Tafel slope of 61 mV/dec and robust stability. It is ascribed to that the locally introduced 1T phase MoS<sub>2</sub> can not only contribute more active sites but also markedly promote the electronic conductivity [61].

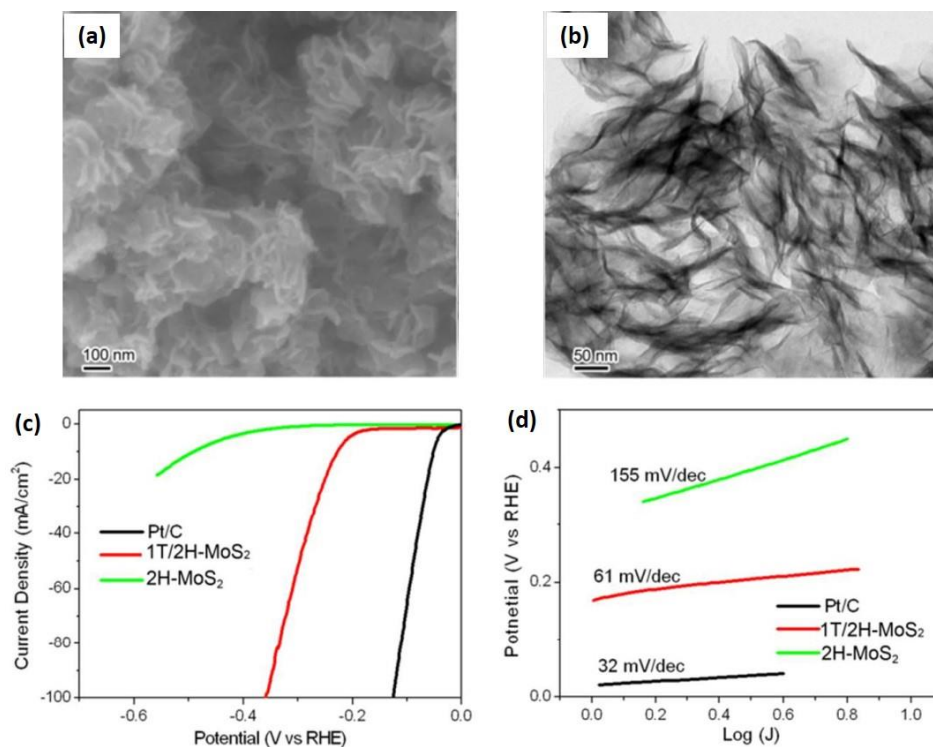


Figure 1.7. (a) Typical FESEM and (b) TEM images of 2D 1T/2H-MoS<sub>2</sub> nanosheets. Electrocatalytic performance of 1T/2H-MoS<sub>2</sub> and 2H-MoS<sub>2</sub>, (c) Polarization curves, (d) corresponding Tafel slopes [61].

### 1.4.2 Photocatalysts

Due to their low cost, earth abundance, and nontoxicity, TMO&Ds have been the most popular photocatalysis candidates in the past decades. Among different forms, 2D TMO&Ds are proven to be more promising for photocatalytic applications than the form of 0D, 1D, and 3D structures [62, 57]. Obviously, their large surface area can provide an increased number of active sites for catalytic redox reactions with surface adsorbed species, while also minimizing the necessary catalyst loading. Additionally, charge migration across both interfaces (catalyst–electrolyte and catalyst–charge collector) is also promoted, which leads to the reduction of interfacial charge transfer resistance and the improvement of photocatalytic reaction kinetics [63]. More importantly, the 2D planar configuration allows the dominant exposure of one particular facet with a distinct atomic arrangement, which is more suitable for the separation of photogenerated

charge pairs and the utilization of photons [64, 65]. It is well known that the bandgap energies and band positions of certain 2D TMO&Ds are strongly dependent on their thickness and lateral dimensions. In many cases, the CB edge will shift toward  $H_2$  reduction potential, or the VB edge will shift toward  $O_2$  oxidation potential, or both happen simultaneously. For example, bulk  $MoS_2$  material possesses an indirect bandgap of 1.2 eV, which is unsuitable for photocatalytic reactions because of the insufficient oxidation/reduction potential for activating the photocatalytic process. However, 2D  $MoS_2$  nanosheet has been found to have a direct bandgap of  $\sim 1.96$  eV owing to the quantum confinement effect, which endows  $MoS_2$  nanosheets with proper band positions and the ability for visible-light absorption [57].

#### 1.4.3 Photodetectors

Photodetectors represent a light sensor that can transduce the incident radiation into an electrical signal. Photodetectors have been widely used in various fields including military applications and commercial products for everyday life [66]. So far, photodetectors based on graphene have reported responsivity as high as  $10^7 A \cdot W^{-1}$  through the enhanced light absorption with covering semiconductor quantum dots [67]. However, the gapless graphene structure determines the large dark current and the unsatisfactory photo-responsivity, which is critical for the device to detect weak signals [67, 68]. In contrast to graphene, 2D MT&Ds have also been widely explored for photodetector applications owing to their high transparency, flexibility and tunable bandgap [69].

Gallium oxide ( $\beta$ - $Ga_2O_3$ ), an especially important III-VI semiconductor with a wide band-gap of 4.9 eV, is a potential material for application in solar blind photodetectors. A solar blind photodetector based on 2D  $Ga_2O_3$  fabricated from the corresponding GaSe nanosheets was reported and show a sensitive, fast and stable photoresponse to ultraviolet radiation (254 nm). The responsivity, detectivity and external quantum efficiency of the photodetector are  $3.3 A \cdot W^{-1}$ ,  $4.0 \times 10^{12}$  Jones and 1600%, respectively, as shown in Figure 1.8 [70]. The photodetector based on monolayer  $WO_3$  developed by atomic layer deposition exhibited high responsivity of  $71.6 A \cdot W^{-1}$ , wide-range photoresponse, extremely fast response time of  $\sim 2.5$ – $2.7$  ms and superior long-term stability over more than 250 cycles [71].

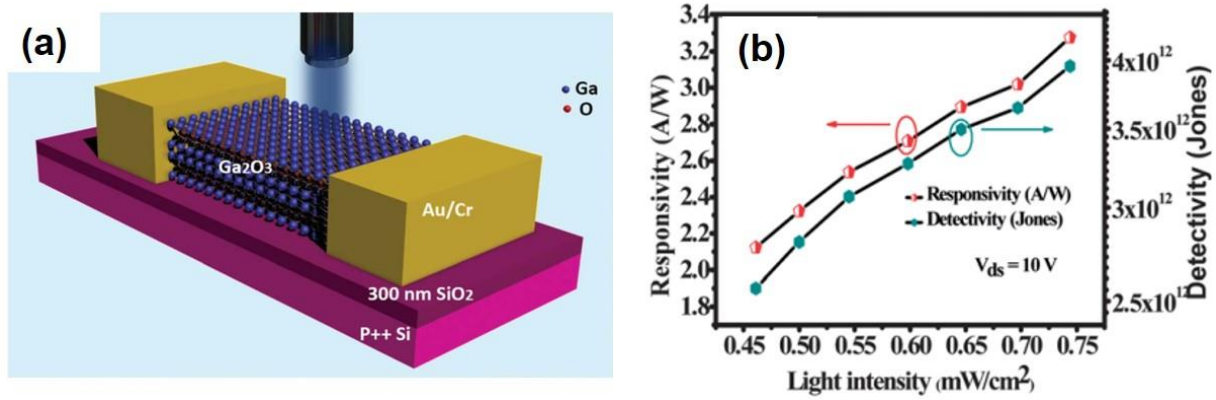


Figure 1.8. (a) Schematic of back-gate 2D  $\beta$ -Ga<sub>2</sub>O<sub>3</sub> solar blind photodetector, (b) responsivity and detectivity dependent light intensity at constant drain-source voltage ( $V_{ds}=10V$ ).

#### 1.4.4 Batteries

The lithium-ion batteries (LIBs) are one of the most important rechargeable energy storage technologies. They can be used for a variety of mobile equipment, including cell phones, laptop computers, and power tools [72-74]. They also can be considered as a valuable candidate for potential green applications in electric vehicles (EVs) and hybrid electric vehicles (HEVs). When the battery is charging up, the positive electrode gives up some of its lithium ions, which move through the electrolyte to the negative, 2D materials electrode and remain there. The battery takes in and stores energy during this process. When the battery is discharging, the lithium ions move back across the electrolyte to the positive electrode, producing the energy that powers the battery. However, the commercially used anode material in LIBs, graphite, with a theoretical specific capacity of only 372 mA h g<sup>-1</sup> and a relatively poor rate capability cannot meet the increasing demand for reliable EVs and HEVs [75]. As an alternative, nanostructure 2D TMO&Ds can be utilized in updated, improved LIBs. For 2D TMDs, their layered structure and the weak Van der Waals interaction between layers enable the easy intercalation of Li<sup>+</sup> ions without a significant increase in volume. For example, MoS<sub>2</sub> exhibited high Li storage capacities of ~670 mA h g<sup>-1</sup> with 4 mol of Li<sup>+</sup> insertion per formula [76]. For 2D TMOs, because of their chemical stability, environmental friendly and higher theoretical lithium-storage capacity, have also been used as electrode materials for LIBs. For example, the theoretical lithium storage capacity value of  $\alpha$ -MoO<sub>3</sub> is very high (1117 mA h g<sup>-1</sup>) being three times higher than that of graphite [77]. Compared with bulk materials, the well-designed 2D TMO&Ds improve the

interaction interfaces with electrolytes and in-plane carrier-transport kinetics, which greatly enhance the storage behavior of  $\text{Li}^+$  and other ions.

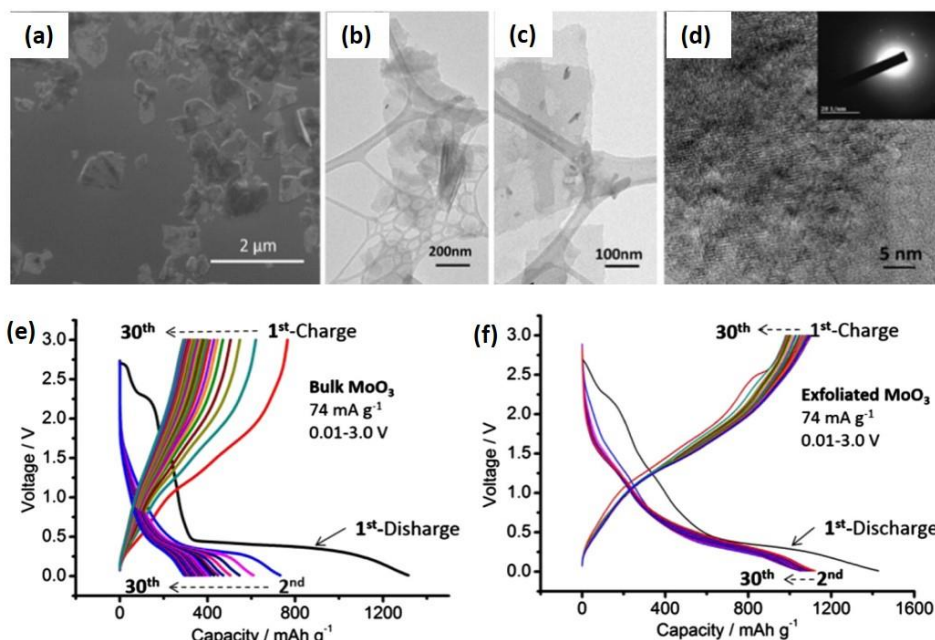


Figure 1.9. (a) Typical FE-SEM and (b, c) TEM and (d) HRTEM images and diffraction pattern of exfoliated  $\text{MoO}_3$  nanosheets. Charge-discharge curves of (e) bulk  $\text{MoO}_3$  and (f)  $\text{MoO}_3$  nanosheets (0.01–3.0 V) [78].

Moreover, the 2D nanostructure provides a large specific surface area, which is beneficial to creating an increased number of active sites, achieving a better charge distribution, and speeding up the insertion-extraction or redox reaction rates. Thirdly, the unique 2D features of the metal oxide nanosheets are effective for suppressing or moderating the volume expansion that arises in the charging-discharging cycles. Figure 1.9 shows the electrochemical performance of as-prepared 2D  $\text{MoO}_3$  nanosheets and bulk  $\text{MoO}_3$  by galvanostatic charge-discharge measurements. The reversible capacity starting from the 2nd cycle around 1100  $\text{mA h g}^{-1}$  was achieved for the  $\text{MoO}_3$  nanosheets electrode, close to the theoretical reversible capacity of  $\alpha\text{-MoO}_3$  (corresponding to 6 Li per Mo atom), which is much higher than that of bulk  $\text{MoO}_3$  [78].

#### 1.4.5 Supercapacitors

Supercapacitors combine the advantages of traditional capacitors, and rechargeable batteries have also attracted tremendous attention owing to their excellent electrical properties of fast

charging, high power density, and long cycling life. There are two types of electrochemical capacitors, electrochemical double-layer capacitors (EDLCs) and pseudo-capacitors, and TMOs, hydroxide, and conducting polymers were employed as electrode materials [79]. The charge storage mechanism in EDLCs is according to the electrosorption of ions and formation of an electrochemical double layer (EDL); however, the pseudocapacitors store the charges through the faradic reactions (redox reactions). Among these materials, TMOs have the highest theoretical specific capacitance. The bulk forms of TMOs have intrinsically low electronic conductivities, limiting fast ion diffusions, which makes them incompetent for high rate performances [80]. However, similar like what mentioned for the battery, developing TMOs in the form of 2D structures can provide a large surface area due to complete exposure of the surface atoms, more chemically reactive sites in the edge sites of 2D nanosheets than basal planes and high mechanical strength and flexibility at atomic electronics [81]. Therefore, nowadays, various 2D layered TMOs have been investigated as electrode materials of supercapacitors, such as  $\text{MoO}_3$ ,  $\text{V}_2\text{O}_5$ ,  $\text{Co}_3\text{O}_4$ ,  $\text{RuO}_2$ ,  $\text{MnO}_2$ , and so on [81-84]. In addition, 2D TMDs, such as  $\text{MoS}_2$ , have been investigated for employment in the electrochemical storage. The use of the metallic 1T phase of  $\text{MoS}_2$  obtained from the semiconducting 2H phase of  $\text{MoS}_2$  during chemical exfoliation of the bulk material can achieve higher electrochemical energy storage performance for the supercapacitor because the 1T  $\text{MoS}_2$  phase is hydrophilic and  $10^7$  times more conductive than the semiconducting 2H phase [27, 85, 86]. It was shown that chemically exfoliated nanosheets of  $\text{MoS}_2$  containing a high concentration of the metallic 1T phase could be electrochemically intercalated by ions such as  $\text{H}^+$ ,  $\text{Li}^+$ ,  $\text{Na}^+$  and  $\text{K}^+$  with extraordinary efficiency and ultimately achieve capacitance values ranging from  $\sim 400$  to  $\sim 700 \text{ F cm}^{-3}$  in a variety of aqueous electrolytes [27]. For example, as shown in Figure 1.10, a 100-fold capacitance increasing in  $\text{MoS}_2$ -based supercapacitors was achieved via optimizing the in-plane 1T-2H phase hybridization of the monolayers with 40% of the 1T phase, which exhibited outstanding performance with a specific capacitance of  $366.9 \text{ F g}^{-1}$  and retention ratio of 92.2% after 1000 cycles at current densities of  $0.5 \text{ A g}^{-1}$  [87]. A mechanism transition from the electric double-layer capacitance behavior to pseudo-capacitive behavior was observed as the 2D  $\text{WO}_3$  film thickness decreased from 6.5 nm to monolayer. Considerable improvement of the specific capacitance from 225.4 to  $650.3 \text{ F g}^{-1}$  was also obtained with the 2D film becoming thinner, whereas its rate capability decayed from 83.9% to 65.4% [88].

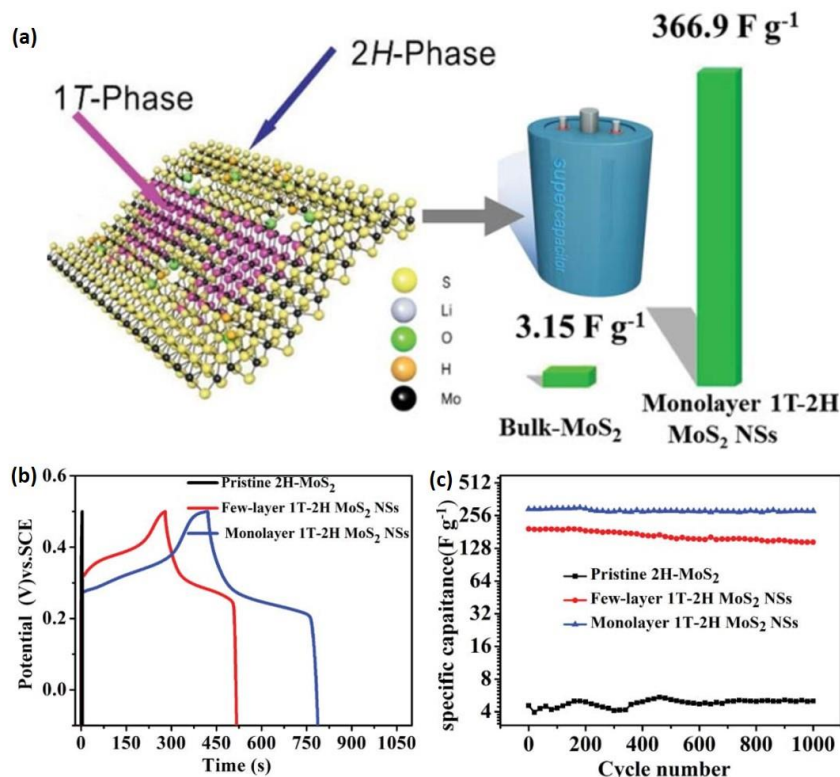


Figure 1.10. (a, b) Charge/discharge curves at a current density of  $0.5 \text{ A g}^{-1}$ . (c) Specific capacitance vs. the number of charge/discharge cycles of supercapacitor based on MoS<sub>2</sub> monolayers with 40% of the 1T phase and their comparison with supercapacitor based on 2H-hybridized MoS<sub>2</sub> micro-powder and based on few layer MoS<sub>2</sub> nanosheets [87].

#### 1.4.6 Sensors

2D materials with the atomic scale thickness magnify the surface to volume ratio, which provides excellent reactive adsorption sites for gaseous molecules, making them become outstanding candidates for gas sensors [89, 90]. Among these 2D materials, 2D TMO&Ds have gained significant interest in the development of a different range of highly sensitive, selective, reliable, and low-cost sensors, and it is worth noting that most 2D TMO&Ds follow surface adsorbed oxygen ions mechanism [91, 92]. Different from the widely researched graphene and other carbon-based materials, 2D TMO&Ds have the semiconducting properties with an appropriate bandgap, which is attractive for modulating the transport characteristics to improve the sensing performance. For example, it was reported that the gas response of 2D MoO<sub>3</sub>-based sensing electrode to 100 ppm ethanol increases from 7 to 33 at the operating temperature of 300°C compared to the bulk MoO<sub>3</sub> (Figure 1.11) [92].

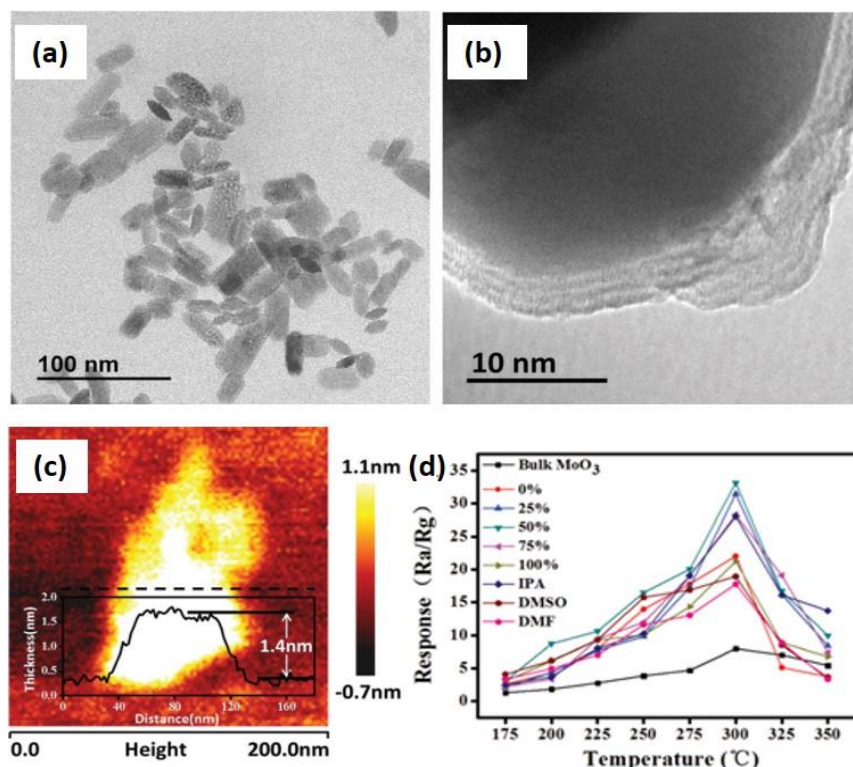


Figure 1.11. (a) Representative TEM image of  $\text{MoO}_3$  nanosheets. (b) Representative HRTEM image showing the layered nature of the  $\text{MoO}_3$  nanosheets. (c) Representative AFM image of the  $\text{MoO}_3$  nanosheet. (d) The results of the sensor response using bulk  $\text{MoO}_3$  and  $\text{MoO}_3$  nanosheets toward 100 ppm alcohol vapor at different operating temperatures [92].

In addition to the determination of different gases, recent works report that 2D TMO&Ds could be the potential materials for the electrochemical sensors, since 2D TMO&Ds could improve the analytical performances of electrochemical sensors by increasing their electrochemically active surface area and electrical conductivity and /or by providing new ways of interacting with the targeted analytes [4, 93]. Electrochemical sensors have been used for decades for the detection of various chemical species due to simplicity, low cost, high sensitivity, and selectivity. Since the first discovery that the electrochemically reduced single-layer  $\text{MoS}_2$  nanosheets can be utilized for glucose detection and selectively measure dopamine at the presence of ascorbic acid (AA) and uric acid (UA) [94], 2D TMO&Ds-based nanostructures have become an excellent electrode material for various electrochemical sensors. Due to the existence of a suitable bandgap, the overall sensitivity of devices based on 2D TMO&Ds is much larger than that of graphene and graphene oxides, which have either no or small bandgap [95]. Owing to the high isoelectric points (IEP), 2D transition metal oxides

generally have high isoelectric points (IEP), which can potentially be used for immobilizing a wide range of biomolecules with relatively lower IEPs via electrostatic interactions that also facilitate charge transfer between them [96].

## 1.5 Approaches to functionalization of 2D TMO&Ds

Although so much attention and efforts have been dedicated to this developing research area and outstanding physical and chemical properties have been reported for 2D TMO&Ds, a lot of challenges still remain for the commercial requirements. For example, the intrinsic low electric conductivity and limited accessibility of active catalytic sites severely hinder their catalytic performance [97], the high operating temperature of TMOs-based sensing devices and inadequate stability of the TMDs-based sensing devices hinder their gas sensing application [98, 94], and so on. Thus, in order to improve their performances and broaden the scope of their applications, research on 2D TMO&Ds -based heterostructures have been attracted more and more attention during the last few years [84, 99]. In the preparation of 2D nanocomposites, due to their ultrathin thickness and large special surface area, 2D TMO&Ds could be used as the universal template for the fabrication of hybrid nanostructures with a lot of materials, including the noble metals, metal oxides and chalcogenides [100-102]. Other materials, such as carbonaceous nanomaterials and metal-organic frameworks (MOFs), could also be incorporated with 2D TMO&Ds owing to their high conductivity and unique physic-chemical properties [103, 104]. Moreover, doping and intercalation of other elements into 2D TMO&Ds have been widely accepted for regulating their intrinsic properties without changing their structured features [105, 106]. Specifically, due to the same honeycomb structure with a closely matched lattice constant, TMDs can form the in-plane alloys with some other TMDs, which are particularly useful for some applications [107].

### 1.5.1 Noble metals

The approach of using noble metal nanostructures for functionalization of different nanostructures has been used in various applications such as catalysis, electronics, sensors and biomedicine [108-111]. Even though the scarcity and expensiveness of noble metals limit their widespread commercialization, it is still a big challenge to find materials that can fully functionally replace the noble metals for specific applications [112-114]. Recent studies on the 2D TMO&Ds decorated by the noble metal nanoparticles have demonstrated that these 2D

nanostructures possess much better properties compared to their undecorated counterparts [115, 116, 59].

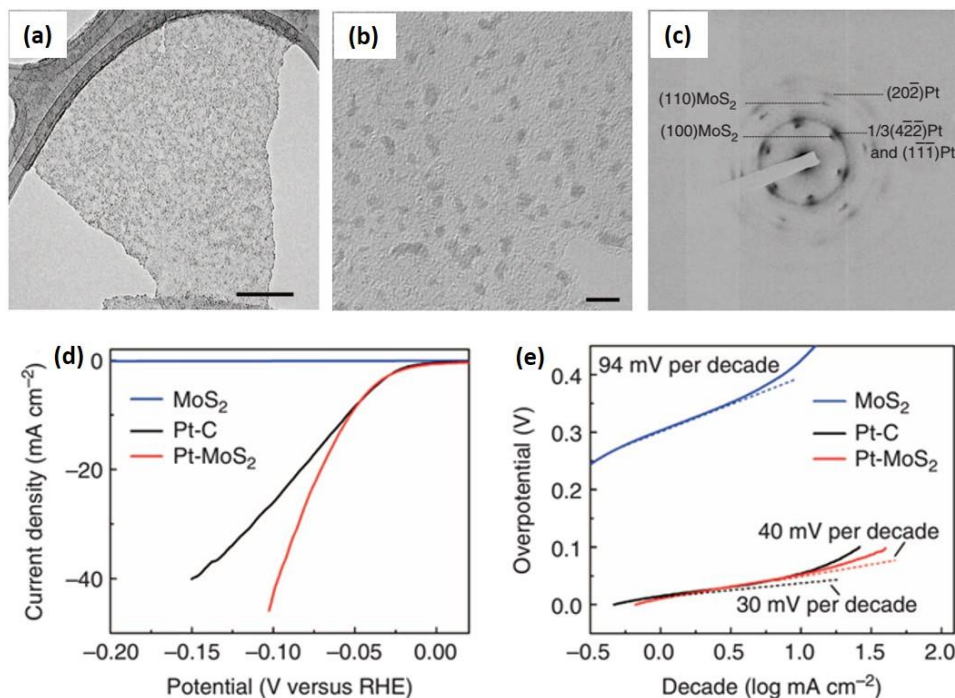


Figure 1.12. (a) TEM image of Pt NPs synthesized on a MoS<sub>2</sub> nanosheet (scale bar, 100 nm). (b) The magnified TEM image of Pt NPs with a size of 1–3 nm on MoS<sub>2</sub> nanosheet (scale bar, 5 nm). (c) SAED pattern of a Pt–MoS<sub>2</sub> hybrid nanosheet with the electron beam perpendicular to the basal plane of the MoS<sub>2</sub> nanosheet. (d) Polarisation curves and (e) the corresponding Tafel plots of Pt–MoS<sub>2</sub>, Pt–C, and MoS<sub>2</sub>, respectively [115].

In fact, 2D TMO&Ds have been considered as promising templates for direct growth of the noble metal nanostructures due to their large specific surface area, strong adsorption ability, and excellent thermal stability. For example, the solution-processable MoS<sub>2</sub> nanosheets were employed to direct the epitaxial growth of Pd, Pt, and Ag nanostructures at the ambient conditions via wet chemical syntheses. Specifically, Pd nanoparticles (NPs) (5 nm), Pt NPs (1–3 nm) and Silver triangular nanoplates were epitaxially grown on MoS<sub>2</sub> nanosheets using poly(vinylpyrrolidone) (PVP), sodium citrate and cetyltrimethyl ammonium bromide (CTAB) or PVP as the surfactants, respectively. Compared to the commercial Pt catalysts with the same Pt loading, 1–3 nm Pt nanostructures on the surface of 2D MoS<sub>2</sub> nanosheets (Figure 1.12(a–c)) have demonstrated much higher electrocatalytic activity towards the HER with a negligible overpotential and a low Tafel slope of 30 mV/decade (Figure 1.12 (d, e)) [115]. Combination of

microwave-assisted hydrothermal method and oil-bath method for the synthesis of Au–MoS<sub>2</sub>, Pt–MoS<sub>2</sub>, and Au@Pt–MoS<sub>2</sub> nanocomposites was reported. Au–MoS<sub>2</sub>, Pt–MoS<sub>2</sub>, and Au@Pt–MoS<sub>2</sub> modified electrodes exhibited better catechol detection performances than the pure MoS<sub>2</sub> nanosheet, and metallic nanoparticles modified electrodes due to their synergistic effect. As expected, the Au@Pt–MoS<sub>2</sub> nanocomposites modified electrode exhibited the linear range of 2–1000 mM and the detection limit of 0.44 mM for catechol, which was better than all MoS<sub>2</sub>-based nanomaterials [117]. In addition, bimetallic nanohybrids that often display enhanced properties than their monometallic counterparts have recently attracted more and more researchers' attention [118-120]. In this regard, MoS<sub>2</sub>-PtAg nanohybrids were fabricated by decorating ultrathin MoS<sub>2</sub> nanosheets with octahedral Pt<sub>74</sub>Ag<sub>26</sub> alloy nanoparticles [118].

### 1.5.2 Metal oxides/chalcogenides

During last few years, constructing heterojunction of 2D TMO&Ds with other semiconductor materials such as metal oxides (e.g., MoO<sub>3</sub>, Co<sub>3</sub>O<sub>4</sub>, SnO<sub>2</sub>, Fe<sub>3</sub>O<sub>4</sub>) [121-125] and metal chalcogenides (e.g. MoS<sub>2</sub>, WS<sub>2</sub>, Bi<sub>2</sub>S<sub>3</sub>, Ag<sub>2</sub>S, CdS) has also been considered as interesting research direction, owing to the ability of fabrication of p-n heterojunctions, changing semiconducting behavior from n-type to p-type, or altering band structures [126-128].

Metal oxides and chalcogenides can also be modified on the surface of 2D TMO&Ds using different approaches. A facile and straightforward chemical deposition method was used for the development of MoS<sub>2</sub> nanosheets decorated with p-type Cu<sub>2</sub>O nanoparticles as co-catalyst for the efficient solar hydrogen production under the visible light. Results confirmed that 1.0 wt % MoS<sub>2</sub> nanosheets decorated Cu<sub>2</sub>O nanoparticles represent the maximum reduction photocurrent density of 0.17 mA cm<sup>-2</sup>, which is about 7-fold higher than that of pristine Cu<sub>2</sub>O, as shown in Figure 1.13 (a-c) [123]. The excellent performance of MoS<sub>2</sub>@Cu<sub>2</sub>O is caused by the introduction of the active sites of MoS<sub>2</sub> nanosheets as co-catalyst to the surface of Cu<sub>2</sub>O nanoparticles, which promoted the dissociation of water, photocurrent density and the production of hydrogen by lowering the electrochemical proton reduction overpotential and inhibited photo-induced corrosion during the measurement. A novel nano-hybrid of SnO<sub>2</sub> nanocrystal (NC)-decorated MoS<sub>2</sub> nanosheet (MoS<sub>2</sub>/SnO<sub>2</sub>) was facilely prepared through a wet chemistry method, and its outstanding stable sensing performance for the room temperature NO<sub>2</sub> detection in a dry air environment are reported, as shown in Figure 1.13 (d-f) [121]. SnO<sub>2</sub>

NCs not only significantly enhanced the stability of MoS<sub>2</sub> nanosheets in dry air by increasing their work function and creating a passivation layer to prevent the interaction between the oxygen and the MoS<sub>2</sub> but also served as strong p-type dopants for MoS<sub>2</sub>, leading to p-type channels in the MoS<sub>2</sub> nanosheets. A novel Fe<sub>3</sub>O<sub>4</sub>/MoS<sub>2</sub> composite by decorating ultra-small Fe<sub>3</sub>O<sub>4</sub> NPs (~3.5 nm) on the surface of graphene-like MoS<sub>2</sub> nanosheets was developed, where MoS<sub>2</sub> nanosheets were synthesized through a facile one - step hydrothermal process, and ultrasmall Fe<sub>3</sub>O<sub>4</sub> NPs decorated on the surface of MoS<sub>2</sub> nanosheets via another hydrothermal method [122]. These composites demonstrated superior cyclic and rate performances with delivering 1033 and 224 mA · h · g<sup>-1</sup> at the current densities of 2000 and 10 000 mA · g<sup>-1</sup>, respectively. Here, Fe<sub>3</sub>O<sub>4</sub> NPs primarily acted as spacers to prevent the restacking of 2D MoS<sub>2</sub> nanosheets, making the active surfaces of MoS<sub>2</sub> nanosheets accessible for electrolyte penetration during charge/discharge processes and thus improving the cyclic performance of composites.

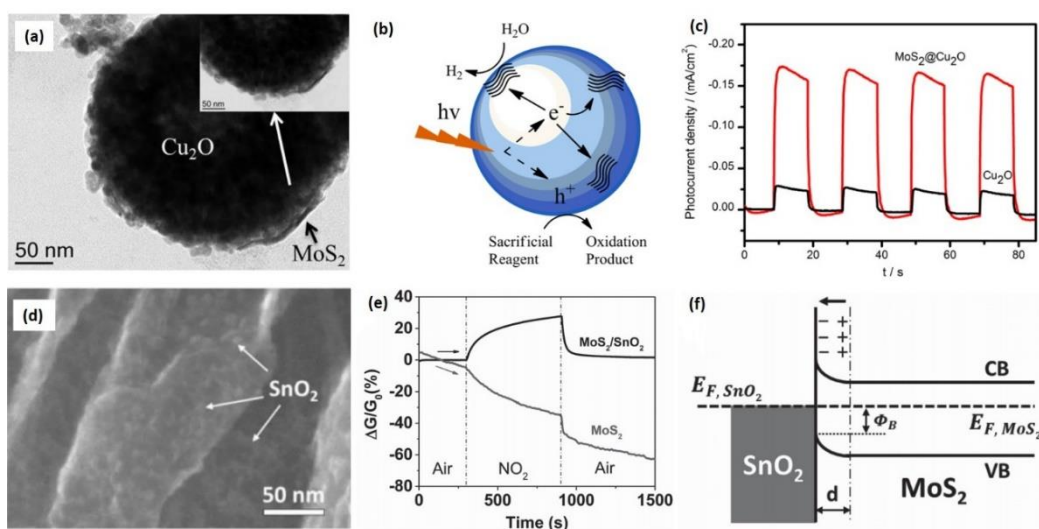


Figure 1.13. (a) TEM image of MoS<sub>2</sub>@Cu<sub>2</sub>O composite. (b) Mechanism and (c) transient photocurrent-time profiles at a bias of -0.1 V versus SCE for MoS<sub>2</sub>@Cu<sub>2</sub>O composite and pristine Cu<sub>2</sub>O nanoparticles [123]. (d) High-resolution SEM images showing that SnO<sub>2</sub> NCs decorate on the MoS<sub>2</sub> nanosheets. (e) The room temperature dynamic sensing response of MoS<sub>2</sub> nanosheets with and without SnO<sub>2</sub> NC decoration against 10 ppm NO<sub>2</sub> in a dry air environment. (f) Band diagram of the MoS<sub>2</sub>/SnO<sub>2</sub> nanohybrid [121].

### 1.5.3 Carbonaceous nanomaterials

Loading of 2D TMO&Ds on the surface of carbonaceous materials, such as graphene, carbon nanotube, conductive polymer, and porous carbon, has exhibited various potential applications

due to their high electronic conductivity, high charger mobility, large surface area, excellent flexibility and high chemical stability [129-134]. Therefore, the hierarchical nanostructures of 2D TMO&Ds on carbonaceous materials could be a feasible and promising way to improve their performance.

Among these carbon materials, chemically treated graphene-based materials, like graphene oxide (GO) and reduced graphene oxide (rGO), have been considered as very effective templates for the nucleation and subsequent growth of nanoparticles owing to the coupling interactions between the nanoparticle precursors and oxygen-containing functional groups on the surface of GO or rGO [135, 136]. Various methods for the preparation of the composites have recently been developed, and the most popular strategy commonly used nowadays is the hydrothermal method [137]. For example, MoSe<sub>2</sub>/rGO hybrids developed by a facile hydrothermal approach showed superior HER activity with the small onset potentials of 50 mV, about 20–30 mV lower than those of MoS<sub>2</sub> and its graphene hybrids reported previously, and a Tafel slope of 69 mV/decade [137]. Better performance is attributed to the fact that the Gibbs free energy for atomic hydrogen adsorption on MoSe<sub>2</sub> edges is closer to the thermos-neutral than that of MoS<sub>2</sub>. These results indicate that MoSe<sub>2</sub> has a valuable potential to be a better HER catalyst than MoS<sub>2</sub>. A flexible gas sensor for detection of formaldehyde (HCHO) at room temperature based on rGO/MoS<sub>2</sub> hybrid films was fabricated on polyethylene naphthalate substrates by a simple self-assembly method [138]. The sensing test results indicated that the rGO/MoS<sub>2</sub> sensors showed higher sensitivities than rGO sensors. Furthermore, two kinds of MoS<sub>2</sub> nanosheets were prepared by either hydrothermal synthesis (HT) or chemical exfoliation (CE) and were compared for their detection of HCHO, which revealed that the hydrothermally produced MoS<sub>2</sub> nanosheets with abundant defects led to enhanced sensitivity of the rGO/MoS<sub>2</sub> sensors, as shown in Figure 1.14 (a-d). For example, the sensing response of the rGO/MoS<sub>2</sub>-HT sensor to 10.0 ppm HCHO was 4.8%, about 1.7 and 2.2 times higher than those of rGO/MoS<sub>2</sub>-CE and rGO sensors. MoS<sub>2</sub>-rGO heterostructures were synthesized by a simple hydrothermal method under the optimized condition, and their binder-free electrode has been fabricated with a high specific capacitance (387.6 F g<sup>-1</sup> at 1.2 A g<sup>-1</sup>) and impressive cycling stability (virtually no loss up to 1000 cycles). The synergistic interplay between layered MoS<sub>2</sub> and rGO in the MoS<sub>2</sub>-rGO hybrid leads to a superior supercapacitor performance [139].

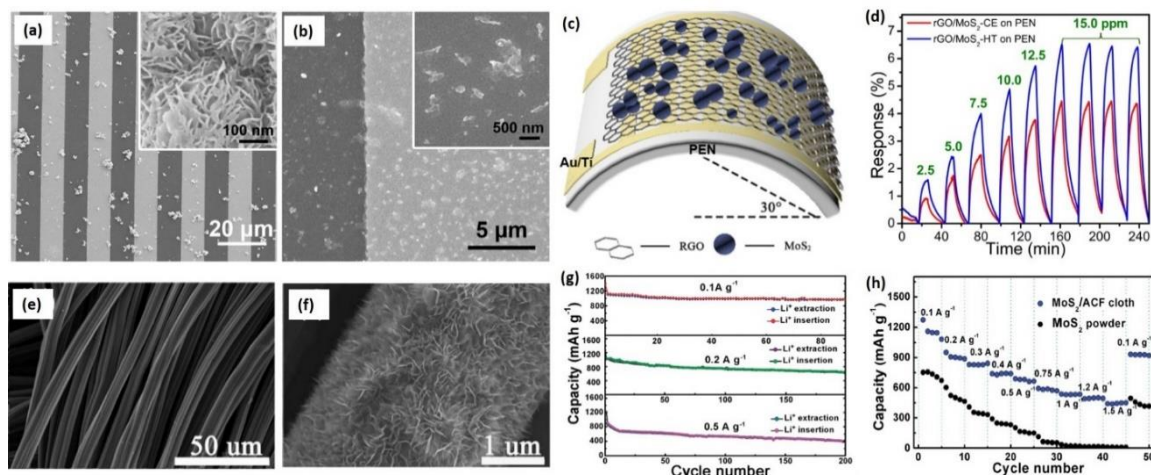


Figure 1.14. SEM images of the devices after loading (a) rGO/MoS<sub>2</sub>-HT and (b) rGO/MoS<sub>2</sub>-CE hybrid films. (c) Schematic illustration of the flexible device based on rGO/MoS<sub>2</sub> hybrid film in the bending state. (d) Real-time sensing response curves of the rGO/MoS<sub>2</sub>-CE sensors to 2.5–15.0 ppm HCHO [138]. SEM images of (e) the original ACF cloth and (f) the as-obtained hierarchical MoS<sub>2</sub>/ACF cloth. (g) Cycling performance of the MoS<sub>2</sub>/ACF cloth at current densities of 0.1 A g<sup>-1</sup>, 0.2 A g<sup>-1</sup>, and 0.5 A g<sup>-1</sup>. (h) Rate performance of the MoS<sub>2</sub>/ACF cloth under various current densities ranging from 0.1 to 1.5 A g<sup>-1</sup> [143].

Moreover, in addition to the chemically treated graphene-based materials, carbon nanotubes (CNTs), carbon fibers, and amorphous carbon have also been utilized to form the hybridization with 2D TMO&Ds [140–142]. Directly growing ultrathin MoS<sub>2</sub> nanosheets on the surface of activated carbon fiber (ACF) cloth to attain the hierarchical MoS<sub>2</sub>/ACF cloth composite was reported (Figure 1.14 (e–h)) [143]. More importantly, the ACF cloth here acts as both the template and the conductivity framework, and the MoS<sub>2</sub>/ACF cloth can be used directly as a free-standing and binder-free electrode, which showed a high specific capacity and excellent reversibility. A discharge capacity as high as 971 mA h g<sup>-1</sup> is obtained at a current density of 0.1 A g<sup>-1</sup> with a fading rate of 0.15% per cycle within 90 cycles. The composite still displayed capacity of 418 mA h g<sup>-1</sup> even after 200 cycles at a high current density of 0.5 A g<sup>-1</sup>. It is the robust structure and the synergistic effects of ultrathin MoS<sub>2</sub> nanosheets and ACF that leads to the superior electrochemical performance of MoS<sub>2</sub>/ACF. As the other typical example, amorphous carbon-supported MoS<sub>2</sub> with unique morphology of MoS<sub>2</sub> nanosheets vertically on the carbon nanosphere was prepared, and consequently, the optimized catalyst employing amorphous carbon substrate exhibited enhanced catalyst activity for electrocatalytic HER with an onset potential as low as 80 mV and a Tafel slope of 40 mV/decade, which are comparable

to platinum [134]. In this structure, amorphous carbon acts as the substrate, which can not only disperse the MoS<sub>2</sub> nanosheets to warrant the exposure of active edge sites but also facilitate the electrons transfer during the electro-catalysis and ensure highly improved conductivity of the composite as exhibited.

#### 1.5.4 Metal-Organic Frameworks (MOFs)

MOFs are very versatile nanomaterials in which the metal ions are linked by coordinating organic species with high surface area and large pore volume. They have been in the focus of many researchers during the last two decades due to their rich surface chemistry, structural versatility, and tunable pore size [144]. It is expected that embedding 2D TMO&Ds and their hybrids into the MOFs can further broaden their potential applications.

There are two ways to develop the hybrids of 2D TMO&Ds and MOFs. One is physical mixing of MOFs and 2D TMO&Ds. The other is the in-situ growth of MOFs on the surface of 2D TMO&Ds. A facile two-step method was developed for the synthesis of MoO<sub>3</sub>@ZIF-8 core-shell nanorod photocatalysts (Figure 1.15 (a-c)), which demonstrated excellent stability and activity for chromium degradation from Cr(VI) to Cr(III) [145]. The enhanced photocatalytic activity is mainly derived from the synergistic effect and the new bond between MoO<sub>3</sub> and ZIF-8 that enhances the efficiency of separation of the photo-induced electron-hole. However, the combination of 2D TMOs and MOFs has not been thoroughly investigated. Other researchers have generated single layers of metallic octahedral phase (1T) MoS<sub>2</sub> that contain excess negative charge on the sulphur atoms of the basal-plane for the coordination modulation with the ZIF-8 metal precursors by lithium-ion intercalation, followed by the reaction of the 1T- MoS<sub>2</sub> nanosheets with the precursors of ZIF-8 indicated that there is an interaction between the individual components. For example, it was recently reported that ZIF-8 MOF could be easily coated on MoS<sub>2</sub> nanosheets by a facial process [146]. 2D MoS<sub>2</sub>@ZIF-8 core-shell structures based on functional MoS<sub>2</sub> as a core and MOFs as shells were fabricated by mixing an aqueous solution of 2-methylimidazole and Zn(OAc)<sub>2</sub> with mild shaking and followed by the reaction at room temperature for 2 h. More importantly, this facial and general method is also feasible to coat ZIF-8 on other 2D materials. As the other example, a novel and highly efficient MoS<sub>2</sub>/UiO-66/CdS photocatalyst for H<sub>2</sub> evolution under the visible light irradiation [146]. It demonstrated in Figure 1.15 (d-f) that under the same reaction conditions, its photocatalytic activity was

nearly 60 times higher than the  $H_2$  evolution rate with pure CdS. The enhanced photocatalytic activity of Pt/UIO-66/CdS was ascribed to the larger surface area of UiO-66/CdS composites provided by the introduction of UiO-66 efficiently hinders with the aggregation of CdS during the synthesis. Moreover, the synergic action of  $MoS_2$  and UiO-66 stipulated the efficient separation of the photo-generated charge carriers and simultaneously provided a more significant number of reactive sites.

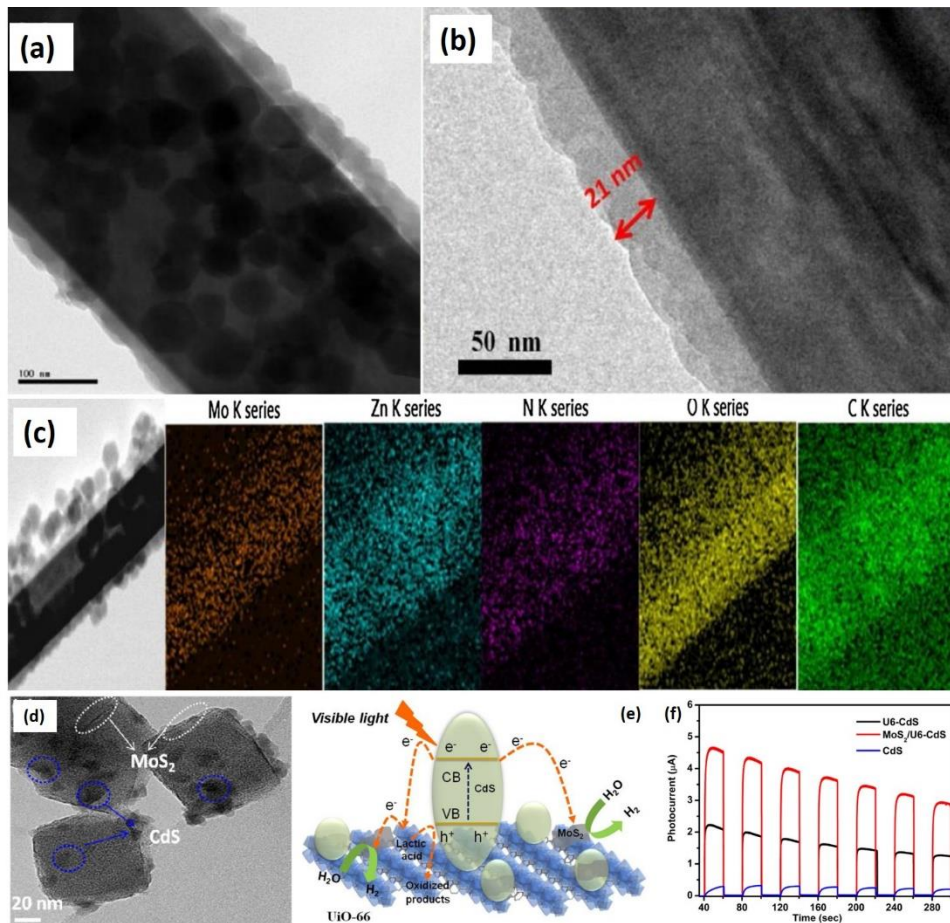


Figure 1.15. (a) TEM of  $MoO_3@ZIF-8$  core-shell nanorods. (b) HRTEM images of  $MoO_3@ZIF-8$  core-shell nanorods. (c) Elemental mapping patterns of  $MoO_3@ZIF-8$  core-shell nanorods [145]. (d) TEM image of  $MoS_2/UIO66-CdS$ . (e) Schematic illustration of the charge transfer in the  $MoS_2/UIO66-CdS$  composite and (f) photocurrent spectra of the pure CdS, UiO66-CdS and  $MoS_2/UIO66-CdS$  under visible light irradiation ( $\geq 420$  nm) [146].

### 1.5.5 Doping

Nano-doping is a viral approach for modification properties of nanostructured semiconductors. It has been widely used to potentially regulate their intrinsic properties, such as changing

conductivity type of semiconductor from n to p by using a lower valence cation as acceptor dopants to produce a hole and increase hole concentration, achieving tuneable p-n junction, modifying band structure, tailoring the electronic characteristics and so on [147, 148]. In relation to 2D TMO&Ds, this approach can also keep their morphology, topology, and crystalline feature without phase separation of 2D TMO&Ds. The main doping methods can be classified as follows: (1) substitution of the transition metal or oxide/dichalcogenides of 2D TMO&Ds with appropriate elements [149], (2) incorporation of surface adatoms or layers of another material [150], (3) surface transfer doping [151] and (4) plasma-based doping [152].

Up to now, several types of metals, including Er, Mn, Nb, Fe, Pt, Re, and Au, have been demonstrated as dopant atoms to substitute the transition metal atoms in 2D TMO&Ds [148, 149, 151]. Among them, by using the potential reduction difference between the Au precursor and MoS<sub>2</sub> work functions, Au nanoparticles were incorporated into chemically exfoliated MoS<sub>2</sub> layers through a simple solution-mixing method. The charge concentration of MoS<sub>2</sub> can be modulated by changing the ratio of Au precursor to MoS<sub>2</sub>. By changing the carrier type in MoS<sub>2</sub> using the Au dopant, an Au-doped MoS<sub>2</sub> sensor positively responding to hydrocarbon molecules lacking oxygen groups (namely, hexane and toluene) and negatively responding with the oxygen-functionalized reducing gases (namely, ethanol, acetaldehyde, and acetone) was developed, exhibited in Figure 1.16 (a-d) [153]. The change in gas response in volatile organic chemical (VOC) chemisorption behavior is due to the n-doping of MoS<sub>2</sub> with Au nanoparticles, which facilitates the electron charge transfer and also leads to tuneable sensing of MoS<sub>2</sub>, enabling it to distinguish between hydrocarbon-based and oxygen-functionalized VOCs. This study has thus made a significant step toward solving the limitations imposed by present MoS<sub>2</sub>-based sensors, which mostly exhibit a single response to various VOC analytes. As a typical example of non-metal dopants with small atomic size to replace oxide/dichalcogenides atoms, different amounts of P atom doped few-layer MoS<sub>2</sub> nanosheets are successfully prepared via a one-pot chemical reaction. It was demonstrated that the P dopants not only could be the new active sites in the basal plane of MoS<sub>2</sub> and help improve the intrinsic electronic conductivity but also show enlarged interlayer spacing that can facilitate hydrogen adsorption and release progress [154]. As shown in Figure 1.16 (e-h), the P-doped MoS<sub>2</sub> nanosheets exhibited a significantly improved activity for hydrogen evolution with a

small Tafel slope of 34 mV/decade and an extremely low overpotential of 43 mV at current benchmark density of 10 mA/cm<sup>2</sup>.

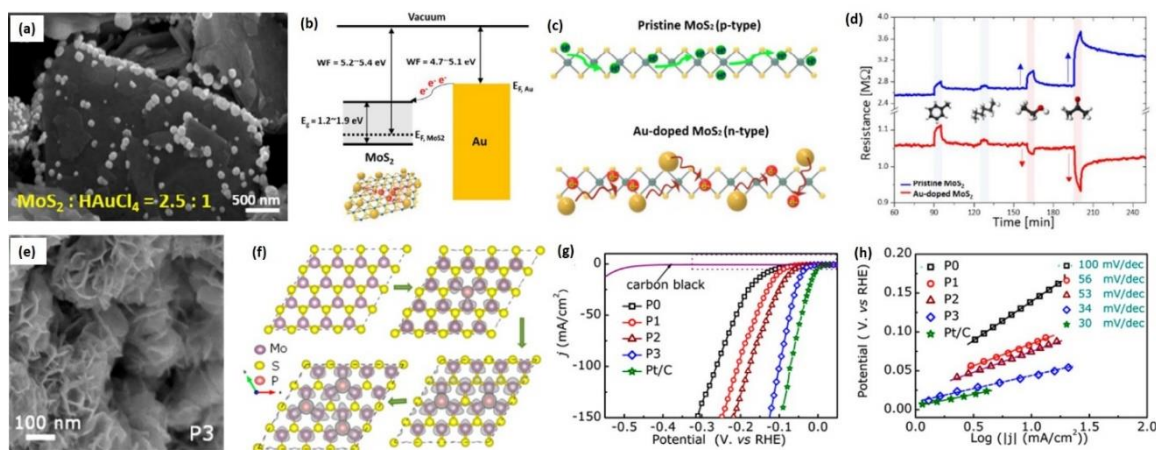


Figure 1.16. (a) SEM images of the Au-doped MoS<sub>2</sub> films. (b) Band diagrams of MoS<sub>2</sub> and Au, showing electron transfer from Au nanoparticles to the MoS<sub>2</sub> channel resulting in n doping effects. (c) Schematic illustration of the mechanism of tuning of VOC sensing using Au in n doping. (d) Real-time resistance of the pristine MoS<sub>2</sub> and Au-doped MoS<sub>2</sub> sensors exposed to various VOCs [153]. (e) SEM of P-doped MoS<sub>2</sub> nanosheets. (f) The partial charge density of the P-doped MoS<sub>2</sub> monolayer with 0–3 dopants for the bands within 0.3 eV below the Fermi level. (g) Polarization curves and (h) corresponding Tafel plots of pure and P-doped MoS<sub>2</sub> nanosheets [154].

### 1.5.6 Intercalation

Generally speaking, intercalation investigates the insertion/extraction of the small guest species like ions into host materials, while retaining their structural features. Intercalation in 2D TMO&Ds could alter the crystal phases and band structures of these few-layered nanomaterials, leading to further enhancement of their electronic, optical, and other various physicochemical properties [155]. The essential prerequisite for guest species to intercalate into 2D host materials is the relative scale between the intercalant and the Van der Waals gap of the 2D host. Specifically, besides the typical ionic intercalants such as H<sup>+</sup>, Li<sup>+</sup>, Na<sup>+</sup>, K<sup>+</sup>, and Mg<sup>2+</sup>, small molecules like H<sub>2</sub> and ammonia could also be employed for intercalation of 2D transition metal oxides and dichalcogenides [156, 157].

The phase transition from 2H-MoS<sub>2</sub> to 1T-MoS<sub>2</sub>, due to the Na<sup>+</sup> ion intercalation is confirmed at the atomic scale with the intercalation partially staged process. The structure of 2D MoS<sub>2</sub> can be partially recovered to 1T-MoS<sub>2</sub> if intercalation depth is less than 1.5 Na<sup>+</sup> ions [158]. Otherwise, the composition of Na<sub>x</sub>S and metallic Mo was obtained. MoO<sub>3</sub> is an indirect

wide bandgap semiconductor, and it is well known that  $\text{MoO}_3$  can be reduced to sub-stoichiometric  $\text{MoO}_{(3-x)}$ , and increasing  $x$  can lower the bandgap. In one example, the bandgap tunability is achieved by hydrogen intercalation into the crystal lattice. Upon exposure to  $\text{H}_2$  gas, the absorbed H atoms form  $\text{H}_y\text{MoO}_3$ , which loses  $\text{H}_2\text{O}$  to ambient producing the desired sub-stoichiometry  $\text{MoO}_{(3-x)}$ . The  $\text{MoO}_3$  bandgap was reduced from 3.25 to 2.65 eV upon exposure to  $\text{H}_2$  gas 40 minutes [159]. Similar to  $\text{MoO}_3$ , there are also reports on the chemical intercalation of  $\text{MoS}_2$  using such ion as  $\text{Li}^+$  to reduce its bandgap [154]. As the other different example,  $\text{Ag}_3\text{PO}_4/\text{WS}_2$  composite was synthesized by controlling the growth of  $\text{Ag}_3\text{PO}_4$  nanoparticles within the interlayers of  $\text{WS}_2$  nanosheets via  $\text{WS}_2$  pre-absorbing silver-ion intercalants, which exhibited excellent photocatalytic degradation of Rhodamine B (RhB) under the visible light irradiation (Figure 1.17) [160].

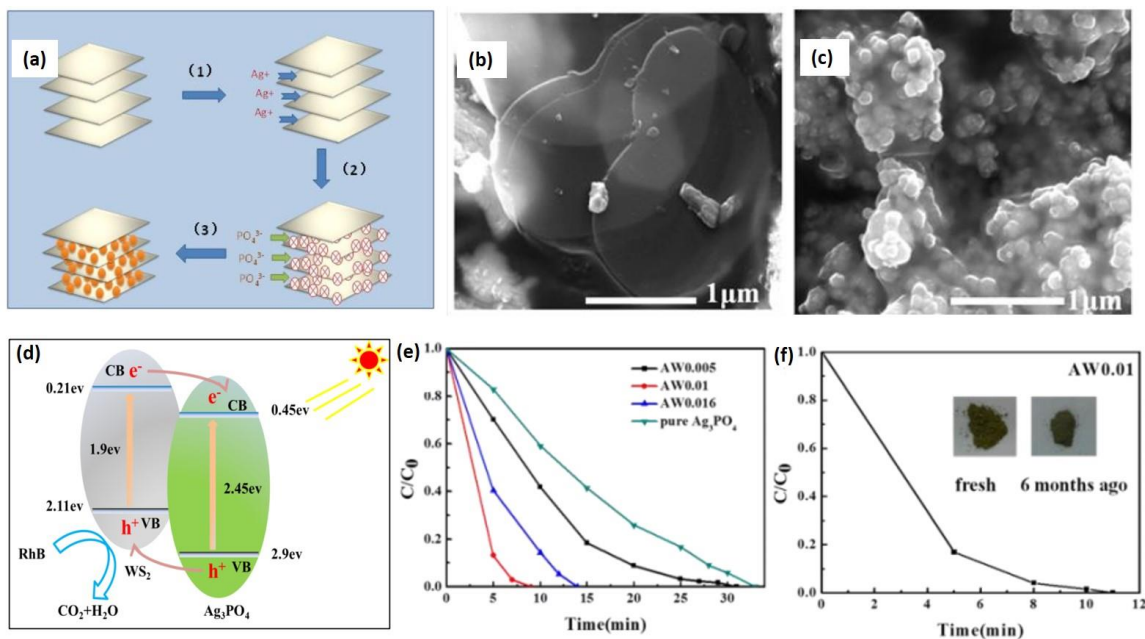


Figure 1.17. (a) Diagram of space-confined growth of  $\text{Ag}_3\text{PO}_4$  nanoparticles within  $\text{WS}_2$  sheets. FESEM images of (b) bare  $\text{WS}_2$  sheets and (c)  $\text{Ag}_3\text{PO}_4/\text{WS}_2$ . (d) Schematic of band structure and expected charge separation of  $\text{Ag}_3\text{PO}_4/\text{WS}_2$  composites under visible-light irradiation. (e) Photocatalytic degradation of RhB solution over the as-prepared  $\text{Ag}_3\text{PO}_4/\text{WS}_2$  composite, bare  $\text{WS}_2$  sheets, and pure  $\text{Ag}_3\text{PO}_4$ . (f) Photocatalytic degradation of RhB solution over  $\text{Ag}_3\text{PO}_4/\text{WS}_2$  prepared six months earlier [160].

### 1.5.7 In-plane alloy

Alloying has been demonstrated to be an effective way to manipulate the bandgap continuously, modulate the carrier type and phase transition of 2D TMDs [161-163]. Previous

calculations have shown that monolayer alloys are thermodynamically stable at room temperature for all compositions [164, 165].

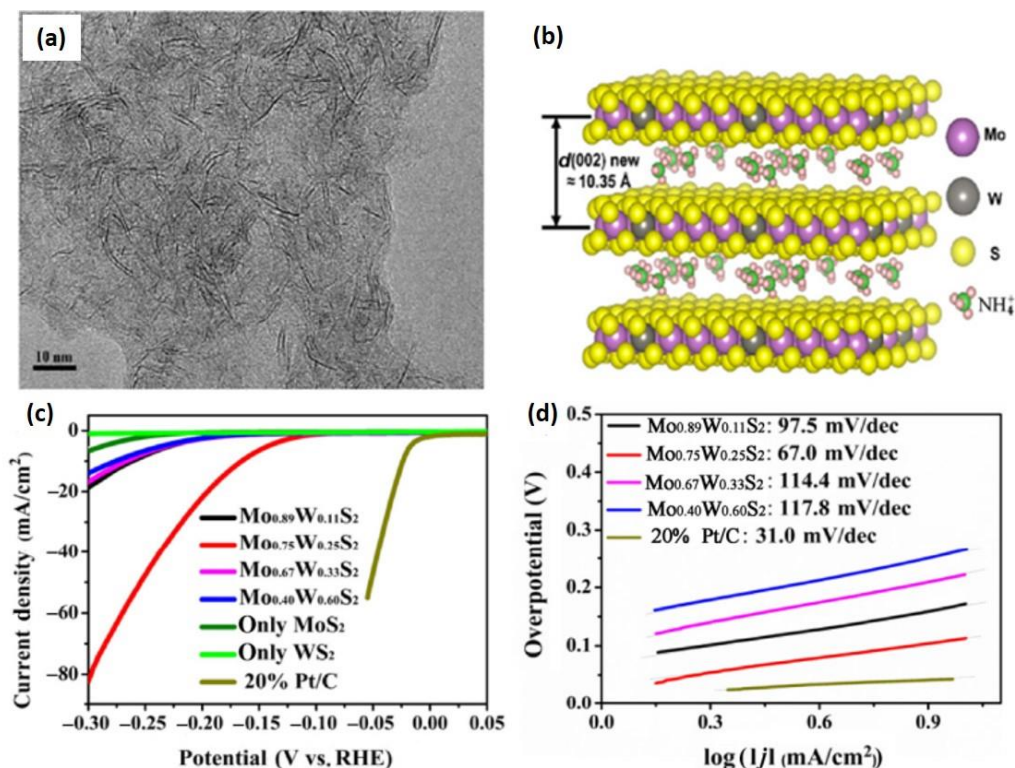


Figure 1.18. (a) HRTEM images of metallic ultrathin Mo<sub>1-x</sub>W<sub>x</sub>S<sub>2</sub> nanosheets with enlarged interlayer spacing. (b) A structural model of the Mo<sub>1-x</sub>W<sub>x</sub>S<sub>2</sub> layers with the intercalation of ammonium ions. (c) Polarization curves and (d) corresponding Tafel slopes of several Mo<sub>1-x</sub>W<sub>x</sub>S<sub>2</sub> nanosheets prepared with different atomic ratios, and of commercial 20% Pt/C catalyst [160].

Ultrathin ternary Mo<sub>x</sub>W<sub>1-x</sub>S<sub>2</sub> nanosheets with excellent stability and a high metallic phase concentration on a gram-scale level were developed using a simple one-step and bottom-up wet-chemistry method. the Mo<sub>0.75</sub>W<sub>0.25</sub>S<sub>2</sub> nanosheets, with the most significant interlayer spacing of  $\sim 10.35 \text{ \AA}$ , exhibited the most efficient HER performance with the lowest overpotential of 155 mV and the smallest Tafel slope of 67 mV/decade, as shown in Figure 1.18 [166]. It was reported that in-plane 2D TMDs alloy could be a new class of electrode material for lithium-ion batteries, as Li can be adsorbed on the surface of 2D TMDs alloy monolayer, maintaining the metallic nature of the system and their layered nature shows higher adsorption energy for Li ion and a negligible Li diffusion barrier [167]. As an example, Mo<sub>1-x</sub>W<sub>x</sub>S<sub>2</sub> ( $0 \leq x \leq 1$ ) alloy composites developed by effective microwave-assisted solvothermal method

exhibited superior rate performance and improved specific capacity [168]. Typically, the  $\text{Mo}_{0.6}\text{W}_{0.4}\text{S}_2$  alloy electrode delivered the capabilities of 847.3 and 428.4  $\text{mA} \cdot \text{h} \cdot \text{g}^{-1}$  at the current densities of 0.1 and 1  $\text{A} \cdot \text{g}^{-1}$ , respectively. In addition,  $\text{Mo}_{1-x}\text{W}_x\text{S}_2$  alloys improve the cycling stability of the transition metal oxides anode materials compared to pure  $\text{MoS}_2$  and  $\text{WS}_2$  for lithium storage, which can be explained by the larger interlayer spacing of the  $\text{Mo}_{1-x}\text{W}_x\text{S}_2$  alloys. The intrinsic expanded interlayer spacing of the alloy composites provides sufficient and stable crystal host lattice structures, which is beneficial for the  $\text{Li}^+$  diffusion and volume accommodation.

## 1.6 Thesis outline

In this chapter, strategies for the development of 2D TMO&Ds -based heterojunctions have been introduced, especially for TMDs-based heterojunctions. However, 2D TMOs have attracted less attention compared to 2D TMDs due to their generally wider bandgap energies and low carrier concentrations in their stoichiometric states. As is known, TMOs are more chemically stable and environmental friendly as well as easier to be prepared than TMDs, especially for some selected TMOs. In this thesis, we focus on the development of some selected 2D TMOs ( $\alpha\text{-MoO}_3$ ,  $\text{WO}_3$ ) and their heterojunctions fabricated by the ALD technique combining with other methods. Moreover, their electrochemical or gas sensing properties were investigated at the same time.

1. To investigate the electrochemical sensing properties of 2D TMOs, Chapter 2 presents of wafer-scale 2D  $\alpha\text{-MoO}_3$  nanofilms with the thickness of 4.9 nm developed on Au- $\text{SiO}_2/\text{Si}$  substrates by ALD technique, and were for the first time used for superior electrochemical sensing to  $\text{H}_2\text{O}_2$ .
2. To study the effect of the thickness on electrochemical sensing properties of 2D TMOs, Chapter 3 illustrated that the wafer-scale 2D  $\text{WO}_3$  films with the different thicknesses from monolayer to 6.5 nm were successfully deposited on Au- $\text{SiO}_2/\text{Si}$  substrates by ALD technique and were utilized for the first time for accurate, sustainable, sensitive, selective and fast  $\text{N}_2\text{H}_4$  detection.
3. In order to research the effect of the noble metal on the electrochemical sensing properties of 2D TMOs, Chapter 4 provides the different noble metal (Ag, Pt, Pd) nanoparticles functionalized 2D  $\text{WO}_3$  (NM- $\text{WO}_3$ ) films for the sensitive and selective

H<sub>2</sub>O<sub>2</sub> determination developed by ALD, followed by electrodeposition. At the same time, the effect of different amounts of noble metal nanoparticles onto the surface of 2D WO<sub>3</sub> films on the electrochemical sensing properties was also studied.

4. In order to investigate the effect of 2D TMOs functionalized with metal oxides on the gas sensing properties. Chapter 5 presents the wafer-scale ultra-thin WO<sub>3</sub>, Ga<sub>2</sub>O<sub>3</sub> nanofilms, and Ga<sub>2</sub>O<sub>3</sub>-WO<sub>3</sub> heterostructures with a thickness of approximately ~8.0 nm fabricated on the SiO<sub>2</sub>/Si substrates by atomic ALD technique for their subsequent usage as sensing materials for the ethanol detection.
5. Chapter 6 summarizes the work on 2D TMOs heterojunctions.

## References

1. Z. Cai, B. Liu, X. Zou, H. Cheng, Chemical vapor deposition growth and applications of two-dimensional materials and their heterostructures, *Chem. Rev.* 118 (2018) 6091-6133.
2. H. Zhang, Ultrathin two-dimensional nanomaterials, *ACS Nano* 9 (2015) 9451-9469.
3. A. K. Geim, K. S. Novoselov, The rise of graphene, *Nanoscience and technology: a collection of reviews from nature journals*, (2010) 11-19.
4. K. Shavanova, Y. Bakakina, I. Burkova, I. Shtepliuk, R. Viter, A. Ubelis, V. Beni, N. Starodub, R. Yakimova, V. Khranovskyy, Application of 2D non-graphene materials and 2D oxide nanostructures for biosensing technology, *Sensors* 16 (2016) 223.
5. Z. Wei, S. Zhuiykov, Challenges and recent advancements of functionalization of two-dimensional nanostructured molybdenum trioxide and dichalcogenides, *Nanoscale* 11 (2019) 15709-15738.
6. Z. Sun, T. Liao, Y. Dou, S. Hwang, M. Park, L. Jiang, J. Kim, S. Dou, Generalized self-assembly of scalable two-dimensional transition metal oxide nanosheets, *Nat. Commun.* 5 (2014) 1-9.
7. M. Osada, T. Sasaki, Exfoliated oxide nanosheets: new solution to nanoelectronics, *J. Mater. Chem.* 19 (2009) 2503-2511.
8. R. Ma, T. Sasaki, Nanosheets of oxides and hydroxides: Ultimate 2D charge-bearing functional crystallites, *Adv. Mater.* 22 (2010) 5082-5104.
9. T. Sasaki, M. Watanabe, H. Hashizume, H. Yamada, H. Nakazawa, Macromolecule-like aspects for a colloidal suspension of an exfoliated titanate. Pairwise association of nanosheets and dynamic reassembling process initiated from it, *J. Am. Chem. Soc.* 118 (1996) 8329-8335.

10. K. Fukuda, I. Nakai, Y. Ebina, R. Ma, T. Sasaki, Colloidal unilamellar layers of tantalum oxide with open channels, *Inorg. Chem.* 46 (2007) 4787-4789.
11. K. Liao, X. Wang, Y. Sun, D. Tang, M. Han, P. He, X. Jiang, T. Zhang, H. Zhou, An oxygen cathode with stable full discharge-charge capability based on 2D conducting oxide, *Energ. Environ. Sci.* 8 (2015) 1992-1997.
12. R. S. Datta, F. Haque, M. Mohiuddin, B. J. Carey, N. Syed, A. Zavabeti, B. Zhang, H. Khan, K. J. Berean, J. Z. Ou, N. Mahmood, T. Daeneke, K. Kalantar-zadeh, Highly active two dimensional  $\alpha$ - $\text{MoO}_{3-x}$  for the electrocatalytic hydrogen evolution reaction, *J. Mater. Chem. A* 5 (2017) 24223-24231.
13. X. Rui, Z. Lu, H. Yu, D. Yang, H. H. Hng, T. M. Lim, Q. Yan, Ultrathin  $\text{V}_2\text{O}_5$  nanosheet cathodes: realizing ultrafast reversible lithium storage, *Nanoscale* 5 (2013) 556-560.
14. Y. Chen, C. Tan, H. Zhang, L. Wang, Two-dimensional graphene analogues for biomedical applications, *Chem. Soc. Rev.* 44 (2015) 2681-2701.
15. B. Radisavljevic, A. Radenovic, J. Brivio, V. Giacometti, A. Kis, Single-layer  $\text{MoS}_2$  transistors, *Nat. Nanotechnol.* 6 (2011) 147.
16. Q. H. Wang, K. Kalantar-Zadeh, A. Kis, J. N. Coleman, M. S. Strano, Electronics and optoelectronics of two-dimensional transition metal dichalcogenides, *Nat. Nanotechnol.* 7 (2012) 699.
17. M. Chhowalla, H. S. Shin, G. Eda, L-J. Li, K. P. Loh, H. Zhang, The chemistry of two-dimensional layered transition metal dichalcogenide nanosheets, *Nat. Chem.* 5 (2013) 263.
18. M. A. Py, R. R. Haering, Structural destabilization induced by lithium intercalation in  $\text{MoS}_2$  and related compounds, *Can. J. Phys.* 61 (1983) 76-84.
19. P. Ganal, W. Olberding, T. Butz, G. Ouvrard, Soft chemistry induced host metal coordination change from octahedral to trigonal prismatic in 1T- $\text{TaS}_2$ , *Solid State Ionics* 59 (1993) 313-319.
20. G. Eda, H. Yamaguchi, D. Voiry, T. Fujita, M. Chen, M. Chhowalla, Photoluminescence from chemically exfoliated  $\text{MoS}_2$ , *Nano Lett.* 11 (2011) 5111-5116.
21. G. Eda, T. Fujita, H. Yamaguchi, D. Voiry, M. Chen, M. Chhowalla, Coherent atomic and electronic heterostructures of single-layer  $\text{MoS}_2$ , *ACS Nano* 6 (2012) 7311-7317.
22. T. Lorenz, D. Teich, J. O. Joswig, G. Seifert, Theoretical study of the mechanical behavior of individual  $\text{TiS}_2$  and  $\text{MoS}_2$  nanotubes, *J. Phys. Chem. C* 116 (2012) 11714-11721.
23. B. Radisavljevic, A. Kis. Mobility engineering and a metal-insulator transition in monolayer  $\text{MoS}_2$ , *Nat. Mater.* 12 (2013) 815-820.

24. Y. Zhang, T. R. Chang, B. Zhou, Y-T. Cui, H. Yan, Z. Liu, F. Schmitt, J. Lee, R. Morre, Y. Chen, H. Lin, H-T. Jeng, S-K. Mo, Z. Hussain, A. Bansil, Z-X. Shen, Direct observation of the transition from indirect to direct bandgap in atomically thin epitaxial MoSe<sub>2</sub>, *Nat. Nanotechnol.* 9 (2014) 111.
25. M. S. Fuhrer, J. Hone, Measurement of mobility in dual-gated MoS<sub>2</sub> transistors, *Nat. Nanotechnol.* 8 (2013) 146-147.
26. W. Choi, N. Choudhary, G. H. Han, J. Park, D. Akinwande, Y. H. Lee, Recent development of two-dimensional transition metal dichalcogenides and their applications, *Mater. Today* 20 (2017) 116-130.
27. M. Acerce, D. Voiry, M. Chhowalla, Metallic 1T phase MoS<sub>2</sub> nanosheets as supercapacitor electrode materials, *Nat. Nanotechnol.* 10 (2015) 313.
28. K. S. Novoselov, A. K. Geim, S. V. Morozov, D. Jiang, Y. Zhang, S. V. Dubonos, I. V. Grigorieva, A. A. Firsov, Electric field effect in atomically thin carbon films, *Science* 306 (2004) 666-669.
29. Z. Zeng, T. Sun, J. Zhu, X. Huang, Z. Yin, G. Lu, Z. Fan, Q. Yan, H. H. Hng, H. Zhang, An effective method for the fabrication of few-layer-thick inorganic nanosheets, *Angew. Chem. Int. Ed.* 51 (2012) 9052-9056.
30. H. Li, J. Wu, Z. Yin, H. Zhang, Preparation and applications of mechanically exfoliated single-layer and multilayer MoS<sub>2</sub> and WSe<sub>2</sub> nanosheets, *Acc. Chem. Res.* 47 (2014) 1067-1075.
31. H. Li, Z. Yin, Q. He, H. Li, X. Huang, G. Lu, D. W. H. Fam, A. L. Y. Tok, Q. Zhang, H. Zhang, Fabrication of single-and multilayer MoS<sub>2</sub> film-based field-effect transistors for sensing NO at room temperature, *Small* 8 (2012) 63-67.
32. H. Li, G. Lu, Y. Wang, Z. Yin, C. Cong, Q. He, L. Wang, F. Ding, T. Yu, H. Zhang, Mechanical exfoliation and characterization of single-and few-layer nanosheets of WSe<sub>2</sub>, TaS<sub>2</sub>, and TaSe<sub>2</sub>, *Small* 9 (2013) 1974-1981.
33. W. Li, Y. Zhang, X. Long, J. Cao, X. Xin, X. Guan, J. Peng, X. Zheng, Gas sensors based on mechanically exfoliated MoS<sub>2</sub> nanosheets for room-temperature NO<sub>2</sub> detection, *Sensors* 19 (2019) 2123
34. V. Nicolosi, M. Chhowalla, M. G. Kanatzidis, M. S. Strano, J. N. Coleman, Liquid exfoliation of layered materials, *Science* 340 (2013) 1226-1229.
35. T. Yang, T. T. Song, M. Callsen, J. Zhou, J. W. Chai, Y. P. Feng, S. J. Wang, M. Yang, Atomically thin 2D transition metal oxides: Structural reconstruction, interaction with substrates, and potential applications, *Adv. Mater. Interfaces* 6 (2019) 1801160.
36. C. Backes, N. C. Berner, X. Chen, P. LaPlace, M. Freeley, G. S. Duesberg, J. N. Coleman, A. R. McDonald, Functionalization of liquid-exfoliated two-dimensional 2H-MoS<sub>2</sub>, *Angew. Chem. Int. Ed.* 54 (2015) 2638-2642.

37. G. Q. Han, Y. R. Liu, W. H. Hu, B. Dong, X. Li, Y-M. Chai, Y-Q. Liu, C-G. Liu, WS<sub>2</sub> nanosheets based on liquid exfoliation as effective electrocatalysts for hydrogen evolution reaction, *Mater. Chem. Phys.* 167 (2015) 271-277.
38. Z. Wei, Z. Hai, M. K. Akbari, D. Qi, K. Xing, Q. Zhao, F. Verpoort, J. Hu, L. Hyde, S. Zhuiykov, Atomic layer deposition-developed two-dimensional  $\alpha$ -MoO<sub>3</sub> windows excellent hydrogen peroxide electrochemical sensing capabilities, *Sens. Actuators B Chem.* 262 (2018) 334-344.
39. W. M. Haynes, *CRC handbook of chemistry and physics*, CRC Press. 2014.
40. R. Lv, Q. Li, A. R. Botello-Méndez, T. Hayashi, B. Wang, A. Berkdemir, Q. Hao, A. L. Elías, R. Cru-Silva, H. R. Gutiérrez, Y. A. Kim, H. Muramatsu, J. Zhu, M. Endo, H. Terrones, J-C. Charlier, M. Pan, M. Terrones, Nitrogen-doped graphene: beyond single substitution and enhanced molecular sensing, *Sci. Rep.* 2 (2012) 586.
41. Y. Yu, C. Li, Y. Liu, L. Su, Y. Zhang, L. Cao, Controlled scalable synthesis of uniform, high-quality monolayer and few-layer MoS<sub>2</sub> films, *Sci. Rep.* 3 (2013) 1866.
42. A. L. Elías, N. Perea-López, A. Castro-Beltrán, A. Berkdemir, R. Lv, S. Feng, A. D. Long, T. Hayashi, Y. A. Kim, M. Endo, H. R. Gutiérrez, N. R. Pradhan, L. Baicas, T. E. Mallouk, F. Lopez-Urias, H. Terrones, M. Terrones, Controlled synthesis and transfer of large-area WS<sub>2</sub> sheets: from single layer to few layers, *ACS Nano* 7 (2013) 5235-5242.
43. S. Wang, M. Pacios, H. Bhaskaran, J. H. Warner, Substrate control for large area continuous films of monolayer MoS<sub>2</sub> by atmospheric pressure chemical vapor deposition, *Nanotechnology* 27 (2016) 085604.
44. B. Liu, M. Fathi, L. Chen, A. Abbas, Y. Ma, C. Zhou, Chemical vapor deposition growth of monolayer WSe<sub>2</sub> with tunable device characteristics and growth mechanism study, *ACS Nano* 9 (2015) 6119-6127.
45. Q. Ji, Y. Zhang, T. Gao, Y. Zhang, D. Ma, M. Liu, Y. Chen, X. Qiao, P-H, Tan, M. Kan, J. Feng, Q. Sun, Z. Liu, Epitaxial monolayer MoS<sub>2</sub> on mica with novel photoluminescence, *Nano Lett.* 13 (2013) 3870-3877.
46. Y. Gong, B. Li, G. Ye, S. Yang, X. Zou, S. Lei, Z. Jin, E. Bianco, S. Vinod, B. I. Yakobson, Direct growth of MoS<sub>2</sub> single crystals on polyimide substrates, *2D Mater.* 4 (2017) 021028.
47. C. S. Blackman, I. P. Parkin, Atmospheric pressure chemical vapor deposition of crystalline monoclinic WO<sub>3</sub> and WO<sub>3-x</sub> thin films from reaction of WCl<sub>6</sub> with O-containing solvents and their photochromic and electrochromic properties, *Chem. Mater.* 17 (2005) 1583-1590.
48. K. L. Siefering, G. L. Griffin, Growth kinetics of CVD TiO<sub>2</sub>: influence of carrier gas, *J. Electrochem. Soc.* 137 (1990) 1206-1208.

49. M. Purica, E. Budianu, E. Rusu, M. Danila, R. Gavrilă, Optical and structural investigation of ZnO thin films prepared by chemical vapor deposition (CVD), *Thin Solid Films* 403 (2002) 485-488.
50. J. Jeong, S. P. Choi, C. I. Chang, D. C. Shin, J. S. Park, B-T Lee, Y-J. Park, H-J. Song, Photoluminescence properties of SnO<sub>2</sub> thin films grown by thermal CVD, *Solid State Commun.* 127 (2003) 595-597.
51. W. Hao, C. Marichy, C. Journet, Atomic layer deposition of stable 2D materials, *2D Mater.* 6 (2018) 012001.
52. Y. Shi, H. Li, L-J. Li, Recent advances in controlled synthesis of two-dimensional transition metal dichalcogenides via vapour deposition techniques, *Chem. Soc. Rev.* 44 (2015) 2744-2756.
53. V. Miiikkulainen, M. Leskelä, M. Ritala, R. L. Puurunen, Crystallinity of inorganic films grown by atomic layer deposition: Overview and general trends, *J. Appl. Phys.* 113 (2013) 2.
54. N. P. Dasgupta, X. Meng, J.W. Elam, A. B. F. Martinson, Atomic layer deposition of metal sulfide materials, *Acc. Chem. Res.* 48 (2015) 341-348.
55. C. Wang, G. Du, K. Ståhl, H. Huang, Y. Zhong, J. Z. Jiang, Ultrathin SnO<sub>2</sub> nanosheets: oriented attachment mechanism, nonstoichiometric defects, and enhanced lithium-ion battery performances, *J. Phys. Chem. C* 116 (2012) 4000-4011.
56. X. Xiao, H. Song, S. Lin, Y. Zhou, X. Zhan, Z. Hu, Q. Zhang, J. Sun, B. Yang, T. Li, L. Jiao, J. Zhou, J. Tang, Y. Gogotsi, Scalable salt-templated synthesis of two-dimensional transition metal oxides, *Nat. Commun.* 7 (2016) 1-8.
57. B. Luo, G. Liu, L. Wang, Recent advances in 2D materials for photocatalysis, *Nanoscale* 8 (2016) 6904-6920.
58. X. Zhang, Z. Lai, C. Tan, H. Zhang, Solution-processed two-dimensional MoS<sub>2</sub> nanosheets: preparation, hybridization, and applications, *Angew. Chem. Int. Ed.* 55 (2016) 8816-8838.
59. J. Kim, S. Byun, A. J. Smith, J. Yu, J. Huang, Enhanced electrocatalytic properties of transition-metal dichalcogenides sheets by spontaneous gold nanoparticle decoration, *J. Phys. Chem. Lett.* 4 (2013) 1227-1232.
60. Q. Lu, Y. Yu, Q. Ma, B. Chen, H. Zhang, 2D transition-metal-dichalcogenide-nanosheet-based composites for photocatalytic and electrocatalytic hydrogen evolution reactions, *Adv. Mater.* 28 (2016) 1917-1933.
61. Z. Liu, Z. Gao, Y. Liu, M. Xia, R. Wang, N. Li, Heterogeneous nanostructure based on 1T-phase MoS<sub>2</sub> for enhanced electrocatalytic hydrogen evolution, *ACS Appl. Mater. Interfaces* 9 (2017) 25291-25297.
62. F. Haque, T. Daeneke, K. Kalantar-zadeh, J. Z. Ou, Two-dimensional transition metal oxide and chalcogenide-based photocatalysts, *Nano-micro Lett.* 10 (2018) 23.

63. M. Nasilowski, B. Mahler, E. Lhuillier, S. Ithurria, B. Dubertret, Two-dimensional colloidal nanocrystals, *Chem. Rev.* 116 (2016) 10934-10982.
64. W.-J. Ong, L. L. Tan, S. P. Chai, S.-T. Yong, A. R. Mohamed, Highly reactive {001} facets of TiO<sub>2</sub>-based composites: synthesis, formation mechanism and characterization, *Nanoscale* 6 (2014) 1946-2008.
65. J. Mei, T. Liao, L. Kou, Z. Sun, Two-dimensional metal oxide nanomaterials for next-generation rechargeable batteries, *Adv. Mater.* 29 (2017) 1700176.
66. P. K. Kannan, D. J. Late, H. Morgan, C. S. Rout, Recent developments in 2D layered inorganic nanomaterials for sensing, *Nanoscale* 7 (2015) 13293-13312.
67. G. Konstantatos, M. Badioli, L. Gaudreau, J. Osmond, M. Bernechea, F. P. G. de Arquer, F. Gatti, F. H. L. Koppes, Hybrid graphene-quantum dot phototransistors with ultrahigh gain, *Nat. Nanotechnol.* 7 (2012) 363-368.
68. Z. Xu, S. Lin, X. Li, S. Zhang, Z. Wu, W. Xu, Y. Lu, S. Xu, Monolayer MoS<sub>2</sub>/GaAs heterostructure self-driven photodetector with extremely high detectivity, *Nano Energy* 23 (2016) 89-96.
69. P. Vabbina, N. Choudhary, A. Chowdhury, R. Sinha, M. Karabiyik, S. Das, W. Choi, N. Pala, Highly sensitive wide bandwidth photodetector based on internal photoemission in CVD grown p-type MoS<sub>2</sub>/graphene Schottky junction, *ACS Appl. Mater. Interfaces* 7 (2015) 15206-15213.
70. W. Feng, X. Wang, J. Zhang, L. Wang, W. Zheng, P. Hu, W. Cao, B. Yang, Synthesis of two-dimensional  $\beta$ -Ga<sub>2</sub>O<sub>3</sub> nanosheets for high-performance solar blind photodetectors, *J. Mater. Chem. C* 2 (2014) 3254-3259.
71. Z. Hai, M. K. Akbari, C. Xue, H. Xu, S. Depuydt, S. Zhuiykov, Photodetector with superior functional capabilities based on monolayer WO<sub>3</sub> developed by atomic layer deposition, *Sens. Actuators B Chem.* 245 (2017) 954-962.
72. M. Winter, B. Barnett, K. Xu, Before Li ion batteries, *Chem. Rev.* 118 (2018) 11433-11456.
73. K. M. Winslow, S. J. Laux, T. G. Townsend, A review on the growing concern and potential management strategies of waste lithium-ion batteries, *Resour. Conserv. Recycl.* 129 (2018) 263-277.
74. P. K. Nayak, L. Yang, W. Brehm, P. Adelhelm, From lithium-ion to sodium-ion batteries: advantages, challenges, and surprises, *Angew. Chem. Int. Ed.* 57 (2018) 102-120.
75. K. Chang, W. Chen, L. Ma, H. Li, H. Li, F. Huang, Z. Xu, Q. Zhang, J.-Y. Lee, Graphene-like MoS<sub>2</sub>/amorphous carbon composites with high capacity and excellent stability as anode materials for lithium ion batteries, *J. Mater. Chem.* 21 (2011) 6251-6257.

76. X. Cao, Y. Shi, W. Shi, X. Rui, Q. Yan, J. Kong, H. Zhang, Preparation of MoS<sub>2</sub>-coated three-dimensional graphene networks for high-performance anode material in lithium-ion batteries, *Small* 9 (2013) 3433-3438.
77. S. Hariharan, K. Saravanan, P. Balaya,  $\alpha$ -MoO<sub>3</sub>: A high performance anode material for sodium-ion batteries, *Electrochem. Commun.* 31 (2013) 5-9.
78. H. Zhang, L. Gao, Y. Gong, Exfoliated MoO<sub>3</sub> nanosheets for high-capacity lithium storage, *Electrochem. Commun.* 52 (2015) 67-70.
79. G. Wang, L. Zhang, J. Zhang, A review of electrode materials for electrochemical supercapacitors, *Chem. Soc. Rev.* 41 (2012) 797-828.
80. K. S. Kumar, N. Choudhary, Y. Jung, J. Thomas, Recent advances in two-dimensional nanomaterials for supercapacitor electrode applications, *ACS Energy Lett.* 3 (2018) 482-495.
81. S. Shi, C. Xu, C. Yang, Y. Chen, J. Liu, F. Kang, Flexible asymmetric supercapacitors based on ultrathin two-dimensional nanosheets with outstanding electrochemical performance and aesthetic property, *Sci. Rep.* 3 (2013) 2598.
82. Q. Yang, Z. Lu, X. Sun, J. Liu, Ultrathin Co<sub>3</sub>O<sub>4</sub> nanosheet arrays with high supercapacitive performance, *Sci. Rep.* 3 (2013) 3537.
83. J. Chang, M. Jin, F. Yao, T. H. Kim, V. T. Le, H. Yue, F. Gunes, B. Li, A. Ghosh, S. Xie, Y. H. Lee, Asymmetric supercapacitors based on graphene/MnO<sub>2</sub> nanospheres and graphene/MoO<sub>3</sub> nanosheets with high energy density, *Adv. Funct. Mater.* 23 (2013) 5074-5083.
84. J. Ping, Z. Fan, M. Sindoro, Y. Ying, H. Zhang, Recent advances in sensing applications of two-dimensional transition metal dichalcogenide nanosheets and their composites, *Adv. Funct. Mater.* 27 (2017) 1605817.
85. X. Geng, Y. Zhang, Y. Han, J. Li, L. Yang, M. Benarmara, L. Chen, H. Zhu, Two-dimensional water-coupled metallic MoS<sub>2</sub> with nanochannels for ultrafast supercapacitors, *Nano Lett.* 17 (2017) 1825-1832.
86. D. Wang, Y. Xiao, X. Luo, X. Luo, Z. Wu, Y-J. Wang, B. Fang, Swollen ammoniated MoS<sub>2</sub> with 1T/2H hybrid phases for high-rate electrochemical energy storage, *ACS Sustain. Chem. Eng.* 5 (2017) 2509-2515.
87. L. Jiang, S. Zhang, S. A. Kulinich, X. Song, J. Zhu, X. Wang, H. Zeng, Optimizing hybridization of 1T and 2H phases in MoS<sub>2</sub> monolayers to improve capacitances of supercapacitors, *Mater. Res. Lett.* 3 (2015) 177-183.
88. Z. Hai, M. K. Akbari, Z. Wei, C. Xue, H. Xu, J. Hu, S. Zhuiykov, Nano-thickness dependence of supercapacitor performance of the ALD-fabricated two-dimensional WO<sub>3</sub>, *Electrochim. Acta* 246 (2017) 625-633.

89. E. Lee, Y. S. Yoon, D. J. Kim, Two-dimensional transition metal dichalcogenides and metal oxide hybrids for gas sensing, *ACS Sens.* 3 (2018) 2045-2060.
90. K. Kalantar-zadeh, J. Z. Ou, T. Daeneke, A. Mitchell, T. Sasaki, M. S. Fuhrer, Two dimensional and layered transition metal oxides, *Appl. Mater. Today* 5 (2016) 73-89.
91. X. Liu, T. Ma, N. Pinna, J. Zhang, Two-dimensional nanostructured materials for gas sensing, *Adv. Funct. Mater.* 27 (2017) 1702168.
92. F. Ji, X. Ren, X. Zheng, Y. Liu, L. Pang, J. Jiang, S. Liu, 2D-MoO<sub>3</sub> nanosheets for superior gas sensors, *Nanoscale* 8 (2016) 8696-8703.
93. P. Bollella, G. Fusco, C. Tortolini, G. Sanzò, G. Favero, L. Gorton, R. Antiochia, Beyond graphene: electrochemical sensors and biosensors for biomarkers detection, *Biosens. Bioelectron.* 89 (2017) 152-166.
94. S. Wu, Z. Zeng, Q. He, Z. Wang, S. Wang, Y. Du, Z. Yin, X. Sun, W. Chen, H. Zhang, Electrochemically reduced single-layer MoS<sub>2</sub> nanosheets: Characterization, properties, and sensing applications, *Small* 8 (2012) 2264-2270.
95. K. Kalantar-zadeh, J. Z. Ou, Biosensors based on two-dimensional MoS<sub>2</sub>, *ACS Sens.* 1 (2016) 5-16.
96. P. Rai, S. M. Majhi, Y-T, Yu, J-H, Lee, Noble metal@ metal oxide semiconductor core@ shell nano-architectures as a new platform for gas sensor applications, *RSC Adv.* 5 (2015) 76229-76248.
97. C. Xu, S. Peng, C. Tan, C. Ang, H. Tan, H. Zhang, Q. Yan, Ultrathin S-doped MoSe<sub>2</sub> nanosheets for efficient hydrogen evolution, *J. Mater. Chem. A* 2 (2014) 5597-5601.
98. D. J. Late, Y-K. Huang, B. Liu, J. Acharya, S. N. Shirodkar, J. Luo, A. Yan, D. Charles, U. V. Waghmare, V. P. Dravid, C. N. R. Rao, Sensing behavior of atomically thin-layered MoS<sub>2</sub> transistors, *ACS Nano* 7 (2013) 4879-4891.
99. J. Azadmanjiri, V. K. Srivastava, P. Kumar, J. Wang, A. Yu, Graphene-supported 2D transition metal oxide heterostructures, *J. Mater. Chem. A* 6 (2018) 13509-13537.
100. S. Su, C. Zhang, L. Yuwen, X. Liu, L. Wang, C. Fan, L. Wang, Uniform Au@ Pt core-shell nanodendrites supported on molybdenum disulfide nanosheets for the methanol oxidation reaction, *Nanoscale* 8 (2016) 602-608.
101. D. Zhang, C. Jiang, P. Li, Y. Sun, Layer-by-layer self-assembly of Co<sub>3</sub>O<sub>4</sub> nanorod-decorated MoS<sub>2</sub> nanosheet-based nanocomposite toward high-performance ammonia detection, *ACS Appl. Mater. Interfaces* 9 (2017) 6462-6471.
102. Y. Li, L. Wang, T. Cai, S. Zhang, Y. Liu, Y. Song, X. Dong, L. Hu, Glucose-assisted synthesize 1D/2D nearly vertical CdS/MoS<sub>2</sub> heterostructures for efficient photocatalytic hydrogen evolution, *Chem. Eng.* 321 (2017) 366-374.

103. X. Zheng, J. Xu, K. Yan, H. Wang, Z. Wang, S. Yang, Space-confined growth of MoS<sub>2</sub> nanosheets within graphite: the layered hybrid of MoS<sub>2</sub> and graphene as an active catalyst for hydrogen evolution reaction, *Chem. Mater.* 26 (2014) 2344-2353.
104. W. Ren, H. Zhang, C. Guan, C. Cheng, Ultrathin MoS<sub>2</sub> nanosheets@ metal organic framework-derived N-doped carbon nanowall arrays as sodium ion battery anode with superior cycling life and rate capability, *Adv. Funct. Mater.* 27 (2017) 1702116.
105. M. R. Laskar, D. N. Nath, L. Ma, E. W. Lee, C. H. Lee, T. Kent, Z. Yang, R. Mishra, M. A. Roldan, J-C. Idrobo, S. T. Pantelides, S. J. Pennnycook, R. C. Myers, Y. Wu, S. Rajan, P-type doping of MoS<sub>2</sub> thin films using Nb, *Appl. Phys. Lett.* 104 (2014) 092104.
106. M. Rahm, R. Hoffmann, N. W. Ashcroft, Atomic and ionic radii of elements 1-96, *Chem. Eur. J.* 22 (2016) 14625-14632.
107. J. Park, M. S. Kim, B. Park, S. H. Oh, S. Roy, J. Kim, W. Choi, Composition-tunable synthesis of large-scale Mo<sub>1-x</sub>W<sub>x</sub>S<sub>2</sub> alloys with enhanced photoluminescence, *ACS Nano* 12 (2018) 6301-6309.
108. M. Haruta, Catalysis of gold nanoparticles deposited on metal oxides, *Cattech* 6 (2002) 102-115.
109. G. P. Wiederrecht, G. A. Wurtz, J. Hranisavljevic, Coherent coupling of molecular excitons to electronic polarizations of noble metal nanoparticles, *Nano Lett.* 4 (2004) 2121-2125.
110. S. Guo, E. Wang, Noble metal nanomaterials: controllable synthesis and application in fuel cells and analytical sensors, *Nano Today* 6 (2011) 240-264.
111. P. K. Jain, X. Huang, I. H. El-Sayed, M. A. El-Sayed, Noble metals on the nanoscale: optical and photothermal properties and some applications in imaging, sensing, biology, and medicine, *Acc. Chem. Res.* 41 (2008) 1578-1586.
112. K. Jiang, D. Zhao, S. Guo, X. Zhang, X. Zhu, J. Guo, G. Lu, X. Huang, Efficient oxygen reduction catalysis by subnanometer Pt alloy nanowires, *Sci. Adv.* 3 (2017) e1601705.
113. M. Luo, Y. Sun, X. Zhang, Y. Qin, M. Li, Y. Li, C. Li, Y. Yang, L. Wang, P. Gao, G. Lu, S. Guo, Stable high-Index faceted Pt skin on zigzag-like PtFe nanowires enhances oxygen reduction catalysis, *Adv. Mater.* 30 (2018) 1705515.
114. Q. Jia, J. Li, K. Caldwell, D. E. Ramaker, J. M. Ziegelbauer, R. S. Kukreja, A. Kongkanand, S. Mukerjee, Circumventing metal dissolution induced degradation of Pt-alloy catalysts in proton exchange membrane fuel cells: revealing the asymmetric volcano nature of redox catalysis, *ACS Catal.* 6 (2016) 928-938.
115. X. Huang, Z. Zeng, S. Bao, M. Wang, X. Qi, Z. Fan, H. Zhang, Solution-phase epitaxial growth of noble metal nanostructures on dispersible single-layer molybdenum disulfide nanosheets, *Nat. Commun.* 4 (2013) 1-8.

116. L. Yuwen, F. Xu, B. Xue, Z. Luo, Q. Zhang, B. Bao, S. Su, L. Weng, W. Huang, L. Wang, General synthesis of noble metal (Au, Ag, Pd, Pt) nanocrystal modified MoS<sub>2</sub> nanosheets and the enhanced catalytic activity of Pd-MoS<sub>2</sub> for methanol oxidation, *Nanoscale* 6 (2014) 5762-5769.
117. S. Su, W. Cao, C. Zhang, X. Han, H. Yu, D. Zhu, J. Chao, C. Fan, L. Wang, Improving performance of MoS<sub>2</sub>-based electrochemical sensors by decorating noble metallic nanoparticles on the surface of MoS<sub>2</sub> nanosheet, *RSC Adv.* 6 (2016) 76614-76620.
118. S. Cai, Q. Han, C. Qi, Z. Lian, X. Jia, R. Yang, C. Wang, Pt<sub>74</sub>Ag<sub>26</sub> nanoparticle-decorated ultrathin MoS<sub>2</sub> nanosheets as novel peroxidase mimics for highly selective colorimetric detection of H<sub>2</sub>O<sub>2</sub> and glucose, *Nanoscale* 8 (2016) 3685-3693.
119. X. Zhong, H. Yang, S. Guo, S. Li, G. Gou, Z. Niu, Z. Dong, Y. Lei, J. Jin, R. Li, J. Ma, In situ growth of Ni-Fe alloy on graphene-like MoS<sub>2</sub> for catalysis of hydrazine oxidation, *J. Mater. Chem.* 22 (2012) 13925-13927.
120. Z. Sun, Q. Zhao, G. Zhang, Y. Li, G. Zhang, X. Fan, Exfoliated MoS<sub>2</sub> supported Au-Pd bimetallic nanoparticles with core-shell structures and superior peroxidase-like activities, *RSC Adv.* 5 (2015) 10352-10357.
121. S. Cui, Z. Wen, X. Huang, J. Chang, J. Chen, Stabilizing MoS<sub>2</sub> nanosheets through SnO<sub>2</sub> nanocrystal decoration for high-performance gas sensing in air, *Small* 11 (2015) 2305-2313.
122. Y. Chen, B. Song, X. Tang, I. Lu, J. Xue, Ultrasmall Fe<sub>3</sub>O<sub>4</sub> nanoparticle/MoS<sub>2</sub> nanosheet composites with superior performances for lithium ion batteries, *Small* 10 (2014) 1536-1543.
123. Y-F. Zhao, Z-Y. Yang, Y-X. Zhang, L. Jing, X. Guo, Z. Ke, P. Hu, G. Wang, Y. Yan, K-N. Sun, Cu<sub>2</sub>O decorated with cocatalyst MoS<sub>2</sub> for solar hydrogen production with enhanced efficiency under visible light, *J. Phys. Chem. C* 118 (2014) 14238-14245.
124. Y. Pi, Z. Li, D. Xu, J. Liu, Y. Li, F. Zhang, G. Zhang, W. Peng, X. Fan, 1T-phase MoS<sub>2</sub> nanosheets on TiO<sub>2</sub> nanorod arrays: 3D photoanode with extraordinary catalytic performance, *ACS Sustain. Chem. Eng.* 5 (2017) 5175-5182.
125. S. V. P. Vattikuti, P. C. Nagajyothi, P. Anil Kumar Reddy, M. K. Kumar, J. Shim, C. Byon, Tiny MoO<sub>3</sub> nanocrystals self-assembled on folded molybdenum disulfide nanosheets via a hydrothermal method for supercapacitor, *Mater. Res. Lett.* 6 (2018) 432-441.
126. M. Wang, P. Ju, W. Li, Y. Zhao, X. Han, Ag<sub>2</sub>S nanoparticle-decorated MoS<sub>2</sub> for enhanced electrocatalytic and photoelectrocatalytic activity in water splitting, *Dalton Trans.* 46 (2017) 483-490.
127. C. Li, H. Wang, J. Ming, M. Liu, P. Fang, Hydrogen generation by photocatalytic reforming of glucose with heterostructured CdS/MoS<sub>2</sub> composites under visible light irradiation, *Int. J. Hydrog. Energy* 42 (2017) 16968-16978.

128. J. Zhang, Z. Zhu, X. Feng, Construction of two-dimensional MoS<sub>2</sub>/CdS p-n nanohybrids for highly efficient photocatalytic hydrogen evolution, *Chem. Eur. J.* 20 (2014) 10632-10635.
129. S. Bhattacharya, D. Dinda, S. K. Saha, Role of trap states on storage capacity in a graphene/MoO<sub>3</sub> 2D electrode material, *J. Phys. D: Appl. Phys.* 48 (2015) 145303.
130. Z. Liu, N. Li, H. Zhao, Y. Du, Colloidally synthesized MoSe<sub>2</sub>/graphene hybrid nanostructures as efficient electrocatalysts for hydrogen evolution, *J. Mater. Chem. A* 3 (2015) 19706-19710.
131. G. Huang, T. Chen, W. Chen, Z. Wang, K. Chang, L. Ma, F. Huang, Graphene-Like MoS<sub>2</sub>/Graphene Composites: Cationic Surfactant-Assisted Hydrothermal Synthesis and Electrochemical Reversible Storage of Lithium, *Small* 9 (2013) 3693-3703.
132. W. Yu, S. Li, Y. Zhang, W. Ma, T. Sun, J. Yuan, K. Fu, Q. Bao, Near-infrared photodetectors based on MoTe<sub>2</sub>/graphene heterostructure with high responsivity and flexibility, *Small* 13 (2017) 1700268.
133. H. Ji, X. Liu, Z. Liu, B. Yan, L. Chen, Y. Xie, C. Liu, W. Hou, G. Yang, In situ preparation of sandwich MoO<sub>3</sub>/C hybrid nanostructures for high-rate and ultralong-life supercapacitors, *Adv. Funct. Mater.* 25 (2015) 1886-1894.
134. X. Zhao, H. Zhu, X. Yang, Amorphous carbon supported MoS<sub>2</sub> nanosheets as effective catalysts for electrocatalytic hydrogen evolution, *Nanoscale* 6 (2014) 10680-10685.
135. K. Chang, W. Chen, L-cysteine-assisted synthesis of layered MoS<sub>2</sub>/graphene composites with excellent electrochemical performances for lithium ion batteries, *ACS Nano* 5 (2011) 4720-4728.
136. D. Sun, D. Ye, P. Liu, Y. Tang, J. Guo, L. Wang, H. Wang, MoS<sub>2</sub>/Graphene nanosheets from commercial bulky MoS<sub>2</sub> and graphite as anode materials for high rate sodium-Ion batteries, *Adv. Energy Mater.* 8 (2018) 1702383.
137. H. Tang, K. Dou, C-C. Kaun, Q. Kuang, S. Yang, MoSe<sub>2</sub> nanosheets and their graphene hybrids: synthesis, characterization and hydrogen evolution reaction studies, *J. Mater. Chem. A* 2 (2014) 360-364.
138. X. Li, J. Wang, D. Xie, J. Xu, Y. Xia, W. Li, L. Xiang, Z. Li, S. Xu, S. Komarneni, Flexible room-temperature formaldehyde sensors based on rGO film and rGo/MoS<sub>2</sub> hybrid film, *Nanotechnology* 28 (2017) 325501.
139. M. Saraf, K. Natarajan, S. M. Mobin, Emerging robust heterostructure of MoS<sub>2</sub>-rGO for high-performance supercapacitors, *ACS Appl. Mater. Interfaces* 10 (2018) 16588-16595.
140. B. Mendoza-Sánchez, D. Hanlon, J. Coelho, S. O'Brien, H. Pettersson, J. Coleman, V. Nicolost, An investigation of the energy storage properties of a 2D  $\alpha$ -MoO<sub>3</sub>-SWCNTs composite films, *2D Mater.* 4 (2016) 015005.

141. S.-Y. Tai, C.-J. Liu, S.-W. Chou, F. S.-S. Chien, J.-Y. Lin, T.-W. Lin, Few-layer MoS<sub>2</sub> nanosheets coated onto multi-walled carbon nanotubes as a low-cost and highly electrocatalytic counter electrode for dye-sensitized solar cells, *J. Mater. Chem.* 22 (2012) 24753-24759.
142. S. Ding, J. S. Chen, X. W. Lou, Glucose-assisted growth of MoS<sub>2</sub> nanosheets on CNT backbone for improved lithium storage properties, *Chem. Eur. J.* 17 (2011) 13142-13145.
143. C. Wang, W. Wan, Y. Huang, J. Chen, H. H. Zhou, X. X. Zhang, Hierarchical MoS<sub>2</sub> nanosheet/active carbon fiber cloth as a binder-free and free-standing anode for lithium-ion batteries, *Nanoscale* 6 (2014) 5351-5358.
144. X. Huang, B. Zheng, Z. Liu, C. Tan, J. Liu, B. Chen, H. Li, J. Chen, X. Zhang, Z. Fan, W. Zhang, Guo, F. Huo, Y. Yang, L. Huang, H. Zhang, Coating two-dimensional nanomaterials with metal-organic frameworks, *ACS Nano* 8 (2014) 8695-8701.
145. Y. Zhang, S. J. Park, Facile construction of MoO<sub>3</sub>@ ZIF-8 core-shell nanorods for efficient photoreduction of aqueous Cr (VI), *Appl. Catal. B: Environ.* 240 (2019) 92-101.
146. L. Shen, M. Luo, Y. Liu, R. Liang, F. Jing, L. Wu, Noble-metal-free MoS<sub>2</sub> co-catalyst decorated UiO-66/CdS hybrids for efficient photocatalytic H<sub>2</sub> production, *Appl. Catal. B: Environ.* 166 (2015) 445-453.
147. G. Bai, S. Yuan, Y. Zhao, Z. Yang, S. Y. Choi, Y. Chai, S. F. Yu, S. P. Lau, J. Hao, 2D layered materials of rare-earth Er-doped MoS<sub>2</sub> with NIR-to-NIR down-and up-conversion photoluminescence, *Adv. Mater.* 28 (2016) 7472-7477.
148. Y. C. Lin, D. O. Dumcenco, H.-P. Komsa, Y. Niimi, A. V. Krasheninnikov, Y.-S. Huang, K. Suenaga, Properties of individual dopant atoms in single-layer MoS<sub>2</sub>: atomic structure, migration, and enhanced reactivity, *Adv. Mater.* 26 (2014) 2857-2861.
149. Q. Q. Sun, Y. J. Li, J.-L. He, W. Yang, P. Zhou, H.-L. Lu, S.-J. Ding, D. W. Zhang, The physics and backward diode behavior of heavily doped single layer MoS<sub>2</sub> based pn junctions, *Appl. Phys. Lett.* 102 (2013) 093104.
150. D. Sarkar, X. Xie, J. Kang, H. Zhang, W. Liu, J. Navarrete, M. Moskovits, K. Banerjee, Functionalization of transition metal dichalcogenides with metallic nanoparticles: implications for doping and gas-sensing, *Nano Lett.* 15 (2015) 2852-2862.
151. D. Kiriya, M. Tosun, P. Zhao, J. S. Kang, A. Javey, Air-stable surface charge transfer doping of MoS<sub>2</sub> by benzyl viologen, *J. Am. Chem. Soc.* 136 (2014) 7853-7856.
152. Y. Wang, J. Z. Ou, A. F. Chrimes, B. J. Carey, T. Daeneke, M. M. Y. A. Alsaif, S. Zhuiykov, N. Medhekar, M. Bhaskaran, J. R. Friend, M. S. Strano, K. Kalantar-Zadeh, Plasmon resonances of highly doped two-dimensional MoS<sub>2</sub>, *Nano Lett.* 15 (2015) 883-890.

153. S.-Y. Cho, H.-J. Koh, H.-W. Yoo, J.-S. Kim, H.-T. Jung, Tunable volatile-organic-compound sensor by using Au nanoparticle incorporation on MoS<sub>2</sub>, *ACS Sens.* 2 (2017) 183-189.
154. F. Xiong, H. Wang, X. Liu, J. Sun, M. Brongersma, E. Pop, Y. Cui, Li intercalation in MoS<sub>2</sub>: in situ observation of its dynamics and tuning optical and electrical properties, *Nano Lett.* 15 (2015) 6777-6784.
155. J. Wan, S. D. Lacey, J. Dai, W. Bao, M. S. Fuhrer, L. Hu, Tuning two-dimensional nanomaterials by intercalation: materials, properties and applications, *Chem. Soc. Rev.* 45 (2016) 6742-6765.
156. J. Z. Ou, J. L. Campbell, D. Yao, W. Wlodarski, K. Kalantar-zadeh, In situ Raman spectroscopy of H<sub>2</sub> gas interaction with layered MoO<sub>3</sub>, *J. Phys. Chem. C* 115 (2011) 10757-10763.
157. F. Z. Wang, M. J. Zheng, B. Zhang, C. Q. Zhu, Q. Li, L. Ma, W. Z. Shen, Ammonia intercalated flower-like MoS<sub>2</sub> nanosheet film as electrocatalyst for high efficient and stable hydrogen evolution. *Sci. Rep.* 6 (2016) 31092.
158. X. Wang, X. Shen, Z. Wang, R. Yu, L. Chen, Atomic-scale clarification of structural transition of MoS<sub>2</sub> upon sodium intercalation, *ACS Nano* 8 (2014) 11394-11400.
159. S. Balendhran, J. Deng, J. Z. Ou, S. Walla, J. Scott, J. Tang, K. L. Wang, M. R. Field, S. Russo, S. Zhuiykov, M. S. Strano, N. Medhekar, S. Sriram, M. Bhaskaran, K. Kalantar-zadeh, Enhanced charge carrier mobility in two-dimensional high dielectric molybdenum oxide, *Adv. Mater.* 25 (2013) 109-114.
160. H. Yu, Y. Yu, J. Liu, P. Ma, Y. Wang, F. Zhang, Z. Fu, Space-confined growth of Ag<sub>3</sub>PO<sub>4</sub> nanoparticles within WS<sub>2</sub> sheets: Ag<sub>3</sub>PO<sub>4</sub>/WS<sub>2</sub> composites as visible-light-driven photocatalysts for decomposing dyes, *J. Mater. Chem. A* 3 (2015) 19439-19444.
161. Z. Wang, Y. Shen, S. Ning, Y. Ito, P. Liu, Z. Tang, T. Fujita, A. Hirata, M. Chen, Chemical selectivity at grain boundary dislocations in monolayer Mo<sub>1-x</sub>W<sub>x</sub>S<sub>2</sub> transition metal dichalcogenides, *ACS Appl. Mater. Interfaces* 9 (2017) 29438-29444.
162. Z. Wang, Y. Shen, Y. Ito, Y. Zhang, J. Du, T. Fujita, A. Hirata, Z. Tang, M. Chen, Synthesizing 1T-1H two-phase Mo<sub>1-x</sub>W<sub>x</sub>S<sub>2</sub> Monolayers by chemical vapor deposition, *ACS Nano* 12 (2018) 1571-1579.
163. K. Yang, X. Wang, H. Li, B. Chen, X. Zhang, S. Li, N. Wang, X. Huang, W. Huang, Composition- and phase-controlled synthesis and applications of alloyed phase heterostructures of transition metal disulphides, *Nanoscale* 9 (2017) 5102-5109.
164. B. Rajbanshi, S. Sarkar, P. Sarkar, The electronic and optical properties of MoS<sub>2(1-x)</sub>Se<sub>2x</sub> and MoS<sub>2(1-x)</sub>Te<sub>2x</sub> monolayers, *Phys. Chem. Chem. Phys.* 17 (2015) 26166-26174.
165. H. Liu, K. K. A. Antwi, S. Chua, D. Chi, Vapor-phase growth and characterization of Mo<sub>1-x</sub>W<sub>x</sub>S<sub>2</sub> (0 ≤ x ≤ 1) atomic layers on 2-inch sapphire substrates, *Nanoscale* 6 (2014) 624-629.

166. Q. He, Y. Wan, H. Jiang, C. Wu, Z. Sun, S. Chen, Y. Zhou, H. Chen, D. Liu, Y. A. Haleem, B. Ge, X. Wu, L. Song, High-metallic-phase-concentration  $\text{Mo}_{1-x}\text{W}_x\text{S}_2$  nanosheets with expanded interlayers as efficient electrocatalysts, *Nano Res.* 11 (2018) 1687-1698.
167. G. Barik, S. Pal, Monolayer Transition-metal dichalcogenide  $\text{Mo}_{1-x}\text{W}_x\text{S}_2$  Alloys as efficient anode materials for lithium-ion batteries, *J. Phys. Chem. C* 122 (2018) 25837-25848.
168. J. Li, H. Yan, W. Wei, L. Meng, Microwave-assisted mass synthesis of  $\text{Mo}_{1-x}\text{W}_x\text{S}_2$  alloy composites with a tunable lithium storage property, *Dalton Trans.* 47 (2018) 15148-15154.

# Chapter 2

## ALD-DEVELOPED 2D $\alpha$ -MoO<sub>3</sub> WINDOWS SUPERIOR HYDROGEN PEROXIDE ELECTROCHEMICAL SENSING CAPABILITIES

---

### 2.1 Abstract

2D  $\alpha$ -MoO<sub>3</sub> nanofilms with a thickness of 4.9 nm were fabricated via the ALD technique for the first time on the wafer-scale and were subsequently annealed at 200°C. The developed MoO<sub>3</sub> nanofilms were composed of flat nanoparticles with an average size of about 35 nm and possessed a layered orthorhombic phase ( $\alpha$ -MoO<sub>3</sub>). The electrochemical sensor based on these 2D  $\alpha$ -MoO<sub>3</sub> nanofilms exhibited high sensitivity of 168.72  $\mu\text{A} \cdot \text{mM}^{-1} \cdot \text{cm}^{-2}$  to hydrogen peroxide (H<sub>2</sub>O<sub>2</sub>) and presented extremely wide linear detection range of 0.4  $\mu\text{M}$  – 57.6 mM with the lowest detection limit of 0.076  $\mu\text{M}$  at the signal to noise ratio of 3. Furthermore, due to the extremely thin nature of 2D  $\alpha$ -MoO<sub>3</sub> nanofilms, an ultra-fast response/recovery time of  $\sim 2.0$  s was achieved under the wide linear H<sub>2</sub>O<sub>2</sub> detection range. Additionally, the sensor based on 2D  $\alpha$ -MoO<sub>3</sub> nanofilms was also demonstrated great long-term stability, excellent selectivity, and high reproducibility. The 2D  $\alpha$ -MoO<sub>3</sub> nanofilms fabricated via the ALD technique in this work represent a unique opportunity for the development of high-performance electrochemical sensors based on 2D transition metal oxides.

### 2.2 Introduction

MoO<sub>3</sub>, as an n-type and wide-bandgap semiconductor, has a high dielectric constant ( $k \sim 500$ ) [1]. Owing to its high dielectric constant, enhanced carrier mobilities and tunable bandgap have been observed in 2D MoO<sub>3</sub> in contrast to other transition metal oxides and transition metal dichalcogenides [2, 3]. Thus, 2D MoO<sub>3</sub> has been established as an ideal material for electronic applications such as resistive memory devices [4], field-effect biosensors [5], and electronic ink based printable transistors [6]. Especially, unlike the phases of monoclinic  $\beta$  and hexagonal  $h$ , orthorhombic MoO<sub>3</sub> ( $\alpha$ -MoO<sub>3</sub>) possesses the well-known layered crystal structure, in which MoO<sub>6</sub> octahedra establish planes that are held together by weak Van der Waals forces [7]. Due to the strong interlayer chemical bonds (Mo-O) and weak vdW interlayer interactions,  $\alpha$ -MoO<sub>3</sub>

can be exfoliated or deposited as two-dimensional films or sheets with considerable surface-to-volume ratios [8, 9]. As is known,  $\alpha$ -MoO<sub>3</sub> can be reduced to form MoO<sub>(3-x)</sub> and increasing  $x$  can lower the bandgap, so intercalation method can be used to manipulate the stoichiometry and band structure of 2D  $\alpha$ -MoO<sub>3</sub>, which is also a vital factor for the improvement of some properties [10, 11]. For example, chromium in 2D  $\alpha$ -MoO<sub>3</sub> is achieved upon the intercalation of ions that change the bandgap value. By reducing the bandgap, the appearance of MoO<sub>3</sub> changes from transparent to Prussian blue, and this aspect can be utilized in optical applications [12]. Even though 2D MoO<sub>3</sub> possesses various interesting properties and it is widely used in many aspects, to the best of our knowledge, the utilization of 2D MoO<sub>3</sub> for the fabrication of electrochemical sensor has rarely reported in the literature.

Up to now, a wide range of approaches has been developed for the synthesis of 2D MoO<sub>3</sub> nanomaterial, such as chemical vapor deposition, atomic layer deposition, hydrothermal and mechanical exfoliation [2, 13-16]. As we mentioned in Chapter 1, the critical challenge of the exfoliation method is the difficulties of controlling the thickness, scale-up, and the size of nanosheets. For the hydrothermal method, the production of the synthesized 2D MoO<sub>3</sub> is still very small. In these strategies, the ALD technique, due to the relative growth rate and surface controlled layer-by-layer process based on self-limiting chemical reactions, large-scale conformal, dense nanofilms with precise thickness, and component control can be developed at the relatively low temperatures [17, 18].

Hydrogen peroxide (H<sub>2</sub>O<sub>2</sub>) has been widely used in pharmaceutical, clinic, environmental, mining, textile, paper, food manufacturing, and chemical industries due to its strong oxidizing and reducing properties [19, 20]. Highly sensitive hydrogen peroxide determination is of prime importance in quality control for the food, chemical, and pharmaceutical industries. On the other hand, in living organisms, hydrogen peroxide is a by-product of the enzymatic reactions, such as glucose oxidase, cholesterol oxidase, glutamate oxidase, urate oxidase, lactate oxidase, alcohol oxidase, D-amino acid oxidase, lysine oxidase and oxalate oxidase [21]. Nevertheless, the excessive amount of hydrogen peroxide accumulation in cells could lead to a series of cell damage and cause aging and disease, including cardiovascular disease, Alzheimer's disease, and cancer [22-24]. Hence, it is closely bound up with people's health and safety. Therefore, selective and accurate measurements of hydrogen peroxide with high convenience and precise are essential. Up to date, different

electrochemical detection methods for hydrogen peroxide, including enzymatic and non-enzymatic methods, have been created and applied in numerous fields, owing to their unique merits like real-time detection, high sensitivity and low cost [25, 26]. At present, most of the hydrogen peroxide sensors that are widely used in commercial use are electrochemical enzyme sensors. Although enzyme sensors have the advantages of high sensitivity, good selectivity, and low detection limit, they are difficult to prepare and purify enzymes, and are easily deactivated and easy to inactivate. Compared to the enzymatic electrochemical method, the non-enzymatic electrochemical detection has a few obvious advantages such as simplicity, high stability, and long lifetime according to the previous studies [27, 28]. Therefore, the applications of non-enzymatic electrochemical detection have attracted increasing attention in recent years.

In this Chapter, 2D  $\alpha$ -MoO<sub>3</sub> nanostructures were developed by the ALD technique using (N<sup>t</sup>BuN)<sub>2</sub>(NMe<sub>2</sub>)<sub>2</sub>Mo as a molybdenum precursor and plasma oxygen gases as oxygen precursor. The morphology, chemical component, and crystalline phases characterization results demonstrated that 2D  $\alpha$ -MoO<sub>3</sub> nanofilms were successfully deposited over a large scale area on the substrate. More importantly, the electrochemical measurements, including CV, electrochemical impedance spectroscopy (EIS) and chronoamperometry, were carried out and analyzed to investigate the electrochemical behaviors of 2D  $\alpha$ -MoO<sub>3</sub> nanofilms for H<sub>2</sub>O<sub>2</sub> detection. The high sensitivity, excellent selectivity, good long-term stability, ultra-fast response/recovery time, and especially the broad wide linear range with a low detection limit indicated the potential utility for the determination of hydrogen peroxide in the real application.

## 2.3 Experimental

### 2.3.1 Chemicals

Bis(ter-butyylimido)bis(dimethylamido)molybdenum precursor, also known as (N<sup>t</sup>BuN)<sub>2</sub>(NMe<sub>2</sub>)<sub>2</sub>Mo, was purchased from the Strem Chemicals Inc. USA and was used for the ALD development of 2D MoO<sub>3</sub> on the wafer scale. All other chemicals were obtained from the Sigma-Aldrich, USA, and were used without further purification.

### 2.3.2 Sample fabrication

Ultra-thin  $\alpha$ -MoO<sub>3</sub> films were deposited on the 4-inch SiO<sub>2</sub>/Si wafers (1 k $\Omega$  cm) by ALD technique using the cross-flow reactor of Savannah S100 (Ultratech/Cambridge Nanotech)

with  $(\text{N}^t\text{BuN})_2(\text{NMe}_2)_2\text{Mo}$  and oxygen plasma gases as the molybdenum precursor and oxygen precursor, respectively, and the machine is shown in Figure 2.1. Prior to the deposition of  $\alpha$ -MoO<sub>3</sub> films, the additional SiO<sub>2</sub> insulating layer with a thickness of 110 nm was deposited on Si wafer by plasma-enhanced chemical vapor deposition (Oxford Instruments PLASMALAB 100). After that, in order to make the SiO<sub>2</sub>/Si wafers electrically conductive to facilitate the subsequent investigation of the properties, Au films were deposited on SiO<sub>2</sub>/Si wafers using an Electron Beam Evaporator method [Nanochrome II (Intivac, USA)] with the thickness of

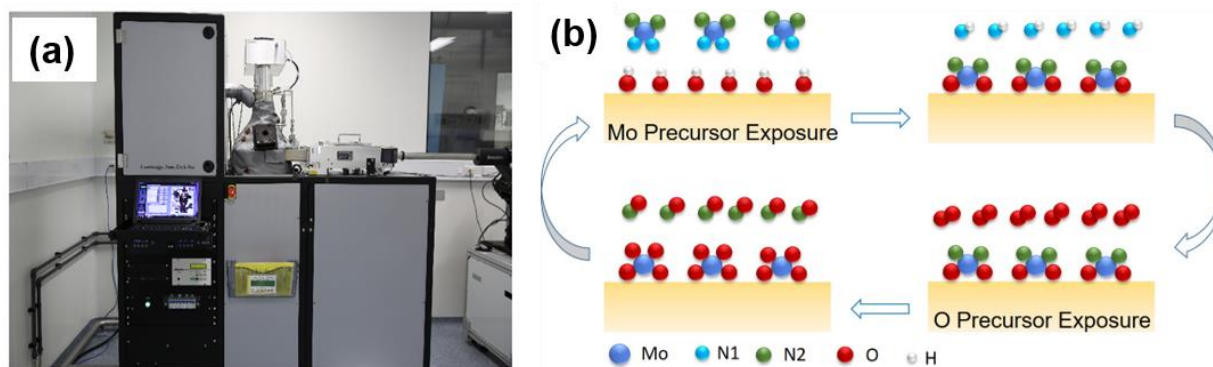


Figure 2.1. (a) The photo of the ALD instrument, (b) Schematic diagram of one ALD cycle for the deposition of 2D MoO<sub>3</sub> nanofilms

150 nm. A 200  $\mu\text{m}$ -wide surface space at the center of the wafer was intentionally left at the same time for the characterization of the developed  $\alpha$ -MoO<sub>3</sub> nanofilms, due to the roughness of Au films. During the process of developing ultra-thin  $\alpha$ -MoO<sub>3</sub> films, the loading of precursors was performed in the glove-box to avoid oxygen and moisture contamination, and argon as the precursor carrier gas was used with the flow rate of 30 standard cubic centimeters per minute (sccm). Then, various deposition temperatures ranging from 100 to 350  $^{\circ}\text{C}$  and different pulse duration and purge time were used to establish the best recipe parameter for ultra-thin  $\alpha$ -MoO<sub>3</sub> film deposition. In doing so, the precursor saturation time and O<sub>2</sub> plasma saturation time were optimized at each deposition temperature. Accordingly, the  $(\text{N}^t\text{BuN})_2(\text{NMe}_2)_2\text{Mo}$  with the flow rate of 80 sccm was pulsed into the reaction chamber for 0.75 s in 4 consecutive cycles with 2 s interval between each precursor pulse to ensure complete monolayer coverage, but also to prevent significant precursor over-saturation which could lead to precursor condensation inside the reaction chamber. Then, the reaction products were purged out of the chamber during 15 s. In the case of plasma exposure, the flow rate of 20 sccm

was selected for O<sub>2</sub> plasma delivery to create the laminar flow for precursor over the substrate surface, and to assure the complete oxidation and ligand combustion and to prevent the incorporation of hydrocarbons and nitrogen in nanofilms. One ALD cycle for the deposition of 2D MoO<sub>3</sub> nanofilms was presented in Figure 2.1 (b).

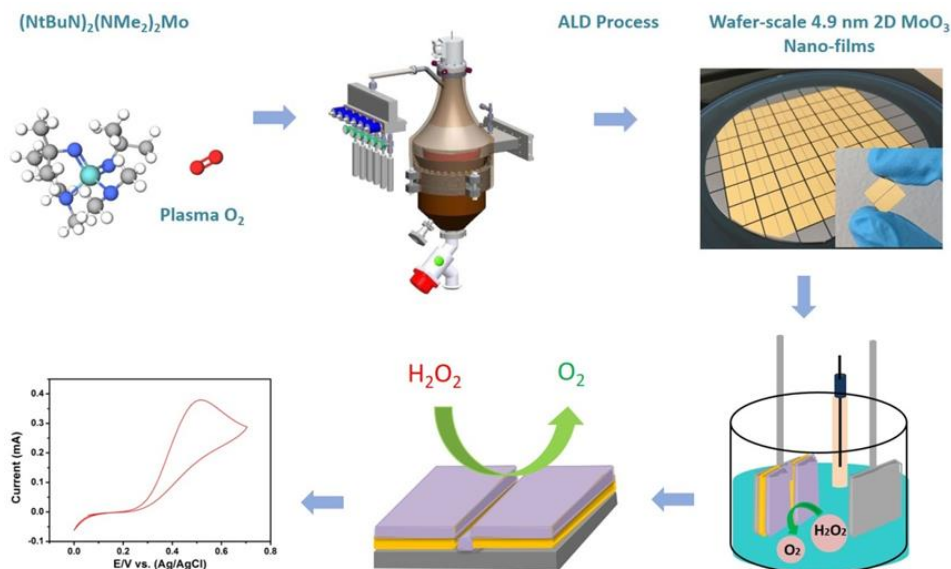


Figure 2.2. Graphical scheme of the development of 2D  $\alpha$ -MoO<sub>3</sub> nanofilms.

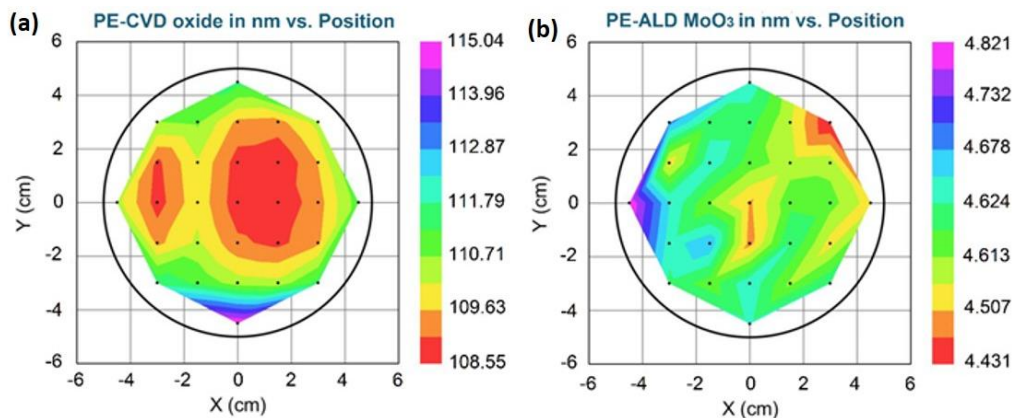


Figure 2.3. The map thickness (color bar in nm) vs. position extracted from the spectral ellipsometry for (a) CVD SiO<sub>2</sub> and (b) ALD MoO<sub>3</sub> ultra-thin nanofilms.

Consequently, the optimum growth conditions for the development of MoO<sub>3</sub> nanofilms were designed, and the final recipe is presented in Table 2.1. Finally, the wafer-scale ALD-fabricated 2D  $\alpha$ -MoO<sub>3</sub> nanofilms with a thickness of 4.9 nm were developed. After the deposition, the wafers were diced into 1.0 × 1.0 cm pieces, and the fabrication process together

Table 2.1. The detailed ALD recipe for development of wafer-scaled MoO<sub>3</sub> ultra-thin nanofilms.

Step	Instruction	Value	Component
0	Flow	0 sccm ( cm <sup>3</sup> /min)	Residual Flow
1	Flow	0 sccm	Residual Flow
2	APC	100%	Confirm APC open
3	Heater	250 °C	Chamber temperature
4	Heater	250 °C	Chamber temperature
5	Heater	250 °C	Chamber temperature
6	Heater	250 °C	Chamber temperature
7	Heater	150 °C	Precursor delivery temperature
8	Heater	150 °C	ALD valves temperature
9	Heater	150 °C	Temperature of APC valve
10	Stabilize	-	Stabilize heater
11	Stabilize	-	Stabilize heater
12	Stabilize	-	Stabilize heater
13	Stabilize	-	Stabilize heater
14	Stabilize	-	Stabilize heater
15	Stabilize	-	Stabilize heater
16	Stabilize	-	Stabilize heater
17	Heater	60 °C	Temperature of Mo precursor
18	Stabilize	60 sec	Stabilize heater
19	MFC Valve	1/0	Oxygen mass flow controller
20	Flow	30 sccm	Manifold process flow
21	Flow	80 sccm	Main chamber process flow
22	Flow	0 sccm	Oxygen flow
23	Wait	600 sec	Wait for substrate to reach temperature
24	APC	0%	APC closed
25	Wait	2 sec	Wait for pressure increase
26	Pulse	0.25 sec	Ar precursor boost, Mo precursor cycle start
27	Wait	0.5 sec	Boost stabilize
28	Pulse	0.75 sec	Mo precursor dose
29	Wait	2 sec	Mo precursor reaction time
30	Go to 26	4 cycles	Mo precursor cycle end
31	APC	100 %	APC open
32	Wait	15 sec	Mo purge
33	Flow	20 sccm	O <sub>2</sub> flow on
34	Wait	5 sec	Wait for conformal flow
35	Plasma	300 W	Plasma on
36	Wait	20 sec	O* Reaction
37	Plasma	0 W	Plasma off
38	Flow	0 sccm	O <sub>2</sub> flow off
39	Wait	8 sec	O <sub>2</sub> purge
40	Go to 24	38 cycles	Deposition cycles
41	heater	0 oC	Mo precursor heater off
42	Flow	20 sccm	Residual flow
43	Flow	40 sccm	Residual flow
44	Flow	0 sccm	Oxygen flow
45	MFCV valve	0	Oxygen mass flow controller off
46	APC	100%	Confirm APC open

with H<sub>2</sub>O<sub>2</sub> measurements, as schematically presented in Figure 2.2. Finally, the samples were annealed in air at 200 °C for 1 h, with the heating rate of 0.5 °C/min.

Following the successful deposition of ultrathin MoO<sub>3</sub> nanofilms, the ellipsometry technique was employed to verify the thickness of the deposited materials. The variations of the thickness (nm) are depicted by the color bar adjacent to the graphs. The ellipsometry map analysis of the CVD-deposited SiO<sub>2</sub> insulating layer and ALD-deposited MoO<sub>3</sub> nanofilms are demonstrated in Figure 2.3(a) and (b), respectively, with the incident angle of 65°. The average thickness of the CVD-deposited SiO<sub>2</sub> insulating layer was 110 nm, and ALD-deposited MoO<sub>3</sub> nanofilms were 4.6 nm, respectively.

### 2.3.3 Characterization

The surface morphology of the ALD-developed  $\alpha$ -MoO<sub>3</sub> sample was characterized by Field Emission Scanning Electron Microscope (FE-SEM, JEOL 7800F) and Atomic Force Microscopy (AFM, JPK System, Nano Wizard). X-ray Photoelectron Spectroscopy (Rigakudenki model XPS-7000) with monochromatic Mg-K $\alpha$  radiation at 300 W was employed to study the surface composition and chemical state. Raman spectroscopy of the MoO<sub>3</sub> sample was performed on a spectrometer (Lab Ram ARAMIS, Horiba Jobin-Yvon, Edison, NJ, USA) using  $\lambda$  = 532.2 nm argon-ion lasers.

### 2.3.4 Electrochemical testing

Electrochemical performances of 2D  $\alpha$ -MoO<sub>3</sub> nanofilms were evaluated on the Autolab PGSTAT204 (Metrohm Autolab. B.V., Netherlands) with a conventional three-electrode system, which includes the Pt wire as the counter electrode, Ag/AgCl (3.0 M KCl) as the reference electrode and 2D  $\alpha$ -MoO<sub>3</sub> nanofilms on Au/Cr deposited SiO<sub>2</sub>/Si substrate with the area of 1 cm × 0.5 cm as the working electrodes (Figure 2.4), and all the electrochemical experiments were conducted at the room temperature (20 °C) unless it was stated. The electrochemical characterization of 2D  $\alpha$ -MoO<sub>3</sub> nanofilms was performed in 5 mM K<sub>4</sub>Fe(CN)<sub>6</sub> solution containing 0.1 M KCl under the CV measurement in the potential range of -0.2 V to 0.6 V at a scan rate of 10 mV/s and EIS measurements within the frequency ranging from 10<sup>5</sup> to 0.1 Hz at an AC amplitude of 5 mV under the open-circuit potential conditions. For the experiments on the detection of hydrogen peroxide, all of the tests were accomplished in 0.1 M phosphate-buffered saline (PBS, pH 7.0). The CVs of the samples were measured in the potential range

from 0 to 0.7 V. Chronoamperometry was tested at an applied potential of 0.5 V under 330 rpm magnetic stirring. The response/recovery time was defined as the time to achieve 90% of the total current change.

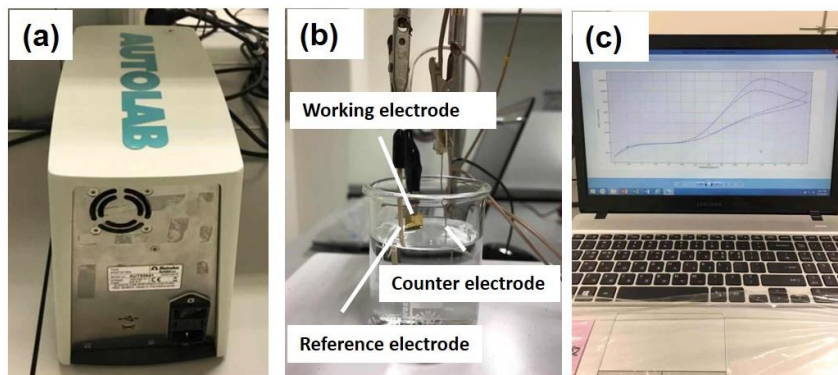


Figure 2.4. Electrochemical properties testing system.

## 2.4 Results and discussion

### 2.4.1 Characterization of 2D $\alpha$ -MoO<sub>3</sub> nanofilms

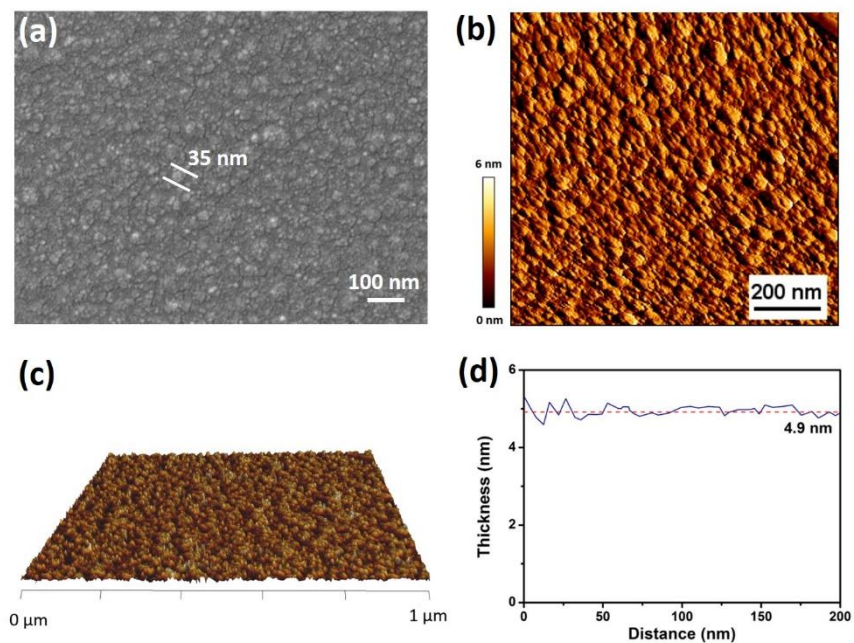


Figure 2.5. (a) SEM, (b) AFM, and (c) 3D topographical AFM images of MoO<sub>3</sub> films. (d) Film thickness versus distance.

SEM and AFM techniques were employed to examine the surface morphology and the thickness of ALD-fabricated 2D  $\alpha$ -MoO<sub>3</sub> nanofilms. Figure 2.5(a) displays the typical high-resolution SEM image of the surface morphology of annealed MoO<sub>3</sub> films. The relative smoothly and uniformly distributed films can be observed over a large scale area of SiO<sub>2</sub>/Si substrate. The thin films were aggregated with MoO<sub>3</sub> nanoparticles, and the average diameter of the nanoparticles is 35 nm measured by the SEM apparatus. Similar characterization results can be seen from the AFM image of the MoO<sub>3</sub> films in Figure 2.5(b) and its corresponding 3D image in Figure 2-5(c). The variation of the film thickness measured by AFM across 200 nm of the sample surface was shown in Figure 2.5(d). As it is depicted, the measured average thickness of MoO<sub>3</sub> films was 4.9 nm, indicating that the dense and smooth 4.9 nm 2D MoO<sub>3</sub> nanofilms were successfully fabricated by the ALD method.

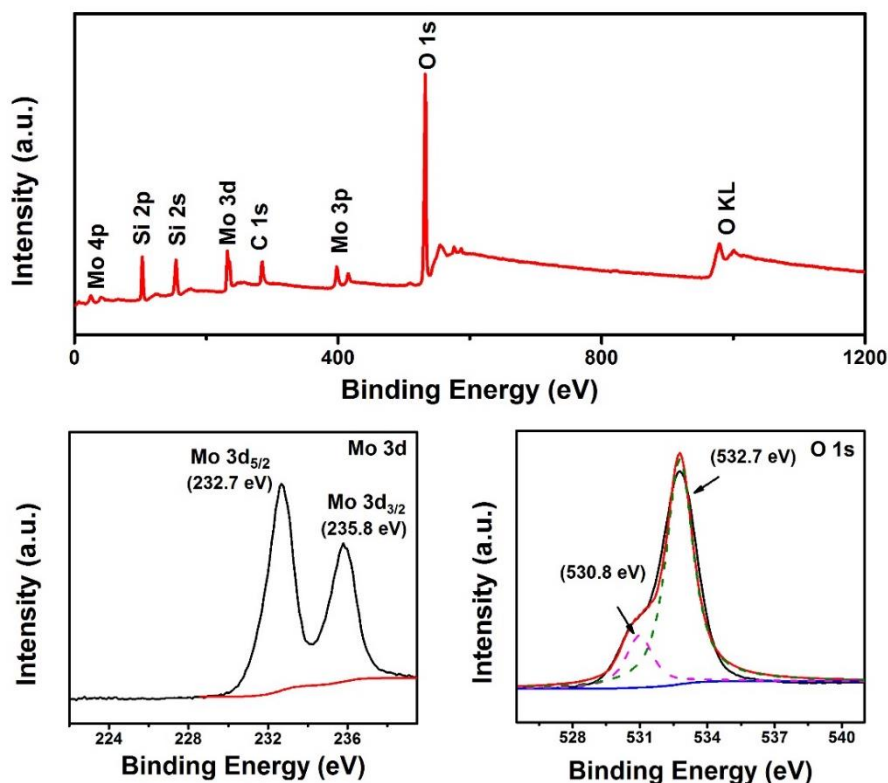


Figure 2.6. (a) XPS spectrum of the 2D MoO<sub>3</sub> nanofilms and high-resolution XPS scan of (b) Mo 3d region and (c) O 1s region.

The chemical state and composition of the deposited 2D MoO<sub>3</sub> nanofilms were investigated by XPS analysis, and the results are shown in Figure 2.6. The signals for elements of molybdenum, silicon, carbon, and oxygen can be observed from the survey scan spectrum in Figure 2.6(a), where the peaks of silicon originated from the SiO<sub>2</sub>/Si substrate and C 1s peak of graphite carbon (284.6 eV) was used as a reference to calibrate the binding energies of the peaks. In the narrow scan spectrum of Mo 3d in Figure 2.6(b), a spin-orbit doublet with peaks at 232.7 eV and 235.8 eV are attributed to the Mo 3d<sub>5/2</sub> and Mo 3d<sub>3/2</sub>, respectively [29]. The energy separation between Mo 3d<sub>5/2</sub> and Mo 3d<sub>3/2</sub> peak is 3.1 eV, and the peak ratio of Mo 3d<sub>5/2</sub> and Mo 3d<sub>3/2</sub> is 1.25, which is in good harmony with the previous reports on MoO<sub>3</sub> [30]. The O 1s peak in the XPS spectrum can be decomposed with Gaussian distribution, as shown in Figure 2.6(c). The low binding energy component located at 530.8 eV is originated from the lattice oxygen in MoO<sub>3</sub> [31], and the peak at 532.7 eV is due to the substrate of SiO<sub>2</sub> [29, 32].

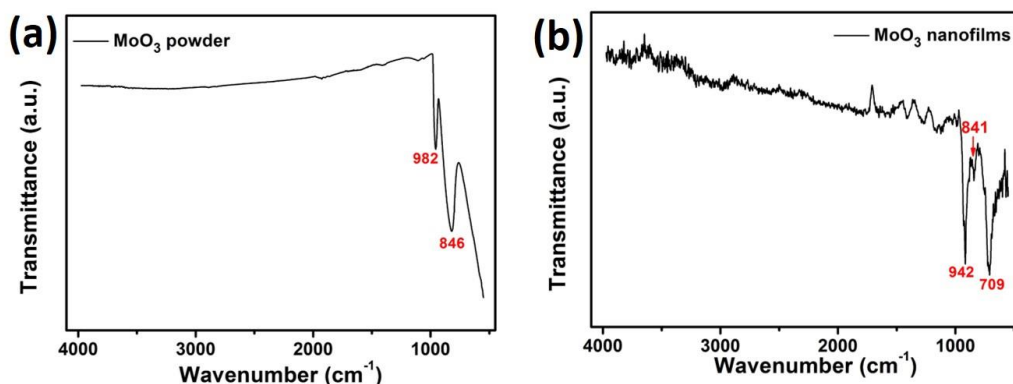


Figure 2.7. FTIR spectra of (a) commercial MoO<sub>3</sub> powder and (b) 2D  $\alpha$ -MoO<sub>3</sub> nanofilms.

FTIR spectroscopy was performed to investigate the chemical bonding states between the molybdenum and oxygen atoms in ALD-developed 2D MoO<sub>3</sub> nanofilms. Figure 2.7 shows the FTIR spectra (measured in the 550–4000 cm<sup>-1</sup> range) for the commercial MoO<sub>3</sub> powder and 2D MoO<sub>3</sub> nanofilms annealed at 200°C. The commercial MoO<sub>3</sub> powder exhibited two main vibrational modes at 982 cm<sup>-1</sup> and 846 cm<sup>-1</sup> due to the symmetric stretching mode (vs) of Mo=O and asymmetric stretch mode (vas) of Mo-O-Mo. However, both two peaks in the 2D MoO<sub>3</sub> nanofilms shift towards the lower bands [33–35] and were located at 942 cm<sup>-1</sup> and 841 cm<sup>-1</sup>, respectively, which specifies a layered orthorhombic  $\alpha$ -MoO<sub>3</sub> phase. Additionally, a new peak

at 709 cm<sup>-1</sup> appeared in the 2D MoO<sub>3</sub> nanofilms, due to ( $\nu$ Mo-O) and ( $\delta$ Mo-O) vibrations, which was the reason of the low annealed temperature [36].

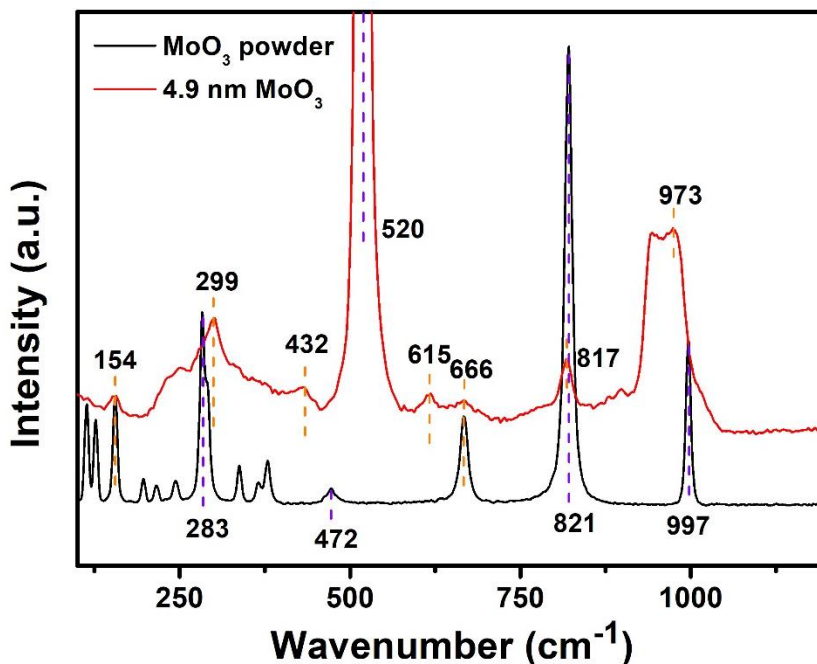


Figure 2.8. Raman spectra of commercial MoO<sub>3</sub> powder and 2D  $\alpha$ -MoO<sub>3</sub> nanofilms.

Raman spectroscopy, as a powerful technique for characterizing crystalline structures of fabricated materials, was performed using a 532.2 nm excitation and the comparison of Raman between commercial MoO<sub>3</sub> powder and 2D MoO<sub>3</sub> nanofilms in the range of 100-1200 cm<sup>-1</sup> was shown in Figure 2.8. A main band at 520 cm<sup>-1</sup> is assigned to the Si peak from SiO<sub>2</sub>/Si substrate. The strong and typical peaks at 973, 817, 666, 299 and 154 cm<sup>-1</sup> are observed from the spectrum of 2D MoO<sub>3</sub> nanofilms and compared with those of the commercial powder material, the peaks were broadened and had the tendency to shift, which might due to the phonon confinement resulted from the decrease in the particle dimensions of 2D MoO<sub>3</sub> to the nanometer scale, which has been observed with many semiconductor and oxide materials [37]. The band in the lower-frequency of 154 and 299 cm<sup>-1</sup> originates from the translation of the rigid chains and bending mode for the double bond (Mo=O) vibration [38], respectively. A band at 666 cm<sup>-1</sup> is assigned to Mo-O stretching mode of triply coordinated oxygen, which results from edge-shared oxygen in common with three octahedra [39]. The intense Raman band at 817 cm<sup>-1</sup> is the doubly coordinated bridge-oxygen Mo-O-Mo, which results from corner-shared oxygen in

common with two octahedra [40]. The Raman-active band at 973 cm<sup>-1</sup> is a asymmetric stretch of the terminal oxygen atom (Mo<sup>6+</sup>=O) mode, which results from unshared oxygen, and it is responsible for the structure of  $\alpha$ -MoO<sub>3</sub> [36]. These peak positions indicated the orthorhombic  $\alpha$ -MoO<sub>3</sub> crystalline phase was formed in this work. Interestingly, new bands appeared at 432 and 614 cm<sup>-1</sup>, and the peaks in the range of 300-400 cm<sup>-1</sup>, 160-280 cm<sup>-1</sup> and lower than 150 cm<sup>-1</sup> of 2D  $\alpha$ -MoO<sub>3</sub> nanofilms become weaker and even disappeared, which are similar with other 2D MoO<sub>3</sub> when the films become much thinner, illustrating the ultra-thin nature of ALD-developed 2D  $\alpha$ -MoO<sub>3</sub> nanofilms [38, 431, 42].

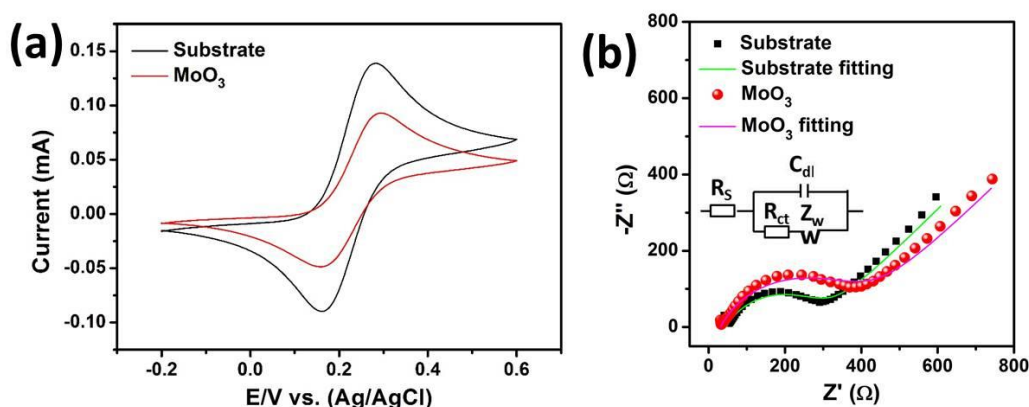


Figure 2.9. (a) CV curves of the blank substrate and 2D  $\alpha$ -MoO<sub>3</sub> nanofilms with 5mM [Fe(CN)<sub>6</sub>]<sup>3-/4-</sup> in 0.1M KCl at the scanning rate of 10mV/s. (b) Nyquist plots of the blank substrate and 2D  $\alpha$ -MoO<sub>3</sub> films with 5mM [Fe(CN)<sub>6</sub>]<sup>3-/4-</sup> in 0.1M KCl from 100kHz to 0.1Hz at an AC amplitude of 5mV under open-circuit potential condition.

The CV and EIS measurements of potassium ferricyanide could be used as valuable and convenient tools to monitor the surface state and charge transfer properties of the 2D  $\alpha$ -MoO<sub>3</sub> nanofilms. As shown in Figure 2.9(a), compared with the blank substrate, the anodic and cathodic peaks are decreased for  $\alpha$ -MoO<sub>3</sub> nanofilms, due to the high conductive native nature of Au and low conductivity properties of MoO<sub>3</sub> that hindered the charge transfer, which can also illustrate that 2D MoO<sub>3</sub> nanofilms were successfully deposited on the substrate. The capacity of electron transfer of MoO<sub>3</sub> nanofilms was investigated by EIS. There were a linear portion and a semicircle portion in the impedance spectra (Figure 2.9(b)). The elongated portion at lower frequencies reflected the diffusion process, and the semicircle portion at high-frequency regions corresponds to the electron transfer resistance (R<sub>ct</sub>), which controls the

electron-transfer kinetics of the redox probe. According to the obtained data in Table 2.2 fitted with the Randles equivalent circuit model (inset of Figure 2.9(b)), the  $R_{ct}$  of 2D MoO<sub>3</sub> nanofilms was 360.6  $\Omega$ , which was higher than that of the blank electrode (280.6  $\Omega$ ). These results confirmed the results obtained by CVs.

Table 2.2. The EIS parameters ( $R_s$ ,  $R_{ct}$ , and  $C_{dl}$ ) comparison of 2D  $\alpha$ -MoO<sub>3</sub> and blank substrate

Material	$R_s$ ( $\Omega$ )	$R_{ct}$ ( $\Omega$ )	$C_{dl}$ ( $\mu$ F)
4.9 nm 2D $\alpha$ -MoO <sub>3</sub>	39.1	360.6	78.7
Blank substrate	43.2	280.6	58.1

#### 2.4.2 Electrochemical performance of H<sub>2</sub>O<sub>2</sub> sensor based on 2D $\alpha$ -MoO<sub>3</sub> nanofilms

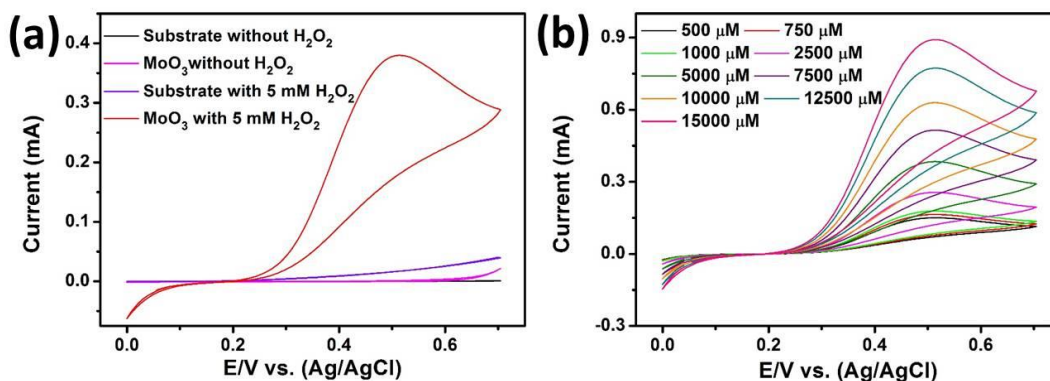


Figure 2.10. (a) CV curves of the blank substrate and ALD-developed 2D  $\alpha$ -MoO<sub>3</sub> nanofilms at the absence and presence of 5 mM H<sub>2</sub>O<sub>2</sub> in 0.1 M PBS (pH=7.0) at a scan rate of 10 mV/s. (b) CV curves of 2D  $\alpha$ -MoO<sub>3</sub> nanofilms with the different concentrations of H<sub>2</sub>O<sub>2</sub> in 0.1 M PBS (pH=7.0) at a scan rate of 10 mV/s.

The electrocatalytic activity of the sensor based on ALD-developed 2D  $\alpha$ -MoO<sub>3</sub> nanofilms towards H<sub>2</sub>O<sub>2</sub> was investigated in 0.1M PBS solutions at a scan rate of 10 mV/s. Figure 2.10(a) shows the CV curves of the blank electrode and ALD-fabricated 2D  $\alpha$ -MoO<sub>3</sub> nanofilms in the absence and presence of 5 mM H<sub>2</sub>O<sub>2</sub> in 0.1 M PBS solution, respectively. As can be seen, the blank electrode and 2D  $\alpha$ -MoO<sub>3</sub> nanofilms show almost no electrochemical response in the absence of H<sub>2</sub>O<sub>2</sub>. However, a visible oxidation peak was observed during the anodic scanning for  $\alpha$ -MoO<sub>3</sub> nanofilms at 0.5V with the current value of 0.37 mA when 5 mM H<sub>2</sub>O<sub>2</sub> was added into the solution. Although there also has the oxidation of hydrogen peroxide for the blank electrode, its oxidation current was apparently weak. Additionally, there is no cathodic current

Table 2.3. Performance comparison of the H<sub>2</sub>O<sub>2</sub> sensor based on ALD-developed 2D  $\alpha$ -MoO<sub>3</sub> nanofilms to other H<sub>2</sub>O<sub>2</sub> sensors based on nanostructured and hetero-structured materials reported to date.

Electrode material	Potential work (V)	Sensitivity ( $\mu\text{A mM}^{-1}\text{ cm}^{-2}$ )	Linear range ( $\mu\text{M}$ )	LOD ( $\mu\text{M}$ )	Response time (s)	Refs
4.9 nm 2D $\alpha$ -MoO <sub>3</sub> nanofilms	0.5 (vs Ag/AgCl)	168.72	0.4 -57600	0.076	<1.5	this work
Co <sub>3</sub> N NW/TM	-0.2 (vs SCE)	139.3	2-28000	1	<5	[43]
RGO-Pt/GCE	-0.08 (vs Ag/AgCl)	459	0.5-3.47	0.2	/	[44]
MnO <sub>2</sub> -Co <sub>3</sub> O <sub>4</sub> /GP	0.5 (vs SCE)	53.5	5-1200	0.8	<3	[45]
ox-SWCNHs@CeO <sub>2</sub>	-0.2 (vs Ag/AgCl)	160	10-1400	2.7	/	[46]
AuNPs-N-GQDs	-0.3 (vs Ag/AgCl)	186.22	0.25-13327	0.12	<5	[24]
Au/MnO <sub>2</sub> /ERGO/CF	-0.4 (vs SCE)	167	50-1400	2	<3	[47]
Au-MnO <sub>2</sub> -rGO	-0.2 (vs SCE)	980	0.1-0.022	0.05	<5	[48]
RGO-AgNPs	-0.2 (vs. SCE)	99.5	5-16370	2	<3	[49]
V <sub>2</sub> O <sub>5</sub> /GCE	-0.4 (vs Ag/AgCl)	9.87	0.1-408	0.06	/	[50]
Au/Cu <sub>2</sub> O/GCE	0.45 (vs SCE)	2.72	0-1400	1.42	/	[51]
Nafion/Pt NPs/RGO	-0.5 (vs Ag/AgCl)	132.8	5-3000	0.4	<6	[52]
CQDs/octahedral Cu <sub>2</sub> O NPs	-0.2 (vs Ag/AgCl)	130	5-53000	2.8	10	[53]
AuEPG films	0.5 (vs Ag/AgCl)	75.9	0.5-4900	0.1	<3	[54]
RGO-PMS@AuNPs	-0.75 (vs Ag/AgCl)	39.2	0.5-50000	0.06	<2	[23]
Ag/FeOOH/Au	-0.2 (vs SCE)	8.07	30-15000	22.8	<3	[55]
Fe <sub>2</sub> O <sub>3</sub> /CP	-0.75 (vs SCE)	0.032	200-5000	0.13	<1	[56]
Ag-Fe <sub>2</sub> O <sub>3</sub> -RGO	-0.2 (vs. SCE)	50.8	1.6-57000	0.5	<3	[57]
Cu <sub>2</sub> O/grapheme	-0.4 (vs Ag/AgCl)	/	300-7800	20.8	<9	[28]
f-MWCNTs/MnO <sub>2</sub> NFs	-0.4 (vs Ag/AgCl)	219.05	5-4530	0.952	<4	[58]
CuO/Cu <sub>2</sub> O-NWs/PVA	-0.2 (vs SCE)	39.5	1-3000	0.35	<5	[59]
MnO <sub>2</sub> -ERGO paper	-0.5 (vs SCE)	59	100-45400	10	<3	[60]
CuO/rGO/Cu <sub>2</sub> O	-0.3 (vs SCE)	366.2	0.5-9700	0.05	0.5	[61]

peak corresponding to reducing reaction observed during the reverse sweep, as shown in Figure 2.11. The measured results indicated that  $\alpha$ -MoO<sub>3</sub> nanofilms have a high electrocatalytic performance towards H<sub>2</sub>O<sub>2</sub>. Consequently, ALD-fabricated 2D  $\alpha$ -MoO<sub>3</sub> nanofilms are suitable

as a mediator to transfer electron between H<sub>2</sub>O<sub>2</sub> and working electrode and make possible electrochemical regeneration following electron exchange with H<sub>2</sub>O<sub>2</sub>.

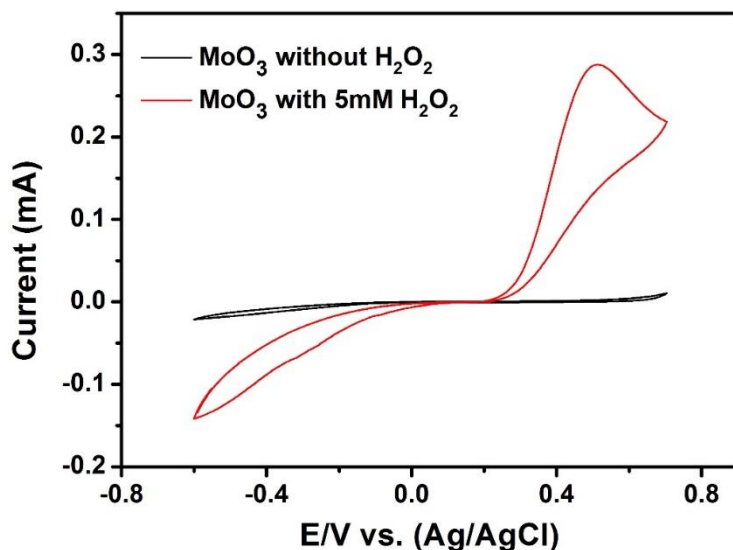


Figure 2.11. CV curves of the ALD-developed 2D  $\alpha$ -MoO<sub>3</sub> nanofilms at the absence of H<sub>2</sub>O<sub>2</sub> in 0.1 M PBS at a scan rate of 10 mV/s.

In addition, the electrocatalytic activity of 2D  $\alpha$ -MoO<sub>3</sub> nanofilms to different concentrations of H<sub>2</sub>O<sub>2</sub> was evaluated using CV and chronoamperometric measurements. Figure 2.10(b) displays the CV curves obtained from  $\alpha$ -MoO<sub>3</sub> nanofilms in the presence of different H<sub>2</sub>O<sub>2</sub> concentrations from 500  $\mu$ M to 15 mM. It is clear that with the rising of hydrogen peroxide concentration, the catalytic current also gradually increases, and the peak potential located at 0.5V keeps almost stable, which makes the quantitative assessment of hydrogen peroxide in the amperometric experiment possible. The typical steady-state current-time (i-t) response plot with continuous addition of different concentrations into the stirring PBS solution approximately every 50 s at the applied potential of 0.5 V using the chronoamperometry method is shown in Figure 2.12(a). As expected, a well-defined stepwise increment in the current responses was observed upon the addition of hydrogen peroxide. The linear detection to hydrogen peroxide range from 0.4  $\mu$ M to 57.6 mM (correlation coefficient = 0.9991) of  $\alpha$ -MoO<sub>3</sub> nanofilms calculated from the calibration curve (current versus concentration) was obtained, which is a wide linear detection scale range from nanomolar to several millimolar. Moreover, the calibration curve has been divided into three parts, which were shown as an

inset in Figure 2.12(b, c, d). It is clearly seen that the slopes of the three parts are close with each other, illustrating the excellent linearity in the range from 0.4  $\mu$ M to 57.6 mM. Besides, according to the equation of “*sensitivity=slope/surface of the electrode*” and “*low detection limit=3S<sub>b</sub>/sensitivity*” [9], where S<sub>b</sub> is the standard deviation of the blank signal. The 2D  $\alpha$ -MoO<sub>3</sub> nanofilms showed the remarkable sensitivity of 168.72  $\mu$ A mM<sup>-1</sup> cm<sup>-2</sup> with a low limit of detection (LOD) of 0.076  $\mu$ M at the signal to noise ratio of 3. The error bars in the inset of Figure 2.12(b), representing the standard deviation, are relatively small, suggesting a high accuracy of results. There were many reports dedicated to the development of the H<sub>2</sub>O<sub>2</sub> sensor. Their typical characteristics, including sensitivity, linear response range, **response time** and the LOD, are summarized in Table 2.3. It is worth noting that the sensitivity of 2D  $\alpha$ -MoO<sub>3</sub> nanofilms is lower than that of some

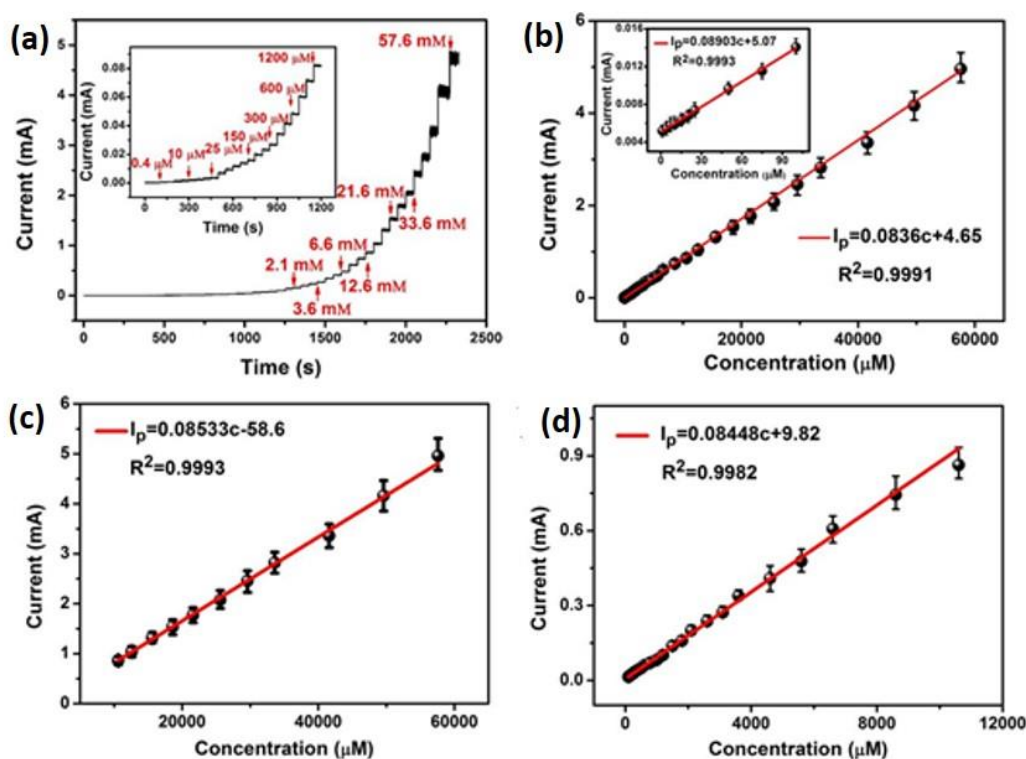


Figure 2.12. (a) Chronoamperometric current response of 2D  $\alpha$ -MoO<sub>3</sub> nanofilms to the changes H<sub>2</sub>O<sub>2</sub> concentration from 0.4  $\mu$ M to 57.6 mM in 0.1 M PBS (pH=7.0); Inset: chronoamperometric current response to lower concentration range from 0.4  $\mu$ M to 1200  $\mu$ M. (b) Corresponding linear plot of the current versus H<sub>2</sub>O<sub>2</sub> concentration; Inset: Corresponding linear plot of the current at H<sub>2</sub>O<sub>2</sub> concentration of 0.4  $\mu$ M to 100  $\mu$ M. Corresponding linear plot of the current at H<sub>2</sub>O<sub>2</sub> concentration of (c) 100  $\mu$ M to 10 mM and (d) 10 mM to 57.6 mM.

composites of specific graphene, due to their larger specific area and the synergy effect between

the composite materials. However, the synthesis of the specific graphene is much more complicated, and the ALD method can deposit large-scale conformal, dense oxide nanofilms with precise thickness, which is the critical parameter for tuning the electrochemical performances. Moreover, the wide linear range of the ALD-developed 2D  $\alpha$ -MoO<sub>3</sub> nanofilms is superior, which makes 2D  $\alpha$ -MoO<sub>3</sub> nanofilms based sensor qualified for the possible H<sub>2</sub>O<sub>2</sub> detection released from the living cells both in the normal physiological condition ( $10^{-8}$ - $10^{-7}$  M) and at the emergency (about  $10^{-4}$  M) [22]. These excellent electrochemical performances have demonstrated that the ALD-fabricated 2D  $\alpha$ -MoO<sub>3</sub> nanofilms in this work are suitable for

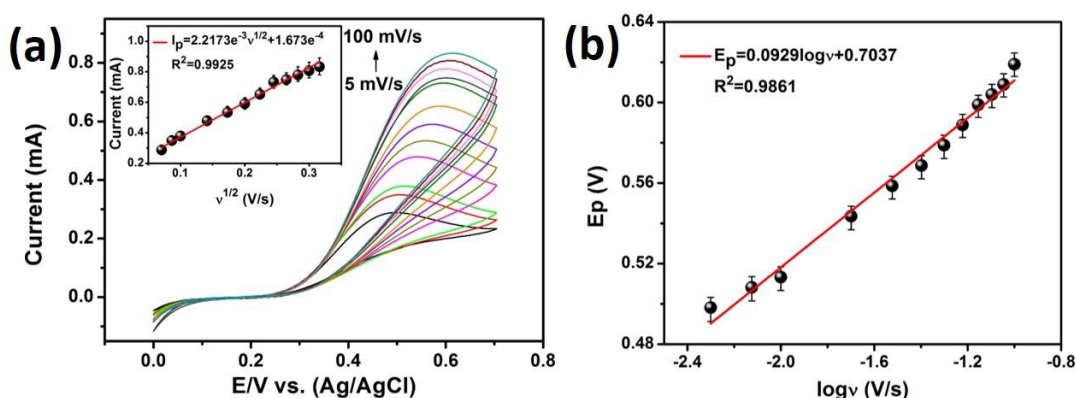


Figure 2.13. (a) CV curves of 2D MoO<sub>3</sub> nanofilms in the presence of 5 mM H<sub>2</sub>O<sub>2</sub> at the different scan rates in 0.1 M PBS (pH=7.0). Inset: plot peak currents versus square root of scan rates. (b) Plot of oxidation peak potentials versus logarithm of scan rates.

sensitive H<sub>2</sub>O<sub>2</sub> detection.

In order to gain further insight into the electrochemical oxidation mechanism of 2D  $\alpha$ -MoO<sub>3</sub> nanofilms on the detection of hydrogen peroxide, CV measurements for 5 mM H<sub>2</sub>O<sub>2</sub> in 0.1M PBS solution were recorded at different scan rates and the summarized results are in Figure 2.13(a). The obtained CV curves obviously confirmed that the oxidation peak currents gradually increase with the rising of the scan rates from 5 to 100 mV/s. Due to the background, current responses at the different scan rates are so much lower than that of the current response to 5 mM H<sub>2</sub>O<sub>2</sub> (Figure 2.14), the effect of current background responses is negligible. Furthermore, a good linear relationship was observed between the peak currents and square root of the scan rates (Inset of Figure 2.13(a)), proving diffusion-controlled rather than surface controlled electron transfer kinetics. The corresponding linear regression equation can be

expressed as  $I_p = 2.21563e^{-3}v^{1/2} + 1.5394e^{-3}$  (where  $I_p$  is in A and  $v$  is in V/s), for which  $R^2 = 0.9925$ . Additionally, the peak potentials shift positively with increasing scanning rates and a plot of peak potential  $E_p$  versus  $\log v$  in Figure 2.13(b) exhibits a linear relationship, which indicated that the hydrogen peroxide oxidation on 2D  $\alpha$ -MoO<sub>3</sub> nanofilms is an irreversible process. The corresponding linear regression equation can be expressed as  $E_p(V) = 0.0929\log v + 0.704$ . For an irreversible diffusion-controlled process,  $E_p$  can be represented by the Tafel equation based on the equation of  $E_p(V) = b/2\log v + \text{constant}$ , and the Tafel slope of  $b$  was found to be 185.8 mV/decade. The value of the Tafel slope indicates a transfer coefficient of  $\alpha = 0.68$  for a one-electron transfer in the rate-determining step.

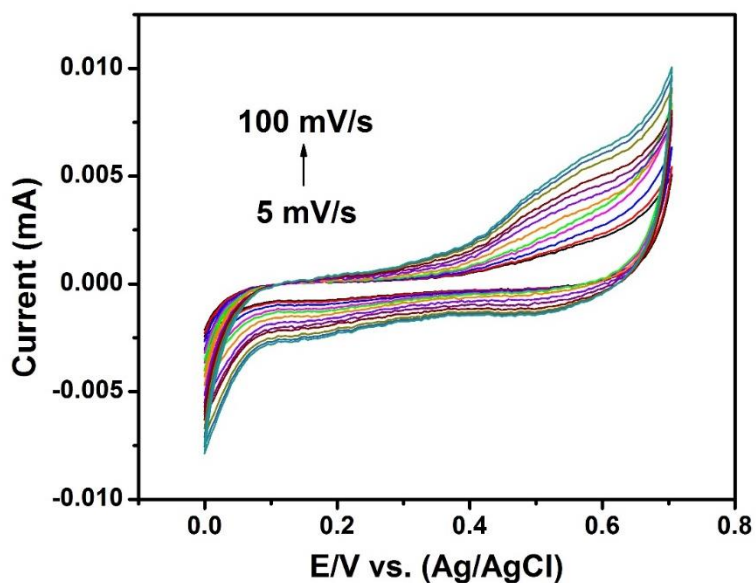


Figure 2.14. CV curves of 2D MoO<sub>3</sub> nanofilms in the absence of 5 mM H<sub>2</sub>O<sub>2</sub> at the different scan rates in 0.1 M PBS (pH=7.0).

The response-recovery characteristic is an important parameter that determines the electrochemical sensing performance of the fabricated materials since it emphasizes the abilities of the reaction to the detection substance and the recovery to the previous state, which is related to the repeatability and reusability of the electrochemical sensors. Figure 2.14(a) depicts the response and recovery time plots of  $\alpha$ -MoO<sub>3</sub> nanofilms with 5 mM hydrogen peroxide at the applied potential of 0.5 V using the chronoamperometric method. As can be seen, the current increased rapidly when the H<sub>2</sub>O<sub>2</sub> was added into the solution, and 90% of the steady-state

current value was achieved within 0.8 seconds. Then after the fast-dilution method was used, the current decreased abruptly, and it only needs 1.65 seconds to reach 10% of the baseline. The measured results illustrated the biosensor of 2D  $\alpha$ -MoO<sub>3</sub> nanofilms has ultra-fast response and recovery time, and the thickness of  $\alpha$ -MoO<sub>3</sub> nanofilms (4.9 nm) enabled such fast response and

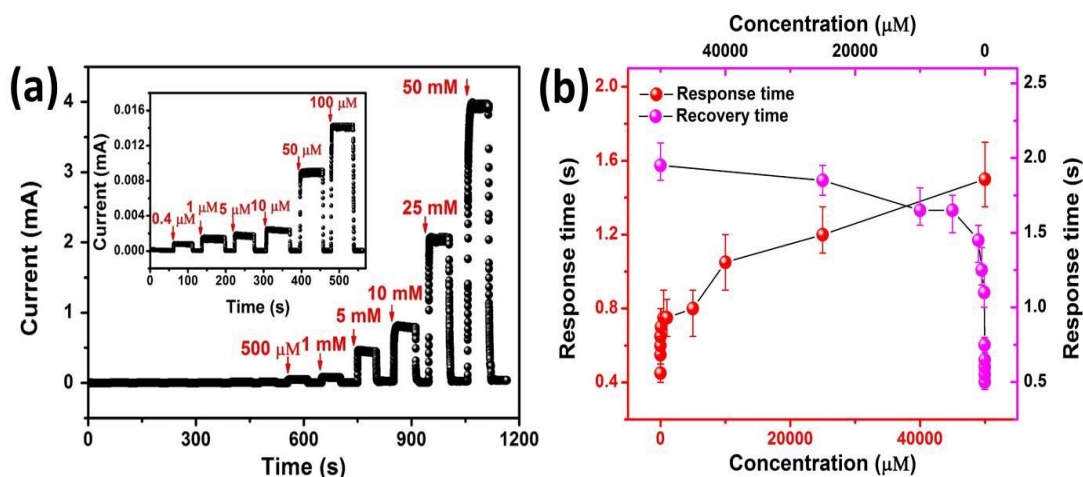


Figure 2.15. (a) The dynamic current response of 2D  $\alpha$ -MoO<sub>3</sub> films to H<sub>2</sub>O<sub>2</sub> under the different concentrations. (b) Current response/recovery time measured at different H<sub>2</sub>O<sub>2</sub> concentrations.

recovery time.

In order to investigate the response/recovery time of 2D  $\alpha$ -MoO<sub>3</sub> nanofilms towards the different H<sub>2</sub>O<sub>2</sub> concentrations in the wide linear range, a similar method to the method mentioned above was employed, and the corresponding curves were presented in Figure 2.15(a). Clearly, the current increases with the increasing of H<sub>2</sub>O<sub>2</sub> concentration, and the current value at every concentration is similar to the results in Figure 2.12(c). Besides, the detailed response/recovery time for ALD-developed 2D  $\alpha$ -MoO<sub>3</sub> nanofilms to the different H<sub>2</sub>O<sub>2</sub> concentrations is presented in Figure 2.15(b). The response/recovery time of 0.45/0.50 s can be seen under the H<sub>2</sub>O<sub>2</sub> concentration of 0.4  $\mu$ M. While increasing the H<sub>2</sub>O<sub>2</sub> concentration, the response/recovery time becomes larger within the range of 0.45/0.50 s - 1.50/1.95 s under the H<sub>2</sub>O<sub>2</sub> concentration range of 0.4  $\mu$ M - 50 mM. Thus, the obtained ultra-fast response/recovery ability towards the different H<sub>2</sub>O<sub>2</sub> concentrations revealed outstanding capabilities of 2D  $\alpha$ -MoO<sub>3</sub> nanofilms.

The influence of temperature on the response/recovery time of 2D  $\alpha$ -MoO<sub>3</sub> nanofilms based sensor was also investigated using 5 mM by chronoamperometric measurements. The results depicted in Figure 2.15(b) showed that  $\alpha$ -MoO<sub>3</sub> nanofilms could work well in the temperature range of 20-50 °C, and the response/recovery time decreased from 0.8/1.65 s to 0.55/1 s as the temperature increasing from 20 to 50 °C. Moreover, the current response also increased with the rising of temperature. Because electrochemical detection towards hydrogen peroxide of 2D  $\alpha$ -MoO<sub>3</sub> nanofilms is a diffusion-controlled process, the higher temperature can facilitate the diffusion process, resulting in the higher current response, and shorter response/recovery time. The results also illustrated 2D  $\alpha$ -MoO<sub>3</sub> nanofilms can be used for hydrogen peroxide detection in a wide range of temperatures.

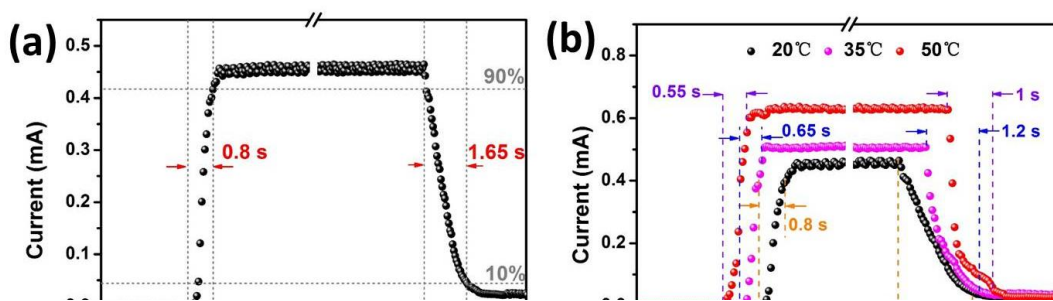


Figure 2.16. (a) Response and recovery time of 2D  $\alpha$ -MoO<sub>3</sub> films to 5 mM H<sub>2</sub>O<sub>2</sub>. (b) Current response/recovery time of the sensor based on 2D  $\alpha$ -MoO<sub>3</sub> films to 5 mM H<sub>2</sub>O<sub>2</sub> at the different temperatures.

The influence of temperature on the response/recovery time of 2D  $\alpha$ -MoO<sub>3</sub> nanofilms based sensor was also investigated using 5 mM by chronoamperometric measurements. The results depicted in Figure 2.16(b) showed that  $\alpha$ -MoO<sub>3</sub> nanofilms could work well in the temperature range of 20-50 °C, and the response/recovery time decreased from 0.8/1.65 s to 0.55/1 s as the temperature increasing from 20 to 50 °C. Moreover, the current response also increased with the rising of temperature. Because electrochemical detection towards hydrogen peroxide of 2D  $\alpha$ -MoO<sub>3</sub> nanofilms is a diffusion-controlled process, the higher temperature can facilitate the diffusion process, resulting in the higher current response, and shorter response/recovery time. The results also illustrated 2D  $\alpha$ -MoO<sub>3</sub> nanofilms can be used for hydrogen peroxide detection in a wide range of temperatures.

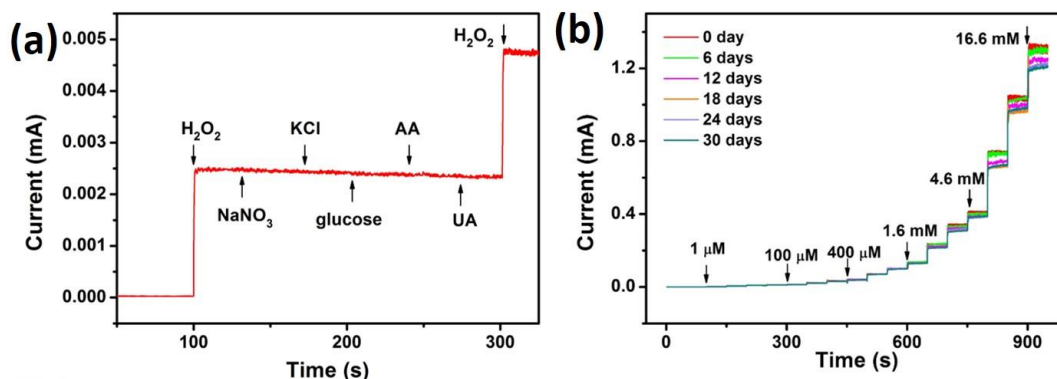


Figure 2.17. (a) Interference study for 2D  $\alpha$ -MoO<sub>3</sub> nano-films in the presence of 10  $\mu$ M  $\text{H}_2\text{O}_2$  and 1 mM interfering chemicals ( $\text{NaNO}_3$ , KCl, glucose, ascorbic acid and uric acid) in 0.1 M PBS (pH = 7.0). (b) The chronoamperometric current of 2D  $\alpha$ -MoO<sub>3</sub> nano-films with different concentration of  $\text{H}_2\text{O}_2$ .

When the fabricated materials were used for the practical measurements, there are a variety of interferences present in the real environment. Therefore, interference experiments were performed to investigate the selectivity of the sensors based on ALD-developed 2D  $\alpha$ -MoO<sub>3</sub> nanofilms towards the  $\text{H}_2\text{O}_2$  detection at the presence of common chemicals such as  $\text{NaNO}_3$ , KCl, glucose, ascorbic acid (AA) and uric acid (UA). Figure 2.17(a) shows the amperometric responses of 2D  $\alpha$ -MoO<sub>3</sub> nanofilms with the successive addition of 10  $\mu$ M  $\text{H}_2\text{O}_2$  and 100-fold higher concentration (1mM) of the different interfering species. Quick and stable response was observed, and there were no apparent subsequent responses due to the successive addition of various interferences. In addition, amperometric  $\text{H}_2\text{O}_2$  detection at various concentrations in the presence of 1 mM interfering substances was also conducted. As shown in Figure 2.18, sensors based on 2D  $\alpha$ -MoO<sub>3</sub> nanofilms showed excellent linearity under the interfering condition and exhibited a sensitivity of  $158.40 \mu\text{A mM}^{-1} \text{cm}^{-2}$ , which is much closer to the sensitivity of  $168.72 \mu\text{A mM}^{-1} \text{cm}^{-2}$  under no interference conditions. These results demonstrate and reaffirm that the sensors based on 2D  $\alpha$ -MoO<sub>3</sub> nanofilms have excellent selectivity towards  $\text{H}_2\text{O}_2$  detection. The selectivity against UA and AA at 0.5 V may be related to the repelling effect occurring on the 2D MoO<sub>3</sub> nanofilms. The isoelectric point of MoO<sub>3</sub> is close to 2 [64], which means that the surface of MoO<sub>3</sub> films would be negatively charged in the PBS (pH=7). The interfering reagents (UA and AA) are also negatively charged at this pH. Consequently, the negatively charged 2D MoO<sub>3</sub> nanofilms surface could strongly repel the negatively-charged molecules, reducing the electrooxidation of interfering reagents on the

surface of MoO<sub>3</sub> nanofilms and resulting in an improved selectivity. Furthermore, the long-time stability is also a crucial practical parameter of any H<sub>2</sub>O<sub>2</sub> sensors. Thus, the H<sub>2</sub>O<sub>2</sub> sensors based on the ALD-developed 2D  $\alpha$ -MoO<sub>3</sub> nanofilms were tested by conducting amperometric experiments every 6 days, and the detailed results are presented in Figure 2.17(b). The relative standard deviation (RSD) of the sensitivity can be calculated from Figure 2.19(a), and the result of 5.9 % can un-doubly prove that the sensors based on ALD-fabricated 2D  $\alpha$ -MoO<sub>3</sub> nanofilms have excellent long-term stability. In addition, the reproducibility was also investigated from six electrodes prepared at the same condition, and the RSD of the amperometric responses calculated from the results of Figure 2.19(b) was found to be 2.1 %. Consequently, considering all the results obtained, the H<sub>2</sub>O<sub>2</sub> electrochemical sensors based on ALD-developed 2D  $\alpha$ -MoO<sub>3</sub> nanofilms have demonstrated excellent repeatability and reproducibility throughout the detection of H<sub>2</sub>O<sub>2</sub>.

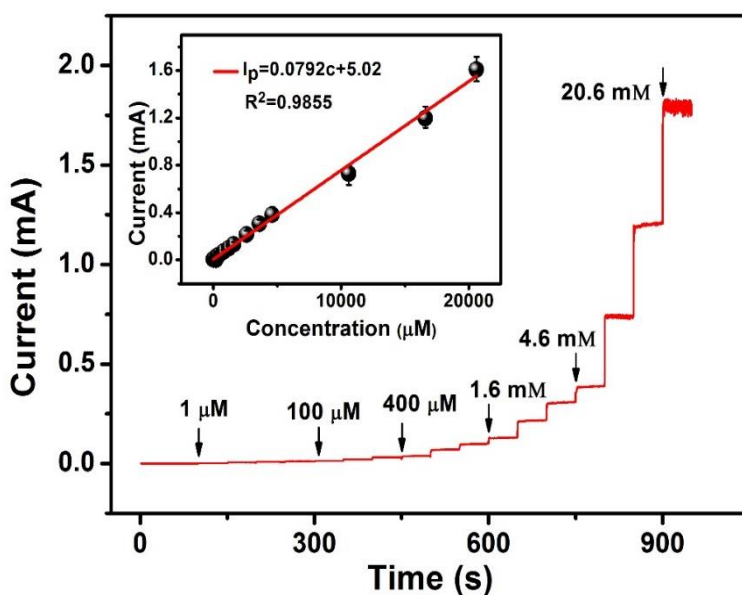


Figure 2.18. Amperometric current response in the presence of 1 mM interfering substances in 0.1 M PBS (pH=7.0); Inset: Corresponding linear plot of current vs. H<sub>2</sub>O<sub>2</sub> concentration.

Table 2.4. Determination of H<sub>2</sub>O<sub>2</sub> concentration in the milk sample (n=3).

Sample	Added ( $\mu$ M)	measured ( $\mu$ M)	Recovery (%)	RSD (% , n=3)
1	25	26.14	104.56	2.6
2	50	48.96	97.92	3.1
3	100	101.35	101.35	3.5

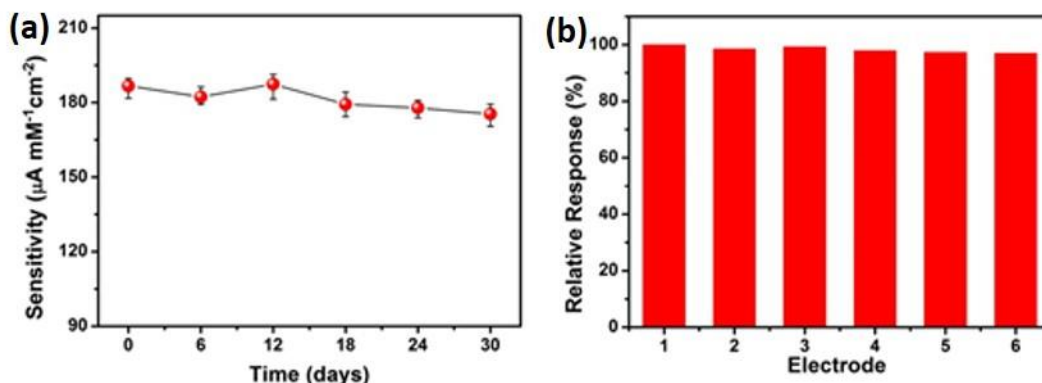


Figure 2.19. (a) The corresponding sensitivity obtained every six days. (b) Reproducibility studies of 2D  $\alpha$ -MoO<sub>3</sub> nano-films towards 5 mM H<sub>2</sub>O<sub>2</sub>.

In order to validate the sensor, the determination of H<sub>2</sub>O<sub>2</sub> in milk was performed. For this purpose, 10  $\mu\text{L}$  of milk was added into 10 mL of 0.1 mol/L PBS (pH 7.0), as H<sub>2</sub>O<sub>2</sub> is widely used as a preservative in milk, due to its potential to inhibit microbial proliferation and milk spoilage [46]. Subsequently, three known concentrations of H<sub>2</sub>O<sub>2</sub> were added, and their chronoamperometric responses of the sensor were recorded at 0.5 V. All of the measurements were performed four times ( $n=3$ ), and the results were summarized in Table 2.4. The RSD and mean recovery values were well acceptable, suggesting that the developed sensor based on 2D  $\alpha$ -MoO<sub>3</sub> nanofilms could be actually applied for the H<sub>2</sub>O<sub>2</sub> detection in the real samples.

## 2.5 Conclusions

In summary, smoothly and uniformly distributed ultra-thin 2D  $\alpha$ -MoO<sub>3</sub> nano-films have developed on the substrate as high-performance electrocatalysts towards hydrogen peroxide at various conditions. 2D  $\alpha$ -MoO<sub>3</sub> nanofilms were successfully fabricated by the ALD technique using (N<sup>t</sup>BuN)<sub>2</sub>(NMe<sub>2</sub>)<sub>2</sub>Mo and oxygen plasma gas as the molybdenum precursor and oxygen precursor, respectively. To the best knowledge of us, it is the first time to report the utilization of 2D  $\alpha$ -MoO<sub>3</sub> nanofilms for the electrochemical detection of hydrogen peroxide. Electrochemical measurements confirmed that 2D  $\alpha$ -MoO<sub>3</sub> nanofilms biosensor possessed a superior capacity towards the detection of hydrogen peroxide with relatively high sensitivity ( $168.72 \mu\text{A mM}^{-1}\text{cm}^{-2}$ ), an extensive linear range (0.4  $\mu\text{M}$  to 57.6 mM) with a low detection limit (0.076  $\mu\text{M}$ ). The response/recovery time at different hydrogen peroxide concentration and the

different working temperature was studied thoroughly, and ultra-fast response/recovery time (within 1.5/2 s) was obtained compared with the previous reports. Furthermore, 2D  $\alpha$ -MoO<sub>3</sub> nanofilms biosensor also exhibited excellent repeatability, reproducibility, anti-interfering ability, and long-time stability (30 days).

## References

1. A. Arash, T. Ahmed, A. G. Rajan, S. Walia, F. Rahman, A. Mazumder, R. Ramanathan, S. Sriram, M. Bhakaran, E. Mayes, Large-area synthesis of 2D MoO<sub>3-x</sub> for enhanced optoelectronic applications, *2D Mater.* 6 (2019) 035031.
2. S. Balendhran, J. Deng, J. Z. Ou, S. Walla, J. Scott, J. Tang, K. L. Wang, M. R. Field, S. Russo, S. Zhuiykov, M. S. Strano, N. Medhekar, S. Sriram, M. Bhaskaran, K. Kalantar-zadeh, Enhanced charge carrier mobility in two-dimensional high dielectric molybdenum oxide, *Adv. Mater.* 25 (2013) 109-114.
3. M. Osada, T. Sasaki, Two-dimensional dielectric nanosheets: novel nanoelectronics from nanocrystal building blocks, *Adv. Mater.* 24 (2012) 210-228.
4. F. Rahman, T. Ahmed, S. Walia, E. Mayes, S. Sriram, M. Bhaskaran, S. Balendhran, Reversible resistive switching behaviour in CVD grown, large area MoO<sub>x</sub>, *Nanoscale* 10 (2018) 19711-19719.
5. S. Balendhran, S. Walia, M. Alsaif, E. P. Nguyen, J. Z. Ou, S. Zhuiykov, S. Sriram, M. Bhaskaran, K. Kalantar-zadeh, Field effect biosensing platform based on 2D  $\alpha$ -MoO<sub>3</sub>, *ACS Nano* 7 (2013) 9753-9760.
6. M. M. Y. Alsaif, A. F. Chrimes, T. Daeneke, S. Balendhran, D. O. Bellisario, Y. Son, M. R. Field, W. Zhang, H. Nili, E. P. Nguyen, K. Latham, J. V. Embden, M. S. Strano, J. Z. Ou, K. Kalantar-zadeh, High-performance field effect transistors using electronic inks of 2D molybdenum oxide nanoflakes, *Adv. Funct. Mater.* 26 (2016) 91-100.
7. C. S. Yang, D. S. Shang, N. Liu, G. Si, X. Shen, R. C. Yu, Y. Q. Li, Y. Sun, A Synaptic Transistor based on Quasi-2D Molybdenum Oxide, *Adv. Mater.* 29 (2017) 1700906.
8. M. Y. A. Alsaif, K. Latham, M. R. Field, D. D. Yao, N. V. Medehkar, G. A. Beane, R. B. Kaner, S. P. Russo, J. Z. Ou, K. Kalantar-zadeh, Tunable plasmon resonances in two-dimensional molybdenum oxide nanoflakes, *Adv. Mater.* 26 (2014) 3931-3937.
9. R. S. Datta, F. Haque, M. Mohiuddin, B. J. Carey, N. Syed, A. Zavabeti, B. Zhang, H. Khan, K. J. Berean, J. Z. Ou, N. Mahmood, T. Daeneke, K. Kalantar-zadeh, Highly active two dimensional  $\alpha$ -

- MoO<sub>3-x</sub> for the electrocatalytic hydrogen evolution reaction, *J. Mater. Chem. A* 5 (2017) 24223-24231.
10. X. K. Hu, Y. T. Qian, Z. T. Song, J. R. Huang, R. Cao, J. Q. Xiao, Comparative study on MoO<sub>3</sub> and H<sub>x</sub>MoO<sub>3</sub> nanobelts: Structure and electric transport, *Chem. Mater.* 20 (2008) 1527-1533.
  11. X. Sha, L. Chen, A. C. Cooper, G. P. Pez, H. Cheng, Hydrogen absorption and diffusion in bulk  $\alpha$ -MoO<sub>3</sub>, *J. Phys. Chem. C* 113 (2009) 11399-11407.
  12. S. Balendhran, S. Walia, H. Nili, J. Z. Ou, S. Zhuiykov, R. B. Kaner, S. Sriram, M. Bhaskaran, K. Kalantar-zadeh, Two-dimensional molybdenum trioxide and dichalcogenides, *Adv. Funct. Mater.* 23 (2013) 3952-3970.
  13. K. A. Gesheva, T. M. Ivanova, G. Bodurov, Transition metal oxide films: Technology and "Smart Windows" electrochromic device performance, *Prog. Org. Coat.* 74 (2012) 635-639.
  14. M. Diskus, O. Nilsen, H. Fjellvåg, Growth of thin films of molybdenum oxide by atomic layer deposition, *J. Mater. Chem.* 21 (2011) 705-710.
  15. A. Guerfi, R. W. Paynter, L. H. Dao, Characterization and stability of electrochromic MoO<sub>3</sub> thin films prepared by electrodeposition, *J. Electrochem. Soc.* 142 (1995) 3457.
  16. Z. Hai, M. K. Akbari, Z. Wei, C. Xue, H. Xu, J. Hu, S. Zhuiykov, Nano-thickness dependence of supercapacitor performance of the ALD-fabricated two-dimensional WO<sub>3</sub>, *Electrochim. Acta* 246 (2017) 625-633.
  17. S. Zhuiykov, L. Hyde, Z. Hai, M. K. Akbari, E. Kats, C. Detavernier, C. Xue, H. Xu, Atomic layer deposition-enabled single layer of tungsten trioxide across a large area, *Appl. Mater. Today* 6 (2017) 44-53.
  18. S. Zhuiykov, M. K. Akbari, Z. Hai, C. Xue, H. Xu, L. Hyde, Wafer-scale fabrication of conformal atomic-layered TiO<sub>2</sub> by atomic layer deposition using tetrakis (dimethylamino) titanium and H<sub>2</sub>O precursors, *Mater. Des.* 120 (2017) 99-108.
  19. Y. Tian, F. Wang, Y. Liu, F. Pang, X. Zhang, Green synthesis of silver nanoparticles on nitrogen-doped graphene for hydrogen peroxide detection, *Electrochim. Acta* 146 (2014) 646-653.
  20. K. Ramachandran, A. Zahoor, T. R. Kumar, K. S. Nahm, A. Balasubramani, G. G. Kumar, MnO<sub>2</sub> nanorods grown NGNF nanocomposites for the application of highly sensitive and selective electrochemical detection of hydrogen peroxide, *J. Ind. Eng. Chem.* 46 (2017) 19-27.
  21. W. Chen, S. Cai, Q. Q. Ren, W. Wen, Y-D. Zhao, Recent advances in electrochemical sensing for hydrogen peroxide: a review, *Analyst* 137 (2012) 49-58.
  22. Y. Liu, X. Liu, Z. Guo, Z. Hu, Z. Xue, X. Lu, Horseradish peroxidase supported on porous graphene as a novel sensing platform for detection of hydrogen peroxide in living cells sensitively, *Biosens. Bioelectron.* 87 (2017) 101-107.

23. S. K. Maji, S. Sreejith, A. K. Mandal, X. Ma, Y. Zhao, Immobilizing gold nanoparticles in mesoporous silica covered reduced graphene oxide: a hybrid material for cancer cell detection through hydrogen peroxide sensing, *ACS Appl. Mater. Interfaces* 6 (2014) 13648-13656.
24. J. Ju, W. Chen, In situ growth of surfactant-free gold nanoparticles on nitrogen-doped graphene quantum dots for electrochemical detection of hydrogen peroxide in biological environments, *Anal. Chem.* 87 (2015) 1903-1910.
25. H. Wang, Y. Bu, W. Dai, K. Li, H. Wang, X. Zuo, Well-dispersed cobalt phthalocyanine nanorods on graphene for the electrochemical detection of hydrogen peroxide and glucose sensing, *Sens. Actuators B Chem.* 216 (2015) 298-306.
26. R. Zhang, W. Chen, Recent advances in graphene-based nanomaterials for fabricating electrochemical hydrogen peroxide sensors, *Biosens. Bioelectron.* 89 (2017) 249-268.
27. D. Lin, Y. Li, P. Zhang, W. Zhang, J. Ding, J. Li, G. Wei, Z. Su, Fast preparation of MoS<sub>2</sub> nanoflowers decorated with platinum nanoparticles for electrochemical detection of hydrogen peroxide, *RSC Adv.* 6 (2016) 52739-52745.
28. Liu M, Liu R, Chen W, Graphene wrapped Cu<sub>2</sub>O nanocubes: non-enzymatic electrochemical sensors for the detection of glucose and hydrogen peroxide with enhanced stability, *Biosens. Bioelectron.* 45 (2013) 206-212.
29. J. Wang, X. Li, S. Zhang, R. Lu, Facile synthesis of ultrasmall monodisperse “raisin-bun”-type MoO<sub>3</sub>/SiO<sub>2</sub> nanocomposites with enhanced catalytic properties, *Nanoscale* 5 (2013) 4823-4828.
30. Y. Mao, W. Li, X. Sun, Y. Ma, J. Xia, Y. Zhao, X. Lu, J. Gan, Z. Liu, J. Chen, P. Liu, Y. Tong, Room-temperature ferromagnetism in hierarchically branched MoO<sub>3</sub> nanostructures, *CrystEngComm* 14 (2012) 1419-1424.
31. T. Wang, J. Li, G. Zhao, Synthesis of MoS<sub>2</sub> and MoO<sub>3</sub> hierarchical nanostructures using a single-source molecular precursor, *Powder Technol.* 253 (2014) 347-351.
32. Z. Hai, M. K. Akbari, C. Xue, H. Xu, L. Hyde, S. Zhuiykov, Wafer-scaled monolayer WO<sub>3</sub> windows ultra-sensitive, extremely-fast and stable UV-A photodetection, *Appl. Surf. Sci.* 405 (2017) 169-177.
33. D. Chen, M. Liu, L. Yin, T. Li, Z. Yang, X. Li, B. Fan, H. Wang, R. Zhang, Z. Li, H. Xu, H. Lu, D. Yang, J. Sun, L. Gao, Single-crystalline MoO<sub>3</sub> nanoplates: topochemical synthesis and enhanced ethanol-sensing performance, *J. Mater. Chem.* 21 (2011) 9332-9342.
34. L. Q. Mai, B. Hu, W. Chen, Y. Y. Qi, C. S. Lao, R. S. Yang, Y. Dai, Z. L. Wang, Lithiated MoO<sub>3</sub> nanobelts with greatly improved performance for lithium batteries, *Adv. Mater.* 19 (2007) 3712-3716.

35. M. Afsharpour, A. Mahjoub and M. M. Amini, Synthesis of molybdenum oxide nanohybrids as efficient catalysts in oxidation of alcohols, *J. Inorg. Organomet. Polym. Mater.* 19 (2009) 298-305.
36. T. H. Chiang, H. C. Yeh. The synthesis of  $\alpha$ -MoO<sub>3</sub> by ethylene glycol, *Mater.* 6 (2013) 4609-4625.
37. C. Y. Xu, P. X. Zhang, L. Yan, Blue shift of Raman peak from coated TiO<sub>2</sub> nanoparticles, *J. Raman Spectrosc.* 32 (2001) 862-865.
38. F. Ji, X. Ren, X. Zheng, Y. Liu, L. Pang, J. Jiang, S. Liu, 2D-MoO<sub>3</sub> nanosheets for superior gas sensors, *Nanoscale* 8 (2016) 8696-8703.
39. J. Chen, M. Wang, X. Liao, Z. Liu, J. Zhang, L. Ding, L. Gao, Y. Li, Large-scale synthesis of single-crystal molybdenum trioxide nanobelts by hot-wire chemical vapour deposition, *J. Alloy. Compd.* 619 (2015) 406-410.
40. C. Julien, A. Khelfa, O. M. Hussain, G. A. Nazri, Synthesis and characterization of flash-evaporated MoO<sub>3</sub> thin films, *J. Cryst. Growth* 156 (1995) 235-244.
41. V. Kumar, A. Sumboja, J. Wang, V. Bhavanasi, V. C. Nguyen, P. S. Lee, Topotactic phase transformation of hexagonal MoO<sub>3</sub> to layered MoO<sub>3</sub>-II and its two-dimensional (2D) nanosheets, *Chem. Mater.* 26 (2014) 5533-5539.
42. J. Dagar, P. Tyagi, R. Ahmad, O. P. Sinha, C. K. Suman, R. Srivastava, Application of 2D-MoO<sub>3</sub> nano-flakes in organic light emitting diodes: effect of semiconductor to metal transition with irradiation, *RSC Adv.* 5 (2015) 8397-8403.
43. F. Xie, X. Cao, F. Qu, A. M. Asiri, X. Sun, Cobalt nitride nanowire array as an efficient electrochemical sensor for glucose and H<sub>2</sub>O<sub>2</sub> detection, *Sens. Actuators B Chem.* 255 (2018) 1254-1261.
44. Y. Zhang, X. Bai, X. Wang, K. K. Shiu, Y. Zhu, H. Jiang, Highly sensitive graphene-Pt nanocomposites amperometric biosensor and its application in living cell H<sub>2</sub>O<sub>2</sub> detection, *Anal. Chem.* 86 (2014) 9459-9465.
45. S. J. Li, Y. Xing, H. Y. Yang, J. Y. Huang, W. T. Wang, R. T. Liu, Electrochemical synthesis of a binary Mn-Co oxides decorated graphene nanocomposites for application in nonenzymatic H<sub>2</sub>O<sub>2</sub> sensing, *Int. J. Electrochem. Sci.* 12 (2017) 6566-6576.
46. M. V. Bracamonte, M. Melchionna, A. Giuliani, L. Nasi, C. Tavagnacco, M. Prato, P. Fornasiero, H<sub>2</sub>O<sub>2</sub> sensing enhancement by mutual integration of single walled carbon nanohorns with metal oxide catalysts: The CeO<sub>2</sub> case, *Sens. Actuators B Chem.* 239 (2017) 923-932.
47. A. A. M. Abdurhman, Y. Zhang, G. Zhang, S. Wang, Hierarchical nanostructured noble metal/metal oxide/graphene-coated carbon fiber: in situ electrochemical synthesis and use as microelectrode for real-time molecular detection of cancer cells, *Anal. Bioanal. Chem.* 407 (2015) 8129-8136.

48. L. Wang, M. Deng, G. Ding, S. Chen, F. Xu, Manganese dioxide based ternary nanocomposite for catalytic reduction and nonenzymatic sensing of hydrogen peroxide, *Electrochim. Acta*, 114 (2013) 416-423.
49. S. J. Li, J. C. Zhang, J. Li, W. T. Wang, R. T. Liu, One-step electrochemically modulated synthesis of reduced graphene oxide-silver nanocomposites as efficient nonenzymatic H<sub>2</sub>O<sub>2</sub> sensor, *Int. J. Electrochem. Sci*, 12 (2017) 5692-5703.
50. M. Sivakumar, M. Sakthivel, S. M. Chen, V. Veeramani, W. L. Chen, G. Bharath, R. Madhu, N. Miyamoto, A facile low-temperature synthesis of V<sub>2</sub>O<sub>5</sub> flakes for electrochemical detection of hydrogen peroxide sensor, *Ionics* 23 (2017) 2193-2200.
51. D. Li, L. Meng, S. Dang, D. Jiang, W. Shi, Hydrogen peroxide sensing using Cu<sub>2</sub>O nanocubes decorated by Ag-Au alloy nanoparticles, *J. Alloy. Compd.* 690 (2017) 1-7.
52. C. Zhang, H. Jiang, R. Ma, Y. Zhang, Q. Chen, Simple non-enzymatic electrochemical sensor for hydrogen peroxide based on nafion/platinum nanoparticles/reduced graphene oxide nanocomposite modified glassy carbon electrode, *Ionics* 23 (2017) 1309-1317.
53. Y. Li, Y. Zhong, Y. Zhang, W. Weng, S. Li, Carbon quantum dots/octahedral Cu<sub>2</sub>O nanocomposites for non-enzymatic glucose and hydrogen peroxide amperometric sensor, *Sens. Actuators B Chem.* 206 (2015) 735-743.
54. Q. Xi, X. Chen, D. G. Evans, W. Yang, Gold nanoparticle-embedded porous graphene thin films fabricated via layer-by-layer self-assembly and subsequent thermal annealing for electrochemical sensing, *Langmuir* 28 (2012) 9885-9892.
55. J. Zhang, J. Zheng, An enzyme-free hydrogen peroxide sensor based on Ag/FeOOH nanocomposites, *Anal. Methods* 7 (2015) 1788-1793.
56. B. Šljukić, C. E. Banks, A. Crossley, R. G. Compton, Iron (III) oxide graphite composite electrodes: application to the electroanalytical detection of hydrazine and hydrogen peroxide, *Electroanal.* 18 (2006) 1757-1762.
57. N. Zhang, J. Zheng, Synthesis of Ag-Fe<sub>2</sub>O<sub>3</sub>-RGO nanocomposites for the electrocatalytic reduction of H<sub>2</sub>O<sub>2</sub>, *J. Mater. Sci. –Mater. Electron.* 28 (2017) 11209-11216.
58. K. K. Rani, R. Devasenathipathy, S. F. Wang, C. Yang, Simple preparation of birnessite-type MnO<sub>2</sub> nanoflakes with multi-walled carbon nanotubes for the sensitive detection of hydrogen peroxide, *Ionics* 23 (2017) 219-3226.
59. D. Chirizzi, M. R. Guascito, E. Filippo, C. Malitesta, A. Tepore, A novel nonenzymatic amperometric hydrogen peroxide sensor based on CuO@Cu<sub>2</sub>O nanowires embedded into poly (vinyl alcohol), *Talanta* 147 (2016) 124-131.

60. S. Dong, J. Xi, Y. Wu, H. Liu, C. Fu, H. Liu, F. Xiao, High loading MnO<sub>2</sub> nanowires on graphene paper: facile electrochemical synthesis and use as flexible electrode for tracking hydrogen peroxide secretion in live cells, *Anal. Chim. Acta* 853 (2015) 200-206.
61. C. Zhao, X. Wu, P. Li, C. Zhao, X. Qian, Hydrothermal deposition of CuO/rGO/Cu<sub>2</sub>O nanocomposite on copper foil for sensitive nonenzymatic voltammetric determination of glucose and hydrogen peroxide, *Microchim. Acta* 184 (2017) 2341-2348.
62. J. R. Regalbuto, J. W. Ha, A corrected procedure and consistent interpretation for temperature programmed reduction of supported MoO<sub>3</sub>, *Catal. Lett.* 29 (1994) 189-207.

# Chapter 3

## ALD DEVELOPED 2D WO<sub>3</sub> NANOFILMS WITH DIFFERENT THICKNESS AND THEIR ELECTROCHEMICAL HYDRAZINE DETECTION

---

### 3.1 Abstract

Wafer-scale two-dimensional (2D) WO<sub>3</sub> films with different thickness of 0.78, 1.4, 3.6, and 6.5 nm were fabricated on Au-SiO<sub>2</sub>/Si substrates using an atomic layer deposition technique. Their surface morphologies and chemical components were examined by field-emission scanning electron microscopy, atomic force microscopy, and X-ray photoelectron spectroscopy. Cyclic voltammetry, chronoamperometry, and electrochemical impedance spectroscopy were utilized for the analysis of the electrochemical behavior of 2D WO<sub>3</sub> films towards hydrazine detection under various conditions. The effect of the thickness of 2D WO<sub>3</sub> on the electrochemical performance was also analyzed. Significant improvement in hydrazine sensing capabilities was obtained for monolayer 2D WO<sub>3</sub> (0.78 nm), demonstrating a high sensitivity of 1.24  $\mu\text{A } \mu\text{M}^{-1} \text{cm}^{-2}$ , a linear hydrazine concentration detection ranging from 0.2 to 2100  $\mu\text{M}$ , high long-term stability, excellent selectivity and the lowest limit of detection of 0.015  $\mu\text{M}$  reported to date, which provides a great potential method for materials fabrication in the development of high-performance hydrazine detection.

### 3.2 Introduction

WO<sub>3</sub> possesses a widely tunable optical bandgap of ca. 2.5–3.7 eV and is also generally constructed by corner and edge-sharing WO<sub>6</sub> octahedra with many transformable phases such as monoclinic, triclinic, orthorhombic, and tetragonal phases, which have led to the intensive investigation of WO<sub>3</sub> for the various applications [1-6]. Like other transition metal oxides, tungsten oxide can be synthesized into many different morphologies. Among these morphologies, 2D WO<sub>3</sub> has a high specific surface area and great potential for tuning electronic structures [7, 8]. As an example, it was reported that the specific surface area of 2D nanosheets could be 157  $\text{m}^2 \cdot \text{g}^{-1}$  [9]. In addition, the

ultraviolet-visible (UV-vis) absorption spectra of 2D WO<sub>3</sub> showed an apparent blue shift, which results from a larger bandgap and more positive conduction and valence band edges of 2D WO<sub>3</sub> due to the significant quantum confinement effect in the thinnest dimension [9, 10]. Owing to high surface area and tunable electronic properties, 2D WO<sub>3</sub> has shown more attractive in the application of electrochromic devices, gas sensors, lithium-ion batteries, photovoltaics, and catalysts [11-15]. Even though 2D WO<sub>3</sub> possesses various interesting properties and is widely used in many aspects, to the best of our knowledge, the utilization of 2D WO<sub>3</sub> for the fabrication of electrochemical sensor has not yet been reported.

For the electrochemical sensor based on 2D WO<sub>3</sub>, the thickness should be an essential parameter to be considered for the design of applicable devices, since depending on the different thickness, 2D nanomaterials exhibit different properties [15-19]. For example, semiconductor → half-metal → metal transition with nonmagnetic → magnetic transfer can be achieved for AlN nanosheets by surface hydrogenation and increasing nanosheet thickness [19]. As the other example, graphene films with a higher content of multilayer graphene flakes are more conductive, and their resistance is more easily reduced by thermal annealing, making them suitable as transparent conducting films. Graphene films with a higher content of bilayer graphene flakes show instead higher capacitance when used as an electrode in a supercapacitor [16]. It was also reported that the thickness of 2D materials influences the charge transfer and transport versus charge trapping and recombination, thus affecting the electrochemical performances [18]. Besides, it is well known that the electro-catalytic activity of nanostructured materials is significantly dependent on their distribution on the substrate. However, the methods of top-down strategies and hydrothermal synthesis have no reasonable control over the distribution of the material on the electrodes. They have difficulty in maintaining the long-term stability because of the gradual detachment and dissolution of the catalyst from the substrate [20].

In order to solve the problem mentioned above and investigate the effect of thickness on the electrochemical performance, the atomic layer deposition technique was utilized as a valuable alternative to other technologies in the development of

different thicknesses of 2D WO<sub>3</sub>. Compared to other thin film deposition methods, such as CVD and PVD, ALD can make uniform distribution of atomically thin nanofilms on the substrate because of the milder process conditions, which is necessary for the development of electrochemical sensors with the excellent performance [21]. In addition, due to the self-limiting character of the ALD reactions and its slow growth rate, the thickness of the as-deposited WO<sub>3</sub> nanofilms with high-quality atomically thin level is simply controlled by the number of cycles with precision at the angstrom level under the set deposition temperature[22].

Hydrazine, as a colorless flammable liquid with an ammonia-like odor, has been widely used in many fields, such as fuel cells, rocket fuels, polymerization catalysts, corrosion inhibitors, and antioxidants, emulsifiers, pesticides, plant-growth regulators, dyes stuff and explosives [23-25]. As of 2000, approximately 120,000 tons of hydrazine hydrate (corresponding to a 64% solution of hydrazine in water by weight) was manufactured worldwide per year [26]. However, hydrazine has also been recognized as a carcinogenic, hepatotoxic substance, which has adverse effects on the liver and brain and can cause DNA damage, blood abnormalities, and irreversible deterioration of the nervous system [27-29]. According to the World Health Organization and Environmental Protection Agency (EPA), hydrazine has been classified as a B2 group human carcinogenic agent [30]. The permissible exposure limit (PEL) for N<sub>2</sub>H<sub>4</sub> in the air is 1.0 ppm, and its concentration in the workplace should be below 0.03 mg/mL for a 2 h period [31, 32]. Notably, the US Environmental Protection Agency defined HZ as one of the potent carcinogens, which would limit the threshold in the drinking water to below 10 ppb (0.3  $\mu\text{mol L}^{-1}$ ). Therefore, fast and accurate hydrazine detection at low concentrations is especially vital for the aqueous environment. The commercial hydrazine detection method needs complicated equipment and instrumentation, and are expensive, so electrochemical sensors provide a convenient and cheap way.

In this part, WO<sub>3</sub> nanostructures, prepared by the ALD technique with different thickness, were utilized for the first time for accurate, sustainable, sensitive, selective, and fast hydrazine detection. The thickness of 2D WO<sub>3</sub> varied from ~0.78 nm (monolayer) up to ~6.5 nm (a few layers of WO<sub>3</sub>). The effect of thickness of 2D WO<sub>3</sub> on the hydrazine

detection was comprehensively studied using the cyclic voltammetry (CV), electrochemical impedance spectroscopy (EIS), and chronoamperometry methods, which confirmed the impact of changes in nano-thickness of WO<sub>3</sub> on their sensing performance. The results obtained unambiguously showed that the monolayer WO<sub>3</sub> exhibited the highest sensitivity and excellent selectivity to hydrazine in a wide concentration range (0.2–2100 µM) with a fast response time (less than 2 s) and the lowest limit of detection (LOD) of 0.015 µM reported to date.

### 3.3 Experimental section

#### 3.3.1 Materials

Bis(tertbutylimino)bis(dimethylamino)tungsten(VI) precursor, also known as (tBuN)<sub>2</sub>(Me<sub>2</sub>N)<sub>2</sub>W, was purchased from the Strem Chemicals Inc. USA and was used for the ALD development of 2D WO<sub>3</sub> with the different thickness on the wafer scale. Hydrazine hydrate (N<sub>2</sub>H<sub>4</sub>·H<sub>2</sub>O, 80%), sodium dihydrogen phosphate (NaH<sub>2</sub>PO<sub>4</sub>), disodium hydrogen phosphate (Na<sub>2</sub>HPO<sub>4</sub>), hydrogen peroxide (H<sub>2</sub>O<sub>2</sub>) and glucose were obtained from the Sigma-Aldrich, USA. All these reagents and chemicals were used without further purification. Deionized water (> 18 MW) was from a Milli-Q water purification system (Millipore, France). Phosphate buffers solution (PBS) used as the supporting electrolyte was prepared with 0.1 M NaH<sub>2</sub>PO<sub>4</sub>/Na<sub>2</sub>HPO<sub>4</sub>. High resistivity (1 KW cm) 4'' SiO<sub>2</sub>/Si wafers were utilized for the fabrication of ALD-deposited 2D WO<sub>3</sub> films using (tBuN)<sub>2</sub>(Me<sub>2</sub>N)<sub>2</sub> W and H<sub>2</sub>O precursors.

#### 3.3.2 Sample Preparation

All 2D WO<sub>3</sub> films were synthesized on SiO<sub>2</sub>/Si wafers by the ALD technique using the cross-flow reactor of Savannah S100 (Ultratech/Cambridge Nanotech) and specifically developed the recipe for this precursor. In this deposition process, (tBuN)<sub>2</sub>(Me<sub>2</sub>N)<sub>2</sub>W was employed as the metal ALD precursor along with H<sub>2</sub>O vapor as a source of oxygen. Prior the deposition, in order to make the SiO<sub>2</sub>/Si wafers electrically conductive to facilitate the subsequent investigation of 2D -WO<sub>3</sub> films properties, Au/Cr films were deposited on the SiO<sub>2</sub>/Si wafers using an Electron Beam Evaporator method [Nanochrome II (Intivac, USA)] with the thickness of ~150 nm. A 200 µm-wide gap at the center of the

wafer was intentionally left at the same time for the characterization of the developed nanofilms, due to the roughness of Au/Cr films. Then the wafer-scale ALD deposition of WO<sub>3</sub> ultra-thin films with the target thickness of ~0.78 nm, ~1.4 nm, ~3.6 nm, and ~6.5 nm was performed. The recently developed recipe provided the following ALD growth conditions at a deposition temperature of 350°C: (tBuN)<sub>2</sub>(Me<sub>2</sub>N)<sub>2</sub>W pulse 2 s, N<sub>2</sub> purge 10 s, H<sub>2</sub>O pulse 50 ms, N<sub>2</sub> flow 5 s without pumping (exposure mode) and then 10 s with pumping as the purge/evacuation step. After deposition, all wafers were subsequently diced into 1.0×1.0 cm pieces for further annealing and characterization. 2D WO<sub>3</sub> samples were annealed in air at 200°C for 1 h with the heating rate of 0.58°C/min. The fabrication process, together with N<sub>2</sub>H<sub>4</sub> measurements, was schematically presented in Figure 3.1.

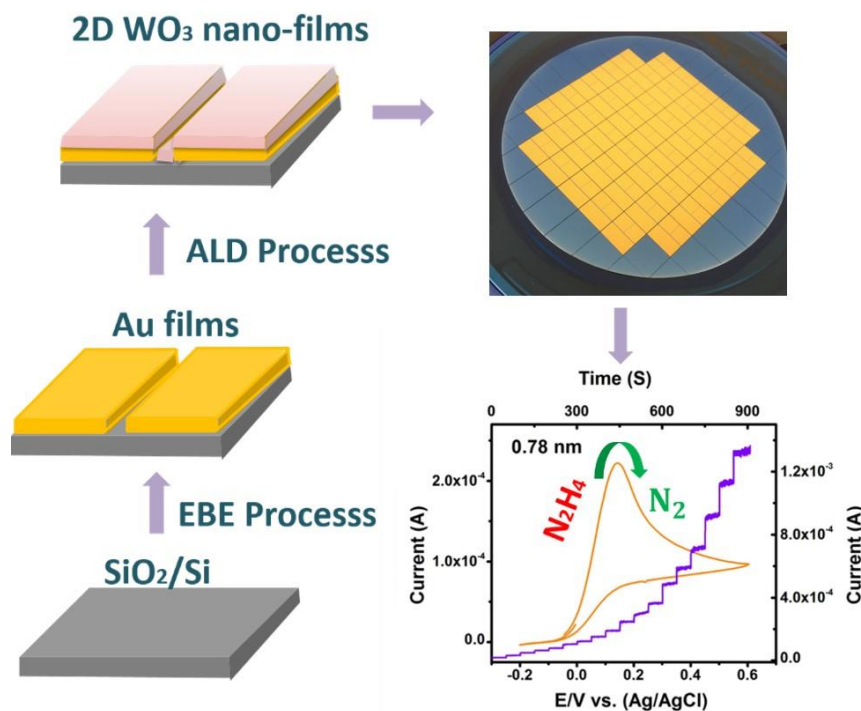


Figure 3.1. Graphical scheme of the development of 2D WO<sub>3</sub> nanofilms for electrochemical N<sub>2</sub>H<sub>4</sub> detection.

### 3.3.3 Characterization

Variable Angle Spectroscopic Ellipsometry (M2000-DI model, JA Woollam) was used for the thickness measurement of the ALD developed 2D WO<sub>3</sub> films. The reproducibility of

all deposited 2D WO<sub>3</sub> samples was high. The surface morphology of all samples was characterized by FE-SEM (JEOL 7800F) and AFM (JPK System, Nano Wizard). The surface composition and the chemical state of 2D WO<sub>3</sub> films were characterized using XPS. A Rigakudenki model XPS-7000 X-ray photoelectron spectrometer with monochromatic Mg-K $\alpha$  radiation at 300 W is used for the XPS analysis, and the takeoff angle of the instrument was 90°.

### 3.3.4 Electrochemical Testing

The electrochemical performance of the developed 2D WO<sub>3</sub> films with different thicknesses was evaluated on Autolab PGSTAT204 (Metrohm Autolab. B.V., Netherlands) at the room temperature. A conventional three-electrode system consists of fabricated 2D WO<sub>3</sub> samples with an area of 1×0.5 cm as working electrodes, Pt wire as the counter electrode, and Ag/AgCl (3.0 M KCl) as the reference electrode was employed to carry out the electrochemical measurements. For the experiments on oxidation of hydrazine, all of the tests were performed in 0.1 M PBS, which can change the value of pH by varying the ratio of NaH<sub>2</sub>PO<sub>4</sub> and Na<sub>2</sub>HPO<sub>4</sub>. The CVs of all samples were measured in the potential range from 0.2 to 0.6 V. Chronoamperometry was performed at an applied potential of 0.14 V under 330 rpm magnetic stirring with hydrazine added stepwise. In addition, EIS measurements were conducted in 1 mM K<sub>4</sub>Fe(CN)<sub>6</sub> solution containing 0.1 M KCl within the frequency ranging from 10<sup>5</sup> to 0.1 Hz at an AC amplitude of 5 mV under the open-circuit potential conditions.

## 3.4 Results and Discussion

The surface morphologies of ALD-developed 2D WO<sub>3</sub> with different thicknesses on the top of the Au electrodes were characterized by field-emission scanning electron microscopy (FE-SEM) and atomic force microscopy (AFM). Figure 3.2(a) shows the SEM image of nanostructured Au films deposited on the SiO<sub>2</sub>/Si wafers. It exhibits a relatively rough surface of the Au grains with the average size ranged from 70 to 100 nm. No open porosity was observed. The surface morphology of ALD developed monolayer WO<sub>3</sub> on the Au films deposited SiO<sub>2</sub>/Si wafers was depicted in Figure 3.2(b). WO<sub>3</sub> films were aggregated with nanoparticles, and the nanoparticles with the average

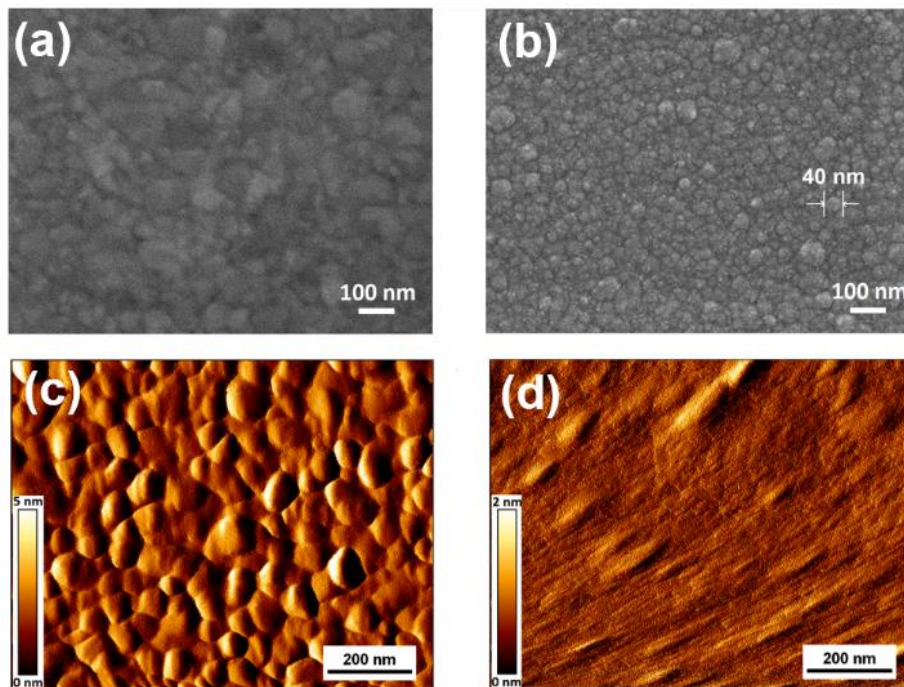


Figure 3.2. SEM images of (a) nanostructured Au films and (b) monolayer WO<sub>3</sub> deposited on the top of Au films. AFM images of (c) the surface of Au films and (d) the surface morphology of monolayer WO<sub>3</sub>

measured particle diameter of  $\sim 40$  nm were dense and uniformly distributed on the top of Au electrodes. In addition, it was clearly observed that with increasing the thickness of WO<sub>3</sub> films, there was no noticeable change in their morphologies. The surface

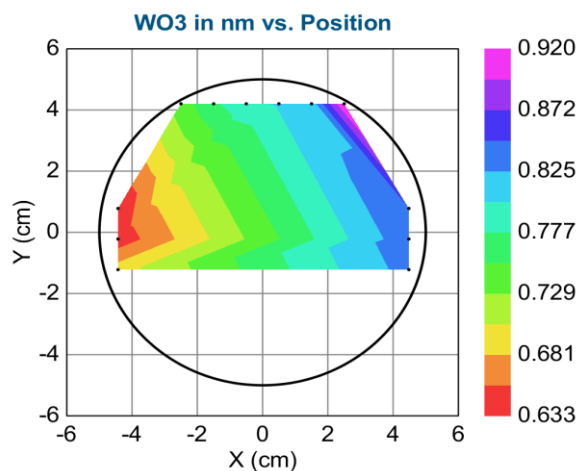


Figure 3.3. Ellipsometry measurement data for the monolayer WO<sub>3</sub> films.

morphology of Au films was also characterized by AFM, as displayed in Figure 3.2(c).

The surface of Au films was observed to be relatively rough, which is in accordance with the SEM results. Due to rough surface of Au films, the thickness measurement of monolayer WO<sub>3</sub> films was conducted on the 200 mm-wide surface space of SiO<sub>2</sub>/Si substrate using spectroscopic ellipsometry, and the surface morphology of monolayer WO<sub>3</sub> films can be seen from Figure 3.2(d) that the films were very smooth and uniform. The ellipsometry analysis results showed that the average 0.78 nm of monolayer WO<sub>3</sub> films were obtained (Figure 3.3).

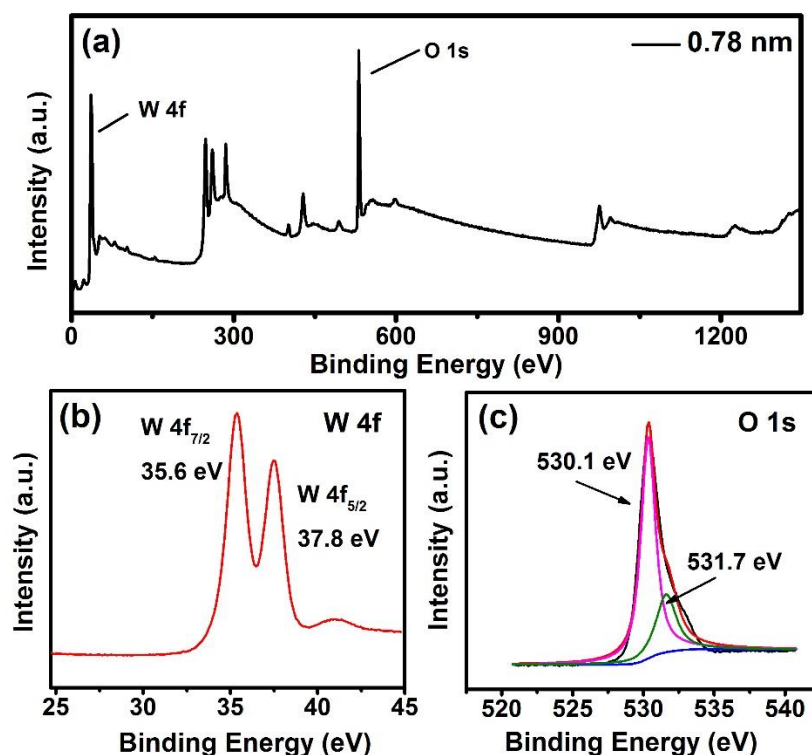


Figure 3.4. (a) XPS spectrum of the monolayer 2D WO<sub>3</sub> films and high-resolution XPS scan of (b) W 4f region and (c) O 1s region.

The successful development of monolayer WO<sub>3</sub> on the top of Au electrodes was also confirmed by X-ray photoelectron spectroscopy (XPS) in Figure 3.4. The survey of those spectra identified W4f as the major constituent of the WO<sub>3</sub> monolayer. In the high-resolution XPS spectra, two strong doublets were present at 35.6 and 37.8 eV in the W4f region, corresponding to W 4f<sub>7/2</sub> and W 4f<sub>5/2</sub>, respectively. The binding energies were

consistent with those for tungsten (VI) in the surface-bound species (Figure 3.4(b)) and confirmed the existence of the W-O bond, which was reported in the previous works [33]. According to the XPS results, the peaks for O 1s could be deconvoluted in two peaks centered at 530.1 and 531.7 eV. The main binding energy component located at 530.1 eV can be the characteristic of the lattice oxygen of WO<sub>3</sub>, and the minor binding energy at 531.7 eV is assigned to oxygen-deficient sub-oxides [34,35].

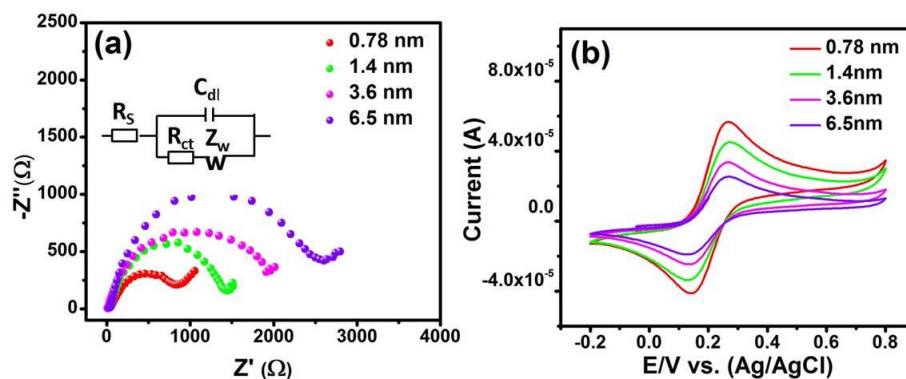


Figure 3.5. (a) Nyquist plots of different thickness 2D WO<sub>3</sub> films with 1mM [Fe(CN)<sub>6</sub>]<sup>3-/4-</sup> in 0.1M KCl from 100kHz to 0.1Hz at an AC amplitude of 5mV under open-circuit potential condition. (b) CVs of different thickness 2D WO<sub>3</sub> films with 1mM [Fe(CN)<sub>6</sub>]<sup>3-/4-</sup> in 0.1M KCl at the scanning rate of 10mV/s.

EIS and CV were used for investigation of electron transfer kinetics and effective surface area of each ALD-developed 2D WO<sub>3</sub>. It was clear from the results obtained in Figure 3.5(a) that monolayer WO<sub>3</sub> films have the smallest semicircle. As the thickness of WO<sub>3</sub> films increase, the semicircle also increases, which illustrated that monolayer WO<sub>3</sub> films have the lowest electron transfer resistance (about 800  $\Omega$ ) and suggested the best conductivity of monolayer WO<sub>3</sub> films among all fabricated 2D WO<sub>3</sub> films. Moreover, results of CV measurements in Figure 3.5(b) showed that the redox peak currents of monolayer WO<sub>3</sub> films are higher than those of 1.4, 3.6 and 6.5 nm WO<sub>3</sub> films, owing to the largest active surface area of monolayer WO<sub>3</sub>, which resulted in an increase in current density and surface charge. The effective surface area of different thicknesses of 2D WO<sub>3</sub> films was calculated to form CVs in Figure 3.6 at the different scanning rates. The effective surface area of different thickness WO<sub>3</sub> films can be calculated using a

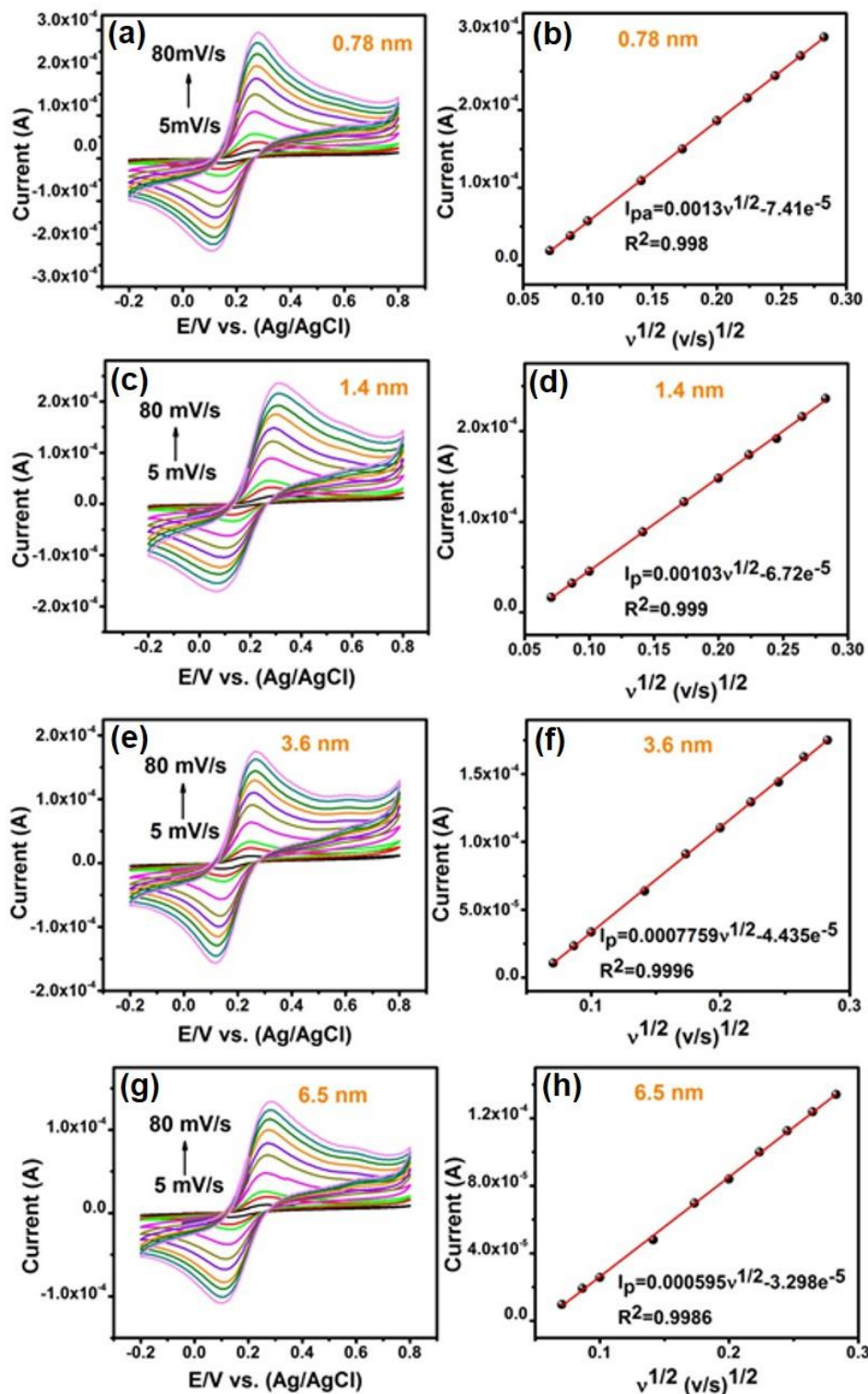


Figure 3.6. (a, c, e, g) CVs of different thickness of WO<sub>3</sub> films with 1mM [Fe(CN)<sub>6</sub>]<sup>3-/4-</sup> in 0.1M KCl at the different scanning rates. (b, d, f, h) The corresponding linear plot of currents versus scanning rates.

known concentration of K<sub>4</sub>Fe(CN)<sub>6</sub> as the electrolyte based on the Randles-Sevcik

equation [36]:

$$I_p = 2.69 \times 10^5 AD^{1/2} n^{3/2} \nu^{1/2} C, \quad (3.1)$$

where  $I_p$  refers to the anodic peak current (A),  $\nu$  is the scanning rate (V/s),  $n$  is the electron transfer number ( $n = 1$ ),  $A$  is the surface area of the electrode (cm<sup>2</sup>),  $C$  is the concentration (mol/cm<sup>3</sup>), and  $D$  is the diffusion coefficient of K<sub>4</sub>Fe(CN)<sub>6</sub> which is  $7.6 \times 10^{-6} \text{ cm}^2 \text{ s}^{-1}$  [37]. The slope of the  $I_p$  and  $\nu^{1/2}$  relations of different thickness 2D WO<sub>3</sub> films were shown in Figure 3.6. The effective surface area of 0.78 nm WO<sub>3</sub> films was calculated to 1.77 cm<sup>2</sup> and the values of other thicknesses were 1.45, 1.04, and 0.8 cm<sup>2</sup> for 1.4, 3.6, and 6.5 nm WO<sub>3</sub> films, respectively. Results demonstrated that monolayer WO<sub>3</sub> films have the maximum effective surface area.

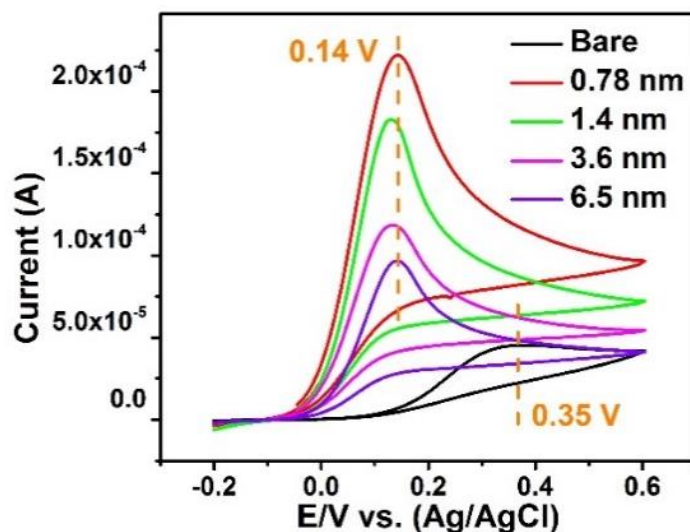


Figure 3.7. CVs of Au electrodes and 2D WO<sub>3</sub> with different thicknesses in 0.1 M PBS at a scanning rate of 10 mV/s.

The electrochemical performance towards hydrazine was carried out in a three-electrode system, as described in the experimental section. In order to investigate the electrocatalytic activity of the ALD-fabricated 2D WO<sub>3</sub> films with different thicknesses, their electrochemical characteristics were studied in 0.1 M PBS. It is well known that the pH value of the solution is critical to the electro-catalytic oxidation reactions of hydrazine. The results illustrated that the oxidation peak potential in CV curves for all 2D WO<sub>3</sub> films shifted toward the negative direction when the pH of PBS increased from

5.8 to 7.8, consistent with the previous report [36,38]. In addition, the peak current is also influenced by the value of pH, and the highest current response is exhibited in 7.4. Therefore, unless it stated otherwise, all following tests were conducted in PBS with a pH value of 7.4.

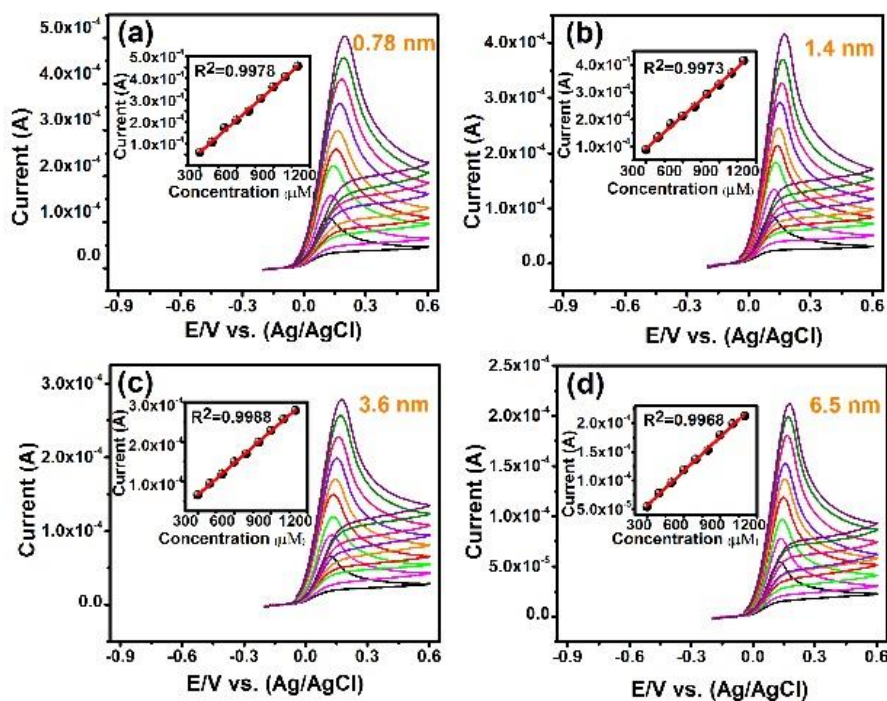


Figure 3.8. CVs of 2D WO<sub>3</sub> with different thickness in the presence of different hydrazine concentrations at a scan rate of 10 mV/s: (a) 0.78 nm, (b) 1.4 nm, (c) 3.6 nm, (d) 6.5 nm. Inset: corresponding linear plot of current versus hydrazine concentration.

Figure 3.7 depicts the CVs of ALD-fabricated 2D WO<sub>3</sub> films with different thicknesses and bare Au electrodes in 0.1 M PBS overpotential of 0.35 V, due to its sluggish electrocatalytic behavior towards electro-oxidation hydrazine. The measured results indicated that compared with bare Au electrodes, 2D WO<sub>3</sub> films possessed lower oxidation potential and higher oxidation peak current for hydrazine electro-oxidation, and the oxidation current values increased with the decreasing of WO<sub>3</sub> films thickness. These results were due to the increased effective surface area. They decreased charge transfer resistance with the decreasing of WO<sub>3</sub> film thickness, which suggested that the thinner WO<sub>3</sub> films provide lower interfacial resistance in the path of charge transport and make the charge transfer between hydrazine and working electrode much faster.

Consequently, the thinner WO<sub>3</sub> films showed better electrocatalytic capability. Moreover, all 2D WO<sub>3</sub> films do not display any characteristic response in the absence of hydrazine as well as bare Au electrodes.

As improvement in the electro-catalytic property towards hydrazine for the ALD-developed 2D WO<sub>3</sub> was evident, in order to understand it further, current responses to the different hydrazine concentrations were investigated for the 2D WO<sub>3</sub> films with the different thickness, as shown in Figure 3.8(a-d). It was observed that with the increase of the hydrazine concentration, all ALD-fabricated 2D WO<sub>3</sub> films exhibited higher oxidation currents. The oxidation peak currents were found to be linearly proportional to the rise of hydrazine concentration, which indicated the efficient electro-catalytic activity of 2D WO<sub>3</sub> films without any fouling effect and reflected the fast electron transfer reactions on the surface of WO<sub>3</sub> films. Moreover, the highest sensitivity to hydrazine detection was obtained for the monolayer WO<sub>3</sub> (0.78 nm) compared to the other thicker WO<sub>3</sub> films.

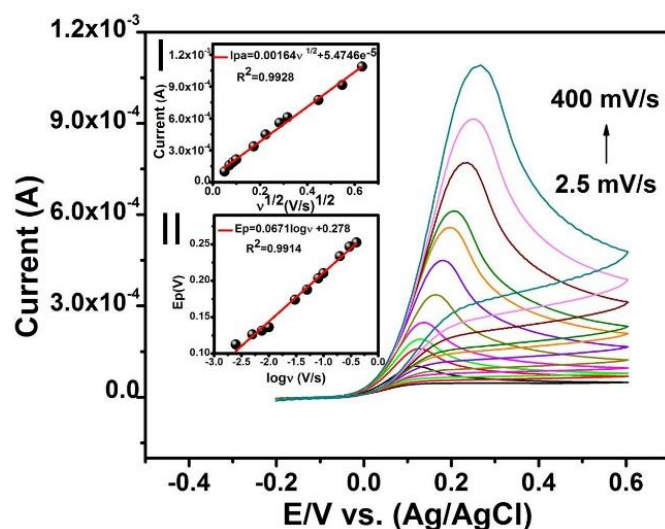


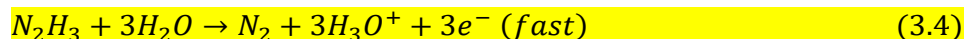
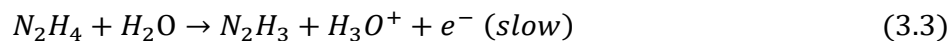
Figure 3.9. CVs of monolayer WO<sub>3</sub> in the presence of 500 μM hydrazine at the different scanning rates. Inset: (I) plot peak currents versus square root of scanning rates and (II) plot of oxidation peak potentials versus the logarithm of scanning rates.

As the changes in the scanning rates may affect the sensing performance of 2D WO<sub>3</sub> films, the electrochemical response of monolayer WO<sub>3</sub> to 500 μM hydrazine in 0.1 M PBS solution was investigated when the scanning rates changed from 2.5 to 400 mV/s

and the summarized results are in Figure 3.9. The obtained CV curves confirmed that the anodic peak currents increase with the rise of the scanning rates and grow linearly with the square root of the scanning rates (Inset I of Figure 3.9), suggesting a diffusion-controlled electrochemical process. The corresponding linear regression equation can be expressed as  $I_p = 0.00164v^{1/2} + 5.4745e^{-5}$  (where  $I_p$  is in A and  $v$  is in V/s), for which  $R^2 = 0.9928$ . In addition, the anodic peak potentials tend to shift to more positive direction with increasing scanning rates, and a plot (Inset II of Figure 3.9) of anodic peak potential  $E_p$  versus  $\log v$  exhibits a linear relationship, which indicated that the hydrazine oxidation on monolayer WO<sub>3</sub> is an irreversible process. The corresponding linear regression equation can be expressed as  $E_p(V) = 0.0671 \log v + 0.278$ . For an irreversible diffusion-controlled process,  $E_p$  can be represented by the Tafel equation based on Equation [39,40]:

$$E_p = [2.303RT/2(1 - \alpha)n_\alpha F] \log v + K \quad (3.2)$$

where  $R$ ,  $T$ , and  $F$  are constant values ( $R = 8.314 \text{ J K}^{-1} \text{ mol}^{-1}$ ,  $T = 298 \text{ K}$  and  $F = 9.65 \times 10^4 \text{ C mol}^{-1}$ ),  $\alpha$  is the electron transfer coefficient,  $n_\alpha$  is the number of electron transfers involved in the rate determining step and  $K$  is a constant. The Tafel slope was obtained 134 mV/decade, which is nearly equal to the theoretical value of 120 mV/decade for the one electron reaction ( $n_\alpha = 1$ ). Therefore, the rate-determining step of hydrazine oxidation involves the one-electron transfer, and  $\alpha$  was found to be 0.55. As a result, the oxidation of unprotonated forms of hydrazine involves one electron transfer in the first rate-determining step, followed by the three electron transfer in a fast second step [27]. The corresponding oxidation reactions have been reported as Equations below:



and the overall reaction of hydrazine oxidation can be expressed as the following equation:



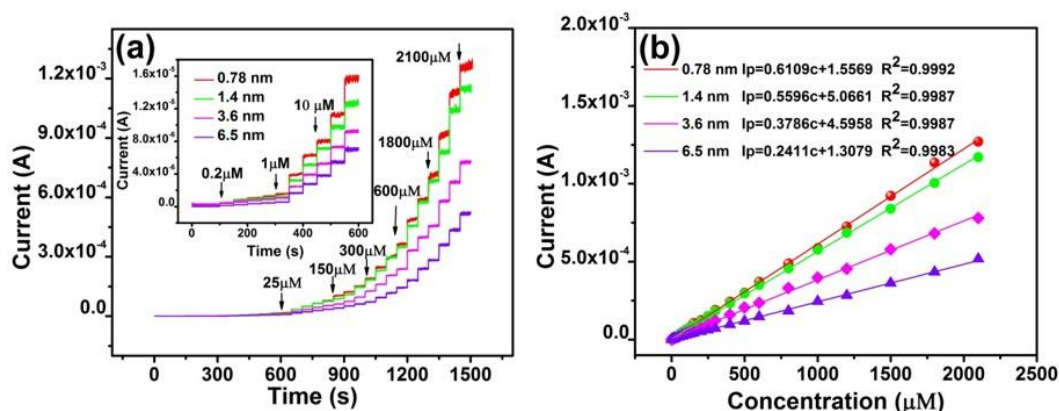


Figure 3.10. (a) Chronoamperometric current response of 2D WO<sub>3</sub> with different thickness to changes hydrazine concentration from 0.2 μM to 2100 μM in 0.1 M PBS (pH=7.4); Inset: Chronoamperometric current response to a lower concentration range of 0.2-20 Mm. (b) Corresponding linear plot of the current versus hydrazine concentration.

In order to evaluate the linear response range, sensitivity, and the LOD of hydrazine, chronoamperometric measurements at various hydrazine concentrations were carried out for 2D WO<sub>3</sub> films. Figure 3.10(a) shows typical current time dynamic response for 0.78 nm, 1.4 nm, 3.6 nm, and 6.5 nm WO<sub>3</sub> films toward hydrazine with successive addition of hydrazine approximately every 50 s at an applied potential of 0.14 V from 0.2 μM to 2100 μM, and the inset image displays the lower concentration range from 0.2 μM to 200 μM. From the i-t curves, the response time to different hydrazine concentrations for all 2D WO<sub>3</sub> films was found. In fact, all of the 2D WO<sub>3</sub> showed a fast response, and all steady-states were achieved within 2 seconds. As expected, the monolayer WO<sub>3</sub> films exhibited the largest catalytic current in response to hydrazine concentration changes compared to the other thickness WO<sub>3</sub> films.

Table 3.1. Characteristics of 2D WO<sub>3</sub> films with different thickness to hydrazine detection

Material	Sensitivity (μA μM <sup>-1</sup> cm <sup>2</sup> )	Linear range (μM)	LOD (μM)	Response time (s)
0.78 nm WO <sub>3</sub> films	1.24	0.2 - 2100	0.015	<2
1.4 nm WO <sub>3</sub> films	1.18	0.2 - 2100	0.022	<2
3.6 nm WO <sub>3</sub> -films	0.74	0.2 - 2100	0.035	<2
6.5 nm WO <sub>3</sub> films	0.48	0.2 - 2100	0.07	<2

Table 3.2. Comparison of characteristics of the present work to the typical characteristics of other nanostructured materials and heterostructures reported to date towards hydrazine.

Electrode material	Sensitivity ( $\mu\text{A mM}^{-1} \text{cm}^{-2}$ )	Linear range ( $\mu\text{M}$ )	LOD ( $\mu\text{M}$ )	Response time (s)	Stability	Refs
WO <sub>3</sub> (0.78 nm)	1.24	0.2 -2100	0.015	< 2	30	this work
WO <sub>3</sub> NPs	0.185	100-1000	144.7	/	/	[43]
Hierarchical ZnO	0.51	0.8-200	0.25	< 3	/	[44]
ZnO nanorods	0.386	0.1-60	59.18	/	56	[45]
CuO spheres	0.007	5-10000	1.9	/	/	[46]
Cu-CuO	0.156	100-1800	/	/	/	[47]
AuNPs/graphite	/	25-1000	3.07	/	/	[48]
MnO <sub>2</sub> / graphite	1.007	3-1120	0.16	/	7	[49]
Graphene/GCE	/	3-300	1	< 3	2	[50]
Au/Hap NRs	0.5	0.5-1429	0.017	< 2	10	[42]
Co-Graphene	0.562	0.25-370	0.1	< 3	60	[51]
Ag/CB-GCE	0.3	50-800	3.47	/	/	[52]
CNT-PdPt	0.6	0.55-1200	0.28	< 5	20	[53]

The corresponding calibration curves for hydrazine detection by 2D WO<sub>3</sub> films are presented in Figure 3.10(b). All 2D WO<sub>3</sub> films demonstrated great linearity in chronoamperometric responses to the changes of hydrazine concentration from 0.2  $\mu\text{M}$  to 2100  $\mu\text{M}$ , with the correlation coefficient higher than 0.99. According to the equation of “sensitivity= slope/surface of the electrode” and “low detection limit=  $3S_b$ /sensitivity” [41,42], where  $S_b$  is the standard deviation of the blank signal. The 0.78 nm WO<sub>3</sub> films showed the highest sensitivity of  $1.24 \mu\text{A } \mu\text{M}^{-1} \text{cm}^{-2}$  with a low detection limit of 0.015  $\mu\text{M}$  at the signal to noise ratio of 3. As for 1.4 nm, 3.6 nm and 6.5 nm WO<sub>3</sub> films, the sensitivity was  $1.18 \mu\text{A } \mu\text{M}^{-1} \text{cm}^{-2}$  with a detection limit of 0.022  $\mu\text{M}$ ,  $0.74 \mu\text{A } \mu\text{M}^{-1} \text{cm}^{-2}$  with a detection limit of 0.035  $\mu\text{M}$  and  $0.48 \mu\text{A } \mu\text{M}^{-1} \text{cm}^{-2}$  with a detection limit of 0.07  $\mu\text{M}$ , respectively. All characteristics of 2D WO<sub>3</sub> films with different thickness towards hydrazine detection were combined into Table 3.1. From the results obtained, it is evident that the monolayer WO<sub>3</sub> exhibited the highest sensitivity and lowest LOD

among all 2D WO<sub>3</sub> samples. Table 3.2 summarizes and provides the comparison of the typical characteristics of hydrazine detection, including LOD, sensitivity, **long-term stability**, linear response and the response time for other nanostructured materials and heterostructures reported to date. The obtained measured results for the ALD-fabricated monolayer WO<sub>3</sub> films confirmed that this nanomaterial possesses superior sensing capabilities towards lower concentration of hydrazine compared to other nano-materials within the wide linear range of the measured concentrations.

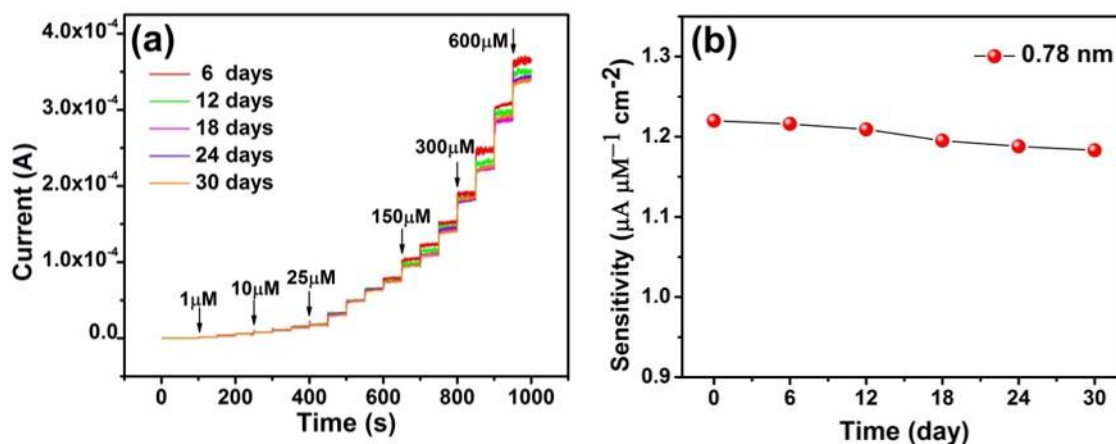


Figure 3.11. Long-term stability test of monolayer WO<sub>3</sub>. (a) The changes in amperometric current obtained every six days and (b) the changes in sensitivity during the 30-day test.

To get further insights into the properties of the ALD-developed monolayer WO<sub>3</sub> films, long-term stability testing was performed. Monolayer WO<sub>3</sub> films were tested by conducting amperometric experiments every 6 days, varying the hydrazine concentration from 1 μM to 600 μM at the room temperature, as shown in Figure 3.11(a). The measured results (Figure 3.11(b)) indicate that the standard deviation of the sensitivity is calculated to be 0.12, which proved the fabricated monolayer WO<sub>3</sub> films have excellent long-term stability.

Chronoamperometry was also utilized for investigation of the anti-interfering ability of fabricated monolayer WO<sub>3</sub> films when the interfering chemicals were added to the aqueous environment containing 10 μM hydrazine. Figure 3.12(a) shows that the amperometric response to hydrazine of monolayer WO<sub>3</sub> films did not change upon introduction of 1000 μM of KCl, NaNO<sub>3</sub> and NaNO<sub>2</sub>, additional 500 mM of glucose and

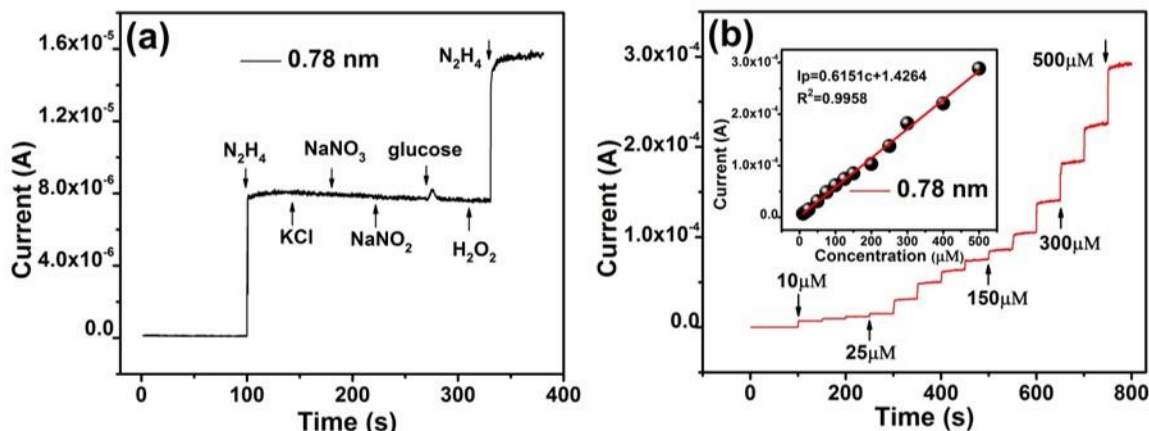


Figure 3.12. (a) Interference study for monolayer WO<sub>3</sub> in the presence of hydrazine and interfering chemicals. (b) Amperometric current response in the presence of 50 μM interfering substances; Inset: Corresponding linear plot of current vs. hydrazine concentration.

H<sub>2</sub>O<sub>2</sub> into the 0.1 M PBS solution at the detection potential of 0.14 V. Only small spike in current was recorded for glucose. Thus, it was evident that the response of monolayer WO<sub>3</sub> films to 10 mM hydrazine was not affected by the addition of a 100-fold concentration of inorganic substances and 50-fold of biological substances. Furthermore, the amperometric hydrazine detection at various concentrations was performed in the presence of 50 μM concentration of interfering substances mentioned above. Figure 3.12(b) clearly illustrates that the monolayer WO<sub>3</sub> showed excellent linearity under the interfering conditions and exhibited a sensitivity of 1.23, which is much closed to the sensitivity of 1.24 under no interference present. All these results indicated that the sensor has excellent anti-interference capability toward the detection of hydrazine.

### 3.5 Conclusions

Wafer-scale 2D WO<sub>3</sub> films with the different thicknesses from monolayer to ~6.5 nm were successfully deposited on Au-SiO<sub>2</sub>/Si substrates by the ALD technique, and their electro-catalytic behaviors toward the hydrazine oxidation were comprehensively investigated. The ALD-fabricated 2D WO<sub>3</sub> films have demonstrated excellent electrocatalytic activity with a notable decrease in over-potential and enhanced oxidation current peaks compared to the bare Au electrode. Among those 2D WO<sub>3</sub> samples, the monolayer WO<sub>3</sub> films with the thickness of ~0.78 nm showed superior

sensing capabilities towards the electrochemical hydrazine detection, including the lowest LOD of 0.015  $\mu\text{M}$  reported to date, the wide linear range of 0.2–2100  $\mu\text{M}$  and high sensitivity. These improved capabilities of monolayer WO<sub>3</sub> could be attributed to the larger effective surface area and smaller charge transfer resistance. In addition, studies on the long-term stability illustrated that the monolayer WO<sub>3</sub> films exhibited sustainable measurement and great long-term stability for 30-day testing. Monolayer WO<sub>3</sub> also showed enhanced anti-interfering performance in the presence of a 100-fold concentration of inorganic substances and 50-fold of biological substances. Thus, ALD-developed 2D WO<sub>3</sub> films can be considered as highly promising nano-materials for sensitive sustainable and selective hydrazine detection in practical applications.

## References

1. S. Cong, Y. Tian, Q. Li, Z. Zhao, F. Geng, Single-crystalline tungsten oxide quantum dots for fast pseudocapacitor and electrochromic applications, *Adv. Mater.* 26 (2014) 4260-4267.
2. J. He, H. Liu, B. Xu, X. Wang, Highly flexible sub-1 nm tungsten oxide nanobelts as efficient desulfurization catalysts, *Small* 11 (2015) 1144-1149.
3. J. Yan, T. Wang, G. Wu, W. Dai, N. Guan, L. Li, J. Gong, Tungsten oxide single crystal nanosheets for enhanced multichannel solar light harvesting, *Adv. Mater.* 27 (2015) 1580-1586.
4. S. Wang, W. Fan, Z. Liu, A. Yu, X. Jiang, Advances on tungsten oxide based photochromic materials: strategies to improve their photochromic properties, *J. Mater. Chem. C* 6 (2018) 191-212.
5. Z. Hai, Z. Wei, C. Xue, H. Xu, F. Verpoort, Nanostructured tungsten oxide thin film devices: from optoelectronics and ionics to iontronics, *J. Mater. Chem C* 7 (2019) 12968-12990.
6. G. Guan, J. Xia, S. Liu, Y. Cheng, S. Bai, S. Tee, Y. Zhang, M. Han, Electrostatic-driven exfoliation and hybridization of 2D nanomaterials, *Adv. Mater.* 29 (2017) 1700326.
7. X. Xiao, H. Song, S. Lin, Y. Zhou, X. Zhan, Z. Hu, Q. Zhang, J. Sun, B. Yang, T. Li, L. Jiao, J. Zhou, J. Tang, Y. Gogotsi, Scalable salt-templated synthesis of two-dimensional transition metal oxides, *Nat. Commun.* 7 (2016) 1-8.
8. K. Kalantar-zadeh, J. Ou, T. Daeneke, A. Mitchell, T. Sasaki, M. Fuhrer, Two dimensional and layered transition metal oxides, *Appl. Mater. Today* 5 (2016) 73-89.
9. Z. Sun, T. Liao, Y. Dou, S. Hwang, M. Park, L. Jiang, J. Kim, S. Dou, Generalized self-assembly of scalable two-dimensional transition metal oxide nanosheets, *Nat. Commun.* 5 (2014) 1-9.

10. F. Haque, T. Daeneke, K. Kalantar-zadeh, J. Ou, Two-dimensional transition metal oxide and chalcogenide-based photocatalysts, *Nano-micro Lett.* 10 (2018) 23.
11. A. Azam, J. Kim, J. Park, T. Novak, A. Tiwari, S. H. Song, B. Kim, S. Jeon, Two-dimensional WO<sub>3</sub> nanosheets chemically converted from layered WS<sub>2</sub> for high-performance electrochromic devices, *Nano Lett.* 18 (2018) 5646-5651.
12. F. Ji, X. Ren, X. Zheng, Y. Liu, L. Pang, J. Jiang, S. Liu, 2D-MoO<sub>3</sub> nanosheets for superior gas sensors, *Nanoscale* 8 (2016) 8696-8703.
13. M. Karbalaeei, Z. Hai, Z. Wei, C. Detavernier, E. Solano, F. Verpoort, S. Zhuiykov, ALD-developed plasmonic two-dimensional Au-WO<sub>3</sub>-TiO<sub>2</sub> heterojunction architectonics for design of photovoltaic devices, *ACS Appl. Mater. Inter.* 10 (2018) 10304-10314.
14. J. Wang, C. Liu, Preparation of 2D WO<sub>3</sub> nanomaterials with enhanced catalytic activities: current status and perspective, *ChemBioEng Rev.* 2 (2015) 335-350.
15. K. Bao, W. Mao, G. Liu, L. Ye, H. Xie, S. Ji, D. Wang, C. Chen, Y. Li, Preparation and electrochemical characterization of ultrathin WO<sub>3-x</sub>/C nanosheets as anode materials in lithium ion batteries, *Nano Res.* 10 (2017) 1903-1911.
16. J. Liu, M. Notarianni, G. Will, V. Tjong, H. Wang, N. Motta, Electrochemically exfoliated graphene for electrode films: effect of graphene flake thickness on the sheet resistance and capacitive properties, *Langmuir* 29 (2013) 13307-13314.
17. X. Li, W. Han, J. Wu, X. Qiao, J. Zhang, P. Tan, Layer-number dependent optical properties of 2D materials and their application for thickness determination, *Adv. Funct. Mater.* 27 (2017) 1604468.
18. X. Fang, X. Yu, H. Zheng, H. Jin, L. Wang, M. Cao, Temperature-and thickness-dependent electrical conductivity of few-layer graphene and graphene nanosheets, *Phys. Lett. A* 379 (2015) 2245-2251.
19. W. X. Zhang, T. Li, S. B. Gong, C. He, L. Duan, Tuning the electronic and magnetic properties of graphene-like AlN nanosheets by surface functionalization and thickness, *Phys. Chem. Chem. Phys.* 17 (2015) 10919-10924.
20. A. Salimi, M. Roushani, Non-enzymatic glucose detection free of ascorbic acid interference using nickel powder and nafion sol-gel dispersed renewable carbon ceramic electrode, *J. Electroanal. Chem.* 7 (2005) 879-887.
21. M. R. Saleem, R. Ali, M. B. Khan, S. Honkanen, J. Turunen, Impact of atomic layer deposition to nanophotonic structures and devices, *Front. Mater.* 1 (2014) 18.
22. W. Hao, C. Marichy, C. Journet, Atomic layer deposition of stable 2D materials, *2D Mater.* 6 (2018) 012001.

23. Y. Wang, Y. Wan, D. Zhang, Reduced graphene sheets modified glassy carbon electrode for electrocatalytic oxidation of hydrazine in alkaline media, *Electrochem. Comm.* 12 (2010) 187–190.
24. M. Mazloum-Ardakani, A. Khoshroo, An electrochemical study of benzofuran derivative in modified electrode-based CNT/ionic liquids for determining nanomolar concentrations of hydrazine, *Electrochim. Acta* 103 (2013) 77–84.
25. A. A. Ibrahim, G. N. Dar, S. A. Zaidi, A. Umar, M. Abaker, H. Bouzid, S. Baskoutas, Growth and properties of Ag-doped ZnO nanoflowers for highly sensitive phenyl hydrazine chemical sensor application *Talanta* 93 (2012) 257–263.
26. J.-P. Schirmann, P. Bourdauducq, “Hydrazine” in *Ullmann’s encyclopedia of industrial chemistry*, Wiley-VCH, Weinheim, 2002.
27. J. Li, X. Lin, Electrocatalytic oxidation of hydrazine and hydroxylamine at gold nanoparticle – polypyrrole nanowire modified glassy carbon electrode, *Sens. Actuators B Chem.* 126 (2007) 527–535.
28. S. M. Golabi, H. R. Zare, Electrocatalytic oxidation of hydrazine at a chlorogenic acid (CGA) modified glassy carbon electrode, *J. Electroanal. Chem.* 465 (1999) 168–176.
29. H. Zhang, J. Huang, H. Hou, T. You, Electrochemical detection of hydrazine based on electrospun palladium nanoparticle/Carbon nanofibers, *Electroanal.* 21 (2009) 1869–1874.
30. D. Steinhoff, U. Mohr U, The question of carcinogenic effects of hydrazine, *Experimental pathology* 33 (1988) 133–143.
31. Z. Zhao, Y. Sun, P. Li, S. Sang, W. Zhang, J. Hu, K. Lian, A sensitive hydrazine electrochemical sensor based on zinc oxide nano-wires, *J. Electrochem. Soc.* 161 (2014) B157–B162.
32. M. Mazloum-Ardakani, Z. Taleat, H. Beitollahi, H. Naeimi, Nanomolar concentrations determination of hydrazine by a modified carbon paste electrode incorporating TiO<sub>2</sub> nanoparticles, *Nanoscale* 3 (2011) 1683–1689.
33. D. Zhou, D. Xie, F. Shi, D. Wang, X. Ge, X. Xia, X. Wang, C. Gu, J. Tu, Crystalline/amorphous tungsten oxide core/shell hierarchical structures and their synergistic effect for optical modulation, *J. Colloid Interface Sci.* 460 (2015) 200–208.
34. A. P. Shpak, A. M. Korduban, M. M. Medvedskij, V. O. Kandyba, XPS studies of active elements surface of gas sensors based on WO<sub>3-x</sub> nanoparticles, *J. Electron. Spectrosc. Relat. Phenom.* 156 (2007) 172–175.
35. S. Zhuiykov, E. Kats, B. Carey, S. Balendhran, Proton intercalated two-dimensional WO<sub>3</sub> nano-flakes with enhanced charge-carrier mobility at room temperature, *Nanoscale* 6 (2014) 15029–15036.

36. S. Daemi S, A. A. Ashkarran, Bahari, A. Bahari, S. Ghasemi, Fabrication of a gold nanocage/graphene nanoscale platform for electrocatalytic detection of hydrazine, *Sens. Actuators B Chem.* 245 (2017) 55-65.
37. H. Beitollah, M. Goodarzian, M. A. Khalilzadeh, H. Karimi-Maleh, M. Hassanzadeh, M. Tajbakhsh, Electrochemical behaviors and determination of carbidopa on carbon nanotubes ionic liquid paste electrode, *J. Mol. Liq.* 173 (2012) 137-143.
38. S. Zhao, L. Wang, T. Wang, Q. Han, S. Xu, Ag<sub>2</sub>O nanoparticles decorated TiO<sub>2</sub> nanofibers as a p-n heterojunction for enhanced photocatalytic decomposition of RhB under visible light irradiation, *Appl. Surf. Sci.* 369 (2016) 36-42.
39. C. Liu, H. Zhang, Y. Tang, S. Luo, Controllable growth of graphene/Cu composite and its nanoarchitecture-dependent electrocatalytic activity to hydrazine oxidation, *J. Mater. Chem. A* 2 (2014) 4580-4587.
40. S. Zhao, L. Wang, T. Wang, Q. Han, S. Xu, A high-performance hydrazine electrochemical sensor based on gold nanoparticles/single-walled carbon nanohorns composite film, *Appl. Surf. Sci.* 369 (2016) 36-42.
41. R. Devasenathipathy, V. Mani, S. M. Chen, D. Arulraj, V. S. Vasantha, Highly stable and sensitive amperometric sensor for the determination of trace level hydrazine at cross linked pectin stabilized gold nanoparticles decorated graphene nanosheets, *Electrochim. Acta* 135 (2014) 260-269.
42. G. Bharath, A. Naldoni, K. H. Ramsait, A. Abdel-Wahab, R. Madhu, E. Alsharaeh. N. Ponpandian, Enhanced electrocatalytic activity of gold nanoparticles on hydroxyapatite nanorods for sensitive hydrazine sensors, *J. Mater. Chem. A* 4 (2016) 6385-6394.
43. S. Shukla, S. Chaudhary, A. Umar, G. R. Chaudhary, S. K. Mehta, Tungsten oxide (WO<sub>3</sub>) nanoparticles as scaffold for the fabrication of hydrazine chemical sensor, *Sens. Actuators B Chem.* 196 (2014) 231-237.
44. Y. Ni, J. Zhu, L. Zhang, J. Hong, Hierarchical ZnO micro/nanoarchitectures: hydrothermal preparation, characterization and application in the detection of hydrazine, *Cryst. Eng. Comm.* 12 (2010) 2213-2218.
45. R. Ahmad, N. Tripathy, Y. B. Hahn, Highly sensitive hydrazine chemical sensor based on ZnO nanorods field-effect transistor, *Chem. Commun.* 50 (2014) 1890-1893.
46. S. B. Khan, M. Faisal, M. M. Rahman, I. A. Abdel-Latif, A. A. Ismail, K. Akhtar, A. Al-Hajry, A. M. Asiri, K. A. Alamry, Highly sensitive and stable phenyl hydrazine chemical sensors based on CuO flower shapes and hollow spheres, *New J. Chem.* 37 (2013) 1098-1104.

47. V. C. Bassetto, A. E. Russell, L. T. Kubota, P. N. Bartlett, Preparation of copper sphere segment void templates for electrochemical SERS and their use to study the interaction of amino acids with copper under potentiostatic control, *Electrochim. Acta* 144 (2014) 400–405.
48. M. A. Aziz, A. N. Kawde, Gold nanoparticle-modified graphite pencil electrode for the high-sensitivity detection of hydrazine, *Talanta* 115 (2013) 214–221.
49. J. Lei, X. Lu, W. Wang, X. Bian, Y. Xue, C. Wang, L. Li, Fabrication of MnO<sub>2</sub>/graphene oxide composite nanosheets and their application in hydrazine detection, *RSC Adv.* 2 (2012) 2541–2544.
50. C. Wang, L. Zhang, Z. Guo, J. Xu, H. Wang, K. Zhai, X. Zhou, A novel hydrazine electrochemical sensor based on the high specific surface area graphene, *Microchim. Acta* 169 (2010) 1–6.
51. He Y, Zheng J, Dong S, Ultrasonic-electrodeposition of hierarchical flower-like cobalt on petal-like graphene hybrid microstructures for hydrazine sensing, *Analyst* 137 (2012) 4841–4848.
52. C. Tan, X. H. Xu, F. Wang, Z. L. Li, J. J. Liu, J. Ji, Carbon black supported ultra-high loading silver nanoparticle catalyst for electro-oxidation and determination of hydrazine, *Sci. China Chem.* 56 (2013) 911–916.
53. S. P. Kim, S. G. Lee, M. Y. Choi, H. C. Choi, H. C. Choi, Highly Sensitive Hydrazine Chemical Sensor Based on CNT-PdPt Nanocomposites, *J. Nano. Mater.* 16 (2015) 298.

# Chapter 4

## SURFACE FUNCTIONALIZATION OF WAFER-SCALE 2D WO<sub>3</sub> NANOFILMS BY NM ELECTRODEPOSITION (NM=AG, PT, PD) FOR ELECTROCHEMICAL H<sub>2</sub>O<sub>2</sub> REDUCTION IMPROVEMENT

---

### 4.1 Abstract

Surface functionalization of two-dimensional WO<sub>3</sub> nanofilms by noble metal (NM) nanoparticles (NM = Ag, Pt, and Pd) was successfully achieved via a combination of the atomic layer deposition process and electrochemical deposition method. Deposited NM nanoparticles were uniformly in the particle size and homogeneously dispersed on the surface of 2D WO<sub>3</sub>. They represented electrochemically active metal-semiconductor hybrid nanocomposites with the larger electroactive area, and consequently, substantially enhanced the electrochemical H<sub>2</sub>O<sub>2</sub> detection of the device based on functionalized 2D WO<sub>3</sub> nanofilms. Functionalization by Ag nanoparticles was found to be more efficient compared to the same functionalization by Pt and Pd nanoparticles. Particularly, Ag<sub>200</sub>-WO<sub>3</sub> nanofilms exhibited the best electrochemical performance with a high sensitivity of 282  $\mu\text{A mM}^{-1} \text{cm}^{-2}$ , extremely wide linear H<sub>2</sub>O<sub>2</sub> concentrations range from 0.2  $\mu\text{M}$  to 33.6 mM, a low detection limit of 0.1  $\mu\text{M}$ , a fast response time of 2 s and an excellent selectivity and long-term stability. Surface functionalization by NM nanoparticles approach has demonstrated the great potential in the development of a hybrid nanostructured electrode for various devices with enhanced electrochemical capabilities.

### 4.2 Introduction

In order to further improve the performance of 2D TMOs for the electrochemical sensing applications, a lot of strategies have been engaged in many cases [1-4]. Since the surface area of electrode materials plays a vital role in the development of electrochemical sensor devices, functionalization is verified an efficient way to modify the surface of 2D TMOs to improve the sensing properties, which enabled the development of the combination of two or more dissimilar nanomaterials to form the hybrid

nanocomposites. Carbon nanomaterial-based 2D metal transition oxides composites are also gaining attention in sensing applications since carbon nanomaterials can be used as highly porous and conductive platforms [5, 6]. When they are functionalized with 2D metal transition oxides nanosheets, their electrocatalytic performances are significantly improved. Loading of 2D TMOs on the surface of carbonaceous materials, such as graphene, carbon nanotube, and porous carbon, has exhibited various potential applications due to their high electronic conductivity, excellent flexibility, high charge carriers mobility, large surface area, and high chemical stability [7-9]. Conducting polymers have obtained tremendous attention in the development of sensing devices [10, 11]. The electrically conducting polymers can be used as excellent electrode materials for the immobilization of biomolecules and accelerating electron transfer kinetics. NMs emerged as a new class of materials, are particularly interesting for materials science due to their unique electronic, optical, magnetic, and catalytic properties [12-14]. Forming the hybrid nanocomposites, especially metal-semiconductor hybrids, is considered as one of the most effective strategies to enhance the intrinsic properties of the individual components and generate other novel functions and properties [2-4]. 2D semiconductor nanomaterials with the thickness of just a few nm are also a novel template for fabrication of the functional composites owing to their high specific surface area [15].

On the other hand, NM nanoparticles, as 0D functional nanoparticles, exhibit a large percentage of active surface atoms and extraordinary electronic structure and hence have generally been used to improve the electrochemical capabilities of various devices [16-19]. In this regard, it is also established that the size and distribution of NM nanoparticles play a vital role in the electrocatalytic ability of the functionalized materials [20, 21]. Therefore, the strategies for surface modification and functionalization of the 2D semiconductor nanomaterials by NM nanoparticles to form the metal-semiconductor hybrids on the 2D surface were investigated in many developed ways, including photochemical synthesis, electrochemical deposition and electrostatic deposition [22-24]. Among these techniques, the electrochemical deposition has clear advantages of controlling the distribution, shape, and the size of nanoparticles

and forming nanoparticles directly on the 2D surface owing to its simplicity, low cost, and convenient approach [25].

Herein, different NM (Ag, Pt, Pd) nanoparticles functionalized wafer-scale 2D WO<sub>3</sub> (NM-WO<sub>3</sub>) nanofilms for the sensitive and selective H<sub>2</sub>O<sub>2</sub> determination were developed by ALD, followed by electrodeposition of the different amount of NM nanoparticles onto the surface of 2D WO<sub>3</sub> nanofilms as a function of various electrodeposition time. The deposited NM nanoparticles are uniform in the particle size and were homogeneously dispersed on the surface of 2D WO<sub>3</sub> nanofilms. Subsequent electrochemical studies and optimization of the electro-catalytic abilities of NM nanoparticles functionalized 2D WO<sub>3</sub> nanofilms for the H<sub>2</sub>O<sub>2</sub> reduction have demonstrated the superior electrochemical capabilities of functionalized 2D NM-WO<sub>3</sub> towards the significant improvement in H<sub>2</sub>O<sub>2</sub> reduction. This work confirmed that the functionalized 2D NM-WO<sub>3</sub> nanofilms exhibited a considerable advancement in facilitating the excellent potential for the practical, highly sensitive H<sub>2</sub>O<sub>2</sub> detection.

### 4.3 Experimental section

#### 4.3.1 Wafer-scale development of 2D WO<sub>3</sub> nanofilms

The details of ALD fabrication of ultra-thin 2D WO<sub>3</sub> nanofilms and the optimal recipe parameters for the ultra-thin 2D WO<sub>3</sub> nanofilms were established in Chapter 3. Prior to 2D WO<sub>3</sub> deposition, Au/Cr films with the thickness of approximately ~150 nm were fabricated on SiO<sub>2</sub>/Si substrate by the Electron Beam Evaporator method (Nanochrome II (Intivac, USA)) to develop conductive electrodes for subsequent investigation of the electrochemical performance. The optimal recipe parameters for the ultra-thin 2D WO<sub>3</sub> nanofilms were established in Chapter 3. Variable angle in-situ spectroscopic ellipsometry measurements (J.A. Woollam M2000 DI) were conducted at different angles over the wavelengths of 250-1690 nm to measure the thickness of the ALD-deposited 2D WO<sub>3</sub> films. It was established that all ALD-fabricated 2D WO<sub>3</sub> samples have an average thickness of ~6.5 nm over the wafer, as being confirmed by ellipsometry measurements (see Figure 4.1). Consequently, unless it stated otherwise, 2D WO<sub>3</sub> samples in this investigation had an average thickness of 6.5 nm. Finally, all 2D WO<sub>3</sub>

samples were subsequently annealed in air at 250 °C for 1 h, with the average heating/cooling rate of 0.5 °C per minute.

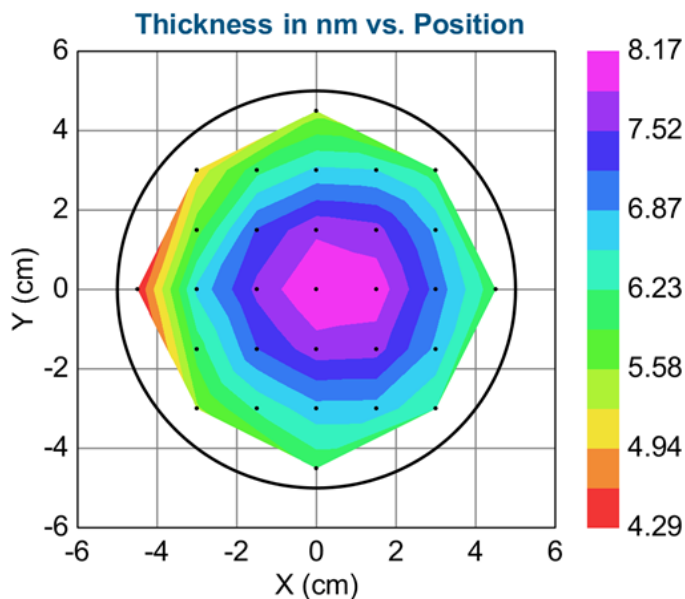


Figure 4.1. Ellipsometry measurement data for the developed 2D WO<sub>3</sub> nanofilms.

#### 4.3.2 Fabrication of 2D NM-WO<sub>3</sub> nanofilms (NM=Ag, Pt and Pd)

For Ag-modified WO<sub>3</sub> nanofilms, the electrolyte of 0.1 M KNO<sub>3</sub> solution containing 1.0 mM AgNO<sub>3</sub> was prepared, and then 2D WO<sub>3</sub> samples were immersed into it. The electrochemical deposition process was conducted at 0.2 V (vs. Ag/AgCl), and the deposition time was varied from 50 to 400 s in order to obtain the different amounts of Ag-modified 2D WO<sub>3</sub> nanofilms as a function of the different electrodeposition time. The same approach was undertaken for the electrochemical deposition of other NMs, only changing the electrolyte 0.1 M KNO<sub>3</sub> with 1.0 mM AgNO<sub>3</sub> into 0.1 M KCl with 1.0 mM H<sub>2</sub>PtCl<sub>6</sub> · 6H<sub>2</sub>O and 0.1 M KCl with 1.0 mM PdCl<sub>2</sub>, respectively. For comparison, a different amount of NM-modified Au (NM-Au) electrodes were also prepared. The obtained samples at the different deposition times were appropriately designated as Ag<sub>t</sub>-WO<sub>3</sub>, Ag<sub>t</sub>-Au, Pt<sub>t</sub>-WO<sub>3</sub>, Pt<sub>t</sub>-Au, Pd<sub>t</sub>-WO<sub>3</sub> and Pd<sub>t</sub>-Au. All NM-functionalized samples were dried at 60°C overnight in a vacuum.

## 4.4 Results and discussion

### 4.4.1. Characterization of 2D NM<sub>200</sub>-WO<sub>3</sub> nanofilms

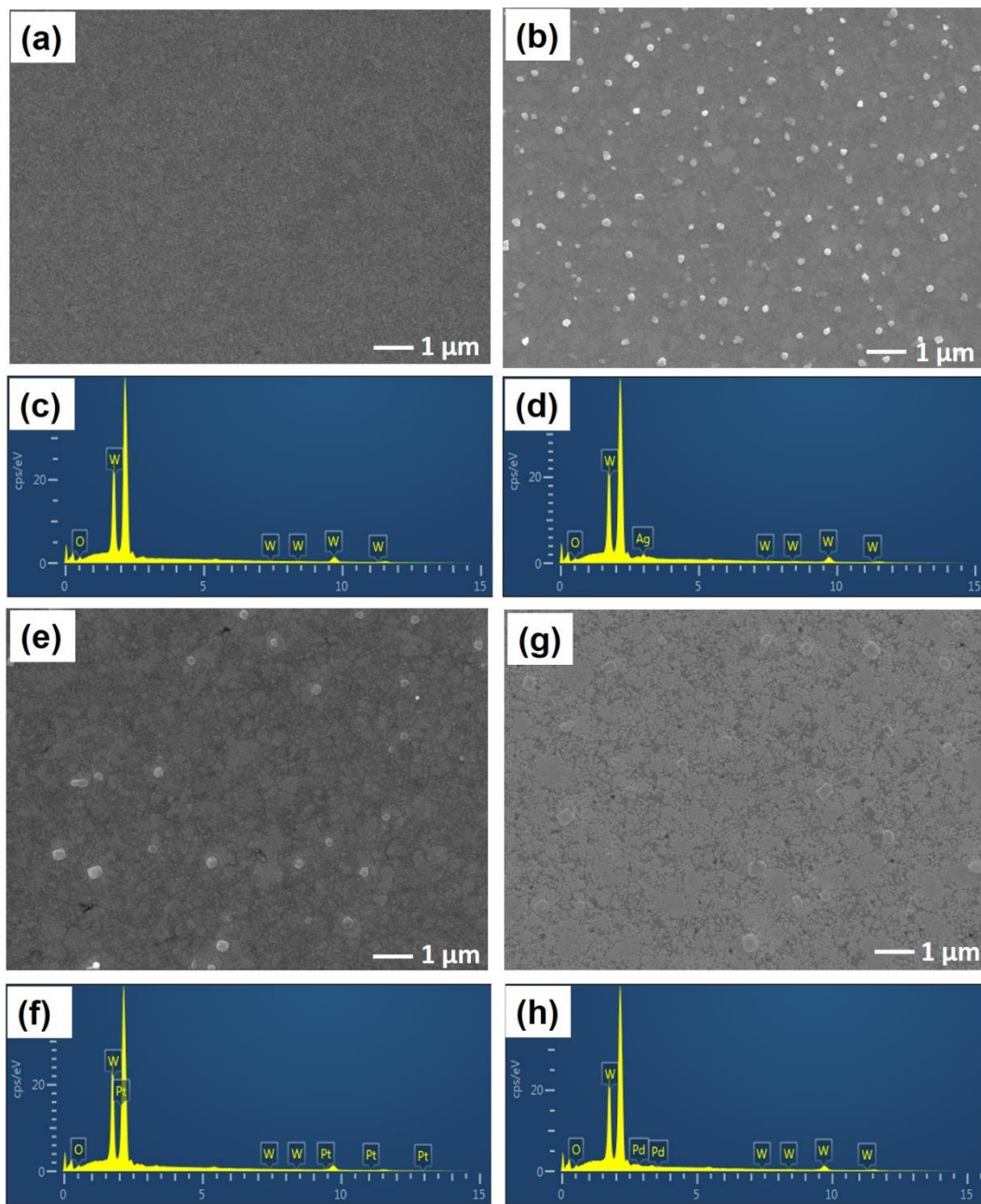


Figure 4.2. SEM images and EDS analysis of (a, c) 2D WO<sub>3</sub>, (b, d) Ag<sub>200</sub>-WO<sub>3</sub>, (e, f) Pt<sub>200</sub>-WO<sub>3</sub>, and (g, h) Pd<sub>200</sub>-WO<sub>3</sub> nanofilms, respectively.

The morphology and structure of 2D WO<sub>3</sub> and 2D NM<sub>200</sub>-WO<sub>3</sub> nanofilms were studied by SEM characterization. As shown in Figure 4.2(a), 2D WO<sub>3</sub> nanofilms were relatively

smooth and uniformly distributed on the surface of the Au/Cr electrode on a large scale. The EDS measurement of 2D WO<sub>3</sub> nanofilms in Figure 4.2(b) displays signals of tungsten and oxygen (signals related to the substrate were omitted), indicating that the developed 2D films had no impurities. Figure 4.2(c, e, g) depict SEM images of the surface morphology of 2D WO<sub>3</sub> nanofilms on which the Ag, Pt, and Pd nanoparticles were electrodeposited for 200 s. It could be clearly seen that nanoparticles were homogeneously distributed on the surface of 2D WO<sub>3</sub> nanofilms. Among them, the Ag nanoparticles possess denser distribution with the average diameters of about ~150 nm. Pt nanoparticles have an average diameter of about ~200 nm, and Pd nanoparticles have the largest average diameter of about ~300 nm. However, as the diameter of nanoparticles increased their density on the surface of 2D WO<sub>3</sub> is decreased. Moreover, the formation of Ag, Pt, and Pd nanoparticles on the surface of 2D WO<sub>3</sub> nanofilms has been confirmed by EDS analysis with the emergency of Ag, Pt, and Pd elemental peaks, as shown in Figure 4.2 (d, f, h). In addition, the atomic concentration of the elements of interest has been done based on the obtained EDS experimental results. However, authors must admit that due to extremely thin thickness of the ALD-deposited WO<sub>3</sub> samples, the EDS measurements used for atomic concentrations were very challenging and not very precise. Specifically, Ag<sub>200</sub>-WO<sub>3</sub>, Pt<sub>200</sub>-WO<sub>3</sub>, and Pd<sub>200</sub>-WO<sub>3</sub> are ~15.7%, ~10.2%, and ~12.3%, respectively.

XPS was carried out to investigate the composition of 2D WO<sub>3</sub>, and NM<sub>200</sub>-WO<sub>3</sub> nanofilms, and the chemical state of the metal in NM<sub>200</sub>-WO<sub>3</sub> nanofilms could also be examined. As shown in Figure 4.3(a), the doublets of W 4f<sub>7/2</sub> and W 4f<sub>5/2</sub> were centered at 35.6 eV and 37.8 eV with the spin-orbit splitting of the doublet of 2.2 eV and the peak ratio of 4:3, while a third broad peak of W 5p<sub>3/2</sub> was located at 41.7 eV, revealing W atoms with an oxidation state of WO<sub>3</sub> [26]. The O 1s peak in the XPS spectrum (Figure 4.3(b)) could be deconvoluted into two peaks. The main binding energy component centered at 530.1 eV can be characteristic of the lattice oxygen of WO<sub>3</sub> [27], and the second binding energy at 531.7 eV is attributed to oxygen vacancies [28]. Figure 4.3(c-h) provides the binding energies of the three different NMs in 2D NM<sub>200</sub>-WO<sub>3</sub> nanofilms. The clear XPS peaks of NM species confirmed their presence. For 2D Ag<sub>200</sub>-WO<sub>3</sub> and 2D Pt<sub>200</sub>-WO<sub>3</sub> nanofilms, two peaks are observed, and no other peaks can be deconvoluted.

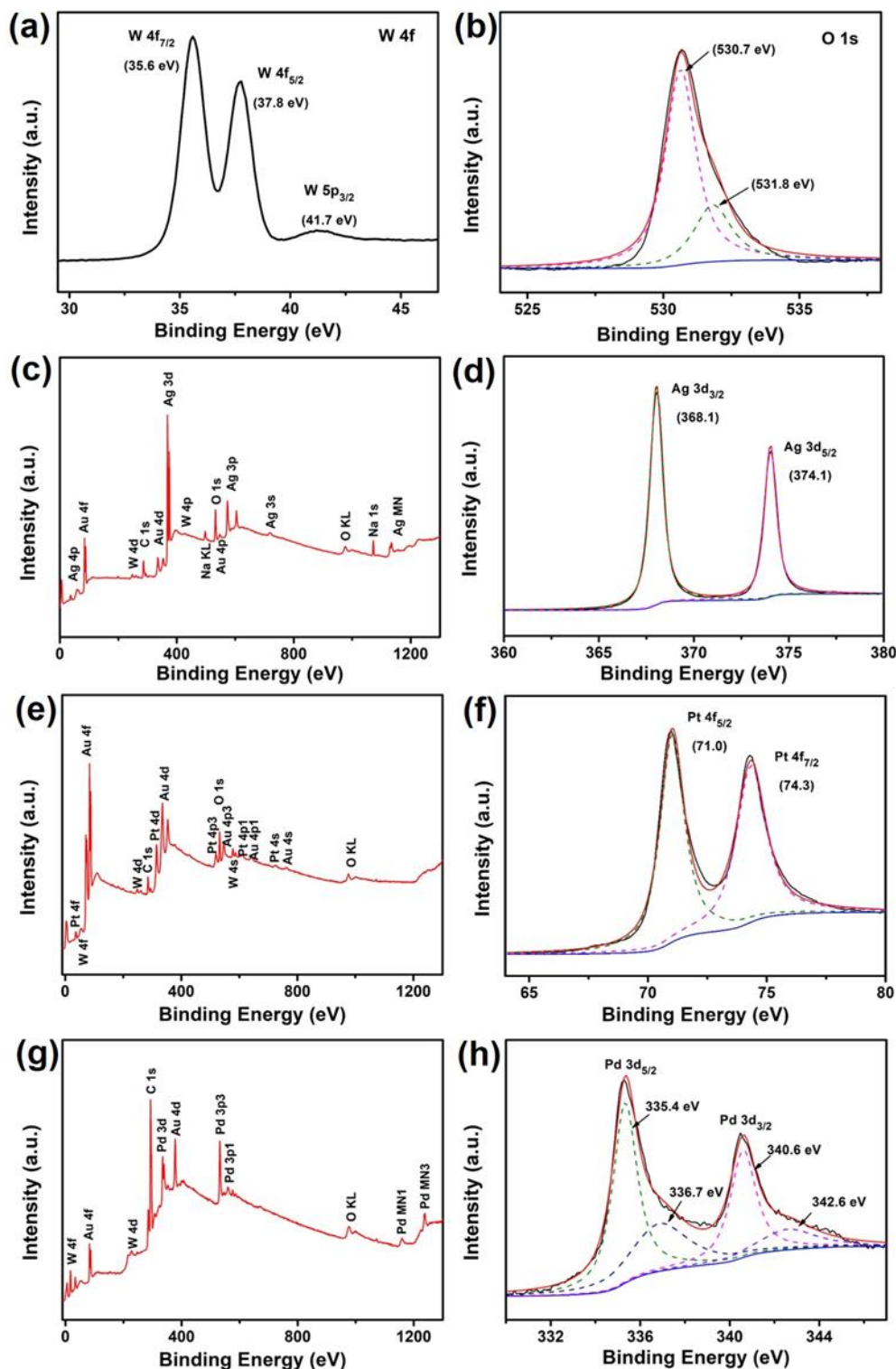


Figure 4.3. XPS spectra of 2D WO<sub>3</sub> nanofilms (a, b) and the NM<sub>200</sub>-WO<sub>3</sub> nanofilms ((c, d) for Ag<sub>200</sub>-WO<sub>3</sub>, (e, f) for Pt<sub>200</sub>-WO<sub>3</sub>, (g, h) for Pd<sub>200</sub>-WO<sub>3</sub>.

Peaks located at 374.1 eV and 368.1 eV belong to Ag 3d<sub>3/2</sub> and Ag 3d<sub>5/2</sub>, respectively, and

the splitting distance of the doublet is 6.0 eV, which could be assigned to the metallic Ag [29]. Peaks representing Pt 4f<sub>5/2</sub> and Pt 4f<sub>7/2</sub> are near 74.3 eV and 71.0 eV, which correlate to those peaks reported for metallic Pt [30]. For 2D Pd<sub>200</sub>-WO<sub>3</sub> nanofilms, two peaks at 340.6 eV and 335.4 eV corresponding respectively to 3d<sub>3/2</sub> and 3d<sub>5/2</sub> of the metallic Pd were clearly detected. In addition, two weak peaks at 342.6 eV and 336.7 eV assigned to 3d<sub>3/2</sub> and 3d<sub>5/2</sub> of Pd<sup>2+</sup> appeared in the XPS spectrum [31]. Since the peak intensities of Pd<sup>2+</sup> are significantly weaker than those of the metallic Pd, indicating that the metallic Pd is the dominant species. These results indicate that the electrochemical reduction has decreased the ionic metals into the metallic states. In other words, different NM nanoparticles have been successfully deposited onto the surface of 2D WO<sub>3</sub> nanofilms.

#### 4.4.2. Electrochemical characterization of 2D NM<sub>200</sub>-WO<sub>3</sub> nanofilms

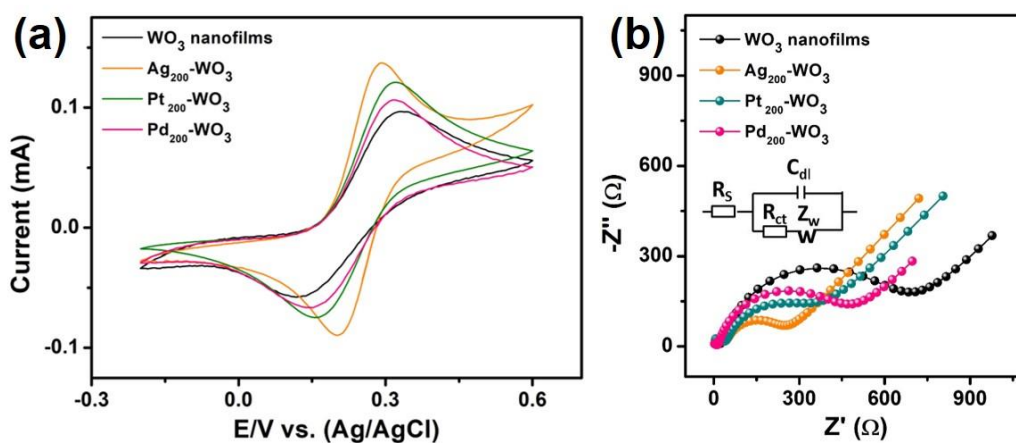


Figure 4.4. (a) CV curves of 2D WO<sub>3</sub> and NM<sub>200</sub>-modified WO<sub>3</sub> nanofilms in 0.1 M KCl containing 5 mM K<sub>4</sub>Fe(CN)<sub>6</sub> at a scan rate of 10 mV/s. (b) Nyquist plots of 2D WO<sub>3</sub> and NM<sub>200</sub>-modified WO<sub>3</sub> nanofilms in 0.1 M KCl containing 5 mM K<sub>4</sub>Fe(CN)<sub>6</sub> from 100 kHz to 0.1 Hz at an AC amplitude of 5 mV under open-circuit potential condition.

CV and EIS were used to characterize the interfacial electrochemical properties of all functionalized 2D WO<sub>3</sub> electrodes in 0.1 M KCl solutions containing 5 mM ferrocene carboxylic acid. As presented in Figure 4.4(a), the reversible redox peaks of 2D WO<sub>3</sub> nanofilms were relatively broad with the peak potential separation ( $\Delta E_p$ ) of about 216 mV. In contrast, the peak potential separation of 2D NM<sub>200</sub>-WO<sub>3</sub> nanofilms decreased significantly with 110 mV, 150 mV, and 170 mV for Ag<sub>200</sub>-WO<sub>3</sub>, Pt<sub>200</sub>-WO<sub>3</sub>, and

Pd<sub>200</sub>-WO<sub>3</sub> nanofilms, respectively. The redox peak currents also increased, and the order is coinciding with the sequence. These results suggested that the structure of NM nanoparticles provides a more conductive interlayer for the electrons transfer. In addition, the Ag<sub>200</sub>-WO<sub>3</sub> nanofilms possess the lowest  $\Delta E_p$  value, indicating that electrons transfer is more facilitated at the surface of Ag<sub>200</sub>-WO<sub>3</sub> nanofilms.

Figure 4.4(b) expresses the Nyquist plots of each NM<sub>200</sub>-WO<sub>3</sub> nanofilms along with the corresponding Randles equivalent circuit model as the insert. Nyquist plots include a semicircle portion at high frequency, corresponding to the electron-transfer process and a linear portion at the low frequency, corresponding to the diffusion process. Based on the equivalent electric circuit, the charge transfer resistance ( $R_{ct}$ ) of the [Fe(CN)<sub>6</sub>]<sup>3-/4-</sup> redox couple at the 2D WO<sub>3</sub> nanofilms substrate was 510  $\Omega$ . It decreased down to 183, 289, and 418  $\Omega$  for Ag<sub>200</sub>-WO<sub>3</sub>, Pt<sub>200</sub>-WO<sub>3</sub>, and Pd<sub>200</sub>-WO<sub>3</sub>, respectively, indicating improved electron transfer rate between the redox probe and the electrode surface. The decrease of the charge transfer resistances at the 2D NM<sub>200</sub>-WO<sub>3</sub> nanofilms substrates, especially at Ag<sub>200</sub>-WO<sub>3</sub> nanofilms substrate, illustrated the enhancement of charge transfer, which is in good agreement with obtained CVs results. 2D Ag-WO<sub>3</sub> nanofilms exhibited the smallest electron transfer resistance ( $R_{ct}$ ) in Figure 4.4(b), due to uniformly distributed, relatively smaller size and the larger amount of Ag nanoparticles on the surface of 2D WO<sub>3</sub> nanofilms compared to Pt and Pd nanoparticles electrodeposited deposited at the same time. Moreover, these results have also confirmed the fact that these NM nanoparticles have been successfully modified on the surface of 2D WO<sub>3</sub> nanofilms.

#### 4.4.3 Electrochemical performance of 2D NM<sub>200</sub>-WO<sub>3</sub> nanofilms towards H<sub>2</sub>O<sub>2</sub>

In order to evaluate the electrocatalytic performance of NM-WO<sub>3</sub> nanofilms, CV was carried out in 0.1 M PBS (pH=7.0) at the scan rate of 10 mV/s, and the active electrocatalytic behavior of Ag<sub>200</sub>-WO<sub>3</sub>, Pt<sub>200</sub>-WO<sub>3</sub> and Pd<sub>200</sub>-WO<sub>3</sub> nanofilms for the reduction of 5 mM H<sub>2</sub>O<sub>2</sub> is illustrated in Figure 4.5. It can be seen from Figure 4. 5(a), there were no peaks in the potential range from -0.6 to +0.3 V for the bare Au/Cr electrode and 2D WO<sub>3</sub> nanofilms. However, compared with the bare Au/Cr electrode, the CV current of 2D WO<sub>3</sub> nanofilms slightly increased due to the larger surface area of 2D WO<sub>3</sub> nanofilms. After the electrodeposition of Ag nanoparticles,

current peak values of  $-180.4 \mu\text{A}$  at  $-0.398 \text{ V}$  and  $-499.8 \mu\text{A}$  at  $-0.419 \text{ V}$  were recorded for the Ag<sub>200</sub>-Au electrode and Ag<sub>200</sub>-WO<sub>3</sub> nanofilms, respectively. Figure 4.5(c, e) shows that similar results were also observed for Pt<sub>200</sub>-WO<sub>3</sub> nanofilms and Pd<sub>200</sub>-WO<sub>3</sub> nanofilms within the potential range from  $-0.2$  to  $+0.6 \text{ V}$  with the current peak values of  $-418.2 \mu\text{A}$  at  $-0.046 \text{ V}$  and  $-333.1 \mu\text{A}$  at  $0.006 \text{ V}$ , respectively.

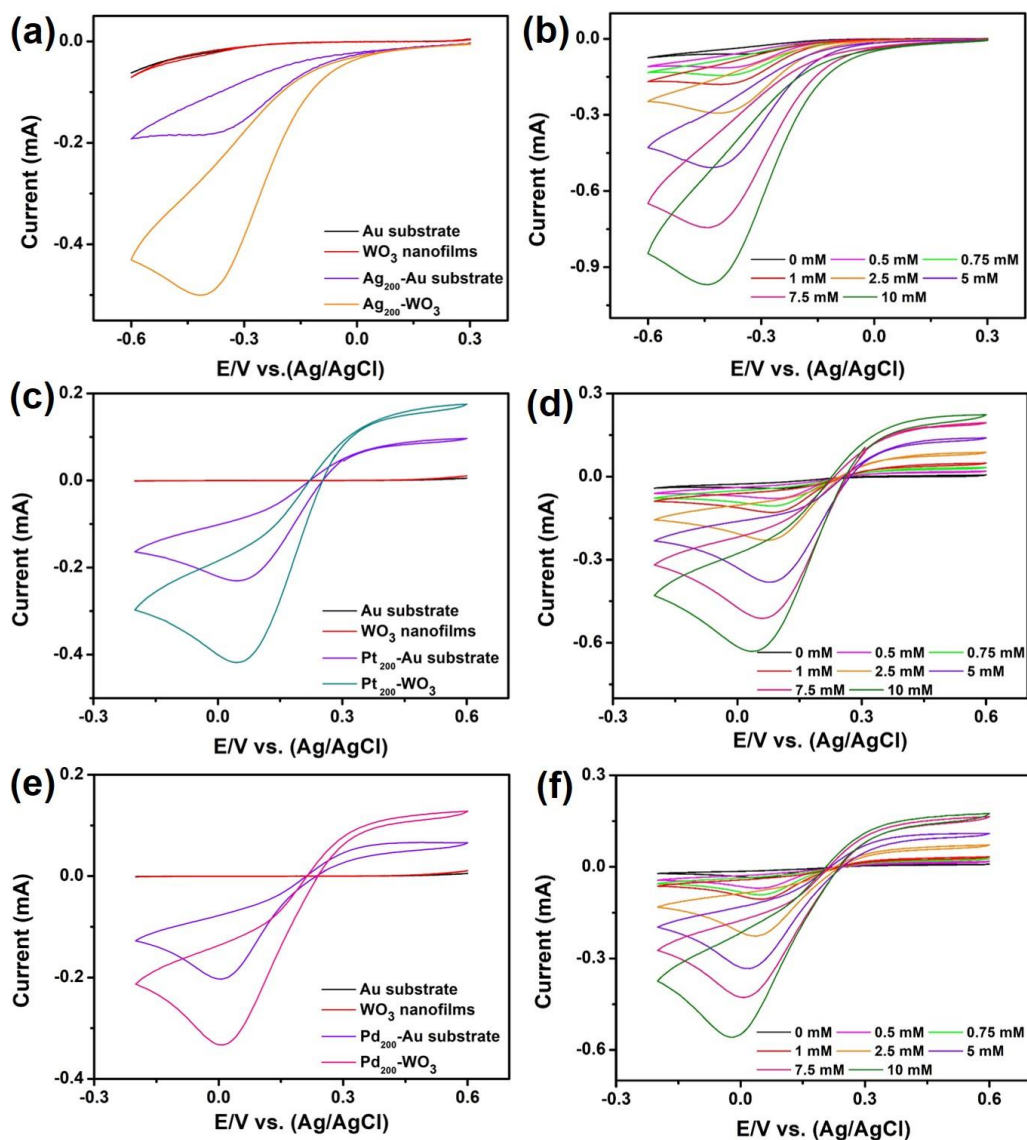


Figure 4.5. CV curves of Au/Cr bare electrode, 2D WO<sub>3</sub> nanofilms, NM<sub>200</sub>-Au electrodes, and NM<sub>200</sub>-WO<sub>3</sub> nanofilms ((a) Ag; (c) Pt; (e) Pd) at the presence of 5 mM H<sub>2</sub>O<sub>2</sub> in 0.1 M PBS (pH=7.0) at a scan rate of 10 mV/s. CV curves of NM<sub>200</sub>-WO<sub>3</sub> nanofilms ((b) Ag; (d) Pt; (f) Pd) with the different concentration of H<sub>2</sub>O<sub>2</sub> in 0.1 M PBS (pH=7.0) at a scan rate of 10 mV/s.

Furthermore, CV was also performed for 2D NM<sub>200</sub>-WO<sub>3</sub> nanofilms in 0.1 M PBS without H<sub>2</sub>O<sub>2</sub> in order to obtain the reduction peak current. The reduction peak currents in 5 mM H<sub>2</sub>O<sub>2</sub> were calculated by subtracting the background current from the peak current without H<sub>2</sub>O<sub>2</sub>, and the reduction peak current for Ag<sub>200</sub>-WO<sub>3</sub> nanofilms is 458.6  $\mu$ A, which is higher than that of reduction current for both Pt<sub>200</sub>-WO<sub>3</sub> nanofilms (385.7  $\mu$ A) and Pd<sub>200</sub>-WO<sub>3</sub> nanofilms (302.3  $\mu$ A). Therefore, Ag<sub>200</sub>-WO<sub>3</sub> nanofilms exhibited excellent electrocatalytic performance and the lowest potential for H<sub>2</sub>O<sub>2</sub> reduction. Furthermore, the electrocatalytic activity measurements of 2D NM<sub>200</sub>-WO<sub>3</sub> nanofilms to the different H<sub>2</sub>O<sub>2</sub> concentrations ranging from 0.5 mM to 10 mM were conducted, and the experimental results (Figure 4.5(b, d, f)) displayed that the reduction peak current increased with the rising of H<sub>2</sub>O<sub>2</sub> concentration, proving that the 2D NM<sub>200</sub>-WO<sub>3</sub> nanofilms could effectively determine different H<sub>2</sub>O<sub>2</sub> concentrations.

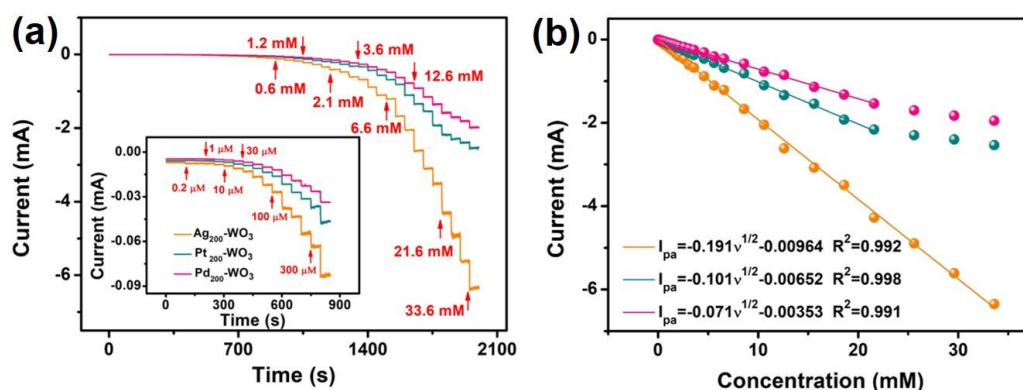


Figure 4.6. (a) Chronoamperometric current response of 2D NM<sub>200</sub>-WO<sub>3</sub> nanofilms (Ag, Pt, and Pd) to the different H<sub>2</sub>O<sub>2</sub> concentrations ranging from 0.2  $\mu$ M to 33.6 mM in 0.1 M PBS (pH=7.0). Inset: chronoamperometric current response to the lower concentrations range of 0.2  $\mu$ M to 400  $\mu$ M. (b) Corresponding linear plot of the current versus H<sub>2</sub>O<sub>2</sub> concentration.

Figure 4.6(a) displays the amperometric measurements for NM<sub>200</sub>-WO<sub>3</sub> nanofilms upon successive addition of the different H<sub>2</sub>O<sub>2</sub> concentrations from 0.2  $\mu$ M to 33.6 mM into the stirring PBS solution at the peak potential of -0.419, -0.046 and 0.006 V, respectively. The inset image represents the amperometric current responses at the lower concentrations range of 0.2 to 400  $\mu$ M. NM<sub>200</sub>-WO<sub>3</sub> nanofilms displayed rapid and sensitive response to the addition of H<sub>2</sub>O<sub>2</sub>, and the response could achieve 95 % of the steady-state value within 2 s. Among all functionalized NM<sub>200</sub>-WO<sub>3</sub> nanofilms, the Ag<sub>200</sub>-WO<sub>3</sub> nanofilms exhibited the highest current

response at all H<sub>2</sub>O<sub>2</sub> concentrations, implying that Ag<sub>200</sub>-WO<sub>3</sub> nanofilms possessed the efficient electrocatalytic ability towards H<sub>2</sub>O<sub>2</sub>.

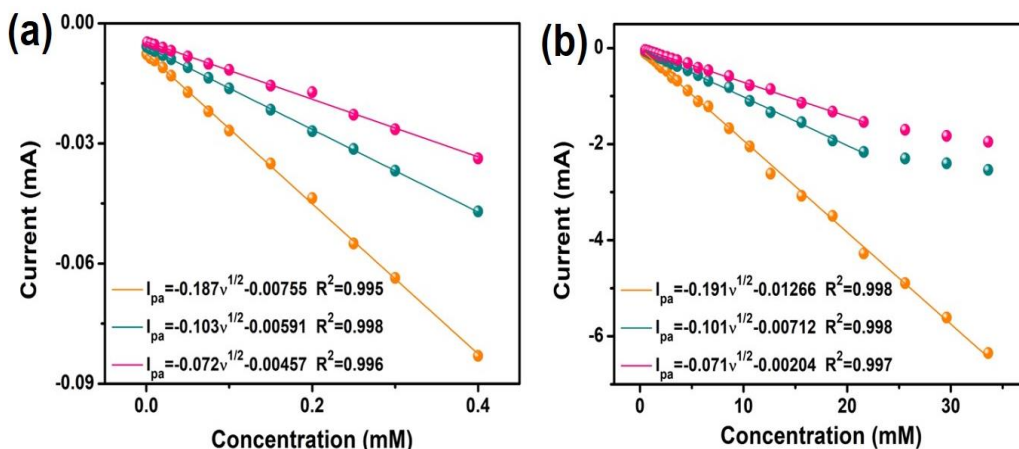


Figure 4.7. Corresponding linear plot of the current versus H<sub>2</sub>O<sub>2</sub> concentration of (a) 0.2 μM to 200 μM and (b) 250 μM to 33.6 mM.

The corresponding calibration curves for NM<sub>200</sub>-WO<sub>3</sub> nanofilms are shown in Figure 4.6(b). Ag<sub>200</sub>-WO<sub>3</sub> nanofilms demonstrated a wide linear detection range from 0.2 μM to 33.6 mM, which is wider than that of Pt<sub>200</sub>-WO<sub>3</sub> nanofilms (0.2 μM to 21.6 mM) and Pd<sub>200</sub>-WO<sub>3</sub> nanofilms (1 μM to 21.6 mM), respectively. Similar calibration curves for the different concentration ranges are illustrated in Figure 4.7. The slopes of different parts are very close, proving the excellent linearity of NM<sub>200</sub>-WO<sub>3</sub> nanofilms. The linear equation of Ag<sub>200</sub>-WO<sub>3</sub> nanofilms can be written as  $I_{pa} = -0.191c - 0.00964$  with the correlation coefficient  $R^2 = 0.9991$ . Thus, the sensitivity for Ag<sub>200</sub>-WO<sub>3</sub> nanofilms is 282 μA mM<sup>-1</sup> cm<sup>-2</sup> with a low detection limit of 0.1 μM at the signal to noise ratio of 3. Meanwhile, the sensitivity for Pt<sub>200</sub>-WO<sub>3</sub> nanofilms and Pd<sub>200</sub>-WO<sub>3</sub> nanofilms was calculated to be 202 μA mM<sup>-1</sup> cm<sup>-2</sup> and 142 μA mM<sup>-1</sup> cm<sup>-2</sup>, respectively. It is evident from the results obtained that the Ag<sub>200</sub>-WO<sub>3</sub> nanofilms exhibited the highest sensitivity, lowest detection limit, and the largest linear range among the functionalized 2D WO<sub>3</sub> nanofilms. In order to compare the performance of functionalized Ag<sub>200</sub>-WO<sub>3</sub> nanofilms, our main results were compared with the previously reported Ag-based H<sub>2</sub>O<sub>2</sub> electrochemical devices in Table 4.1. From the data presented in Table 4.1, a wide linear detection range with a low detection limit of Ag<sub>200</sub>-WO<sub>3</sub> nanofilms for the H<sub>2</sub>O<sub>2</sub> detection could be observed compared with other Ag-based H<sub>2</sub>O<sub>2</sub> devices, which makes Ag<sub>200</sub>-WO<sub>3</sub> nanofilms great potential candidate for the practical H<sub>2</sub>O<sub>2</sub> determination. Moreover, the functionalized

H<sub>2</sub>O<sub>2</sub> device also possesses a relatively high sensitivity because of the hybrid nanocomposite structure. Therefore, Ag<sub>200</sub>-functionalized 2D WO<sub>3</sub> nanofilms have clearly demonstrated the most distinguishable electrochemical characteristics for the H<sub>2</sub>O<sub>2</sub> determination among the other devices listed in Table 4.1.

Table 4.1. Comparison of Ag<sub>200</sub>-WO<sub>3</sub> nanofilms with various Ag-based electrochemical H<sub>2</sub>O<sub>2</sub> devices.

Electrode material	Potential work (V)	Sensitivity ( $\mu\text{A mM}^{-1} \text{cm}^{-2}$ )	Linear range ( $\mu\text{M}$ )	LOD ( $\mu\text{M}$ )	Refs
Ag <sub>200</sub> -WO <sub>3</sub> nanofilms	-0.4 (vs Ag/AgCl)	282	0.2 -33600	0.1	this work
AgNPs-CNT-rGO	-0.3 (vs Ag/AgCl)	/	10-10000	1	[32]
AgNPs/N-G	-0.3 (vs Ag/AgCl)	44.6	100-126400	1.2	[33]
AgNPs-MWCNT-rGO/GCE	-0.35 (vs Ag/AgCl)	53.5	100-100000	0.9	[34]
Ag/FeOOH/Au	-0.2 (vs SCE)	8.07	30-15000	22.8	[35]
Ag-Fe <sub>2</sub> O <sub>3</sub> -RGO	-0.2 (vs. SCE)	50.8	1.6-57000	0.5	[36]
TiO <sub>2</sub> NTs/r-GO/AgNPs	-0.6 (vs SCE)	1151.98	50-15500	2.2	[37]
Nafion/Gr-CCS-AgNPs/GCE	-0.2 (vs SCE)	14.9	20-5020	2.49	[38]
		17.6	5020-34100	9.51	
Gel/AgNPs-FHLC	-0.4 (vs SCE)	16.7	200-12300	0.6	[39]
GC/rGO-Nf@Ag <sub>6</sub>	-0.65 (vs SCE)	450.8	1-10	0.535	[40]
Ag@SiO <sub>2</sub> @Ag/GCE	-0.2 (vs SCE)	56.07	5-24000	1.7	[41]
AgNPs-Zn-MOF	-0.8 (vs Ag/AgCl)	/	1-5000	0.067	[42]
Ag/boehmite nanotubes/rGO/GCE	-0.2 (vs SCE)	80.14	0.5-10000	0.17	[43]

#### 4.4.4. Effect of the amount of Ag nanoparticles on H<sub>2</sub>O<sub>2</sub> detection

The diameter, amount as well as the distribution of the NM nanoparticles on the surface of 2D WO<sub>3</sub> nanofilms have a significant influence on the electrochemical capabilities of the device based on these functionalized nanomaterials. Therefore, it is necessary to investigate what the role the different amounts of Ag nanoparticles play on the electrochemical performance and to find the optimal electrodeposition conditions for Ag nanoparticles. Figure 4.8(a) shows the CVs to 5 mM H<sub>2</sub>O<sub>2</sub> for all Ag<sub>t</sub>-WO<sub>3</sub> nanofilms functionalized with the different

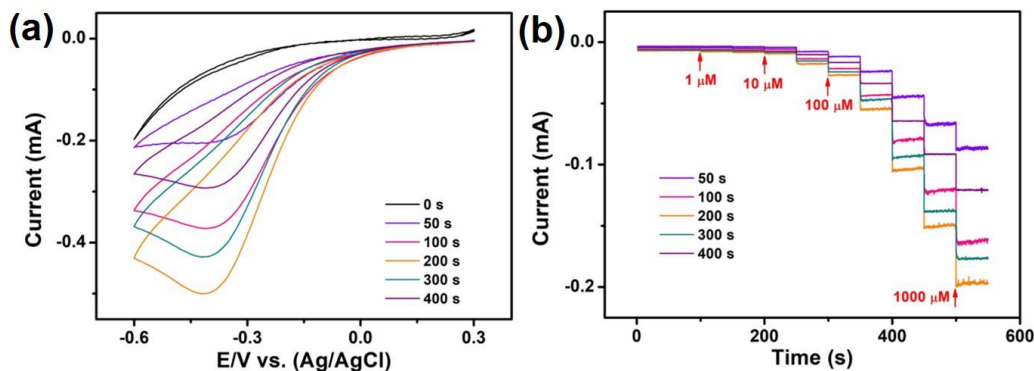


Figure 4.8. (a) CV curves of AgI-WO<sub>3</sub> nanofilms ( $t = 0, 50, 100, 200, 300$  and  $400$  s) at the presence of  $5 \text{ mM}$  H<sub>2</sub>O<sub>2</sub> in  $0.1 \text{ M}$  PBS ( $\text{pH}=7.0$ ) at a scan rate of  $10 \text{ mV/s}$ . (b) Amperometric responses of AgI-WO<sub>3</sub> nanofilms ( $t = 0, 50, 100, 200, 300$  and  $400$  s) with different electrodeposition for successive addition of H<sub>2</sub>O<sub>2</sub> ( $1\text{--}1000 \text{ }\mu\text{M}$ ) in  $0.1 \text{ M}$  PBS ( $\text{pH}=7.0$ ) at the potential of  $0.4 \text{ V}$ .

electrodeposition time ( $50, 100, 200, 300$ , and  $400 \text{ s}$ , respectively). The current value increased with the rising of the electrodeposition time and reached its maximum at  $200 \text{ s}$ . Then as the electrodeposition time continues growing, the response current value is gradually decreased. Similar results were obtained for the amperometric testing with the successive addition of the

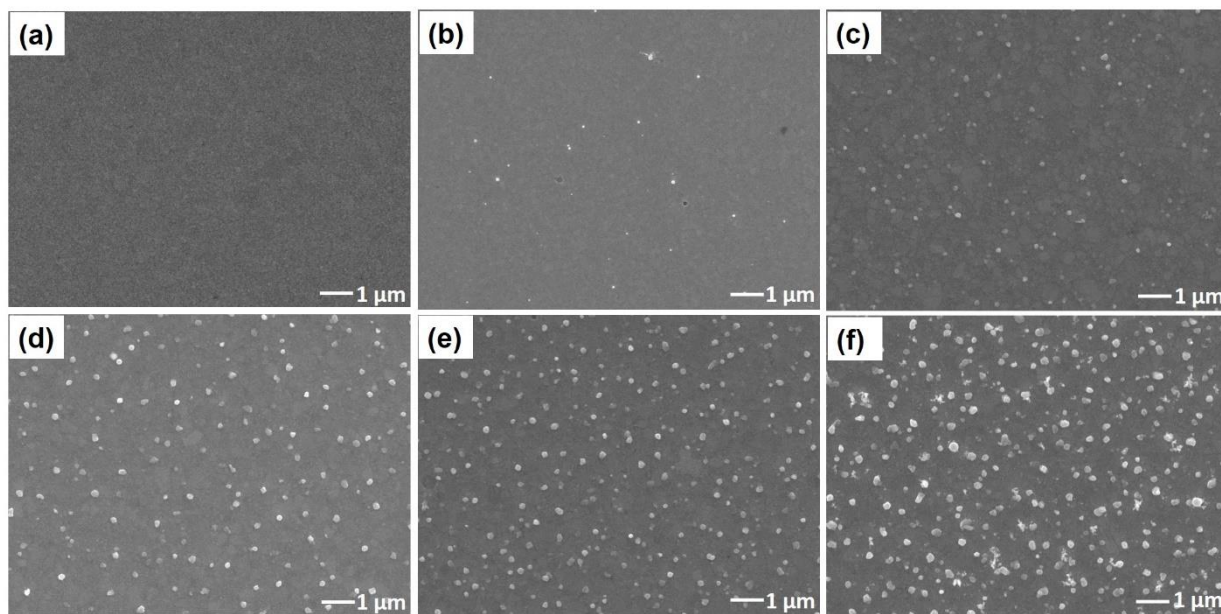


Figure 4.9. SEM images of AgI-WO<sub>3</sub> nanofilms at different electrodeposition time; (a)  $0 \text{ s}$ , (b)  $50 \text{ s}$ , (c)  $100 \text{ s}$ , (d)  $200 \text{ s}$ , (e)  $300 \text{ s}$ , (f)  $400 \text{ s}$ .

different H<sub>2</sub>O<sub>2</sub> concentrations (Figure 4.8(b)). It can be explained that with the increase of the electrodeposition time, more Ag nanoparticles will be loaded on the surface of 2D WO<sub>3</sub> nanofilms, whereas the Ag nanoparticles' electroactive area of the electrode is increased, and

consequently, the electrochemical behavior is also enhanced. However, a longer electrodeposition time will coherently lead to the slight increase of the size of Ag nanoparticles and the aggregation of Ag nanoparticles on the 2D WO<sub>3</sub> surface, especially at 400 s (Figure 4.9), which can result in the counteractive effect on the electrocatalytic performance. Therefore, the best electrochemical performance was achieved on Ag<sub>200</sub>-WO<sub>3</sub> nanofilms.

#### 4.4.5. Scan rate dependence investigation

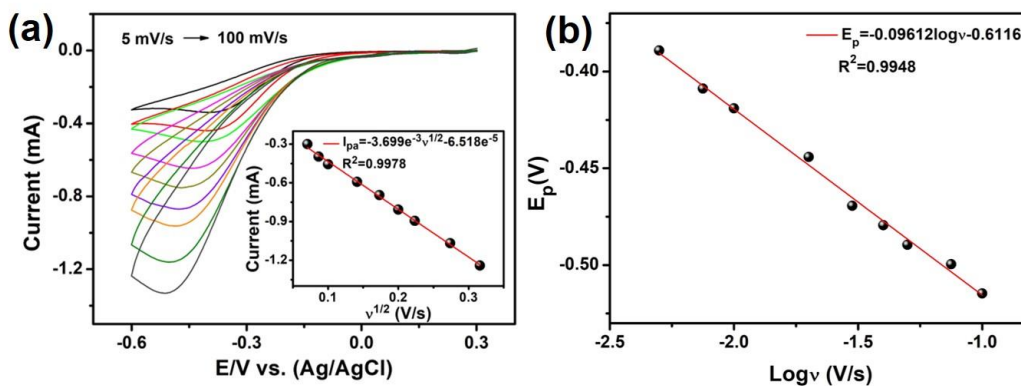


Figure 4.10. (a) CV curves of Ag<sub>200</sub>-WO<sub>3</sub> nanofilms at the presence of 5 mM H<sub>2</sub>O<sub>2</sub> in 0.1 M PBS (pH=7.0) at the different scan rates. Inset: Plot peak currents versus square of the scan rates. (b) The plot of oxidation peak potentials vs. logarithm of the scan rates.

To assess the kinetic of the H<sub>2</sub>O<sub>2</sub> determination by functionalized Ag<sub>200</sub>-WO<sub>3</sub> nanofilms, CV responses of Ag<sub>200</sub>-WO<sub>3</sub> nanofilms in 5 mM H<sub>2</sub>O<sub>2</sub> solution were measured at the different scan rates from 5 mV/s to 100 mV/s, as demonstrated in Figure 4.10(a). It can be observed that the current reduction values increased with the increasing scan rate, and a linear relationship between the cathodic peak current values and square of the scan rates was obtained in the inset of Figure 4.10(a), demonstrating the diffusion-controlled electrochemical process. It should also be noted that the inset of Figure 4.10(a) is adequately plotted by subtracting background at the different scan rates. In addition, as peak current was increased with the increasing of scan rate, the peak potential value shifted towards the more negative direction with the corresponding linear regression equation of  $E_p = -0.09612\log v - 0.6116$ , as shown in Figure 4.10(b), proving the irreversible electrochemical process.  $E_p$  can be expressed by the Tafel equation of  $E_p = [2.303RT/2(1 - \alpha)n_{\alpha}F]\log v + K$  for an irreversible diffusion-controlled electrochemical

process [44], the transfer coefficient of  $\alpha=0.69$  was obtained, demonstrating one-electron transfer in the rate-determining step.

#### 4.4.6. The selectivity and long-time stability study

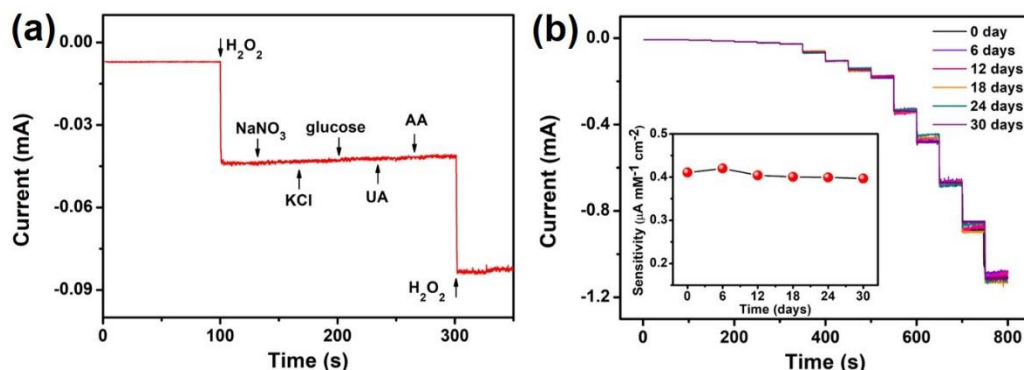


Figure 4.11. (a) Interference study for Ag<sub>200</sub>-WO<sub>3</sub> nanofilms at the presence of 100 μM H<sub>2</sub>O<sub>2</sub> and 1 mM interfering chemicals (NaNO<sub>3</sub>, KCl, glucose, ascorbic acid, and uric acid) in 0.1 M PBS (pH=7.0). (b) The chronoamperometric current of Ag<sub>200</sub>-WO<sub>3</sub> nanofilms at the different H<sub>2</sub>O<sub>2</sub> concentrations and their corresponding sensitivity (inset) obtained every six days of the test period.

The anti-interference ability is an essential and essential parameter for evaluation of the performance of functionalized Ag<sub>200</sub>-WO<sub>3</sub> nanofilms towards practical applications. Hence, the influence of some common chemicals such as NaNO<sub>3</sub>, KCl, glucose, ascorbic acid, and uric acid was investigated on the H<sub>2</sub>O<sub>2</sub> determination. The amperometric response of Ag<sub>200</sub>-WO<sub>3</sub> nanofilms to the successive addition of such chemicals was carried out at -0.4 V in 0.1 M PBS solution, and the results are summarized in Figure 4.11(a). There was no significant fluctuation observed, indicating that functionalized Ag<sub>200</sub>-WO<sub>3</sub> nanofilms have the high selectivity towards unipolar H<sub>2</sub>O<sub>2</sub> detection. The high selectivity could be attributed to the relatively low potential applied for the H<sub>2</sub>O<sub>2</sub> detection that minimized the response of interfering chemicals. In addition, long-term stability is also a vital requirement for the performance evaluation of electrochemical devices. Thus, the amperometric current responses of functionalized Ag<sub>200</sub>-WO<sub>3</sub> nanofilms to the different H<sub>2</sub>O<sub>2</sub> concentrations ranged from 10 μM to 6.6 mM were successfully detected every 6 days during the test period of 30 days and the obtained results are presented in Figure 4.11(b). It is evident from the presented results that the relative standard deviation of the sensitivity was only ~7.8 % indicating the excellent long-term stability of functionalized Ag<sub>200</sub>-WO<sub>3</sub> nanofilms.

## 4.5 Conclusions

NM-functionalized 2D WO<sub>3</sub> nanofilms have been developed by a combination of ALD and electrochemical deposition methods with the subsequent investigation of their electrochemical capabilities towards the electrochemical H<sub>2</sub>O<sub>2</sub> reduction. It was found that NM nanoparticles were uniformly deposited on the surface of 2D WO<sub>3</sub> nanofilms, which represented the electrochemically active metal-semiconductor hybrid nanocomposites. They provided larger electroactive area, and consequently, substantially improved the electrochemical performance of the device based on functionalized 2D WO<sub>3</sub> nanofilms for the sensitive and selective H<sub>2</sub>O<sub>2</sub> detection within the wide measuring concentrations range. It was also found that functionalization by Ag nanoparticles is much more effective compared to the same functionalization by Pt and Pd nanoparticles. Consequently, the optimization of the electro-deposition time for the Ag-functionalized 2D WO<sub>3</sub> nanofilms revealed that the deposition time of 200 s resulted in the best electrochemical performance of 2D WO<sub>3</sub> electrode. It should be stressed that among those NM<sub>t</sub>-WO<sub>3</sub> nanofilms, functionalized Ag<sub>200</sub>-WO<sub>3</sub> nanofilms exhibited the superior sensing capabilities towards the H<sub>2</sub>O<sub>2</sub> detection with high sensitivity of 282  $\mu\text{A mM}^{-1} \text{cm}^{-2}$ , extremely wide linear range from 0.2  $\mu\text{M}$  to 33.6 mM and a lower detection limit of 0.1  $\mu\text{M}$ . The work provides an alternative route for improvement of the ALD-developed 2D nanofilms. Surface functionalization of the 2D semiconductor oxides by NM nanoparticles can be applied as a very effective way of enhancement of the electro-catalytic performance for various electrochemical devices.

## References

1. E. Nguyen, B. Carey, J. van Embden, A. F. Chrimes, M. J. S. Spencer, S. Zhuiykov, K. Kalantar-zadeh, T. Daeneke, Electronic tuning of 2D MoS<sub>2</sub> through surface functionalization, *Adv. Mater.* 27 (2015) 6225-6229.
2. Y. Yin, A.P. Alivisatos, Colloidal nanocrystal synthesis and the organic-inorganic interface, *Nature* 437 (2004) 664.
3. S. Wang, L. Yi, J. E. Halpert, X. Lai, Y. Liu, H. Cao, R. Yu, D. Wang, Y. Li, A novel and highly efficient photocatalyst based on P25-graphdiyne nanocomposite, *Small* 8 (2012) 265-271.

4. H. Gu, Y. Yang, J. Tian, G. Shi, Photochemical synthesis of noble metal (Ag, Pd, Au, Pt) on graphene/ZnO multihybrid nanoarchitectures as electrocatalysis for H<sub>2</sub>O<sub>2</sub> reduction, *ACS Appl. Mater. Inter.* 5 (2013) 6762-6768.
5. Z. Tang, X. Deng, Y. Zhang, X. Guo, J. Yang, C. Zhu, J. Fan, Y. Shi, B. Qing, F. Fan, MoO<sub>3</sub> nanoflakes coupled reduced graphene oxide with enhanced ethanol sensing performance and mechanism, *Sens. Actuators B Chem.* 297 (2019) 126730.
6. J. Shi, Z. Cheng, L. Gao, Y. Zhang, J. Xu, H. Zhao, Facile synthesis of reduced graphene oxide/hexagonal WO<sub>3</sub> nanosheets composites with enhanced H<sub>2</sub>S sensing properties, *Sens. Actuators B Chem.* 230 (2016) 736-745.
7. S. Bhattacharya, D. Dinda, S. K. Saha, Role of trap states on storage capacity in a graphene/MoO<sub>3</sub> 2D electrode material, *J. Phys. D Appl. Phys.* 48 (2015) 145303.
8. Z. Liu, N. Li, H. Zhao, Y. Du, Colloidally synthesized MoSe<sub>2</sub>/graphene hybrid nanostructures as efficient electrocatalysts for hydrogen evolution, *J. Mater. Chem. A* 3 (2015) 19706-19710.
9. G. Huang, T. Chen, W. Chen, Z. Wang, K. Chang, L. Ma, F. Huang, D. Chen, J. Lee, Graphene-Like MoS<sub>2</sub>/Graphene Composites: Cationic Surfactant-Assisted Hydrothermal Synthesis and Electrochemical Reversible Storage of Lithium, *Small* 9 (2013) 3693-3703.
10. B. D. Malhotra, A. Chaudhary, S. P. Singh, Prospects of conducting polymers in biosensors, *Anal. Chim. Acta* 578 (2006) 59-74.
11. M. H. Naveen, N. G. Gurudatt, Y.-B. Shim, Applications of conducting polymer composites to electrochemical sensors: a review, *Appl. Mater. Today* 9 (2017) 419-433.
12. M. Haruta, Catalysis of gold nanoparticles deposited on metal oxides, *Cattech* 6 (2002) 102-115.
13. G. P. Wiederrecht, G. A. Wurtz, J. Hranisavljevic, Coherent coupling of molecular excitons to electronic polarizations of noble metal nanoparticles, *Nano Lett.* 4 (2004) 2121-2125.
14. S. Guo, E. Wang, Noble metal nanomaterials: controllable synthesis and application in fuel cells and analytical sensors, *Nano Today* 6 (2011) 240-264.
15. C. Tan, H. Zhang, Two-dimensional transition metal dichalcogenide nanosheet-based composites, *Chem. Soc. Rev.* 44 (2015) 2713-2731.
16. P. Herve, M. Perez-Lorenzo, L. M. Liz-Marzan, J. Dzubiella, Y. Lu, M. Ballauff, Catalysis by metallic nanoparticles in aqueous solution: model reactions, *Chem. Soc. Rev.* 41 (2012) 5577-5587.
17. S. Zhuikov, Carbon monoxide detection at low temperatures by semiconductor sensor with nanostructured Au-doped CoOOH films, *Sens. Actuators B Chem.* 129 (2008) 431-441.
18. L. Yuwen, F. Xu, B. Xue, Z. Luo, Q. Zhang, B. Bao, S. Su, L. Weng, W. Huang, L. Wang, General synthesis of noble metal (Au, Ag, Pd, Pt) nanocrystal modified MoS<sub>2</sub> nanosheets and the enhanced catalytic activity of Pd-MoS<sub>2</sub> for methanol oxidation, *Nanoscale* 6 (2014) 5762-5769.

19. S. Zhuiykov, Morphology of Pt-doped nanofabricated RuO<sub>2</sub> sensing electrodes and their properties in water quality monitoring sensors, *Sens, Actuators B Chem.* 136 (2009) 248-256.
20. M. C. R. González, A. G. Orive, R. C. Salvarezza, A. H. Creus, Electrodeposition of gold nanoparticles on aryl diazonium monolayer functionalized HOPG surfaces, *Phys. Chem. Chem. Phys.* 18 (2016) 1953-1960.
21. H. Ji, M. Li, Y. Wang, F. Gao, Electrodeposition of graphene-supported PdPt nanoparticles with enhanced electrocatalytic activity, *Electrochem. Commun.* 24 (2012) 17-20.
22. P. Zuo, L. Jiang, X. Li, B. Li, P. Ran, X. Li, L. Qu, Y. Lu, Metal (Ag, Pt)-MoS<sub>2</sub> Hybrids Greenly Prepared Through Photochemical Reduction of Femtosecond Laser Pulses for SERS and HER, *ACS Sustain. Chem. Eng.* 6 (2018) 7704-7714.
23. M. Q. Yang, Y. J. Xu, W. Lu, K. Zeng, H. Zhu, Q. H. Xu, G. W. Ho, Self-surface charge exfoliation and electrostatically coordinated 2D hetero-layered hybrids, *Nat. Commun.* 8 (2017) 14224.
24. Z. Fan, H. Zhang, Crystal phase-controlled synthesis, properties and applications of noble metal nanomaterials, *Chem. Soc. Rev.* 45 (2016) 63-82.
25. S. E. F. Kleijn, S. C.S. Lai, M. T. M. Koper, P. R. Unwin, Electrochemistry of nanoparticles, *Angew. Chem. Int. Edi.* 53 (2014) 3558-3586.
26. M. Vasilopoulou, L. C. Palilis, D. G. Georgiadou, A. M. Douvas, P. Argitis, S. Kennou, L. Sygellou, G. Papadimitropoulos, I. Kostis, N. A. Stathopoulos, D. Davazoglou, Reduction of Tungsten Oxide: A path towards dual functionality utilization for efficient anode and cathode interfacial layers in organic light-emitting diodes, *Adv. Funct. Mater.* 21 (2011) 1489-1497.
27. C. Wang, M. Long, B. Tan, L. Zheng, J. Cai, J. Fu, Facilitated photoinduced electron storage and two-electron reduction of oxygen by reduced graphene oxide in rGO/TiO<sub>2</sub>/WO<sub>3</sub> composites, *Electrochim. Acta* 250 (2017) 108-116.
28. S. Zhuiykov, E. Kats, B. Carey, S. Balendhran, Proton intercalated two-dimensional WO<sub>3</sub> with enhanced charge-carrier mobility at room temperature, *Nanoscale* 6 (2014) 15029-15036.
29. L. Ma, Y. Huang, M. Hou, Z. Xie, Z. Zhang, Ag nanorods coated with ultrathin TiO<sub>2</sub> shells as stable and recyclable SERS substrates, *Sci. Rep-UK* 5 (2015) 15442.
30. S. Pande, M. G. Weir, B. A. Zaccheo, R. M. Crooks, Synthesis, characterization, and electrocatalysis using Pt and Pd dendrimer-encapsulated nanoparticles prepared by galvanic exchange, *New J. Chem.* 35 (2011) 2054-2060.
31. H. Tao, X. Sun, S. Back, Z. Han, Q. Zhu, A. W. Robertson, T. Ma, Q. Fan, B. Han, Y. Jung, Z. Sun, Doping palladium with tellurium for the highly selective electrocatalytic reduction of aqueous CO<sub>2</sub> to CO, *Chem. Sci.* 9 (2018) 483-487.

32. Y. Zhang, Z. Wang, Y. Ji, S. Liu, T. Zhang, Synthesis of Ag nanoparticle-carbon nanotube-reduced graphene oxide hybrids for highly sensitive non-enzymatic hydrogen peroxide detection, *RSC Adv.* 5 (2015) 39037-39041.
33. Y. Tian, F. Wang, Y. Liu, F. Pang, X. Zhang, Green synthesis of silver nanoparticles on nitrogen-doped graphene for hydrogen peroxide detection, *Electrochim. Acta* 146 (2014) 646-653.
34. F. Lorestani, Z. Shahnava, P. Mn, Y. Alias, N. S. A. Manan, One-step hydrothermal green synthesis of silver nanoparticle-carbon nanotube reduced-graphene oxide composite and its application as hydrogen peroxide sensor, *Sens. Actuators B Chem.* 208 (2015) 389-398.
35. J. Zhang, J. Zheng, An enzyme-free hydrogen peroxide sensor based on Ag/FeOOH nanocomposites, *Anal. Methods* 7 (2015) 1788-1793.
36. N. Zhang, J. Zheng, Synthesis of Ag-Fe<sub>2</sub>O<sub>3</sub>-RGO nanocomposites for the electrocatalytic reduction of H<sub>2</sub>O<sub>2</sub>, *J. Mater. Sci. Mater. Electron.* 28 (2017) 11209-11216.
37. W. Wang, Y. Xie, C. Xia, H. Du, F. Tian, Titanium dioxide nanotube arrays modified with a nanocomposite of silver nanoparticles and reduced graphene oxide for electrochemical sensing, *Microchim. Acta* 181 (2014) 1325-1331.
38. H. Wang, H. Wang, T. Li, J. Ma, K. Li, X. Zuo, Silver nanoparticles selectively deposited on graphene-colloidal carbon sphere composites and their application for hydrogen peroxide sensing, *Sens. Actuators B Chem.* 239 (2017) 1205-1212.
39. Y. Guan, X. Sun, L. Yin, X. Hao, S. Guo, Y. Huang, AgNPs modified glass carbon electrode prepared with gelatin as an additive for hydrogen peroxide sensor, *Int. J. Electrochem. Sci.* 13 (2018) 7696-7705.
40. N. Yusoff, P. Rameshkumar, M. S. Mehmood, A. Pandikumar, H. W. Lee, N. M. Huang, Ternary nanohybrid of reduced graphene oxide-nafion@silver nanoparticles for boosting the sensor performance in non-enzymatic amperometric detection of hydrogen peroxide, *Biosens. Bioelectron.* 87 (2017) 1020-1028.
41. H. Hao, Q. Sheng, J. Zheng, One-step synthesis of Ag@SiO<sub>2</sub>@Ag nanomaterial and its application as hydrogen peroxide sensor, *Colloid. Surface. A* 518 (2017) 124-129.
42. P. Arul, S. A. John, Silver nanoparticles built-in zinc metal organic framework modified electrode for the selective non-enzymatic determination of H<sub>2</sub>O<sub>2</sub>, *Electrochim. Acta* 235 (2017) 680-689.
43. C. Zhao, H. Zhang, J. Zheng, A non-enzymatic electrochemical hydrogen peroxide sensor based on Ag decorated boehmite nanotubes/reduced graphene oxide nanocomposites, *J. Electroanal. Chem.* 784 (2017) 55-61.

44. C. Liu, H. Zhang, Y. Tang, S. Luo, Controllable growth of graphene/Cu composite and its nanoarchitecture-dependent electrocatalytic activity to hydrazine oxidation, *J. Mater. Chem. A* 2 (2014) 4580-4587.

# Chapter 5

## SUB-10 NM $\text{Ga}_2\text{O}_3$ - $\text{WO}_3$ HETEROSTRUCTURES DEVELOPED BY ALD FOR SENSITIVE AND SELECTIVE $\text{C}_2\text{H}_5\text{OH}$ DETECTION ON PPM LEVEL

---

### 5.1 Abstract

Wafer-scale ultra-thin  $\text{WO}_3$ ,  $\text{Ga}_2\text{O}_3$  nanofilms, and  $\text{Ga}_2\text{O}_3$ - $\text{WO}_3$  heterostructures with the thickness of approximately  $\sim 8.0$  nm were fabricated on the  $\text{SiO}_2/\text{Si}$  substrates by atomic layer deposition (ALD) technique for their subsequent usage as sensing materials for the ethanol detection. Structure and morphology of the developed ultra-thin samples were characterized by scanning electron microscopy (SEM), X-ray photoelectron spectroscopy (XPS), Raman spectroscopy, etc. Sensing properties of the developed ultra-thin nanostructures were investigated at the different temperatures and ethanol concentrations. The results showed that the  $\text{Ga}_2\text{O}_3$ - $\text{WO}_3$  heterostructures based gas sensor exhibited about 4 and a 10-fold improvement in response to ethanol compared to that of  $\text{WO}_3$  and  $\text{Ga}_2\text{O}_3$  nanofilms at  $275^\circ\text{C}$ . Furthermore, ethanol sensors based on  $\text{Ga}_2\text{O}_3$ - $\text{WO}_3$  heterostructures exhibited shorter response/recover time and excellent selectivity towards ethanol. The improvement of sensing capabilities of  $\text{Ga}_2\text{O}_3$ - $\text{WO}_3$  heterostructures provides a superb material fabrication method in the development of a high-performance gas sensor.

### 5.2 Introduction

2D materials with the atomic scale thickness magnify the surface to volume ratio, which provides excellent reactive adsorption sites for gaseous molecules, making them become outstanding candidates for gas sensors [1, 2]. Among these 2D materials, 2D TMOs have gained significant interest in the development of a different range of highly sensitive, selective, reliable, and low-cost sensors [3, 4]. Layer-structured TMOs, including  $\text{TiO}_2$ ,  $\text{MoO}_3$ , and  $\text{WO}_3$ , is the most studied for the application of chemical gas sensors, due to their stability at elevated temperature in the air [4]. For example, the gas response of two-dimensional  $\text{MoO}_3$  nanosheet to 100 ppm ethanol increases from 7 to 33 at the operating temperature of  $300^\circ\text{C}$ , compared with bulk  $\text{MoO}_3$  [5]. It was found that ultra-thin  $\text{WO}_3$  nanosheets exhibit an extraordinary response factor of  $\sim 30$

to ultralow 40 ppb  $\text{NO}_2$  at a relatively low operating temperature of  $150^\circ\text{C}$  [6]. Moreover, the previous investigation illustrated that the thickness of ultra-thin layered transition metal oxides plays an important role in determining the gas sensing performance, particularly when that thickness is on the order of the Debye length [6-8]. Besides, it was reported that ultra-thin layer-structured transition metal oxides are the best candidates in chemical sensors for volatile organic compounds (VOC) [9, 10], and the utilization of ultra-thin  $\text{WO}_3$  for the fabrication of VOC sensor has not yet been reported.

With the development of technology and industrialization, the application of VOC becomes more and more widespread, and they bring great convenience to our daily life. However, because of their high volatility and strong excitant, human health has been threatened by them gravely like dizziness, headaches, nausea, choking sensation in the chest, muzziness, and even death [11]. Among them, ethanol is one of the most extensively used in biochemical, health & safety, chemical, food, and transportation industries. Moreover, one of the main reasons for car accidents in the world is due to ethanol consumption. Thus, the demand for miniature, rapid, and accurate  $\text{C}_2\text{H}_5\text{OH}$  detection at *ppm* level is very high, indeed [12]. The commercial semiconductor based breath ethanol detector generally uses tin oxide materials. However, according to the gas sensing mechanism, pristine metal oxide semiconductors usually exhibits a comparable response to those gases with similar surface chemophysical properties [8]. Therefore, improving the selectivity for the practical application becomes essential.

Up to now, many efforts have been made to improve the selectivity of metal oxide semiconductors further to meet the practical application in the complex and harsh environment. It has been reported that defects play an important role in metal oxides based gas sensors [13], and element doping is an effective means to increase defect concentration since the doped ions not only cause lattice distortion but also generate different types of defects to ensure charge conservation [14]. Hence element doping is expected to improve the gas sensing performances of metal oxides significantly. Functionalization 2D transition metal oxides with noble metals are the other way to improve the gas sensing properties. Since noble metals, as the catalysts, can affect the contact region between 2D metal transition oxides and noble metals in two ways and hence affect the resistance of 2D metal transition oxides. One is Fermi energy control

(electronic sensitization) and the other is the spillover mechanism (chemical sensitization) [15, 16]. However, the development of heterojunctions has been proven the most simple and cheapest in achieving enhanced sensing performance in the gas sensor by organizing a heterojunction at the interface between the two materials with the creation of either an n/p-type nanostructure or an n/n-(p/p-) type structure [17-19]. Among the metal oxides, monoclinic  $\text{Ga}_2\text{O}_3$  ( $\beta$ - $\text{Ga}_2\text{O}_3$ ), as an energy bandgap of approximately 4.8 eV (direct) at room temperature, is one of the promising wide bandgap semiconductor materials for next-generation high-power electronics, an excellent candidate for solar-blind photodetection, a sensitive materials for detection of VOC, such as acetone, isopropyl alcohol, ethanol and ethyl acetate [20-22]. Its performance can even be improved by means of Schottky junctions, p-n junctions and heterojunctions. Many efforts have been made to find out the best suitable technologies of  $\text{Ga}_2\text{O}_3$  deposition at the nanoscale. As more tightly contacted interfaces can facilitate the improvement of the sensing performance, two-dimensional heteronanostructures in the planar form can satisfy this requirement better compared to zero and one-dimensional heteronanostructures [8]. ALD technology is distinguished for developing the planar structure of heteronanostructures, among other approaches such as *sol-gel*, CVD, and RF sputtering, due to the fabrication of large-scale conformal, dense nanofilms with precise thickness control [23-25]. To the best of our knowledge, such a planar form of  $\text{Ga}_2\text{O}_3$ - $\text{WO}_3$  heteronanostructures has not yet been synthesized for high-performance gas sensors.

In this work,  $\text{Ga}_2\text{O}_3$ - $\text{WO}_3$  heterostructures have been fabricated by ALD on the wafer-scale for the first time with the thickness of less than 10 nm using  $(^t\text{BuN})_2(\text{Me}_2\text{N})_2\text{W}$  and  $\text{Ga}(\text{TMHD})_3$  as  $\text{WO}_3$  and  $\text{Ga}_2\text{O}_3$  precursors, respectively. The thickness of  $\text{WO}_3$  and  $\text{Ga}_2\text{O}_3$  is 6.5 nm and 1.5 nm, respectively, which are less than Debye length for  $\text{WO}_3$  and  $\text{Ga}_2\text{O}_3$ , so the electrical conductivity of  $\text{Ga}_2\text{O}_3$ - $\text{WO}_3$  heterostructures should be modulated dramatically by oxygen vacancies, or ions sorbed oxygen species [7]. Their sensing performance towards sensitive and selective ethanol detection at *ppm* level was subsequently investigated. The developed sub-10 nm  $\text{Ga}_2\text{O}_3$ - $\text{WO}_3$  heteronanostructures utilized as sensing electrodes in miniature ethanol chemical sensors have demonstrated substantial enhancement of their main sensing characteristics compared to  $\text{WO}_3$  and  $\text{Ga}_2\text{O}_3$  counterparts, which provides a tremendous potential method for material fabrication in the development of high-performance gas sensor.

## 5.3 Experimental

### 5.3.1 Fabrication of $\text{Ga}_2\text{O}_3$ - $\text{WO}_3$ heterostructures

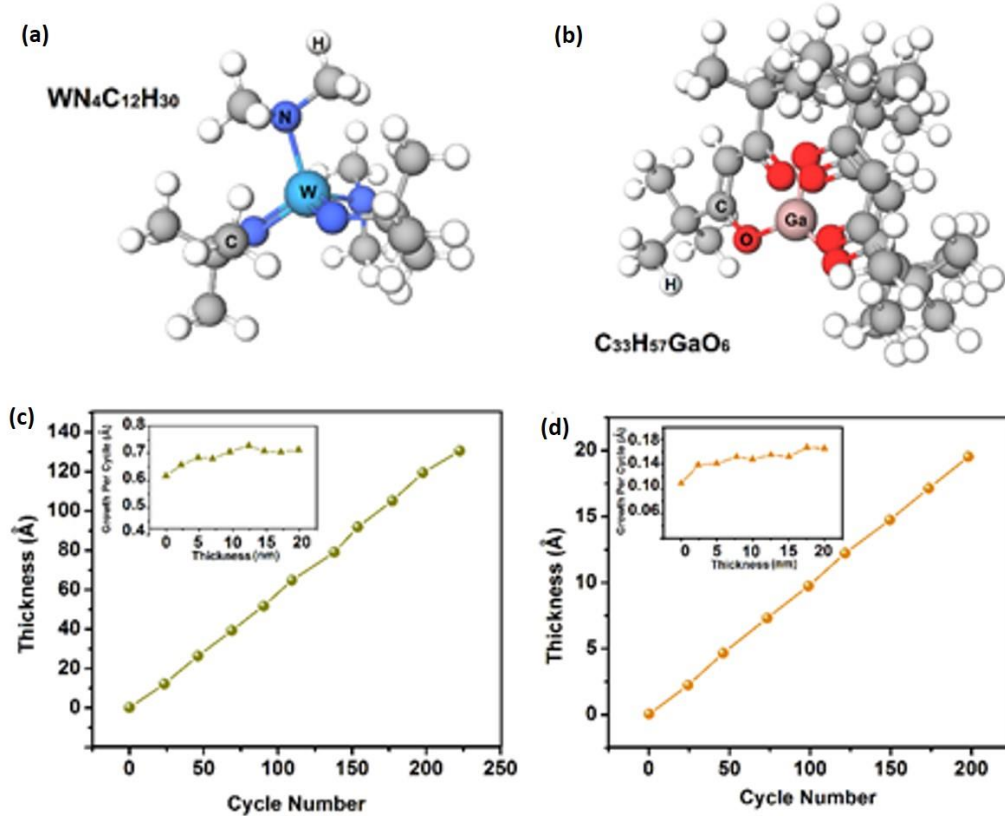


Figure 5.1. (a) the graphical scheme of chemical formula of  $\text{WN}_4\text{C}_{12}\text{H}_{30}$  precursor. (b) The graphical scheme of chemical formula of  $\text{C}_3\text{H}_{57}\text{GaO}_6$  precursors. (c) The graph of thickness versus ALD cycle number of  $\text{WO}_3$  with the average growth rate of  $0.7 \text{ \AA}/\text{cycle}$  (Inset), (d) and graph of thickness versus ALD cycle of  $\text{Ga}_2\text{O}_3$  films with the average growth rate of  $0.16 \text{ \AA}/\text{cycle}$  (Inset).

The four-inch Si/SiO<sub>2</sub> wafers ( $12 \text{ } \Omega/\text{cm}$ ) were utilized as substrates, where the thickness of the native oxide was  $\sim 1.78\text{-}1.9 \text{ nm}$ .  $\text{Ga}_2\text{O}_3$ - $\text{WO}_3$  heterostructures were fabricated on these SiO<sub>2</sub>/Si substrates via a two-step ALD process, and all solvents and reagents involved in their development were purchased from the chemical suppliers and represented analytical grade. Prior to the deposition, in order to reduce the influence of Si wafer on electrical measurements, additional  $\sim 100 \text{ nm}$  thick SiO<sub>2</sub> insulating layer was applied on the Si wafers CVD (Oxford Instruments PLASMALAB 100). After that, approximately  $150 \text{ nm}$ -thick nanostructured Au/Cr films were deposited on SiO<sub>2</sub>/Si substrate using a custom made optical photomask by the

Electron Beam Evaporator method (Nanochrome II (Intivac, USA)) to develop a conductive testing electrode for the subsequent gas sensing performance investigation. For the  $\text{WO}_3$  nanofilms deposition  $(^t\text{BuN})_2(\text{Me}_2\text{N})_2\text{W}$  (Strem Chemicals Inc., USA) and  $\text{H}_2\text{O}$  vapor were employed as precursors, and the graphical interpretation of tungsten precursor was presented in Figure 5.1(a). The details of ALD fabrication of ultra-thin 2D  $\text{WO}_3$  nanofilms and the optimal recipe parameters for the ultra-thin 2D  $\text{WO}_3$  nanofilms were established in Chapter 3. After each deposition cycle, the variable angle *in-situ* spectroscopic ellipsometry measurements (J.A. Woollam M2000 DI) was carried out at the different angles over the wavelengths of 250-1690 nm to monitor the uniformity and to measure the thickness of the deposited  $\text{WO}_3$  films. Some of the samples were used for the fabrication of  $\text{Ga}_2\text{O}_3$ - $\text{WO}_3$  heterostructures, and some  $\text{WO}_3$  samples were used for comparison in the chemical gas sensors.

The second step was to fabricate  $\text{Ga}_2\text{O}_3$  films on the top of  $\text{WO}_3$  nanofilms using tris (2,2,6,6-tetramethyl-3,5-heptanedionato) gallium (III),  $[\text{Ga}(\text{TMHD})_3]$  (Strem Chemicals, 99%) and  $\text{O}_2$  plasma as the metal and oxygen precursors, respectively. Figure 5.1(b) shows the graphical interpretation of  $\text{Ga}(\text{TMHD})_3$  precursor used for  $\text{Ga}_2\text{O}_3$  ALD deposition. The depositions were carried out in a home-built pump type ALD reactor [26] with an operating base pressure of below  $5 \times 10^{-6}$  mbar. The details of the process can be found elsewhere [27]. A pulse time of 5 s was used for both the  $\text{Ga}(\text{TMHD})_3$  and  $\text{O}_2$  plasma, at a pressure of  $3 \times 10^{-3}$  mbar. At the same time, some  $\text{Ga}_2\text{O}_3$  samples were also developed for the subsequent study. Since the thickness measurements were found difficult on the heterostructure, the  $\text{Ga}_2\text{O}_3$  film growth was followed, using *in-situ* spectroscopic ellipsometry measurement, on a native  $\text{SiO}_2/\text{Si}$  substrate that was placed on the heater block, together with the sample. After the deposition, the  $\text{Ga}_2\text{O}_3$  film thickness on the heterostructure was confirmed by comparing the amount of material deposited on it, and the reference  $\text{SiO}_2/\text{Si}$  using X-ray fluorescence (XRF) measurements [28]. The developed  $\text{Ga}_2\text{O}_3$  nanofilms had an average thickness of  $\sim 1.5$  nm after 90-deposited cycles, which resulted in the total thickness of developed  $\text{Ga}_2\text{O}_3$ - $\text{WO}_3$  heterostructures to be about  $\sim 8.0$  nm. All of the fabricated samples were subsequently annealed in the air for 1 h at  $250^\circ\text{C}$  with the heating rate of  $0.5^\circ\text{C}/\text{min}$ .

In order to determine the growth per cycle of  $\text{WO}_3$  and  $\text{Ga}_2\text{O}_3$  nanofilms, different thickness of samples were deposited under the same deposition conditions, and the relations

between the thicknesses of ALD-developed  $\text{WO}_3$  and  $\text{Ga}_2\text{O}_3$  and the number of ALD cycles were depicted in Figure 5.1(c, d). The growth curves were linear without any nucleation delay for both of the samples, implying that the self-limited property of the ALD growth process and the film thickness could be developed precisely by varying the number of ALD cycles. The growth per cycle (GPC) yielded from the slopes of growth curves shown in the inset of Figure 5.1(c, d) were calculated to be around  $0.7 \text{ \AA/cycle}$  and  $0.16 \text{ \AA/cycle}$  for deposition of  $\text{WO}_3$  and  $\text{Ga}_2\text{O}_3$  nanofilms, respectively. The lower growth per cycle of  $\text{Ga}_2\text{O}_3$  nanofilms makes its applications on the doping and modification possible [27].

### 5.3.2 Apparatus and Instruments

The morphology and surface elemental analysis of the samples were characterized by field emission scanning electron microscopy (FE-SEM, JEOL 7800F) along with energy dispersive spectroscopy (EDS, JEOL). X-ray photoelectron spectroscopy (XPS, Rigakudenki model, 7000) with monochromatic  $\text{Mg-K}\alpha$  radiation at 300 W was used to investigate the surface composition

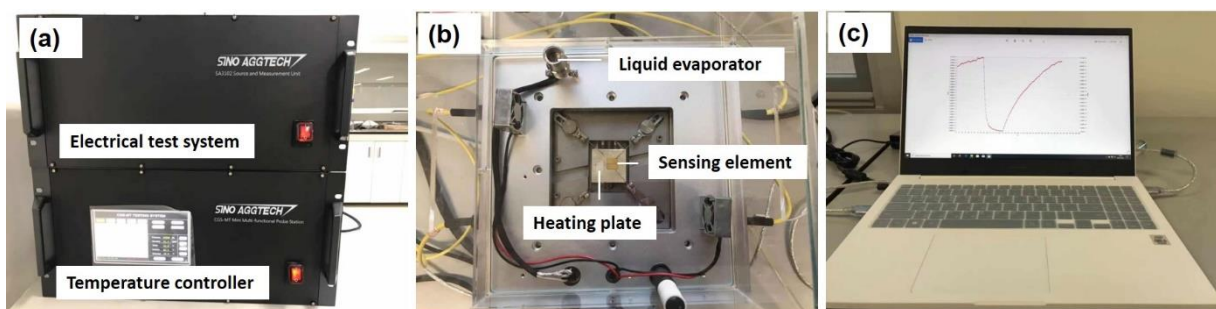


Figure 5.2. The intelligent gas sensing analysis system of gas sensor.

and chemical state of ALD-developed heterostructures. The reported binding energy values were corrected for charging effects by assigning binding energy of 284.6 eV to the C1s signal. Raman spectroscopy measurements were conducted on the laser Raman spectrometer (Lab Ram ARAMIS, Horiba Jobin-Yvon, Edison, NJ, USA) with  $\lambda=532.2 \text{ nm}$  argon-ion laser to identify the crystallinity of heterostructures. Hall Effect measurement systems (HMS3000) was used at room temperature to measure the Hall coefficient of  $\text{Ga}_2\text{O}_3$  thin films by using 0.55T Magnet. Finally, the gas sensing properties of the sensors based on ALD-developed ultra-thin samples were measured by CGS-ITP (Chemical gas sensor-1 temperature pressure) intelligent gas sensing analysis system (Beijing Elite Tech Co., Ltd, China) under the relative humidity

(HR) of 25%, shown in Figure 5.2. The gas response was defined as  $S=R_a/R_g$ , where  $R_a$  and  $R_g$  are the resistances of the sensor in air and target gas, respectively.

## 5.4 Results and discussion

### 5.4.1 Characterization of $\text{Ga}_2\text{O}_3$ - $\text{WO}_3$ heterostructures

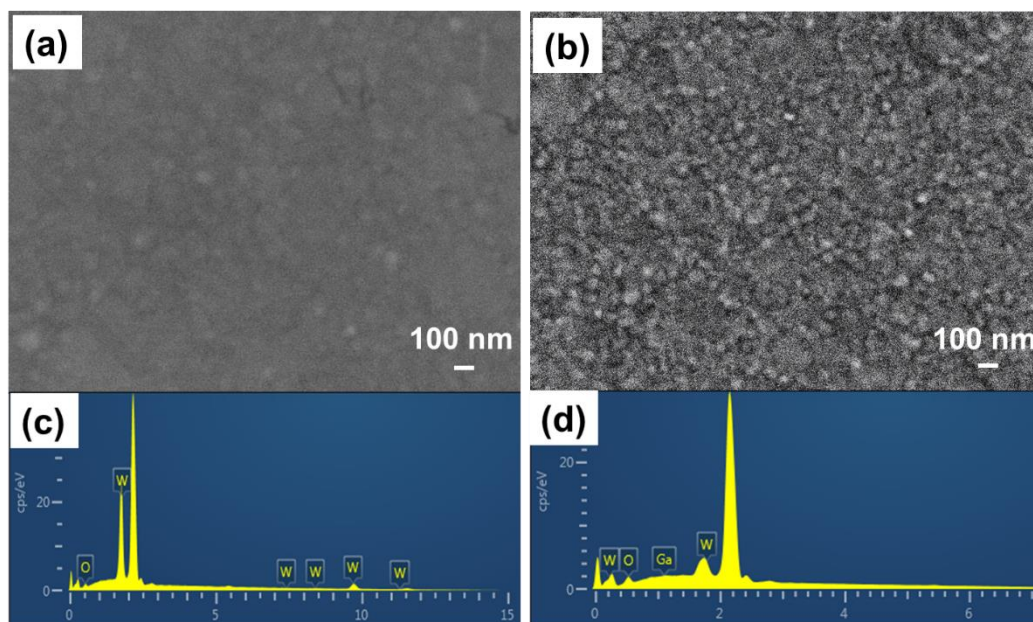


Figure 5.3. SEM images of the ALD-deposited (a)  $\text{WO}_3$  and (b)  $\text{Ga}_2\text{O}_3$ - $\text{WO}_3$  heterostructures with their EDS analysis (c) and (d).

Figure 5.3 depicts SEM and EDS analysis of the surface morphology of ALD-developed  $\text{WO}_3$  with a thickness of 6.5 nm and  $\text{Ga}_2\text{O}_3$  with a thickness of  $\sim 1.5$  nm deposited on the top of  $\text{WO}_3$  nanofilms. As  $\text{WO}_3$  films were not annealed prior to  $\text{Ga}_2\text{O}_3$  deposition, the SEM picture of  $\text{WO}_3$  films in Figure 5.3(a) presents that flat nanoparticles with the average measured diameter of  $\sim 50$  nm were uniformly and smoothly distributed on the surface of the substrate and represent not fully crystalline structure [29]. On the contrary, the SEM picture of  $\text{Ga}_2\text{O}_3$  deposited on the top of  $\text{WO}_3$  films annealed at  $250^\circ\text{C}$  shows a slightly rougher surface compared to that of  $\text{WO}_3$  films. It is visible that  $\text{Ga}_2\text{O}_3$ - $\text{WO}_3$  heterostructures were aggregated with small particles with an average size of  $\sim 40$  nm. Meanwhile, the chemical compositions of  $\text{WO}_3$  and  $\text{Ga}_2\text{O}_3$ - $\text{WO}_3$  heterostructures were determined by EDS, and the measured result of  $\text{WO}_3$  shows signals for tungsten and oxygen (Signals related to the substrate were omitted). In addition, the EDS result

of  $\text{Ga}_2\text{O}_3$ - $\text{WO}_3$  heterostructures portrays the signals of tungsten, oxygen, and gallium. The existence of a gallium signal along with tungsten and oxygen proved that  $\text{Ga}_2\text{O}_3$  nanofilms might successfully be deposited on the surface of  $\text{WO}_3$  nanofilms. It has to be stressed that unfortunately, due to extreme thin nature of ALD deposited  $\text{Ga}_2\text{O}_3$ - $\text{WO}_3$  heterostructures, investigation of their crystallinity by the X-ray diffraction technique was not possible.

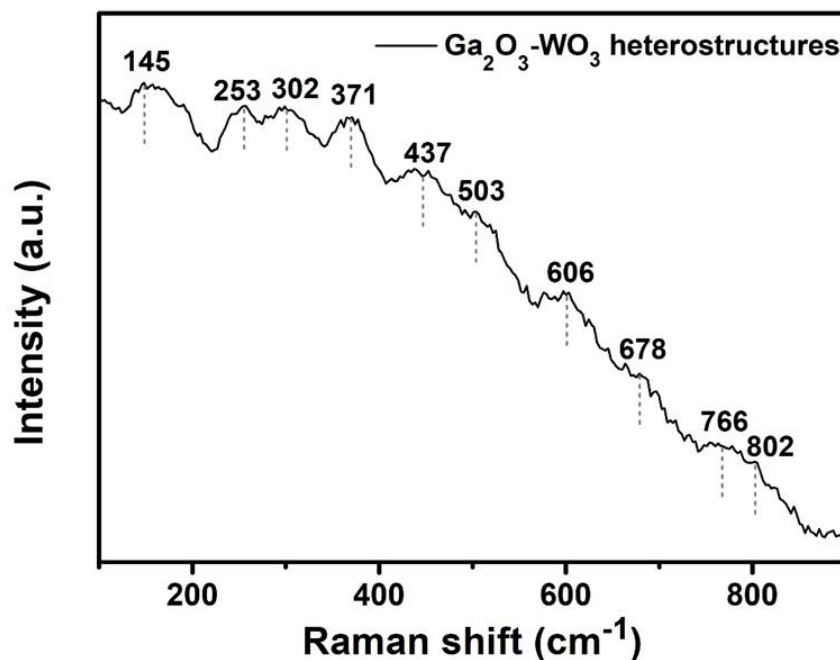


Figure 5.4. Raman spectra of  $\text{Ga}_2\text{O}_3$ - $\text{WO}_3$  heterostructures.

In order to gain insight into the structure of 2D  $\text{Ga}_2\text{O}_3$ - $\text{WO}_3$  heterostructures, the functional groups in the sample were analyzed by Raman spectrum in the range from 100 to 900  $\text{cm}^{-1}$ , as displayed in Figure 5.4. Eight leading vibrational bands can be identified from the spectrum. As has been reported in previous literature, three Raman bands appeared at 253, 302 and 803  $\text{cm}^{-1}$ , which are characteristic features of monoclinic  $\text{WO}_3$  [30]. The two peaks at 253 and 302  $\text{cm}^{-1}$  are assigned to W-O-W bending vibration, while the peak of 803  $\text{cm}^{-1}$  is ascribed to stretching modes of the bridging oxygen of  $\text{WO}_6$  octahedra. Moreover, four Raman modes at 146, 371, 437, 606, and 766  $\text{cm}^{-1}$  are also visible in the spectrum. The low-frequency mode 146  $\text{cm}^{-1}$  is assigned to the translation and libration of tetrahedraoctahedra chain. The mild frequency modes of 371 and 437  $\text{cm}^{-1}$  are associated with the deformation of  $\text{Ga}_2\text{O}_6$  octahedra.

The high-frequency modes of 606 and 766  $\text{cm}^{-1}$  are assigned to bending and stretching of  $\text{GaO}_4$  tetrahedra. The experimental Raman modes correspond well to  $\beta$ - $\text{Ga}_2\text{O}_3$  [31]. In addition, it was observed that the Raman modes of  $\text{Ga}_2\text{O}_3$ - $\text{WO}_3$  heterostructures are 0.4-40  $\text{cm}^{-1}$  red-shift compared to the bulk  $\text{WO}_3$  and  $\text{Ga}_2\text{O}_3$  powder Raman modes reported in the literature, which might be due to the phonon confinement resulted from the decrease in the particle dimension to the nanometer scale [32, 19].

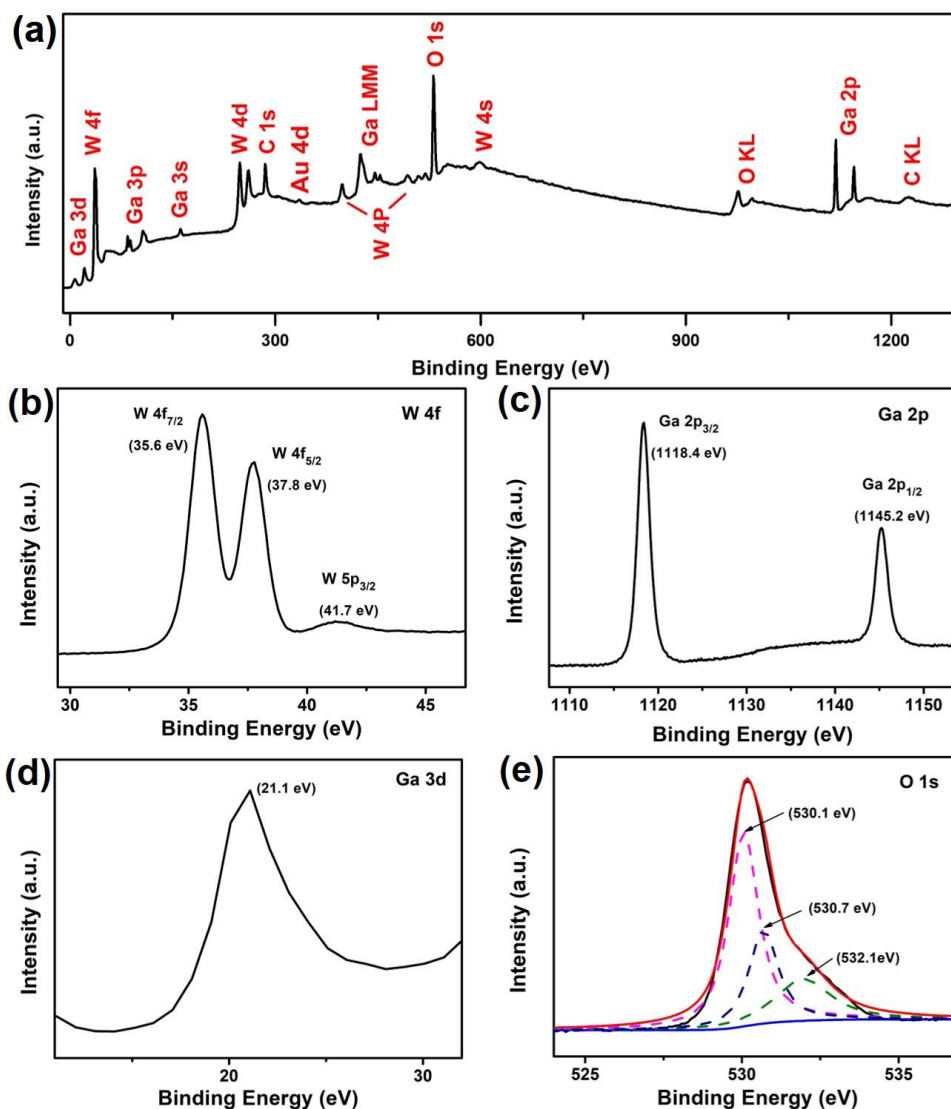


Figure 5.5. XPS spectra of  $\text{Ga}_2\text{O}_3$ - $\text{WO}_3$  heterostructures, (a) full survey scan spectrum, (b) W 4f region, (c) Ga 2p region, (d) Ga 3d region and (e) O 1s region.

Chemical composition and bonding states of the developed  $\text{Ga}_2\text{O}_3$ - $\text{WO}_3$  heterostructures were studied by XPS. The charge shift spectrum was calibrated using the fortuitous C 1s peak at 284.8 eV. Figure 5.5(a) shows the survey scan of  $\text{Ga}_2\text{O}_3$ - $\text{WO}_3$  heterostructures collected for the films deposited on the  $\text{SiO}_2/\text{Si}$  substrates. Three main elements of W, O, and Ga can be clearly observed. Besides, the peaks of Au 4d and C 1s were also presented in the survey, which originated from the Au electrode and the reference to calibrate the binding energies of the peaks, respectively. Figure 5.5(b) displayed the high-resolution scan of W 4f. The doublets of W 4f<sub>7/2</sub> and W 4f<sub>5/2</sub> were centered at 37.8 eV and 35.6 eV with the spin-orbit splitting of the doublet of 2.2 and the peak ratio of 4:3, while a third broad peak of W 5p<sub>3/2</sub> was located at 41.7 eV, revealing W atoms with an oxidation state of  $\text{WO}_3$  [33]. It should be noted that the obtained XPS results in this investigation are slightly different from our previous report on the development of  $\text{WO}_3$  monolayer by ALD (36.2 and 35.2 eV for W 4f<sub>7/2</sub> and W 4f<sub>5/2</sub>, respectively) [25]. This difference is reasonable considering the amount of W in the samples.

Figure 5.5(c) depicts two quasi-symmetrical Ga 2p<sub>1/2</sub> and Ga 2p<sub>3/2</sub> peaks for Ga-O bonding at 1145.2 eV and 1118.4 eV with a separation distance of 26.8 eV, which is consistent with the binding energy of Ga 2p for doped  $\beta$ - $\text{Ga}_2\text{O}_3$  [34, 35], and  $\beta$ - $\text{Ga}_2\text{O}_3$  has also been verified by Raman measurements presented in Figure 5.4. The energy peak for Ga 3d is centered at 21.1 eV (Figure 5.5(d)), which is caused by the presence of Ga-O bond reported for p-type  $\beta$ - $\text{Ga}_2\text{O}_3$  films [36], but not observed for the n-type  $\beta$ - $\text{Ga}_2\text{O}_3$  structures [37]. The Ga 3d peak is asymmetrical with the shoulder, which was ascribed to the hybridization of Ga 3d and O 2s states near the valence band [38].

The O 1s peak in the measured XPS spectrum (Figure 5.5(e)) could be deconvoluted into three significant peaks. The main binding energy component centered at 530.1 eV can be characteristic of the lattice oxygen in the of  $\text{Ga}_2\text{O}_3$ - $\text{WO}_3$  ultra-thin films, the second binding energy at 531.7 eV is attributed to oxygen vacancies or OH<sup>-</sup> adsorbed species on the surface [37]. The peak at 532.5 eV might due to the chemically absorbed oxygen. More importantly, this shoulder (532.5 eV) has not been observed in the reported O 1s region for the n-type  $\beta$ - $\text{Ga}_2\text{O}_3$  [37, 39, 40], indirectly confirming the development of p-type  $\beta$ - $\text{Ga}_2\text{O}_3$  in the heterostructure. Very relevant to this investigation was our previous study on ALD fabrication of  $\text{WO}_3$  monolayer, proving the influence of  $\text{SiO}_2$  substrate, where the bottom oxygen of  $\text{WO}_3$  is shared

with  $\text{SiO}_2$  making  $\text{WO}_3$  slightly non-stoichiometric [25]. Therefore, this non-stoichiometry plays a critical role in the development of  $\text{Ga}_2\text{O}_3$ - $\text{WO}_3$  heterostructure, while the thickness of the ALD deposited  $\text{Ga}_2\text{O}_3$  on the top of  $\text{WO}_3$  is only  $\sim 1.5$  nm.

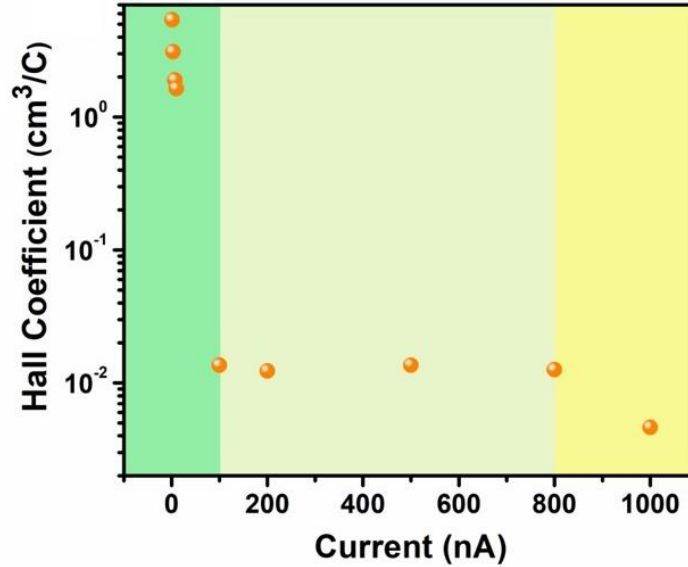


Figure 5.6. The variation of average Hall coefficient vs applied current for 4.8 nm thick  $\text{Ga}_2\text{O}_3$  nanofilms.

For further investigation of the conductivity type of  $\beta$ - $\text{Ga}_2\text{O}_3$ ,  $\text{Ga}_2\text{O}_3$  samples with a thickness of 4.8 nm were subjected to the Hall coefficient measurements at a temperature of  $20^\circ\text{C}$ , and the results are presented in Figure 5.6. The applied magnetic field was 0.55 T. The positive value of the Hall coefficient decreased considerably when the applied current increased from 1 nA to 100 nA. However, its value changed slightly over a long range of applied current from 100 nA to 900 nA. These results further confirm the stable p-type performance of the ALD-developed  $\text{Ga}_2\text{O}_3$  nanofilms.

#### 5.4.2 Gas sensing properties

As the working temperature governs the mobility of the electrons and the electrical conductivity of semiconductor metal oxides, the gas sensing properties of semiconductor metal oxides are greatly influenced by their working temperature. In order to find the optimal working temperature, the gas responses of  $\text{WO}_3$ ,  $\text{Ga}_2\text{O}_3$ , and  $\text{Ga}_2\text{O}_3$ - $\text{WO}_3$  heterostructures to 100 ppm ethanol were measured at the different temperatures from  $175$  to  $325^\circ\text{C}$  and the obtained results are summarized in Figure 5.7. The responses of samples increase with the rising of the

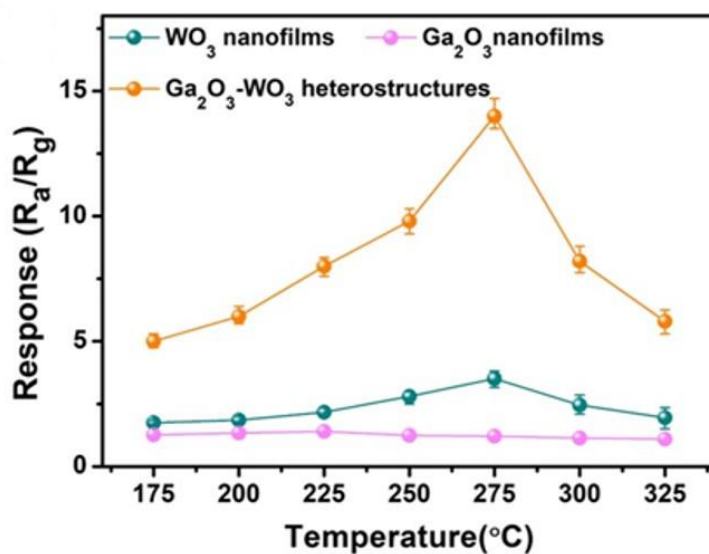


Figure 5.7. Responses of  $\text{WO}_3$ ,  $\text{Ga}_2\text{O}_3$ , and  $\text{Ga}_2\text{O}_3$ - $\text{WO}_3$  heterostructures to 100 ppm ethanol under the different working temperatures.

operating temperature.  $\text{WO}_3$  nanofilms and  $\text{Ga}_2\text{O}_3$ - $\text{WO}_3$  heterostructures reach the maximum at 275°C, while for  $\text{Ga}_2\text{O}_3$  nanofilms, the highest response appeared at 225°C. As the operating temperature continues to increase, the responses gradually decrease. It is also well known that the response of the gas sensor relies on a delicate balance between the speed of chemical reaction and the speed of gas diffusion on the surface of materials [41-43]. The increase of working temperature favors target gas molecules chemisorption, and the reaction rate occurring on the materials' surface leads to an enhanced gas response. However, the diffusion speed of target gas molecules is accelerated at a high temperature. Thus, the two processes will tend to balance at a specific temperature, at which temperature the sensitivity of the gas sensor attains the maximum. The gas response of  $\text{Ga}_2\text{O}_3$ - $\text{WO}_3$  heterostructures to 100 ppm ethanol at the optimal temperature of 275°C is about 14, which is about 4 times and 10 times higher than that of  $\text{WO}_3$  and  $\text{Ga}_2\text{O}_3$  nanofilms, indicating that functionalized  $\text{Ga}_2\text{O}_3$  on the surface of  $\text{WO}_3$  nanofilms can enhance the sensitivity significantly.

The response/recovery times are significant parameters to assess the suitability of sensing material for utilization in the chemical sensors, and the response/recovery time of the sensor is defined as the time taken by the sensor to achieve 90 % of the total resistance change. Figure 5.8 (a-c) depict typical response/recovery resistance transients of  $\text{WO}_3$ ,  $\text{Ga}_2\text{O}_3$ , and

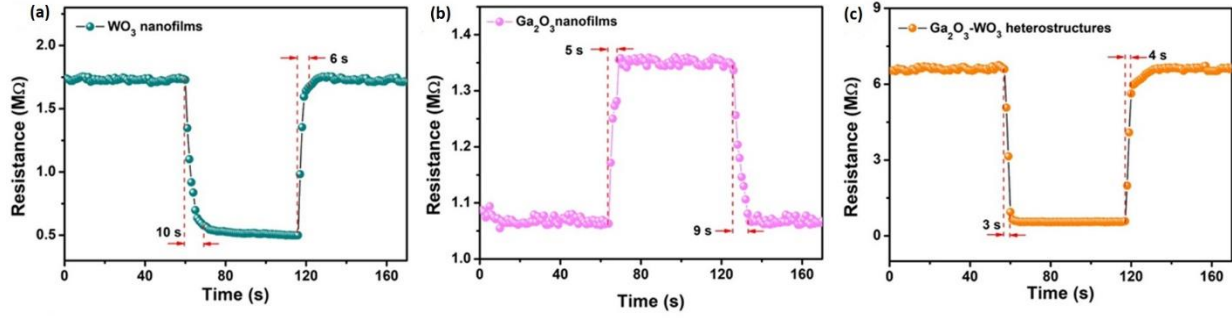


Figure 5.8. Response and recovery curves of (a)  $\text{WO}_3$ , (b)  $\text{Ga}_2\text{O}_3$ , and (c)  $\text{Ga}_2\text{O}_3$ - $\text{WO}_3$  heterostructures to 100 ppm ethanol at  $275^\circ\text{C}$ .

$\text{Ga}_2\text{O}_3$ - $\text{WO}_3$  heterostructures, respectively towards 100 ppm ethanol under  $275^\circ\text{C}$ . For the sensor based on  $\text{Ga}_2\text{O}_3$  nanofilms, the resistances increase in the presence of ethanol, typical behavior for *p*-type semiconductors. While the resistances significantly decrease after exposure to ethanol for  $\text{WO}_3$  and  $\text{Ga}_2\text{O}_3$ - $\text{WO}_3$  heterostructures based sensors, exhibiting the *n*-type behavior for both sensors. Furthermore the large resistance increase of  $\text{Ga}_2\text{O}_3$ - $\text{WO}_3$  heterostructures (6.5 MΩ) than  $\text{WO}_3$  nanofilms (1.7 MΩ) demonstrated that *p-n* heterojunction was successfully incorporated. When the ethanol is removed, the sensor's resistance increased and fully recovered to their initial values. The measured response/recovery times of  $\text{Ga}_2\text{O}_3$ - $\text{WO}_3$  heterostructures are 5/3 s, which is shorter than that of  $\text{WO}_3$  (9/6 s) and  $\text{Ga}_2\text{O}_3$  (5/9 s) nanofilms.

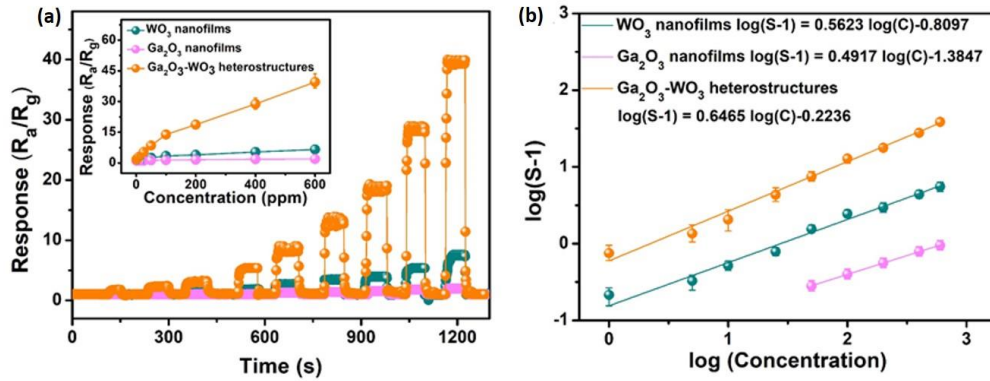


Figure 5.9. (a) Dynamic responses of  $\text{WO}_3$ ,  $\text{Ga}_2\text{O}_3$  nanofilms, and  $\text{Ga}_2\text{O}_3$ - $\text{WO}_3$  heterostructures to the different ethanol concentration and (b) corresponding logarithm plots of the gas responses versus ethanol concentration at  $275^\circ\text{C}$ .

The dynamic response and recovery curves of sensors based on  $\text{WO}_3$ ,  $\text{Ga}_2\text{O}_3$  nanofilms and  $\text{Ga}_2\text{O}_3$ - $\text{WO}_3$  heterostructures towards the different concentrations of ethanol at  $275^\circ\text{C}$  were presented in Figure 5.9(a). It is obvious that  $\text{Ga}_2\text{O}_3$  nanofilms exhibit no response when the concentration of ethanol is lower than 50 ppm, while for  $\text{WO}_3$  and  $\text{Ga}_2\text{O}_3$ - $\text{WO}_3$  heterostructures, the corresponding responses of the sensors increased with increasing of ethanol concentration from 1 to 600 ppm and both sensors have demonstrated good reversibility and reproducibility to ethanol. In addition,  $\text{Ga}_2\text{O}_3$ - $\text{WO}_3$  heterostructures exhibited quite enhanced responses under the same concentration compared to  $\text{WO}_3$  and  $\text{Ga}_2\text{O}_3$  nanofilms. Corresponding plots of gas response versus ethanol concentration are shown as an inset of Figure 5.9(a). The response of  $\text{Ga}_2\text{O}_3$ - $\text{WO}_3$  heterostructures to 1 ppm ethanol is found to reach a value of 1.75, highlighting the excellent sensing performance to the low concentration. In fact, the response of the semiconducting oxide gas sensor can usually be empirically represented as  $S=A[C]^N+1$  [40], where  $A$  is constant and  $[C]$  is the concentration of the target gas.  $N$  usually as a value 0.5 and 1.0, depending on the charge of the surface species and the stoichiometry reaction on the surface. According to the previous report, when  $b$  is 0.5, the adsorbed surface oxygen ion is  $\text{O}^{2-}$  and when  $b$  is 1, the adsorbed surface oxygen is  $\text{O}^-$  [44]. Then the equation of  $S=A[C]^N+1$  also can be rewritten as  $\log(S-1)=N\log[C]+\log A$ . From Figure 5.9(b), we can find that the responses of  $\text{WO}_3$  nanofilms and  $\text{Ga}_2\text{O}_3$ - $\text{WO}_3$  heterostructures based sensors have a good linear relationship with the ethanol concentrations varied from 1 to 600 ppm on the logarithmic scale, keeping with the theory of power laws for the metal oxide semiconductors. The slope values are 0.5442 and 0.6479 for  $\text{WO}_3$  nanofilms and  $\text{Ga}_2\text{O}_3$ - $\text{WO}_3$  heterostructures, respectively, indicating that the adsorbed surface oxygen species are mainly  $\text{O}^{2-}$ .

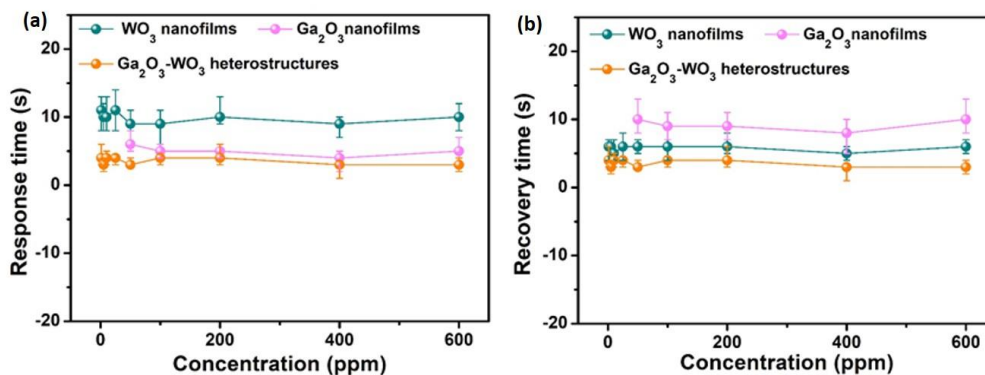


Figure 5.10. Plots of (a) response and (b) recovery time versus different concentrations of ethanol for  $\text{Ga}_2\text{O}_3$ - $\text{WO}_3$  heterostructures at  $275^\circ\text{C}$ .

Furthermore, the response/recovery time of  $\text{Ga}_2\text{O}_3$ - $\text{WO}_3$  heterostructures based sensors under different ethanol concentration at  $275^\circ\text{C}$  was also investigated. Figure 5.10(a, b) illustrated the variations in response/recovery time with ethanol concentration change from 1 to 600 ppm. As can be clearly seen, the response/recovery time of  $\text{Ga}_2\text{O}_3$ - $\text{WO}_3$  heterostructures is shorter than that of  $\text{WO}_3$  and  $\text{Ga}_2\text{O}_3$  nanofilms at all measured ethanol concentration, which can be ascribed to the faster adsorption, reactions and desorption of ethanol gas on the surface of  $\text{Ga}_2\text{O}_3$ - $\text{WO}_3$  heterostructures.

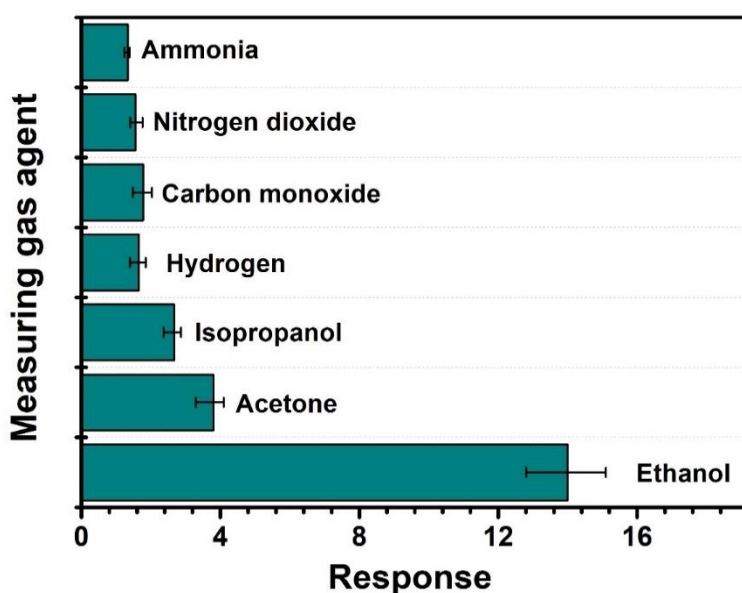


Figure 5.11. Responses of  $\text{Ga}_2\text{O}_3$ - $\text{WO}_3$  heterostructures to 100 ppm various gases at  $275^\circ\text{C}$ .

Selectivity is another critical parameter in the evaluation of gas sensor performance. Specifically, sensor-based on  $\text{Ga}_2\text{O}_3$ - $\text{WO}_3$  heterostructures was tested with reducing gases under the concentration of 100 ppm at the optimal working temperature for investigation of its selectivity. The responses of  $\text{Ga}_2\text{O}_3$ - $\text{WO}_3$  heterostructures to the different reducing gases, including acetone, isopropanol, hydrogen, carbon monoxide, nitrogen dioxide, and ammonia, were clearly displayed in Figure 5.11. It is evident that the response to ethanol is much higher than that of acetone, isopropanol, and the sensor is almost insensitive to hydrogen, carbon

Table 5.1. Comparison of gas sensing performances to ethanol based on different types of nanostructured materials reported recently.

Sensing material	C (ppm)	T (°C)	R	$\tau_{\text{res}}/\tau_{\text{rec}}(\text{s})$	LOD (ppm)	Refs
$\text{Ga}_2\text{O}_3$ - $\text{WO}_3$ heterostructures	100	275	14	5/3	1	this work
$\text{WO}_3$ nanobricks	100	300	6.5	3/5	20	[45]
$\text{WO}_3$ nanofibers	100	250	3.43	-/-	-	[46]
Flower-like $\text{WO}_3$ architectures	100	300	7	1/6	0.9	[47]
$\text{Ga}_2\text{O}_3$ nanowires	200	200	~2	~30/~200	-	[48]
$\text{Cr}_2\text{O}_3$ -functionalized nanorods	$\text{WO}_3$ 100	300	4.23	51.35/48.65	1	[49]
$\text{La}_2\text{O}_3$ - $\text{WO}_3$ nanofibers	100	350	5.1	-/-	-	[50]
$\text{WO}_3$ /3% $\text{SnO}_2$ composite	100	300	2.5	-/-	-	[51]
0.6 at% Co-doped $\text{WO}_3$ FNPs	50	350.	10	-/-	-	[52]
Pt NPs-functionalized nanorods	$\text{WO}_3$ 50	220	3	9/-	1	[53]
C-doped $\text{WO}_3$ fibers	100	350	12	-/-	-	[54]
1.5% $\text{In}_2\text{O}_3$ - $\text{WO}_3$ heterojunction nanofibers	100	275	6.3	-/-	-	[55]
$\text{Au}/\text{SnO}_2$ microstructures	100	340	18	5/10	5	[56]
$\text{MoS}_2$ - $\text{TiO}_2$ composites	100	150	14.2		50	[57]
$\alpha$ - $\text{Fe}_2\text{O}_3$ /g- $\text{C}_3\text{N}_4$ nanocomposites	100	340	7.76	7/30	-	[58]
$\alpha$ - $\text{Fe}_2\text{O}_3$ nanoporous network	100	400	9.5	3/138	-	[59]
$\text{CdO}/\text{ZnO}$ heterostructure composites	100	250	65.5	2/136	0.5	[60]
$\text{NiO}/\text{SnO}_2$ heterojunction thin film	100	250	7.9	15/100	0.1	[61]
$\text{ZnO}/\text{In}_2\text{O}_3$ CSNFs	100	225	31.8	-/-	5	[62]
2D $\text{CeO}_2$ - $\text{SnO}_2$ nanosheets	100	340	44	25/6	5	[63]
$\text{SnO}_2/\text{Fe}_2\text{O}_3$ microspheres	100	260	41.7	3/4	0.1	[64]

monoxide, ammonia, and even nitrogen dioxide, as the testing temperature is far beyond the optimal working temperature for nitrogen dioxide. These obtained results indicated that the sensor based on  $\text{Ga}_2\text{O}_3$ - $\text{WO}_3$  heterostructures is highly specific for ethanol detection at the optimal working temperature of 275°C. In addition, a comparison of ethanol sensing

performances between  $\text{Ga}_2\text{O}_3$ - $\text{WO}_3$  heterostructures prepared in this work and other types of materials reported recently are summarized in Table 5.1. It can be observed that  $\text{Ga}_2\text{O}_3$ - $\text{WO}_3$  heterostructures exhibit superior performance among pristine and functionalized- $\text{WO}_3$  materials except of  $\text{SnO}_2/\text{Fe}_2\text{O}_3$  microspheres. However,  $\text{SnO}_2/\text{Fe}_2\text{O}_3$  microspheres based gas sensor still show relatively high response to formaldehyde. Those results illustrate that this fabrication methods could be extended to other metal oxides for the application in various fields. The results have also confirmed that the comparable response, faster response/recovery time at relatively low working temperature, and lower detection limit among all the materials make  $\text{Ga}_2\text{O}_3$ - $\text{WO}_3$  heterostructures more attractive for possible ethanol detection.

## 5.4 Conclusions

In this work, wafer-scale  $\text{Ga}_2\text{O}_3$ - $\text{WO}_3$  heterostructures with the average thickness of  $\sim 8.0$  nm were successfully fabricated via a two-step ALD process by using modern plasma-enhanced ALD apparatus and appropriate precursors. The ALD-developed  $\text{Ga}_2\text{O}_3$ - $\text{WO}_3$  heterostructures were subsequently annealed at  $250^\circ\text{C}$  and utilized as sensing electrodes for ethanol detection. They achieved their optimum sensitivity at the temperature of  $275^\circ\text{C}$ . The  $\text{Ga}_2\text{O}_3$ - $\text{WO}_3$  heterostructures have clearly demonstrated high performance towards ethanol detection, especially at *ppm* concentration level and unique sensing capabilities. Specifically, the sensor based on  $\text{Ga}_2\text{O}_3$ - $\text{WO}_3$  heterostructure exhibited not only enhanced response (14-100 *ppm*) but also rapid response/recovery time (5/3s) and excellent selectivity compared with the sensors based on  $\text{WO}_3$  and  $\text{Ga}_2\text{O}_3$  nanofilms. Furthermore, as low as 1 *ppm* of ethanol can be determined when  $\text{Ga}_2\text{O}_3$ - $\text{WO}_3$  heterostructures are used as sensing electrode material. Therefore, sub-10 nm heterostructures can be potentially exploited as promising sensing electrode materials for practical ethanol sensing at low concentrations.

## References

1. E. Lee, Y. S. Yoon, D. J. Kim, Two-dimensional transition metal dichalcogenides and metal oxide hybrids for gas sensing, *ACS Sens.* 3 (2018) 2045-2060.
2. K. Kalantar-zadeh, J. Z. Ou, T. Daeneke, A. Mitchell, T. Sasaki, M. S. Fuhrer, Two dimensional and layered transition metal oxides, *Appl. Mater. Today* 5 (2016) 73-89.

3. X. Liu, T. Ma, N. Pinna, J. Zhang, Two-dimensional nanostructured materials for gas sensing, *Adv. Funct. Mater.* 27 (2017) 1702168.
4. F. Ji, X. Ren, X. Zheng, Y. Liu, L. Pang, J. Jiang, S. Liu, 2D- $\text{MoO}_3$  nanosheets for superior gas sensors, *Nanoscale* 8 (2016) 8696-8703.
5. H. Khan, A. Zavabeti, Y. Wang, C. J. Harrison, B. J. Carey, M. Mohiuddin, A. Chrimes, I. A. D. Castro, B. Y. Zhang, Y. M. Sabri, S. K. Bhargava, J. Z. Ou, T. Daeneke, S. P. Russo, Y. Li, K. Kalantar-zadeh, Quasi physisorptive two dimensional tungsten oxide nanosheets with extraordinary sensitivity and selectivity to  $\text{NO}_2$ , *Nanoscale* 9 (2017) 19162-19175.
6. X. Du, S. M. George, Thickness dependence of sensor response for CO gas sensing by tin oxide films grown using atomic layer deposition, *Sens. Actuators B Chem.* 135 (2008) 152-160.
7. X. Du, Y. Du, S. M. George, CO gas sensing by ultrathin tin oxide films grown by atomic layer deposition using transmission FTIR spectroscopy, *J. Phys. Chem. A* 112 (2008) 9211-9219.
8. D. Fu, C. Zhu, X. Zhang, C. Li, Y. Chen, Two-dimensional net-like  $\text{SnO}_2/\text{ZnO}$  heteronanostructures for high-performance  $\text{H}_2\text{S}$  gas sensor, *J. Mater. Chem. A* 4 (2016) 1390-1398.
9. K. S. Novoselov, D. Jiang, F. Schedin, T. J. Booth, V. V. Khotkevich, S. V. Morozov, A. K. Geim, Two-dimensional atomic crystals, *P. Natl. Acad. Sci.* 102 (2005) 10451-10453.
10. M. Osada, T. Sasaki, Two-dimensional dielectric nanosheets: novel nanoelectronics from nanocrystal building blocks, *Adv. Mater.* 24 (2012) 210-228.
11. Z. Zhu, R-J. Wu, The degradation of formaldehyde using a  $\text{Pt@TiO}_2$  nanoparticles in presence of visible light irradiation at room temperature, *J. Taiwan Inst. Chem. E.* 50 (2015) 276-281.
12. A. Mirzaei, S. G. Leonardi, G. Neri, Detection of hazardous volatile organic compounds (VOCs) by metal oxide nanostructures-based gas sensors: A review, *Ceram. Int.* 42 (2016) 15119-15141.
13. S. Wang, D. Huang, S. Xu, W. Jiang, T. Wang, J. Hu, Y. Su, Y. Zhang, Z. Yang, Two-dimensional  $\text{NiO}$  nanosheets with enhanced room temperature  $\text{NO}_2$  sensing performance via Al doping, *Phys. Chem. Chem. Phys.* 19 (2017) 19043-19049.
14. N. Joshi, T. Hayasaka, Y. Liu, H. Liu, O. N. Oliveira Jr, L. Lin, A review on chemiresistive room temperature gas sensors based on metal oxide nanostructures, graphene and 2D transition metal dichalcogenides, *Microchim. Acta* 185 (2018) 213.
15. R. K. Joshi, F. E. Kruis, Influence of Ag particle size on ethanol sensing of  $\text{SnO}_{1.8}$ : Ag nanoparticle films: A method to develop parts per billion level gas sensors, *Appl. Phys. Lett.* 89 (2006) 153116.
16. H. L. Jiang, B. Liu, T. Akita, M. Haruta, H. Sakurai, Q. Xu,  $\text{Au@ZIF-8}$ : CO oxidation over gold nanoparticles deposited to metal-organic framework, *J. Am. Chem. Soc.* 131 (2009) 11302-11303.

17. C. L. Zhu, H. L. Yu, Y. Zhang, T. S. Wang, Q. Y. Ouyang, L. H. Qi, Y. J. Chen, X. Y. Xue,  $\text{Fe}_2\text{O}_3/\text{TiO}_2$  tube-like nanostructures: synthesis, structural transformation and the enhanced sensing properties, *ACS Appl. Mater. Inter.* 4 (2012) 665-671.
18. Y. Liu, G. Li, R. Mi, C. Deng, P. Gao, An environment-benign method for the synthesis of p-NiO/n-ZnO heterostructure with excellent performance for gas sensing and photocatalysis, *Sens. Actuators B Chem.* 191 (2014) 537-544.
19. Y. B. Zhang, J. Yin, L. Li, L. X. Zhang, L. J. Bie, Enhanced ethanol gas-sensing properties of flower-like p-CuO/n-ZnO heterojunction nanorods, *Sens. Actuators B Chem.* 202 (2014) 500-507.
20. G. K. Flingelli, M. M. Fleischer, H. Meixner, Selective detection of methane in domestic environments using a catalyst sensor system based on  $\text{Ga}_2\text{O}_3$ , *Sens. Actuator B Chem.* 48 (1998) 258-262.
21. Y. L. Wu, Q. Luan, S. J. Chang, Z. Jiao, W. Y. Weng, Y. H. Lin, C. L. Hsu, Highly sensitive  $\beta$ - $\text{Ga}_2\text{O}_3$  nanowire nanowires isopropyl alcohol sensor, *IEEE Sens. J.* 14 (2014) 401-405.
22. S. Stegmeier, M. Fleischer, P. Hauptmann, Influence of the morphology of platinum combined with  $\beta$ - $\text{Ga}_2\text{O}_3$  on the VOC response of work function type sensors, *Sens. Actuators B Chem.* 148 (2010) 439-449.
23. Z. Wei, Z. Hai, M. K. Akbari, J. Hu, L. Hyde, S. Depuydt, F. Verpoort, S. Zhuiykov, Ultrasensitive, sustainable, and selective electrochemical hydrazine detection by ALD-developed Two-Dimensional  $\text{WO}_3$ , *ChemElectroChem* 5 (2018) 266-272.
24. Z. Wei, Z. Hai, M. K. Akbari, D. Qi, K. Xing, Q. Zhao, F. Verpoort, J. Hu, L. Hyde, S. Zhuiykov, Atomic layer deposition-developed two-dimensional  $\alpha$ - $\text{MoO}_3$  windows excellent hydrogen peroxide electrochemical sensing capabilities, *Sens. Actuators B Chem.* 262 (2018) 334-344.
25. S. Zhuiykov, L. Hyde, Z. Hai, M.K. Akbari, E. Kats, C. Detavernier, C. Xue, H. Xu, Atomic layer deposition-enabled single layer of tungsten trioxide across a large area, *Appl. Mater. Today* 6 (2017) 44-53.
26. Q. Xie, Y. L. Jiang, C. Detavernier, D. Deduytsche, R. L. V. Meirhaeghe, G. P. Ru, B. Z. Li, X. P. Qu, Atomic layer deposition of  $\text{TiO}_2$  from tetrakis-dimethyl-amido titanium or Ti isopropoxide precursors and  $\text{H}_2\text{O}$ , *J. Appl. Phys.* 102 (2007) 083521.
27. R. K. Ramachandran, J. Dendooven, J. Botterman, S. P. Sree, D. Poelman, J. A. Martens, H. Poelman, C. Detavernier, Plasma enhanced atomic layer deposition of  $\text{Ga}_2\text{O}_3$  thin films, *J. Mater. Chem. A* 2 (2014) 19232-19238.
28. R. K. Ramachandran, J. Dendooven, M. Filez, V. V. Galvita, H. Poelman, E. Solano, M.M. Minjauw, K. Devloo-Casier, E. Fonda, D. Hermida-Merino, W. Bras, G. B. Marin, C. Detavernier,

- Atomic layer deposition route to tailor nanoalloys of noble and non-noble metals, *ACS Nano* 10 (2016) 8770-8777.
29. S. Zhuiykov, Material characterisation and transistor function of quasi two-dimensional substoichiometric  $\text{WO}_{3-x}$  nanoflakes, *Mater. Lett.* 173 (2016) 173-177
  30. S. Balaji, Y. Djaoued, A. S. Albert, R. Brünig, N. Beaudoin, J. Robichaud, Porous orthorhombic tungsten oxide thin films: synthesis, characterization, and application in electrochromic and photochromic devices, *J. Mater. Chem.* 21 (2011) 3940-3948.
  31. R. Rao, A. M. Rao, Blueshifted Raman scattering and its correlation with the [110] growth direction in gallium oxide nanowires, *J. Appl. Phys.* 98 (2005) 094312.
  32. S. Rafique, L. Han, C. A. Zorman, H. Zhao, Synthesis of wide bandgap  $\beta$ - $\text{Ga}_2\text{O}_3$  rods on 3CSiC-on-Si, *Cryst. Growth Des.* 16 (2015) 511-517.
  33. M. Vasilopoulou, L. C. Palilis, D. G. Georgiadou, A. M. Douvas, P. Argitis, S. Kennou, L. Sygellou, G. Papadimitropoulos, I. Kostis, N. A. Stathopoulos, D. Davazoglou, Reduction of Tungsten Oxide: A path towards dual functionality utilization for efficient anode and cathode interfacial layers in organic light-emitting diodes, *Adv. Funct. Mater.* 21 (2011) 1489-1497
  34. W. Mi, Z. Li, C. Luan, H. Xiao, C. Zhao, J. Ma, Transparent conducting tin-doped  $\text{Ga}_2\text{O}_3$  films deposited on  $\text{MgAl}_2\text{O}_4$  (1 0 0) substrates by MOCVD, *Ceram. Int.* 41 (2015) 2572-2575.
  35. W. H. Li, Y. K. Peng, C. Wang, X. L. Zhao, H. Yan, L.H. Li, P. Li, H. Yang, Z. Wu, W. Tang, Structural, optical and photoluminescence properties of Pr-doped  $\beta$ - $\text{Ga}_2\text{O}_3$  thin films, *J. Alloys Comp.* 697 (2017) 388-391.
  36. Y. P. Qian, D. Y. Cuo, X. L. Chu, H. Z. Shi, W. K. Zhu, K. Wang, X. K. Wang, X. K. Huang, H. Wang, S. L. Wang, P. G. Li, X. H. Zhang, W. H. Tang, Mg-doped p-type  $\beta$ - $\text{Ga}_2\text{O}_3$  thin film for solar-blind ultraviolet photodetector, *Mat. Lett.* 209 (2017) 558-561.
  37. E. Chikoidze, A. Fellous, A. Perz-Tomas, G. Sauthier, T. Tchelidze, C. Ton-That, T.T. Huynh, M. Phillips, S. Russell, M. Jennings, B. Berini, F. Jomard, Y. Dumont, P-type  $\beta$ -gallium oxide: A new perspective for power and optoelectronic devices, *Mat. Today Phys.* 3 (2017) 118-126.
  38. A. Navarro-Quezada, S. Alame, N. Esser, J. Purthmuller, F. Bechstedt, Z. Galazka, D. Skuridina, P. Vogt, Near valence-band electronic properties of semiconducting  $\beta$ - $\text{Ga}_2\text{O}_3$  (100) single crystals, *Phys. Rev. B* 92 (2015) 195306.
  39. S. I. Stepanov, V. I. Nikolaev, V. E. Bourgov, A. E. Romanov, Gallium Oxide: properties and applications – a review, *Rev. Adv. Mater. Sci.* 44 (2016) 63.
  40. M. Zhong, Z. Wei, X. Meng, F. Wu, J. Li, High-performance single crystalline UV photodetectors of  $\beta$ - $\text{Ga}_2\text{O}_3$ , *J. Alloys Compd.* 619 (2015) 572-575.

41. C. Wang, S. Ma, A. Sun, R. Qin, F. Yang, X. Li, F. Li, X. Yang, Characterization of electrospun Pr-doped  $\text{ZnO}$  nanostructure for acetic acid sensor, *Sens. Actuators B Chem.* 193 (2014) 326-333.
42. Y. Sun, Z. Wei, W. Zhang, P. Li, K. Lian, J. Hu, Synthesis of brush-like  $\text{ZnO}$  nanowires and their enhanced gas-sensing properties, *J. Mater. Sci.* 51 (2016) 1428-1436.
43. R. W. J. Scott, S. M. Yang, G. Chabanis, N. Coombs, D. E. Williams, G. A. Ozin, Tin Dioxide Opals and Inverted Opals: Near- Ideal Microstructures for Gas Sensors, *Adv. Mater.* 13 (2001) 1468-1472.
44. I. D. Kim, A. Rothschild, T. Hyodo, H. L. Tuller, Microsphere templating as means of enhancing surface activity and gas sensitivity of  $\text{CaCu}_3\text{Ti}_4\text{O}_{12}$  thin films, *Nano Lett.* 6 (2006) 193-198.
45. J. Xiao, C. Song, W. Dong, C. Li, Y. Yin, X. Zhang, M. Song, Synthesis, characterization, and gas sensing applications of  $\text{WO}_3$  nanobricks, *J. Mater. Eng. Perfor.* 24 (2015) 3026-3031.
46. X. Yang, V. Salles, Y. V. Kaneti, M. Liu, M. Mallard, C. Journet, X. Jiang, A. Brioude, Fabrication of highly sensitive gas sensor based on Au functionalized  $\text{WO}_3$  composite nanofibers by electrospinning, *Sens. Actuators B Chem.* 220 (2015) 1112-1119.
47. Z. Wang, P. Sun, T. Yang, Y. Gao, X. Li, G. Lu, Y. Du, Flower-like  $\text{WO}_3$  architectures synthesized via a microwave-assisted method and their gas sensing properties, *Sens. Actuators B Chem.* 186 (2013) 734-740.
48. S. Park, S. Kim, G. J. Sun, C. Lee, Synthesis, structure and ethanol sensing properties of  $\text{Ga}_2\text{O}_3$ -core/ $\text{WO}_3$ -shell nanostructures, *Thin Solid Films* 591 (2015) 341-345.
49. S. Choi, M. Bonyani, G-J. Sun, J. K. Lee, S. K. Hyun, C. Lee,  $\text{Cr}_2\text{O}_3$  nanoparticle-functionalized  $\text{WO}_3$  nanorods for ethanol gas sensors, *Appl. Surf. Sci.* 432 (2018) 241-249.
50. C. Feng, C. Wang, P. Cheng, X. Li, B. Wang, Y. Guan, J. Ma, H. Zhang, Y. Sun, P. Sun, J. Zheng, G. Lu, Facile synthesis and gas sensing properties of  $\text{La}_2\text{O}_3$ - $\text{WO}_3$  nanofibers, *Sens. Actuators B Chem.* 221 (2015) 434-442.
51. Y. Gui, F. Dong, Y. Zhang, Y. Zhang, J. Tian, Preparation and gas sensitivity of  $\text{WO}_3$  hollow microspheres and  $\text{SnO}_2$  doped heterojunction sensors, *Mat. Sci. Semicon. Proc.* 16 (2013) 1531-1537.
52. Z. Liu, B. Liu, W. Xie, H. Li, R. Zhou, Q. Li, T. Wang, Enhanced selective acetone sensing characteristics based on Co-doped  $\text{WO}_3$  hierarchical flower-like nanostructures assembled with nanoplates, *Sens. Actuators B Chem.* 235 (2016) 614-621.
53. X. Liu, J. Zhang, T. Yang, X. Guo, S. Wu, S. Wang, Synthesis of Pt nanoparticles functionalized  $\text{WO}_3$  nanorods and their gas sensing properties, *Sens. Actuators B Chem.* 156 (2011) 918-923.
54. L. Deng, X. Ding, D. Zeng, S. Zhang, C. Xie, High sensitivity and selectivity of C-doped  $\text{WO}_3$  gas sensors toward toluene and xylene, *IEEE Sens. J.* 12 (2012) 2209-2214.

55. C. Feng, X. Li, J. Ma, Y. Sun, C. Wang, P. Sun, J. Zheng, G. Lu, Facile synthesis and gas sensing properties of  $\text{In}_2\text{O}_3$ - $\text{WO}_3$  heterojunction nanofibers, *Sens. Actuators B Chem.* 209 (2015) 622-629.
56. J. Guo, J. Zhang, H. Gong, D. Ju, B. Cao, Au nanoparticle-functionalized 3D  $\text{SnO}_2$  microstructures for high performance gas sensor, *Sens. Actuators B Chem.* 226 (2016) 266-272.
57. P. X. Zhao, Y. Tang, J. Mao, Y. X. Chen, H. Song, J. W. Wang, Y. Song, Y. Q. Liang, X. M. Zhang, One-Dimensional  $\text{MoS}_2$ -Decorated  $\text{TiO}_2$  nanotube gas sensors for efficient alcohol sensing, *J. Alloy. Compd.* 674 (2016) 252-258.
58. Y. Zhang, D. Zhang, W. Guo, S. Chen, The  $\alpha$ - $\text{Fe}_2\text{O}_3$ /g- $\text{C}_3\text{N}_4$  heterostructural nanocomposites with enhanced ethanol gas sensing performance, *J. Alloy. Compd.* 685 (2016) 84-90.
59. N. T. A. Thu, N. D. Cuong, L. C. Nguyen, D. Q. Khieu, P. C. Nam, N. V. Toan, C. M. Hung, N. V. Hieu,  $\text{Fe}_2\text{O}_3$  nanoporous network fabricated from  $\text{Fe}_3\text{O}_4$ /reduced graphene oxide for high-performance ethanol gas sensor, *Sens. Actuators B Chem.* 255 (2018) 3275-3283.
60. T. Wang, X. Kou, L. Zhao, P. Sun, C. Liu, Y. Wang, K. Shimano, N. Yamazoe, G. Lu, Flower-like  $\text{ZnO}$  hollow microspheres loaded with  $\text{CdO}$  nanoparticles as high performance sensing material for gas sensors, *Sens. Actuators B Chem.* 250 (2017) 692-702.
61. J. Fang, Y. Zhu, D. Wu, C. Zhang, S. Xu, D. Xiong, P. Yang, L. Wang, P. K. Chu, Gas sensing properties of  $\text{NiO}/\text{SnO}_2$  heterojunction thin film, *Sens. Actuators B Chem.* 252 (2017) 1163-1168.
62. B. Huang, Z. Zhang, C. Zhao, L. Cairang, J. Bai, Y. Zhang, X. Mu, J. Du, H. Wang, X. Pan, J. Zhou, E. Xie, Enhanced gas-sensing performance of  $\text{ZnO}@ \text{In}_2\text{O}_3$  core@shell nanofibers prepared by coaxial electrospinning, *Sens. Actuators B Chem.* 255 (2018) 2248-2257.
63. S. Yan, X. Liang, H. Song, S. Ma, Y. Lu, Synthesis of porous  $\text{CeO}_2$ - $\text{SnO}_2$  nanosheets gas sensors with enhanced sensitivity, *Ceram. Int.* 44 (2018) 358-363.
64. H. Wang, S. Wei, F. Zhang, Y. Li, L. Liu, X. Guo, L. Song, Sea urchin-like  $\text{SnO}_2/\text{Fe}_2\text{O}_3$  microspheres for an ethanol gas sensor with high sensitivity and fast response/recovery, *J. Mater. Sci-Mater El.* 28 (2017) 9969-9973.

# Chapter 6

## SUMMARY

---

Research dedicated to the development of efficient fabrication methods of 2D TMOs has grown explosively and gained impressive progress during the last few years. ALD method was distinguished from other techniques due to the excellent thickness control, good homogeneity, and conformity. From the survey of the latest research work, compared to 2D TMDs, 2D TMOs have attracted less attention. However, TMOs are more chemically stable and environmental friendly as well as easier to be prepared than TMDs, especially for some selected TMOs. In the present dissertation, two kinds of TMOs ( $\alpha$ -MoO<sub>3</sub> and WO<sub>3</sub> nanofilms) with the controlled thickness were developed by the ALD technique towards their application in various environmental sensors.

2D  $\alpha$ -MoO<sub>3</sub> nanofilms with a thickness of 4.9 nm were successfully fabricated by the ALD technique using (N<sup>t</sup>BuN)<sub>2</sub>(NMe<sub>2</sub>)<sub>2</sub>Mo and oxygen plasma gas as the molybdenum precursor and oxygen precursor, respectively to be utilized as a high-performance electrocatalysts towards hydrogen peroxide at various conditions. To the best of our knowledge, this is the first report of the employment of 2D  $\alpha$ -MoO<sub>3</sub> nanofilms for the electrochemical detection of hydrogen peroxide. The high sensitivity (168.72  $\mu$ A mM<sup>-1</sup> cm<sup>-2</sup>) and an extremely wide linear range (0.4  $\mu$ M to 57.6 mM) with the low detection limit (0.076  $\mu$ M) provide an excellent opportunity for this 2D materials to be used in high-performance electrochemical sensors.

In this regard, the thickness of 2D nanostructure is a vital parameter to be considered for the design of applicable devices. 2D WO<sub>3</sub> nanofilms with the different thicknesses from a monolayer ( $\sim$ 0.78 nm) to  $\sim$ 6.5 nm were successfully deposited on Au-SiO<sub>2</sub>/Si substrates by the ALD technique, and their electro-catalytic behaviors toward the hydrazine oxidation were comprehensively investigated. Among those 2D WO<sub>3</sub> samples, the monolayer WO<sub>3</sub> films with demonstrated the superior performance of 1.24  $\mu$ A  $\mu$ M<sup>-1</sup> cm<sup>-2</sup> with a low detection limit of 0.015  $\mu$ M due to the larger effective surface area and smaller charge transfer resistance.

Notwithstanding many outstanding physical and chemical properties obtained for 2D TMOs, a lot of challenges still remain, such as finding an effective synthetic method which is simple and can be scaled up, low yield production of atomically thin 2D TMOs, and the intrinsic low electric conductivity, which presently unable these 2D nanostructures to meet most of the commercial requirements. At this point, the functionalization of 2D TMOs with other nanomaterials has been considered as a very promising technique for enhancement of various properties of 2D TMOs.

Noble metal nanoparticles are particularly interesting for materials science due to their unique electronic, optical, magnetic, and catalytic properties, which are not easily replaced by other materials. Thus, surface functionalization of 2D  $\text{WO}_3$  nanofilms by NM nanoparticles (NM = Ag, Pt, and Pd) was successfully achieved for the first time via a combination of the ALD process and electrochemical deposition method. The impacts of different kinds and various amounts of NM nanoparticles on the performance of 2D  $\text{WO}_3$  nanofilms were investigated towards  $\text{H}_2\text{O}_2$  detections.  $\text{Ag}_{200}\text{-WO}_3$  nanofilms exhibited the best electrochemical performance with the high sensitivity of  $282 \mu\text{A mM}^{-1} \text{cm}^{-2}$ , extremely wide linear  $\text{H}_2\text{O}_2$  concentrations range from  $0.2 \mu\text{M}$  to  $33.6 \text{ mM}$  and the low detection limit of  $0.1 \text{ mM}$ . These results may indicate that choosing the proper kind and amount of NM enables the **substantial** improvement of the 2D TMOs properties.

In addition, for the application of 2D TMOs in gas sensor, the development of heterojunctions has also been proven to be the most simple and cheapest way in achieving enhanced sensing performance by the development of heterojunction at the interface between the two nanomaterials with the creation of either an n/p-type nanostructure or an n/n-(p/p-) type structure. In this work, wafer-scale  $\text{Ga}_2\text{O}_3\text{-WO}_3$  heterostructures with an average thickness of  $\sim 8.0 \text{ nm}$  were successfully fabricated via a two-step ALD process. The gas sensors based on these  $\text{Ga}_2\text{O}_3\text{-WO}_3$  n/p heterostructures exhibited about 4 and a 10-fold improvement in response to ethanol compared to that of  $\text{WO}_3$  and  $\text{Ga}_2\text{O}_3$  nanofilms at  $275^\circ\text{C}$ .

# HOOFDSTUK 6

## SAMENVATTING

---

Het onderzoek naar de ontwikkeling van efficiënte productiemethodes van 2D transitimetaaloxides and dichalcogenides (TMO&Ds) is in de laatste jaren exponentieel toegenomen en heeft een indrukwekkende vooruitgang geboekt. Atomische laagdepositie (ALD) onderscheidde zich van andere technieken door een uitstekende controle van de dikte, een goede homogeniteit en conformiteit. Echter, vergeleken met 2D TMDs hebben 2D TMO minder aandacht gekregen. Echter, TMOs zijn chemisch meer stabiel en milieuvriendelijker, en zijn bovendien gemakkelijker te bereiden, zeker voor bepaalde soorten. In de onderliggende thesis werden twee soorten TMOs ontwikkeld ( $\alpha$ -MoO<sub>3</sub> and WO<sub>3</sub> nanofilms) door ALD met controle van de dikte, en hun toepassingen als milieusensoren werden toegelicht.

2D  $\alpha$ -MoO<sub>3</sub> nanofilms met een dikte van 4.9 nm werden succesvol ontwikkeld door ALD en het gebruik van (N<sup>t</sup>BuN)<sub>2</sub>(NMe<sub>2</sub>)<sub>2</sub>Mo and zuurstof plasmagas als molybdeen precursor en zuurstof precursor, respectievelijk, en werden gebruikt als hoogwaardige elektrokatalysatoren voor waterstofperoxide onder verschillende omstandigheden. Tot voor zover bij ons gekend, is dit het eerste rapport dat 2D  $\alpha$ -MoO<sub>3</sub> nanofilms gebruikt voor de elektrochemische detectie van waterstofperoxide. De hoge gevoeligheid (168.72  $\mu$ A mM<sup>-1</sup> cm<sup>-2</sup>) en het zeer grote lineaire bereik (0.4  $\mu$ M to 57.6 mM), gecombineerd met een extreem lage detectielimiet (0.076  $\mu$ M) maken deze 2D materialen uitermate geschikt voor dergelijk onderzoek. Voor de ontwikkelingen van toepassingen en apparatuur hierop gebaseerd, is de dikte van de 2D nanostructuur een cruciale paramter. 2D WO<sub>3</sub> nanofilms met verschillende diktes (variërend van een enkelvoudige laag ( $\sim$ 0.78 nm) to  $\sim$ 6.5 nm) werden succesvol gedeponerd op Au-SiO<sub>2</sub>/Si substraten door ALD en hun electro-catalytisch gedrag tegenover hydrazide oxidatie werden uitvoerig onderzocht. Van al deze 2D WO<sub>3</sub> stalen, bleek de *monolayer* WO<sub>3</sub> film superieur met 1.24  $\mu$ A  $\mu$ M<sup>-1</sup> cm<sup>-2</sup> én een detectielimiet van 0.015  $\mu$ M door de grotere effectieve oppervlakte én een lagere ladingtransfer weerstand.

Niettegenstaande de vele uitstekende fysische en chemische eigenschappen van 2D TMOs, blijven er een aantal uitdagingen zoals het vinden van een efficiënte synthesesmethode, die eenvoudig en schaalbaar is, productie van atomisch dunne 2D TMOs met lage opbrengst, en de intrinsieke lage elektrische conductiviteit, die ervoor zorgen dat dergelijke 2D nanostructuren commercieel niet inzetbaar zijn. Verdere functionalisering van 2D TMOs met andere nanomaterialen kan dus worden beschouwd als een beloftevolle techniek om 2D TMOs verder te optimaliseren.

Nanopartikels van edele metalen zijn zeer interessant voor materiaalkunde, wegens hun unieke elektrische, optische, magnetische en katalytische eigenschappen, een kunnen niet eenvoudig vervangen worden door andere materialen. Oppervlakte functionalisering van 2D  $\text{WO}_3$  nanofilms door edele metaal nanopartikels (edele metalen = Ag, Pt, en Pd) werd hier voor het eerst betracht, via een combinatie van ALD en elektrochemische depositie. De impact van verschillende (en verschillende hoeveelheden) van deze edele metaalnanostructuren op de 2D  $\text{WO}_3$  nanofilms werd onderzocht in het kader van  $\text{H}_2\text{O}_2$  detectie.  $\text{Ag}_{200}\text{-WO}_3$  nanofilms vertoonden de beste elektrochemische capaciteit, met een hoge gevoeligheid van  $282 \mu\text{A} \cdot \text{mM}^{-1} \cdot \text{cm}^{-2}$ , een zeer groot lineair bereik van  $\text{H}_2\text{O}_2$  concentraties (van  $0.2 \mu\text{M}$  tot  $33.6 \text{ mM}$ ) en een detectielimiet van  $0.1 \text{ mM}$ . Deze resultaten tonen aan dat de keuze van het edele metaal en de hoeveelheid ervan 2D TMOs gevoelig kunnen verbeteren.

Voor de toepassing van 2D TMOs als gassensoren bleek de ontwikkeling van heterojuncties de meest eenvoudige en goedkope oplossing om de detectie te verbeteren, door de heterojunctie tussen twee nanomaterialen te ontwikkelen met de creatie van ofwel een n/p-type nanostructuur of een n-(p/p-) type structuur. In dit werk werden *wafer*-  $\text{Ga}_2\text{O}_3\text{-WO}_3$  heterostructuren met een gemiddelde dikte van  $\sim 8.0 \text{ nm}$  succesvol ontwikkeld via een tweestaps ALD proces. De ontwikkelde gassensoren vertoonden een 4 tot 10-voudige verbetering in response tegenover ethanol, vergeleken met deze van  $\text{WO}_3$  en  $\text{Ga}_2\text{O}_3$  nanofilms bij  $275^\circ\text{C}$ .